Practical Time Averaging of nonlinear dynamics with application to plasticity from discrete dislocation dynamics

Submitted in partial fulfillment of the requirements for
the degree of
Doctor of Philosophy
in

Computational Mechanics

Sabyasachi Chatterjee

B.Tech., Civil Engineering, Indian Institute of Technology, Kharagpur

M.S., Civil and Environmental Engineering, Carnegie Mellon University

Carnegie Mellon University
Pittsburgh, PA

September 2019

Keywords: Dislocation, Coarse-graining, Singular perturbation, Slow-fast systems, Plasticity, Discrete Dislocation Dynamics, Field Dislocation Mechanics, Multiscale modeling

Dedicated to

my mother

Mrs. Swapna Chatterjee

Acknowledgement

I would like to take this opportunity to thank everyone who helped me during the course of my Ph.D. Firstly, I would like to thank my advisor, Prof. Amit Acharya, for his constant support throughout this period. Without his valuable suggestions, this work would not have been possible. Working with him, I developed an understanding of how to debug a big problem by breaking it into parts and solving them in a systematic manner. He also encouraged me to pay attention to details, as sometimes even small anomalies in the results pointed to some bigger underlying issues in our solution.

Next, I would like to thank our collaborator, Dr. Giacomo Po, who helped me with understanding Discrete Dislocation Dynamics and answered my queries related to the usage of the Discrete Dislocation Dynamics library MODEL. I would like to thank Dr. Xiaohan Zhang and Dr. Saurabh Puri for their suggestions involving this work. I would also like to thank Prof. Nasr Ghoniem.

I would like to extend my gratitude to Prof. Zvi Artstein, who was our collaborator for the paper [CAA18]. He and Prof. Amit Acharya developed the theory and framework of Practical Time Averaging (PTA). In addition to that, his valuable comments regarding the paper helped improve its presentation.

I would like to thank my committee members Prof. Robert Suter, Prof. Jacobo Bielak, Prof. Rahul Panat and Prof. Matteo Pozzi for their constructive feedback and suggestion. Thanks are extented to Rajat Arora for his help throughout this period. I also extend my thanks to my group members Chiqun Zhang and Esteban Zegpi.

I am grateful to my friends Rajat, Ankit, Kshiteej, Arnab, Pratik and Utsav for making my stay at CMU a memorable one. Special thanks to my friends Priyankar and Kamalendu for staying in touch and constantly encouraging me. I would also like to thank my mother for being a constant source of support and encouragement.

I am also grateful to Prof. Nilanjan Mitra, Prof. Kousik Deb, Prof. Baidurya Bhattacharya, Prof. Damodar Maity and Prof. D.K. Baidya from IIT Kharagpur for their support during my undergraduate studies.

Thanks are extended to the administrative staff, Maxine Leffard and David Vey, for their help over the last few years.

I acknowledge support from NSF grant NSF-CMMI-1435624. I would also like to acknowledge the financial support from Dean's Fellowship, Ellegood Fellowship and Smith Fellowship at the Department of Civil and Enviromental Engineering at CMU. The generous computing resources provided by Pittsburgh Supercomputing Center is gratefully acknowledged.

Abstract

A novel approach to meso/macroscale plasticity is proposed that does not involve postulating constitutive assumptions beyond those embodied in Discrete Dislocation Dynamics (DD) methodology and macroscopic elastic response. It involves forefront ideas in the mechanics of solids (e.g. continuum mechanics of defects) and applied mathematics, e.g. Young measure theory of averaging for nonlinear Ordinary Differential Equation (ode) systems and their approximation by numerical techniques. This is achieved by a carefully designed coupling of an exact, non-closed Partial Differential Equation (pde) based theory (Mesoscale Field Dislocation Mechanics, MFDM) representing the evolution of averaged dislocation dynamics with DD simulations, MFDM utilizes inputs obtained from space-time averaged response of fast, local DD simulations. The rationale behind using this coupled pde-ode based approach instead of a completely DD based approach is the vast separation in time scales between plasticity applications that operate at quasi-static loading rate (ranging between 10^{-6} s^{-1} to 1 s^{-1}), and the fundamental time scale of dislocation motion as embodied in DD on the order of nanoseconds. Thus, it is impractical to use conventional DD to reach appreciable strain rates using *realistic* loading rates. We discuss the method behind generating the required constitutive inputs for MFDM from DD simulations using a rigorous mathematical theory of averaging ode response, and its essential adaptation for practical implementation that we have called Practical Time Averaging (PTA). In the final part, we derive statements for the evolution of coarse variables that represent an averaged behavior of microscopic dislocation dynamics. We show that the exact averaged evolution equations are extremely cumbersome and non-closed and, more often than not, an infinite hierarchy, and therefore it is more reasonable to close it at a low level using inputs obtained from averaged, stress-coupled, interaction dynamics of dislocations. This acts as a further justification for our coupled MFMD-DD approach.

Contents

List of Figures

List of Tables

Chapter 1

Motivation and Overview

The objective of this work is to develop and demonstrate a predictive computational tool for microstructure-sensitive design of metallic components subjected to mechanical stress and deformation. This is achieved by coupling of a mathematical coarse-graining technique [CAA18, SA12] for nonlinear ode with a pde based model of meso-macroscopic dislocation mediated crystal plasticity [AR06, Ach11a]. The main challenge is the computation of the plastic strength and associated microstructure at the meso and macroscale *at realistic time scales*, directly from the underlying motion of crystal defects. The pde based theory (Mesoscale Field Dislocation Mechanics) contains well-defined place-holders for microscopic dislocation dynamics based input. These inputs are prescribed by a carefully designed coupling, on the 'slow' time-scale of meso-macro response, with time-averaged response of 'fast', local (on the macroscopic scale) Discrete Dislocation dynamics (DD) simulations.

The rationale behind using a coupled approach instead of a completely DD based approach is the vast separation in time-scales between plasticity applications that operate at quasi-static loading rates and DD. Thus, it would be impractical to reach appreciable strains using DD alone. Therefore, we aim to apply a modern theory for singularly perturbed ode systems to generate inputs for MFDM from DD. The approach does not involve postulating constitutive

assumptions beyond those in DD methodology and macroscopic elastic response. Substantial novel steps in this direction have been made in this thesis towards this challenging goal, and the results of the effort are also critically evaluated.

This thesis is organized as follows. In Chapter 2, a computational tool for coarse-graining singularly perturbed nonlinear odes (based on Young Measure theory of averaging on nonlinear ode systems) is discussed, in order to understand their behavior on a time scale that is much slower than the time scales of the intrinsic dynamics. The tool is based on the works in [SA12, CAA18]. The scheme that we use, which is a mixture of rigorous and heuristic arguments, is called Practical Time Averaging (PTA). A literature review of previous work related to the form of equations we consider in the present study is presented at the end of Section 2.2. Three illustrative model examples are worked out that demonstrate the range of capability of the method. The theory and framework was developed by Dr. Amit Acharya and Dr. Zvi Artstein. The algorithm was designed by Dr. Amit Acharya and me. The numerical implementation of the algorithm and the solution of the example problems were done by me. Chapter 2 has been published as [CAA18].

In Chapter 3, the approach to couple MFDM with DD using PTA is discussed. A literature review of previous work on continuum theory of discrete dislocations is presented. The applicability of PTA to the coupling problem at hand, due to the vast scale of separation between the time period of applied loading and the intrinsic time scale of DD, is explained. The setup for running DD simulations is explained. The algorithm for coarse-graining DD simulations in time is outlined and the results for two loading cases of uniaxial tension and simple shear for a $(1\ \mu m)^3$ box, at realistic loading rates and with high speedup in compute time, is presented. Then we explain the methodology for utilizing many such boxes as part of a much larger domain in which we do regular plasticity calculations and solve equilibrium equations (using MFDM), with the averaged DD response serving as local response. In this way, the constitutive assumptions in MFDM are replaced with time averaged inputs from DD

simulations. The modifications in the algorithm compared to Phenomenological Mesoscale Field Dislocation Mechanics (PMFDM, [AR06]) is highlighted. Results are presented for both load and displacement control for the loading cases of uniaxial tension and simple shear at different (and small) loading rates and for different values of mobile and sessile density. These results demonstrate rate and orientation effect and also how the ratio of mobile to sessile segment density play a huge role in the results. We also point out the limitations in our current approach: (i) the dislocation content that is allowed to be mobile should grow in density and some of it should become sessile (in our methodology they will remain mobile but with very small velocities); however, in our approach, the dislocation content that is allowed to be mobile does not grow in density (ii) the excess/GND/polar dislocation velocity is almost negligible. Both of these limitations are because we do not allow, in this first approximation, increase in mobile density in DD boxes in tune with the GND magnitudes suggested from MFDM. In reality, both the mobile dislocation density and the polar dislocation velocity should evolve and be coupled to the evolution of the microstructure and results of MFDM beyond the local stress (e.g. evolving polar density). The formulation of the scheme was done in consultation with Dr. Amit Acharya. The computational tool involved coupling an existing Finite Element based parallel code based on PETSc (developed chronologically by Prof. Amit Acharya, Dr. Anish Roy and Dr. Saurabh Puri) for solving MFDM, with a PTA routine based on the Dislocation Dynamics library MODEL. The modifications to the MFDM code and the entire PTA coupling code was developed by me, with guidance, when necessary, from Prof. Amit Acharya. Dr. Giacomo Po helped me with questions related to the usage of MODEL. Additional ideas on setting up the code was provided by Dr. Xiaohan Zhang (ex-student in Acharya group).

In Chapter 4, a formal derivation of the governing field equations of a detailed space-time averaged behavior of microscopic dislocation dynamics is presented. We show that the averaged evolution equations, although exact, are not closed, and may result in an infinite hierarchy of equations. They become exceedingly cumbersome as we incorporate more detail

into the description of the defined average variables, thereby providing justification for using closure assumptions, at a low level in the hierarchy, generated from stress coupled DD interaction dynamics, and their averaging at a low level to maintain tractability. This acts as a motivation for the work presented in Chapter 3, where we use space-time averaged inputs from DD to replace the constitutive assumptions in MFDM. The derivation of the averaged evolution equations was done in consultation with Dr. Amit Acharya.

Chapter 2

Computing Singularly Perturbed Differential Equations

2.1 Introduction

We are concerned with a computational tool for understanding the behavior of systems of evolution, governed by (nonlinear) ordinary differential equations, on a time scale that is much slower than the time scales of the intrinsic dynamics. A paradigmatic example is a molecular dynamic assembly under loads, where the characteristic time of the applied loading is very much larger than the period of atomic vibrations. We examine appropriate theory for such applications and devise a computational algorithm. The singular perturbation problems we address contain a small parameter ϵ that reflects the ratio between the slow and the fast time scales. In many cases, the solutions of the problem obtained by setting the small parameter to zero matches solutions to the full problem with small ϵ, except in a small region - a boundary/initial layer. But, there are situations, where the limit of solutions of the original problem as ϵ tends to zero does not match the solution of the problem obtained by setting the small parameter to zero. This chapter covers this aspect as well.

In the next section we present the framework of the present study, and its sources. We also display previous approaches to the computational challenge. It allows us to pinpoint our contribution. Our algorithm is demonstrated through computational examples on three model problems that have been specially designed to contain the complexities in temporal dynamics expected in more realistic systems. The implementation is shown to perform robustly in all cases. These cases include the averaging of fast oscillations as well as of exponential decay, including problems where the evolution of slow variables can display fast, almost-discontinuous, behavior in time. The problem set is designed to violate any ergodic assumption, and the computational technique deals seamlessly with situations that may or may not have a unique invariant measure for averaging fast response for fixed slow variables. Thus, it is shown that initial conditions for the fast dynamics matter critically in many instances, and our methodology allows for the modeling of such phenomena. The method also deals successfully with conservative or dissipative systems. In fact, one example on which we demonstrate the efficacy of our computational tool is a linear, spring-mass, *damped* system that can display permanent oscillations depending upon delicate conditions on masses and spring stiffnesses and initial conditions; we show that our methodology does not require *a-priori* knowledge of such subtleties in producing the correct response.

2.2 The framework

A particular case of the differential equations we deal with is of the form

$$\frac{dx}{dt} = \frac{1}{\epsilon}F(x) + G(x), \tag{2.2.1}$$

with $\epsilon > 0$ a small real parameter, and $x \in \mathbb{R}^n$. For reasons that will become clear in the sequel we refer to the component $G(x)$ as the drift component.

Notice that the dynamics in (2.2.1) does not exhibit a prescribed split into a fast and a slow

dynamics. We are interested in the case where such a split is either not tractable or does not exist.

Another particular case where a split into a fast and slow dynamics can be identified, is also of interest to us, as follows.

$$\begin{aligned} \frac{dx}{dt} &= \frac{1}{\epsilon}F(x,l) \\ \frac{dl}{dt} &= L(x,l), \end{aligned} \tag{2.2.2}$$

with $x \in \mathbb{R}^n$ and $l \in \mathbb{R}^m$. We think of the variable l as a load. Notice that the dynamics of the load is determined by an external "slow" equation, that, in turn, may be affected by the "fast" variable x.

The general case we study is a combination of the previous two cases, namely,

$$\begin{aligned} \frac{dx}{dt} &= \frac{1}{\epsilon}F(x,l) + G(x,l) \\ \frac{dl}{dt} &= L(x,l), \end{aligned} \tag{2.2.3}$$

which accommodates both a drift and a load. In the theoretical discussion we address the general case. We display the two particular cases, since there are many interesting examples of the type (2.2.1) or (2.2.2).

An even more general setting would be the case where the right hand side of (2.2.3) is of the form $H(x,l,\epsilon)$, namely, there is no a priori split of the right hand side of the equation into fast component and a drift or a slow component. A challenge then would be to identify, either analytically or numerically, such a split. We do not address this case here, but our study reveals what could be promising directions of such a general study.

We recall that the parameter ϵ in the previous equation represents the ratio between the slow (or ordinary) part in the equation and the fast one. In Appendix A.2 we examine one

of our examples, and demonstrate how to derive the dimensionless equation with the small parameter, from the raw mechanical equation. In real world situations, ϵ is small yet it is not infinitesimal. Experience teaches us, however, that the limit behavior, as ϵ tends to 0, of the solutions is quite helpful in understanding of the physical phenomenon and in the computations. This is, indeed, demonstrated in the examples that follow.

References that carry out a study of equations of the form (2.2.1) are, for instance, Tao, Owhadi and Marsden [TOM10], Artstein, Kevrekidis, Slemrod and Titi [AKST07], Ariel, Engquist and Tsai [AET09a, AET09b], Artstein, Gear, Kevrekidis, Slemrod and Titi [AGK$^+$11], Slemrod and Acharya [SA12]; conceptually similar questions implicitly arise in the work of Kevrekidis et al. [KGH$^+$03]. The form (2.2.2) coincides with the Tikhonov model, see, e.g., OMalley [OJ14], Tikhonov, Vasileva and Sveshnikov [TVS85], Verhulst [Ver05], or Wasow [Was65]. The literature concerning this case followed, mainly, the so called Tikhonov approach, namely, the assumption that the solutions of the x-equation in (2.2.2), for l fixed, converge to a point $x(l)$ that solves an algebraic equation, namely, the second equation in (2.2.3) where the left hand side is equal to 0. The limit dynamics then is a trajectory $(x(t), l(t))$, evolving on the manifold of stationary points $x(l)$. We are interested, however, in the case where the limit dynamics may not be determined by such a manifold, and may exhibit infinitely rapid oscillations. A theory and applications alluding to such a case are available, e.g., in Artstein and Vigodner [AV96], Artstein [Art02], Acharya [Ach07, Ach10], Artstein, Linshiz and Titi [ALT07], Artstein and Slemrod [AS01].

2.3 The goal

A goal of our study is to suggest efficient computational tools that help revealing the limit behavior of the system as ϵ gets very small, this on a prescribed, possibly long, interval. The challenge in such computations stems from the fact that, for small ϵ, computing the

ordinary differential equation takes a lot of computing time, to the extent that it becomes not practical. Typically, we are interested in a numerical description of the full solution, namely, the progress of the coupled slow/fast dynamics. At times, we may be satisfied with partial information, say in the description of the progress of a slow variable, reflecting a measurement of the underlying dynamics. To that end we first identify the mathematical structure of the limit dynamics on the given interval. The computational algorithm will reveal an approximation of this limit dynamics, that, in turn, is an approximation of the full solution for arbitrarily small ϵ. If only a slow variable is of interest, it can be derived from the established approximation.

2.4 The limit dynamics

In order to achieve the aforementioned goal, we display the limit structure, as $\epsilon \to 0$, of the dynamics of (2.2.3). To this end we identify the *fast time equation*

$$\frac{dx}{d\sigma} = F(x, l), \tag{2.4.1}$$

when l is held fixed (recall that l may not show up at all, as in (2.2.1)). The equation (2.4.1) is the *fast part* of (2.2.3) (as mentioned, $G(x)$ is the *drift* and the solution $l(t)$ of the load equation is the *load*).

Notice that when moving from (2.2.3) to (2.4.1), we have changed the time scale, with $t = \epsilon\sigma$. We refer to σ as the fast time scale.

In order to describe the limit dynamics of (2.2.3) we need the notions of: Probability measures and convergence of probability measures, Young measures and convergence in the Young measures sense, invariant measures and limit occupational measures. In particular, we shall make frequent use of the fact that when occupational measures of solutions of (2.4.1), on long time intervals, converge, the limit is an invariant measure of (2.4.1). A concise explanation

of these notions can be found, e.g., in [AV96, AKST07].

It was proved in [AV96] for (2.2.2) and in [AKST07] for (2.2.1), that under quite general conditions, the dynamics converge, as $\epsilon \to 0$, to a Young measure, namely, a probability measure-valued map, whose values are invariant measures of (2.4.1). These measures are drifted in the case of (2.2.1) by the drift component of the equation, and in the case (2.2.2) by the load. We display the result in the general case after stating the assumptions under which the result holds.

$$\frac{dl}{dt} = \int_{\mathbb{R}^n} L(x,l)\mu(t)dx. \tag{2.4.2}$$

The previous general result has not been displayed in the literature, but the arguments in [AKST07] in regard to (2.2.1) or the proof given in [AV96] for the case (2.2.2), apply to the present setting as well.

2.5 Measurements and slow observables

A prime role in our approach is played by *slow observables*, whose dynamics can be followed. The intuition behind the notion is that the observations which the observable reveals, is a physical quantity on the macroscopic level, that can be detected. Here we identify some candidates for such variables. The role they play in the computations is described in the next section.

In most generality, an *observable* is a mapping that assigns to a probability measure $\mu(t)$ arising as a value of the Young measure in the limit dynamics of (2.2.3), a real number, or a vector, say in $\mathbb{R}^k$. Since the values of the Young measure are obtained as limits of occupational measures (that in fact we use in the computations), we also demand that the observable be defined on these occupational measures, and be continuous when passing from

the occupational measures to the value of the Young measure.

An observable $v(.)$ is a *slow observable* if when applied to the Young measure $\mu(.)$ that determines the limit dynamics in Theorems 4.2, the resulting vector valued map $v(t) = v(\mu(t), l(t))$ is continuous at points where the measure $\mu(.)$ is continuous.

An *extrapolation rule* for a slow observable $v(.)$ determines an approximation of the value $v(t+h)$, based on the value $v(t)$ and, possibly, information about the value of the Young measure $\mu(t)$ and the load $l(t)$, at the time t. A typical extrapolation rule would be generated by the derivative, if available, of the slow observable. Then $v(t+h) = v(t) + h\frac{dv}{dt}(t)$.

A trivial example of a slow observable of (2.2.3) with an extrapolation rule is the variable $l(t)$ itself. It is clearly slow, and the right hand side of the differential equation (2.4.2) determines the extrapolation rule, namely :

$$l(t+h) = l(t) + h\frac{dl}{dt}(t). \tag{2.5.1}$$

An example of a slow observable possessing an extrapolation rule in the case of (2.2.1), is an *orthogonal observable*, introduced in [AKST07]. It is based on a mapping $m(x,l) : \mathbb{R}^n \to \mathbb{R}$ which is a first integral of the fast equation (2.4.1) (with l fixed), namely, it is constant along solutions of (2.4.1). Then we define the observable $v(\mu) = m(x,l)$ with x any point in the support of μ. But in fact, it will be enough to assume that the mapping $m(x,l)$ is constant on the supports of the invariant measures arising as values of a Young measure. The definition of $v(\mu) = m(x,l)$ with x any point in the support of μ stays the same, that is, $m(x,l)$ may not stay constant on solutions away from the support of the limit invariant measure. It was shown in [AKST07] for the case (2.2.1), that if $m(.)$ is continuously differentiable, then $v(t)$ satisfies, almost everywhere, the differential equation

$$\frac{dv}{dt} = \int_{R^n} \nabla m(x) G(x) \mu(t) dx. \tag{2.5.2}$$

It is possible to verify that the result holds also when the observable satisfies the weaker condition just described, namely, it is a first integral only on the invariant measures that arise as values of the limit Young measure. The differential equation (2.5.2) is not in a closed form, in particular, it is not an ordinary differential equation. Yet, if one knows $\mu(t)$ and $v(t)$ at time t, the differentiability expressed in (2.5.2) can be employed to get an extrapolation of the form $v(t+h) = v(t) + h\frac{dv}{dt}(t)$ at points of continuity of the Young measure, based on the right hand side of (2.5.2). A drawback of an orthogonal observable for practical purposes is that finding first integrals of the fast motion is, in general, a non-trivial matter.

A natural generalization of the orthogonal observable would be to consider a moment or a generalized moment, of the measure $\mu(t)$. Namely, to drop the orthogonality from the definition, allowing a general $m : \mathbb{R}^n \to \mathbb{R}$ be a measurement (that may depend, continuously though, on l when l is present), and define

$$v(\mu) = \int_{\mathbb{R}^n} m(x)\mu(dx). \tag{2.5.3}$$

Thus, the observable is an average, with respect to the probability measure, of the bounded continuous measurement $m(.)$ of the state. If one can verify, for a specific problem, that $\mu(t)$ is piecewise continuous, then the observable defined in (2.5.3) is indeed slow. The drawback of such an observable is the lack of an apparent extrapolation rule. If, however, in a given application, an extrapolation rule for the moment can be identified, it will become a useful tool in the analysis of the equation.

A generalization of (2.5.3) was suggested in [AS06, AET09a] in the form of running time-averages as slow variables, and was made rigorous in the context of delay equations in [SA12]. Rather than considering the average of the bounded and continuous function $m(x)$ with respect $\mu(t)$, we suggest considering the average with respect to the values of the Young

measure over an interval $[t-\Delta, t]$, i.e,

$$v(t) = \frac{1}{\Delta} \int_{t-\Delta}^{t} \int_{\mathbb{R}^n} m(x)\mu(s)(dx)ds. \tag{2.5.4}$$

Again, the measurement m may depend on the load. Now the observable (2.5.4) depends not only on the value of the measure at t, but on the "history" of the Young measure, namely its values on $[t-\Delta, t]$. The upside of the definition is that $v(t)$ is a Lipschitz function of t (the Lipschitz constant may be large when Δ is small) and, in particular, is almost everywhere differentiable. The almost everywhere derivative of the slow variable is expressed at the points t where $\mu(.)$ is continuous at t and at $t-\Delta$, by

$$\frac{dv}{dt} = \frac{1}{\Delta} \left(\int_{\mathbb{R}^n} m(x)\mu(t)(dx) - \int_{\mathbb{R}^n} m(x)\mu(t-\Delta)(dx) \right). \tag{2.5.5}$$

This derivative induces an extrapolation rule.

For further reference we call an observable that depends on the values of the Young measure over an interval prior to t, an *H-observable* (where the H stands for history).

An H-observable need not be an integral of generalized moments, i.e., of integrals. For instance, for a given measure μ let

$$r(\mu) = max\{x \cdot e_1 : x \in supp(\mu)\}, \tag{2.5.6}$$

where e_1 is a prescribed unit vector and supp(μ) is the support of μ. Then, when supp(μ) is continuous in μ, (and recall Assumption 4.1) the expression

$$v(t) = \frac{1}{\Delta} \int_{t-\Delta}^{t} r(\mu(\tau))d\tau, \tag{2.5.7}$$

is a slow observable, and

$$\frac{dv}{dt} = \frac{1}{\Delta}\left(r(\mu(t)) - r(\mu(t-\Delta))\right) \tag{2.5.8}$$

determines its extrapolation rule.

The strategy we display in the next section applies whenever slow observables with valid extrapolation rules are available. The advantage of the H-observables as slow variables is that any smooth function $m(.)$ generates a slow observable and an extrapolation rule. Plenty of slow variables arise also in the case of generalized moments of the measure, but then it may be difficult to identify extrapolation rules. The reverse situation occurs with orthogonal observables. It may be difficult to identify first integrals of (2.4.1), but once such an integral is available, its extrapolation rule is at hand.

Also note that in all the preceding examples the extrapolation rules are based on derivatives. We do not exclude, however, cases where the extrapolation is based on a different argument. For instance, on information of the progress of some given external parameter, for instance, a control variable. All the examples computed in this chapter will use H-observables.

2.6 The expected savings in computer time

The motivation behind our scheme of computations is that the straightforward approach, namely, running the entire equation (2.2.3) on the full interval, is not feasible if ϵ is very small. To run (2.4.1) in order to compute the invariant measure at a single point t, or to run (2.2.3) on a short interval $[t-\Delta, t]$, with Δ small, does not consume a lot of computing time. Thus, our scheme replaces the massive computations with computing the values of the Young measure at a discrete number of points, or short intervals, and the computation of the extrapolation rules to get an estimate of the progress of the observables. The latter step does not depend on ϵ, and should not consume much computing time. Thus, if h is large (and

large relative to Δ in the case of H-observables), we achieve a considerable saving.

These arguments are also behind the saving in the cited references, i.e., [VE03, FVE04, ALT07, AGK$^+$11]. In our algorithm there is an extra cost of computing time, namely, the need to detect points in the basin of attraction of the respective invariant measures, i.e., Step 3 in our algorithm. The extra steps amount to, possibly, an addition of a discrete number of computations that reveal the invariant measures. An additional computing time may be accrued when facing a discontinuity in the Young measure. The cost is, again, a computation of the full Young measure around the discontinuity. The possibility of discontinuity has not been address in the cited references.

2.7 Computational Implementation

We are given the initial conditions of the fine and the slow variables, $x(-\Delta) = x_0$ and $l(-\Delta) = l_0$. We aim to produce a good approximation, of the limit solution in the period $[0, T_0]$. Due to the lack of algorithmic specification for determining orthogonal observables, we concentrate on H-observables in this chapter.

In the implementation that follows, we get to the specifics of how the calculations are carried out. Recall that the H-observables are averages of the form

$$v(t) = \frac{1}{\Delta} \int_{t-\Delta}^{t} \int_{\mathbb{R}^n} m(x)\mu(s)(dx)ds. \tag{2.7.1}$$

Namely, the H-observables are slow variables with a time-lag, i.e. the fine/microscopic system needs to have run on an interval of length Δ before the observable at time t can be defined.

We will also refer to any component of the list of variables of the original dynamics (2.2.3) as *fine* variables.

We think of the calculations marching forward in the slow time-scale in discrete steps of size h with $T_0 = nh$. Thus the variable t below in the description of our algorithm takes values of $0h, 1h, 2h, \ldots, nh$.

Step 1: Calculate the rate of change of slow variable

We calculate the rate of change of the slow variable at time t using the following:

$$\frac{dv}{dt}(t) = \frac{1}{\Delta}\left(\int_{\mathbb{R}^n} m(x)\mu(t)(dx) - \int_{\mathbb{R}^n} m(x)\mu(t-\Delta)(dx)\right). \tag{2.7.2}$$

Let us denote the term $\int_{\mathbb{R}^n} m(x)\mu(t)(dx)$ as R_t^m and the term $\int_{\mathbb{R}^n} m(x)\mu(t-\Delta)(dx)$ as $R_{t-\Delta}^m$. The term R_t^m is computed as

$$R_t^m = \frac{1}{N_t}\sum_{i=1}^{N_t} m(x_\epsilon(\sigma_i), l_\epsilon(\sigma_i)). \tag{2.7.3}$$

The successive values ($x_\epsilon(\sigma_i)$,$l_\epsilon(\sigma_i)$) are obtained by running the fine system

$$\begin{aligned} \frac{dx_\epsilon}{d\sigma} &= F(x_\epsilon, l_\epsilon) + \epsilon G(x_\epsilon, l_\epsilon) \\ \frac{dl_\epsilon}{d\sigma} &= \epsilon L(x_\epsilon, l_\epsilon), \end{aligned} \tag{2.7.4}$$

with initial condition $x_{guess}(\sigma = \frac{t}{\epsilon})$ and $l(\sigma = \frac{t}{\epsilon})$.

We discuss in Step 5 how we obtain $x_{guess}(\sigma)$. Here, N_t is the number of increments taken for the value of R_t^m to converge upto a specified value of tolerance. Also, N_t is large enough such that the effect of the initial transient does not affect the value of R_t^m.

Similarly, $R_{t-\Delta}^m$ is computed as:

$$R_{t-\Delta}^m = \frac{1}{N_{t-\Delta}}\sum_{i=1}^{N_{t-\Delta}} m\left(x_\epsilon(\sigma_i), l_\epsilon(\sigma_i)\right), \tag{2.7.5}$$

where successive values $x_\epsilon(\sigma_i)$ are obtained by running the fine system (2.7.4) with initial condition $x_{guess}(\sigma - \frac{\Delta}{\epsilon})$ and $l(\sigma - \frac{\Delta}{\epsilon})$.

We discuss in Step 3 how we obtain $x_{guess}(\sigma - \frac{\Delta}{\epsilon})$. Here, $N_{t-\Delta}$ is the number of increments taken for the value of $R^m_{t-\Delta}$ to converge upto a specified value of tolerance.

Step 2: Find the value of slow variable

We use the extrapolation rule to obtain the predicted value of the slow variable at the time $t + h$:

$$v(t + h) = v(t) + \frac{dv}{dt}(t)\, h, \tag{2.7.6}$$

where $\frac{dv}{dt}(t)$ is obtained from (2.7.2).

Step 3: Determine the closest point projection

We assume that the closest-point projection of any fixed point in the fine state space, on the Young measure of the fine evolution, evolves slowly in any interval where the Young measure is continuous. We use this idea to define a guess $x_{guess}(t + h - \Delta)$, that is in the basin of attraction of $\mu(t + h - \Delta)$. The fixed point, denoted as $x^{arb}_{t-\Delta}$, is assumed to belong to the set of points, $x_\epsilon(\sigma_i)$ for which the value of $R^m_{t-\Delta}$ in (2.7.5) converged. Specifically, we make the choice of $x^{arb}_{t-\Delta}$ as $x_\epsilon(\sigma_{N_{t-\Delta}})$ where $x_\epsilon(\sigma_i)$ is defined in (2.7.5) and $N_{t-\Delta}$ is defined in the discussion following it. Next, we compute the closest point projection of this point (in the Euclidean norm) on the support of the measure at $t - h - \Delta$. This is done as follows.

Define $x^{conv}_{t-h-\Delta}$ as the point $x_\epsilon(\sigma_{N_{t-h-\Delta}})$, where $x_\epsilon(\sigma_i)$ is defined in the discussion surrounding (2.7.5) with σ replaced by $\sigma - \frac{h}{\epsilon}$, and $N_{t-h-\Delta}$ is the number of increments taken for the value of $R^m_{t-h-\Delta}$ to converge (the value of $x^{conv}_{t-h-\Delta}$ is typically stored in memory during calculations for the time $t - h - \Delta$). The fine system (2.7.4) with σ replaced by $\sigma - \frac{h}{\epsilon}$ is initiated from $x^{conv}_{t-h-\Delta}$, and we calculate the distance of successive points on this trajectory with respect to $x^{arb}_{t-\Delta}$ until a maximum number of increments have been executed. We set the maximum

number of increments as $2\,N_{t-h-\Delta}$. The point(s) on this finite time trajectory that records the smallest distance from $x^{arb}_{t-\Delta}$ is defined as the closest point projection, $x^{cp}_{t-h-\Delta}$.

Finally, the guess, $x_{guess}(t+h-\Delta)$ is given by

$$x_{guess}(t+h-\Delta) = 2\,x^{arb}_{t-\Delta} - x^{cp}_{t-h-\Delta},$$

for $t > 0$. For $t = 0$, we set

$$x_{guess}(h-\Delta) = x^{arb}_0 + \frac{(x^{arb}_0 - x^{cp}_{-\Delta})}{\Delta}(h-\Delta),$$

where $x^{arb}_{\cdot}$ and $x^{cp}_{\cdot}$ are defined in the first and the second paragraph respectively in Step 3 above with the time given by the subscripts. This is because the computations start at $t = -\Delta$ and we do not have a measure at $t = -h-\Delta$ and hence cannot compute $x^{cp}_{-h-\Delta}$ to be able to use the above formula to obtain $x_{guess}(t+h-\Delta)$.

Step 4: Accept the measure

We initiate the fine equation (2.7.4) at $(x_{guess}(t+h-\Delta), l(t+h-\Delta))$ and run the equation from $\sigma + \frac{h}{\epsilon} - \frac{\Delta}{\epsilon}$ to $\sigma + \frac{h}{\epsilon}$ (recall $\sigma = \frac{t}{\epsilon}$). We say that there is a match in the value of a slow variable *if* the following equality holds (approximately):

$$v(t+h) = \frac{1}{N'}\sum_{i=1}^{N'} m\left(x_\epsilon(\sigma_i), l_\epsilon(\sigma_i)\right), \tag{2.7.7}$$

where $v(t+h)$ refers to the predicted value of the slow variable obtained from the extrapolation rule in Step 2 above. The successive values $(x_\epsilon(\sigma_i), l_\epsilon(\sigma_i))$ are obtained from system (2.7.4). Here, $N' = \frac{\Delta}{\epsilon\,\Delta\sigma}$ where $\Delta\sigma$ is the fine time step.

If there is a match in the value of the slow variable, we accept the measure which is generated, in principle, by running the fine equation (2.7.4) with the guess $x_{guess}(t+h-\Delta)$ and move on to the next coarse increment.

If not, we check if there is a jump in the measure. We say that there is a jump in the measure if the value of R^m_{t+h} is significantly different from the value of R^m_t. This can be stated as:

$$\left|\frac{R^m_{t+h} - R^m_t}{R^m_t}\right| \gg \frac{1}{N}\sum_n \left|\frac{R^m_{t-(n-1)h} - R^m_{t-nh}}{R^m_{t-nh}}\right|, \tag{2.7.8}$$

where n is such that there is no jump in the measure between $t - nh$ and $t - (n-1)h$ and N is the maximal number of consecutive (integer) values of such n.

If there is no jump in the measure, we try different values of $x_{guess}(t + h - \Delta)$ based on different values of $x^{arb}_{t-\Delta}$ and repeat Steps 3 and 4.

If there is a jump in the measure, we declare $v(t+h)$ to be the the right-hand-side of (2.7.7). The rationale behind this decision is the assumption $x_{guess}(t + h - \Delta)$ lies in the basin of attraction of the measure at $t + h - \Delta$.

Step 5: Obtain fine initial conditions for rate calculation

Step 1 required the definition of $x_{guess}(t)$. We obtain it as

$$x_{guess}(t) = x^{arb}_{t-\Delta} + \frac{\left(x^{arb}_{t-\Delta} - x^{cp}_{t-h}\right)}{(h-\Delta)}\,\Delta,$$

for $t > 0$, and $x^{arb}_{\cdot}$ and $x^{cp}_{\cdot}$ are defined in the same way as in Step 3, but at different times given by the subscripts. For $t = 0$, we obtain $x_{guess}(0)$, which is required to compute R^m_0, by running the fine equation (2.7.4) from $\sigma = -\frac{\Delta}{\epsilon}$ to $\sigma = 0$. This is because the computations start at $t = -\Delta$ and we do not have a measure at $t = -h$ and hence cannot compute x^{cp}_{-h} to be able to use the above formula to obtain $x_{guess}(t)$.

We continue in this manner until an approximation of slow observables is computed on the entire time interval $[0, T_0]$.

Discussion The use of the guess for fine initial conditions to initiate the fine system to

compute R^m_{t+h} and $R^m_{t+h-\Delta}$ is an integral part of this implementation. This allows us to systematically use the coarse evolution equation (2.7.2). This feature is a principal improvement over previous work [TAD13, TAD14].

We will refer to this scheme, which is a mixture of rigorous and heuristic arguments, as Practical Time Averaging (PTA) and we will refer to results from the scheme by the same name. Results obtained solely by running the complete system will be referred to as *fine* results, indicated by the superscript or subscript f when in a formula.

Thus, if v is a scalar slow variable, then we denote the slow variable value obtained using PTA scheme as v^{PTA} while the slow variable value obtained by running the fine system alone is called v^f.

The speedup, $S(\epsilon)$, in compute time between the $fine$ and PTA calculations is presented in the results that follow in subsequent sections. This is defined to be the ratio of the time taken by the $fine$ calculations to that by the PTA calculations for an entire simulation, say consisting of n steps of size h on the slow time-scale.

Let $T^{cpu}_f(\epsilon)$ and $T^{cpu}_{PTA}(\epsilon)$ be the compute times to obtain the *fine* and PTA results per jump on the slow time scale, respectively, for the specific value of ϵ. The compute time to obtain the PTA results for n jumps in the slow time scale is $nT^{cpu}_{PTA}(\epsilon)$ which can be written as

$$nT^{cpu}_{PTA}(\epsilon) = nT^{cpu}_{PTA,1}(\epsilon) + T^{cpu}_{PTA,2}(\epsilon),$$

where $T^{cpu}_{PTA,1}(\epsilon)$ is the compute time to perform the computations mentioned in Step 1 to Step 5 for every jump in the slow time scale. Since we cannot use the formula for $x_{guess}(t)$ mentioned in Step 5 to obtain $x_{guess}(0)$ and we have to run the fine equation (2.7.4) from $\sigma = -\frac{\Delta}{\epsilon}$ to $\sigma = 0$, an additional overhead is incurred in the compute time for the PTA

computations which we denote as $T^{cpu}_{PTA,2}(\epsilon)$. Thus

$$S(\epsilon) = \frac{nT^{cpu}_f(\epsilon)}{nT^{cpu}_{PTA}(\epsilon)} \approx \frac{T^{cpu}_f(\epsilon)}{T^{cpu}_{PTA,1}(\epsilon)}.$$

for large n.

Error in the PTA result is defined as:

$$Error(\%) = \frac{v^{PTA} - v^f}{v^f} \times 100. \tag{2.7.9}$$

We obtain v^f as follows:

Step 1: We run the fine system (2.7.4) from $\sigma = -\frac{\Delta}{\epsilon}$ to $\sigma = \frac{T_0}{\epsilon}$ using initial conditions (x_0, l_0) to obtain $(x_\epsilon(\sigma_i), l_\epsilon(\sigma_i))$ where $\sigma_i = i\,\Delta\sigma$ and $i \in \mathbb{Z}_+$ and $i \leq \frac{T_0+\Delta}{\epsilon\,\Delta\sigma}$.

Step 2: We calculate $v^f(t)$ using:

$$v^f(t) = \frac{1}{N'} \sum_{i=N^0(t)}^{N^0(t)+N'} m\left(x_\epsilon(\sigma_i), l_\epsilon(\sigma_i)\right), \tag{2.7.10}$$

where $N' = \frac{\Delta}{\epsilon\,\Delta\sigma}$ and $N^0(t) = \frac{t+\Delta}{\epsilon\,\Delta\sigma}$ where $\Delta\sigma$ is the fine time step.

2.8 Example I: Rotating planes

Consider the following four-dimensional system, where we denote by x the vector $x = (x_1, x_2, x_3, x_4)$.

$$\frac{dx}{dt} = \frac{F(x)}{\epsilon} + G(x), \tag{2.8.1}$$

where:

$$F(x) = ((1 - |x|)x + \gamma(x)) \tag{2.8.2}$$

with

$$\gamma(x) = (x_3, x_4, -x_1, -x_2). \tag{2.8.3}$$

The drift may be determined by an arbitrary function $G(x)$. For instance, if we let

$$G(x) = (-x_2, x_1, 0, 0), \tag{2.8.4}$$

then we should expect nicely rotating two-dimensional planes. A more complex drift may result in a more complex dynamics of the invariant measures, namely the two dimensional limit cycles.

2.8.1 Discussion

The right hand side of the fast equation has two components. The first drives each point x which is not the origin, toward the sphere of radius 1. The second, $\gamma(x)$, is perpendicular to x. It is easy to see that the sphere of radius 1 is invariant under the fast equation. For any initial condition x_0 on the sphere of radius 1, the fast time equation is

$$\dot{\mathbf{x}} = \begin{pmatrix} 0 & 0 & 1 & 0 \\ 0 & 0 & 0 & 1 \\ -1 & 0 & 0 & 0 \\ 0 & -1 & 0 & 0 \end{pmatrix} \mathbf{x} \ . \tag{2.8.5}$$

It is possible to see that the solutions are periodic, each contained in a two dimensional subspace. An explicit solution (which we did not used in the computations) is

$$\mathbf{x} = cos\,(t) \begin{pmatrix} x_{0,1} \\ x_{0,2} \\ x_{0,3} \\ x_{0,4} \end{pmatrix} + sin\,(t) \begin{pmatrix} x_{0,3} \\ x_{0,4} \\ -x_{0,1} \\ -x_{0,2} \end{pmatrix}. \tag{2.8.6}$$

Thus, the solution at any point of time is a linear combination of $\mathbf{x}_0$ and $\gamma(\mathbf{x}_0)$ and stays in the plane defined by them. Together with the previous observation we conclude that the limit occupational measure of the fast dynamics should exhibit oscillations in a two-dimensional subspace of the four-dimensional space. The two dimensional subspace itself is drifted by the drift $G(x)$. The role of the computations is then to follow the evolution of the oscillatory two dimensional limit dynamics.

2.8.2 Results

We chose the slow observables to be the averages over the limit cycles of the four rapidly oscillating variables and their squares since we want to know how they progress. We define the variables $w_i = x_i^2$ for $i = 1, 2, 3$ and 4. The slow variables are x_1^f, x_2^f, x_3^f, x_4^f and w_1^f , w_2^f , w_3^f, w_4^f. The slow variable x_1^f is given by (2.7.1) with $m(x) = x_1$. The slow variables x_2^f, x_3^f and x_4^f are defined similarly. The slow variable w_1^f is given by (2.7.1) with $m(x) = w_1$. The slow variables w_2^f, w_3^f and w_4^f are defined similarly (we use the superscript f, that indicates the *fine* solution, since in order to compute these observables we need to solve the entire equation, though on a small interval). We refer to the PTA variables as x_1^{PTA}, x_2^{PTA}, x_3^{PTA}, x_4^{PTA} and w_1^{PTA} , w_2^{PTA} , w_3^{PTA}, w_4^{PTA}. A close look at the solution (2.8.6) reveals that the averages, on the limit cycles, of the fine variables, are all equal to zero, and we expect the numerical outcome to reflect that. The average of the squares of the fine variables evolve

slowly in time. In our algorithm, non-trivial evolution of the slow variable does not play a role in tracking the evolution of the measure of the complete dynamics. Instead they are used only to accept the slow variable (and therefore, the measure) at any given discrete time as valid according to Step 4 of Section 2.7. It is the device of choosing the initial guess in Step 3 and Step 5 of Section 2.7 that allows us to evolve the measure discretely in time.

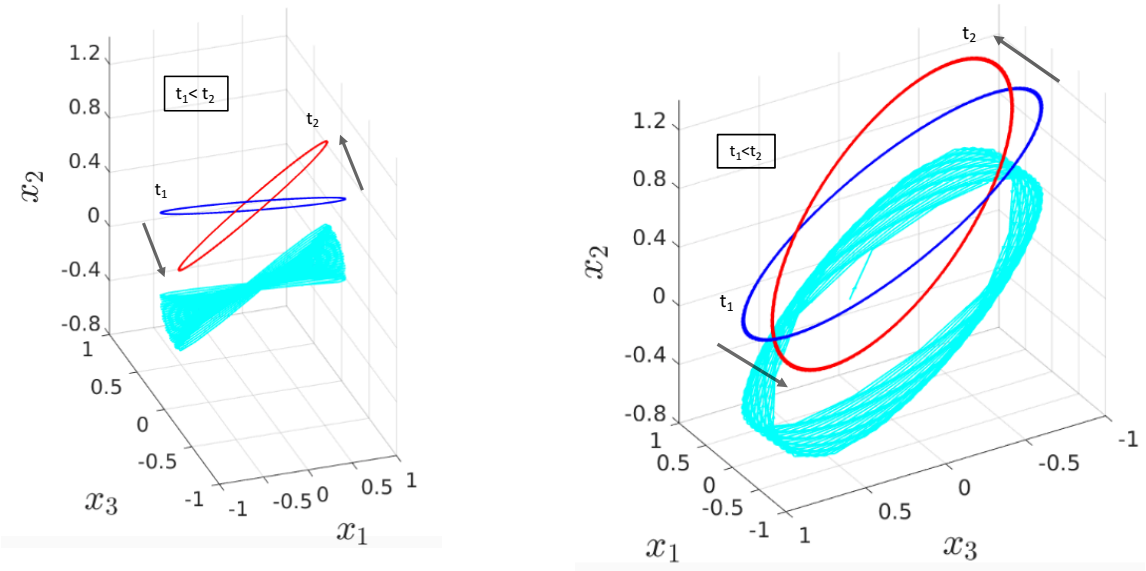

(a) (b)

Figure 2.1: *The curve in cyan shows the phase space diagram of x_1, x_2 and x_3 obtained by running the system (2.8.1) to $t = 2$ with $\epsilon = 10^{-7}$. Part (a) and Part(b) show different views of the phase space diagram. The blue curve shows the portion of the phase portrait obtained around time t_1 while the red curve shows the portion around a later time t_2.*

Fig. 2.1 shows the phase space diagram of x_1, x_2 and x_3.

Fig. 2.2 shows the rapid oscillations of the rapidly oscillating variable x_1 and the evolution of the slow variable x_1^f. Fig. 2.3 shows the rapid oscillations of w_3 and the evolution of the slow variable w_3^f. We find that x_3 and x_4 evolve exactly in a similar way as x_1 and x_2 respectively. We find from the results that x_3^f, x_4^f, w_3^f and w_4^f evolve exactly similarly as x_1^f, x_2^f, w_1^f and w_2^f respectively.

The comparison between the *fine* and the PTA results of the slow variables w_3^f and w_4^f are shown in Fig. 2.4 and Fig. 2.5 (we have not shown the evolution of w_1^f and w_2^f since they

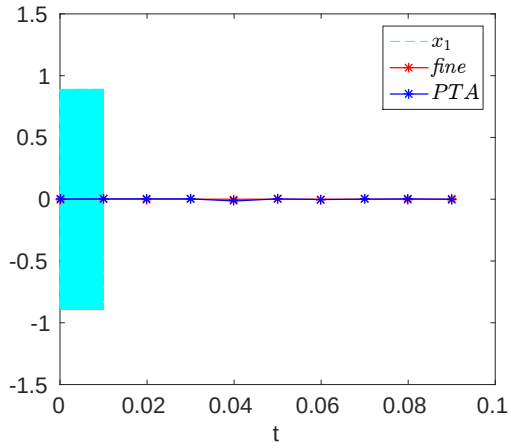

Figure 2.2: *The rapidly oscillating solution of the full equation* of x_1 is given by the plot marked x_1 which shows rapid oscillations around the *fine* and PTA values (which is, as expected, equal to 0). The PTA and the *fine* results overlap.

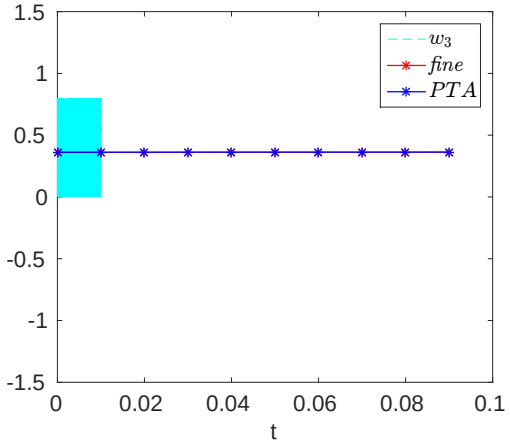

Figure 2.3: *The rapidly oscillating solution of the full equation of* w_3 *is given by the plot marked* w_3. *The drift in the fine and* PTA *values cannot be seen on the given scale. But the drift is visible in Fig. 2.4.* The PTA and the *fine* results overlap.

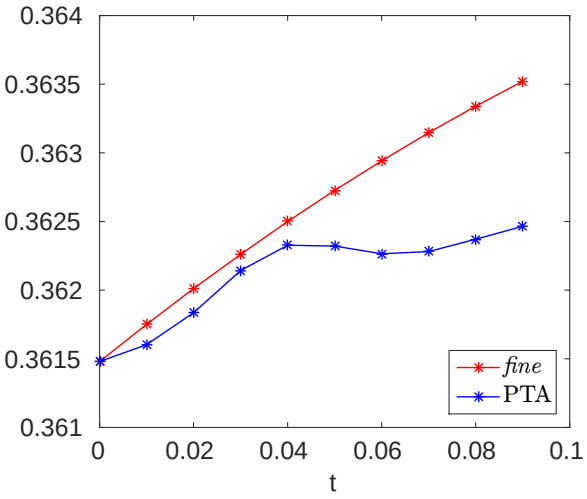

Figure 2.4: *Evolution of* w_3^f.

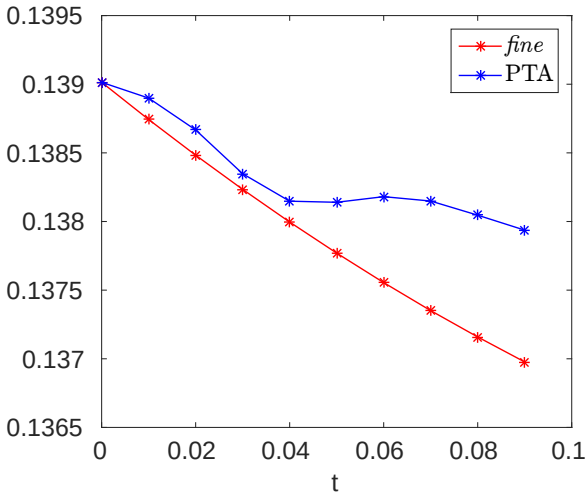

Figure 2.5: *Evolution of* w_4^f.

evolve exactly similarly to w_3^f and w_4^f respectively). The error in the PTA results are shown in Fig. 2.6. Since the values of x_1^f, x_2^f, x_3^f and x_4^f are very close to 0, we have not provided the error in PTA results for these slow variables.

Savings in computer time

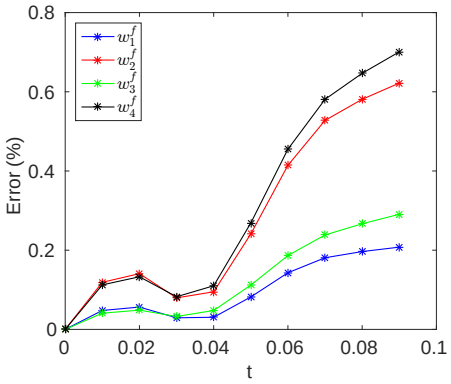

Figure 2.6: *Example I - Error.*

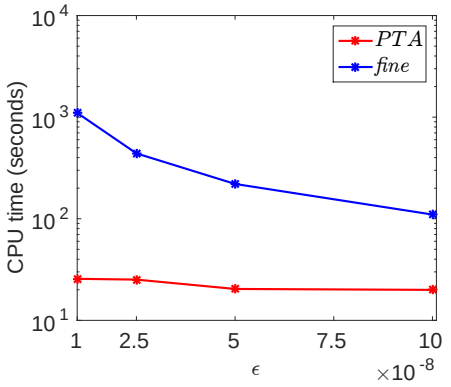

Figure 2.7: *Example I - Compute time comparison for simulations spanning* $t = 0.01$ *to* $t = 0.02$.

In Fig. 2.7, we see that as ϵ decreases, the compute time for the fine run increases very quickly while the compute time for the PTA run increases relatively slowly. The compute times correspond to simulations spanning $t = 0.01$ to $t = 0.02$ with $\Delta = 0.001$. The speedup in compute time, S, obtained as a function of ϵ, is given by the following polynomial:

$$S(\epsilon) = 73.57 - 3.70 \times 10^9\,\epsilon + 6.76 \times 10^{16}\,\epsilon^2 - 3.74 \times 10^{23}\,\epsilon^3. \tag{2.8.7}$$

The function $S(\epsilon)$ is an interpolation of the computationally obtained data to a cubic polynomial. A more efficient calculation yielding higher speedup is to calculate the slow variable v using Simpson's rule. In this problem, we took the datapoint of $\epsilon = 10^{-8}$ and obtained $S(10^{-8}) = 43$. This speedup corresponds to an accuracy of 0.7% error. However, as ϵ

decreases and approaches zero, the asymptotic value of S becomes 74.

2.9 Example II: Vibrating springs

Consider the mass-spring system in Fig. 2.8. The system of equations posed in the slow time scale is

$$\begin{aligned}
\epsilon\frac{dx_1}{dt} &= T_f\, y_1 \\
\epsilon\frac{dy_1}{dt} &= -T_f\left(\frac{k_1}{m_1}(x_1 - w_1) - \frac{\eta}{m_1}(y_2 - y_1)\right) \\
\epsilon\frac{dx_2}{dt} &= T_f\, y_2 \\
\epsilon\frac{dy_2}{dt} &= -T_f\left(\frac{k_2}{m_2}(x_2 - w_2) + \frac{\eta}{m_2}(y_2 - y_1)\right) \\
\frac{dw_1}{dt} &= T_s\, L_1(w_1) \\
\frac{dw_2}{dt} &= T_s\, L_2(w_2)\ .
\end{aligned} \tag{2.9.1}$$

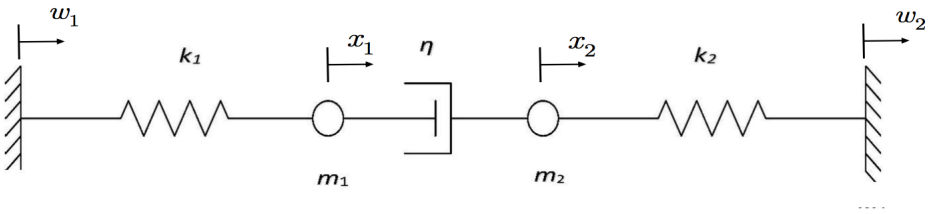

Figure 2.8: Sketch of the mechanical system for problem II.

The derivation of (2.9.1) from the system in dimensional time is given in Appendix A.2. The small parameter ϵ arises from the ratio of the fast oscillation of the springs to the slow application of the load.

2.9.1 Discussion

- For a fixed value of the slow dynamics, that is, for fixed positions w_1 and w_2 of the walls, the dynamics of the fine equation is as follow. If $\frac{k_1}{m_1} \neq \frac{k_2}{m_2}$, then all the energy is dissipated, and the trajectory converges to the origin. If the equality holds, only part of the energy possessed by the initial conditions is dissipated, and the trajectory converges to a periodic one (in rare cases it will be the origin), whose energy is determined by the initial condition. The computational challenge is when fast oscillations persist. Then the limiting periodic solution determines an invariant measure for the fast flow. When the walls move, slowly, the limit invariant measure moves as well. The computations should detect this movement. However, if the walls move very slowly, there is a possibility that in the limit the energy does not change at all as the walls move.

  Notice that the invariant measure is not determined by the position of the walls, and additional slow observables should be incorporated. A possible candidate is the total energy stored in the invariant measure. Since the total energy is constant on the limit cycle, it forms an orthogonal observable as described in section 4. Its extrapolation rule is given by (2.5.1). In order to apply (2.5.1) one has to derive the effect of the movement of the walls on the observable, namely, on the total energy.

  Two other observables could be the average kinetic energy and the average potential energy on the invariant measure. In both cases, the form of H-observables should be employed, as it is not clear how to come up with an extrapolation rules for these observables.

- We define *kinetic energy* (K), *potential energy* (U) and *reaction force* on the right wall

(R_2) as:

$$\begin{aligned} K(\sigma) &= \frac{1}{2}\left(m_1\, y_{1,\epsilon}(\sigma)^2 + m_2\, y_{2,\epsilon}(\sigma)^2\right) \\ U(\sigma) &= \frac{1}{2}k_1(x_{1,\epsilon}(\sigma) - w_{1,\epsilon}(\sigma))^2 + \frac{1}{2}k_2(x_{2,\epsilon}(\sigma) - w_{2,\epsilon}(\sigma))^2 \\ R_2(\sigma) &= -k_2\left(x_{2,\epsilon}(\sigma) - w_{2,\epsilon}(\sigma)\right). \end{aligned} \tag{2.9.2}$$

- The H-observables that we obtained in this example are the *average kinetic energy* (K^f), *average potential energy* (U^f) and *average reaction force* on the right wall (R_2^f) which are calculated as:

$$\begin{aligned} K^f(t) &= \frac{1}{N'}\sum_{i=1}^{N'} K(\sigma_i) \\ U^f(t) &= \frac{1}{N'}\sum_{i=1}^{N'} U(\sigma_i) \\ R_2^f(t) &= \frac{1}{N'}\sum_{i=1}^{N'} R_2(\sigma_i), \end{aligned} \tag{2.9.3}$$

  where N' is defined in the discussion following (2.7.7) and successive values $x_{1,\epsilon}(\sigma_i)$, $x_{2,\epsilon}(\sigma_i)$, $y_{1,\epsilon}(\sigma_i)$ and $y_{2,\epsilon}(\sigma_i)$ are obtained by solving the fine system associated with (2.9.1). The computations are done when $L_1(w_1) = 0$ and $L_2(w_2) = c_2$.

- As we will show in Section 2.9.2 (where we show results for the case corresponding to the condition $\frac{k_1}{m_1} \neq \frac{k_2}{m_2}$ which we call Case 1) and Section 2.9.3 (where we show results for the case corresponding to the condition $\frac{k_1}{m_1} = \frac{k_2}{m_2}$ which we call Case 2) respectively, in Case 1, the fine evolution converges to a singleton (in the case without forcing) while in Case 2, the fine evolution generically converges to a limit set that is not a singleton (which will be shown in Case 2.2 in Section 2.9.3), which shows the distinction between the two cases. This has significant impact on the results of average kinetic and potential energy. Our computational scheme requires no *a-priori*

knowledge of these important distinctions and predicts the correct approximations of the limit solution in all of the cases considered.

- The solutions to the system (2.9.1) corresponding to the Tikhonov framework [TVS85] and the quasi-static assumption commonly made in solid mechanics for mechanical systems forced at small loading rates are provided in Appendix A.3. It is shown that the quasi-static assumption does not apply for this problem. The Tikhonov framework applies in some situations and our computation results are consistent with these conclusions. As a cautionary note involving limit solutions (even when valid), we note that evaluating nonlinear functions like potential and kinetic energy on the weak limit solutions as a reflection of the limit of potential and kinetic energy along sequences of solutions of (2.9.1) as $\epsilon \to 0$ (or equivalently $T_s \to \infty$) does not make sense in general, especially when oscillations persist in the limit. Indeed, we observe this for all results in Case 2.

2.9.2 Results - Case 1 : $\left(\frac{k_1}{m_1} \neq \frac{k_2}{m_2}\right)$

All simulation parameters are grouped in Table 2.1. The total physical time over which the simulation runs is $T_0 T_s$, where T_0 is the total simulation time in the slow time scale (in all computed problems here, we have chosen $T_0 = 1$. The PTA computations done in this section are with the load fixed while calculating R_t^m and $R_{t-\Delta}^m$ using (2.7.3) and (2.7.5) respectively (by setting $\frac{dl_\epsilon}{d\sigma} = 0$ in (2.7.4)). The slow variable value ($v(t+h)$ in (2.7.7)) is calculated using Simpson's rule. The PTA results and the *closed-form* results (denoted by "cf" in the superscript) match for all values of t ($K^{PTA} = 10^{-10} \approx 0 = K^{cf}$, $U^{PTA} = 10^{-10} \approx 0 = U^{cf}$ and $R_2^{PTA} = 10^{-5} \approx 0 = R_2^{cf}$ - note that all the results presented here are non-dimensionalized). In this case, the results from the Tikhonov framework match with our computational approximations. This is because after the initial transient dies out, the whole system displays slow behavior in this particular case. However, the solution under

the quasi-static approximation does not match our computational results (even though the loading rate is small).

Name	Physical definition	Values
k_1	Stiffness of left spring	$10^7\ N/m$
k_2	Stiffness of right spring	$10^7\ N/m$
m_1	Left mass	$1\ kg$
m_2	Right mass	$2\ kg$
η	Damping coefficient of dashpot	$5 \times 10^3\ N\ s/m$
c_2	Velocity of right wall	$10^{-6} = \frac{0.01}{10^4}\ m/s$
h	Jump size in slow time scale	0.25
Δ	Parameter used in rate calculation	0.05

Table 2.1: Simulation parameters for Example 2.

Savings in Computer time

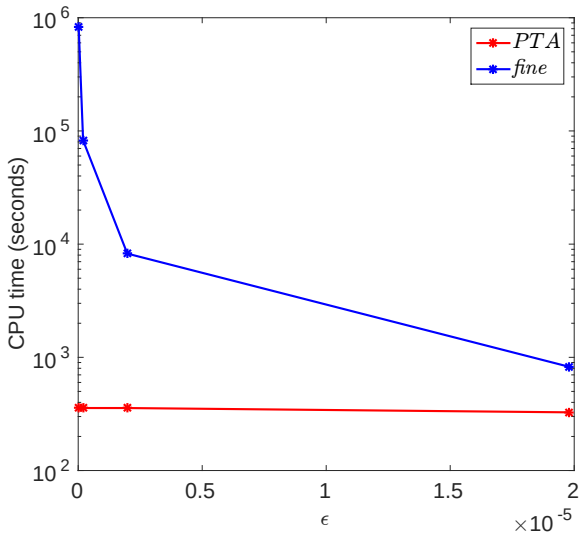

Figure 2.9: *Example II Case 1: Compute time comparison for simulations spanning* $t = 0.25$ *to* $t = 0.5$.

Fig.2.9 shows the comparison between the time taken by the fine and the PTA runs for simulations spanning $t = 0.25$ to $t = 0.5$ with $\Delta = 0.05$. The speedup in compute time is given by the following polynomial:

$$S(\epsilon) = 2.28 \times 10^3 - 1.29 \times 10^{10}\,\epsilon + 6.46 \times 10^{15}\,\epsilon^2 + 2.94 \times 10^{20}\,\epsilon^3. \tag{2.9.4}$$

The function $S(\epsilon)$ is an interpolation of the computationally obtained data to a cubic polynomial. We used the datapoint of $\epsilon = 1.98 \times 10^{-7}$ and obtained $S(1.98 \times 10^{-7}) = 231$. Results obtained in this case have accuracy of 0.0000% error. As ϵ is decreased and approaches zero, the asymptotic value of S is 2.28×10^3.

2.9.3 Results - Case 2: $\left(\frac{k_1}{m_1} = \frac{k_2}{m_2}\right)$

In this case the quasi-static approach is not valid. The closed-form solution to this case is displayed in Appendix A.4 (but it is not used in the computations). Recall that the computations are carried out when $L_1(w_1) = 0$ and $L_2(w_2) = c_2$. The PTA computations done in this section are with the load fixed while calculating R_t^m and $R_{t-\Delta}^m$ using (2.7.3) and (2.7.5) respectively (by setting $\frac{dl_\epsilon}{d\sigma} = 0$ in (2.7.4)). The slow variable value ($v(t+h)$ in (2.7.7)) is calculated using Simpson's rule. All results in this section are non-dimensionalized.

The following cases arise:

- **Case 2.1** When $c_2 = 0$ and the initial condition does not have a component on the modes describing the dashpot being undeformed ($x_1 = x_2$ and $y_1 = y_2$), then the solution will go to rest. For example, the initial conditions ${x_1}^0 = 1.0$, ${x_2}^0 = -0.5$ and ${y_1}^0 = {y_2}^0 = 0.0$ makes the solution go to rest. The simulation results agree with the *closed-form* results and go to zero.

- **Case 2.2** When $c_2 = 0$ and the initial condition has a component on the modes describing the dashpot being undeformed, then in the fast time limit the solution shows periodic oscillations whose energy is determined by the initial conditions. This happens, of course, for almost all initial conditions. One such initial condition is ${x_1}^0 = 0.5$, ${x_2}^0 = -0.1$ and ${y_1}^0 = {y_2}^0 = 0$. The simulation results agree with the *closed-form* results.

  This is in contrast with Case 1 where it is impossible to find initial conditions for which

the solution shows periodic oscillations.

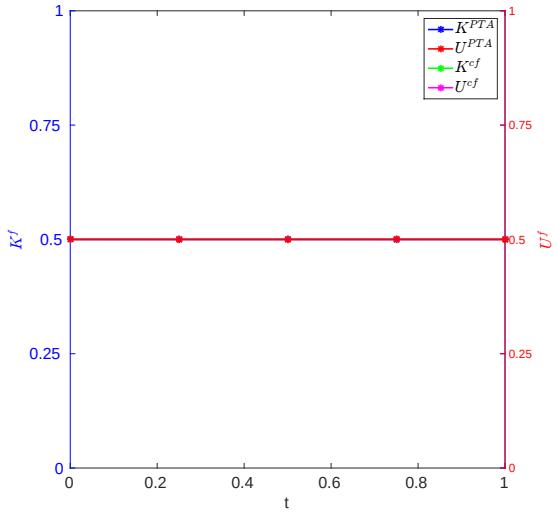

Figure 2.10: *Case 2.2 - Comparison of* K^{PTA}, U^{PTA}, K^{cf} *and* U^{cf}.

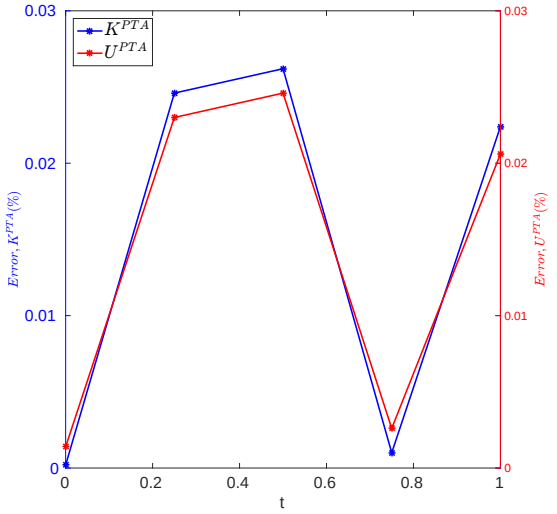

Figure 2.11: *Case 2.2 - Error in* K^{PTA} *and* U^{PTA}.

In Fig. 2.10, we see that the PTA results are very close to the *closed-form* results. The error in PTA results are presented in Fig. 2.11.

Oscillations persist in the limit and the potential and kinetic energies computed based on the Tikhonov framework as well as the quasi-static solution (provided in Appendix A.3) are not expected to, and do not, yield correct answers.

- **Case 2.3** When $c_2 \neq 0$ and the initial condition does not have a component on the modes describing the dashpot being undeformed, then the solution on the fast time scale for large values of σ does not depend on the initial condition. One such initial condition is ${x_1}^0 = 1.0$, ${x_2}^0 = -0.5$ and ${y_1}^0 = 0.0$ and ${y_2}^0 = 10^{-4}$. The *closed-form average kinetic energy* (K^{cf}) and *closed-form average potential energy* (U^{cf}) do not depend on the magnitude of the initial conditions in this case.

- **Case 2.4** The initial condition has a component on the modes describing the dashpot being undeformed. But when $c_2 \neq 0$, the dashpot gets deformed due to the translation of the mass m_2. The *closed-form average kinetic energy* (K^{cf}) and *closed-form average*

potential energy (U^{cf}) depend on the initial conditions.

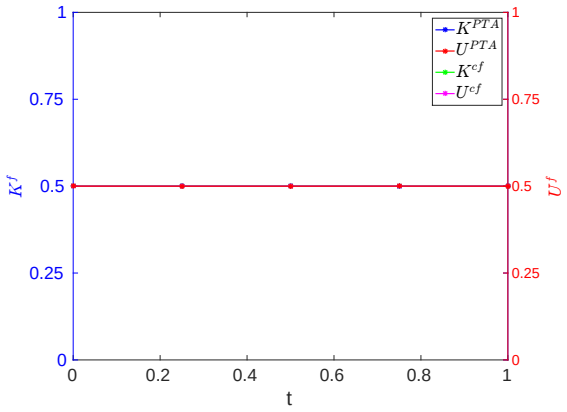

Figure 2.12: *Case 2.4 - Comparison of* K^{PTA}, U^{PTA}, K^{cf} *and* U^{cf}.

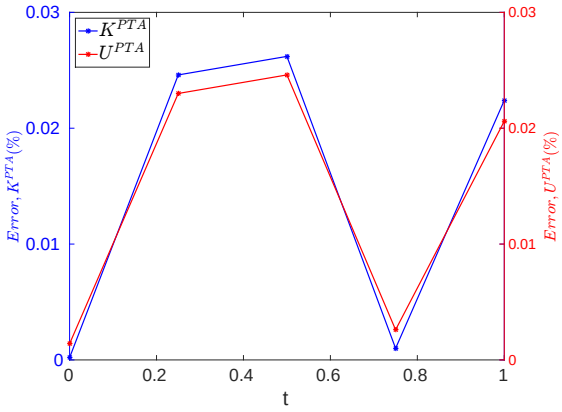

Figure 2.13: *Case 2.4 - Error in* K^{PTA} *and* U^{PTA}.

In Fig. 2.12, we see that the PTA results are very close to the *closed-form* results. The errors in PTA results are presented in Fig. 2.13.

- The comparison between R_2^{PTA} and R_2^{cf} for Case 2.1 to 2.4 is shown in Fig.2.14. The *closed-form* result goes to zero and the PTA result becomes very small.
- Again, oscillations persist in the limit, and the Tikhonov framework and the quasi-static approximation do not work in this case.
- The results do not change if we decrease the value of ϵ. However, the speedup changes as will be shown in *Savings in Computer time* later in this section.

We used the same simulation parameters as in Case 1 (shown in Table 2.1) but with $k_2 = 2 \times 10^7 N/m$ so that $\frac{k_1}{m_1} = \frac{k_2}{m_2}$. Let us assume that the strain rate is $10^{-4}s^{-1}$. Then the slow time period, $T_s = \frac{1}{\epsilon} = 10000s$. The fast time period is obtained as the period of fast oscillations of the spring, given by, $T_f = 2\pi\sqrt{\frac{m_1}{k_1}} = 0.002s$. Thus, we find $\epsilon = \frac{T_f}{T_s} = 1.98 \times 10^{-7}$. While running the PTA code with $\epsilon = 0.002$, we have seen that the PTA scheme is not able to give accurate results and it breaks down.

Savings in Computer time

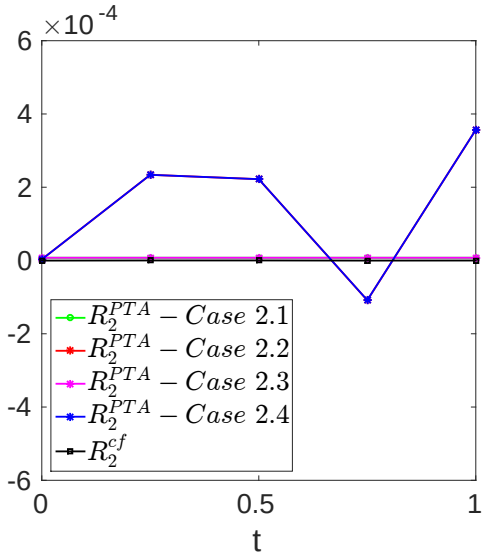

Figure 2.14: *Case 2.1 to 2.4: Comparison of* R_2^{PTA} *and* R_2^{cf}.

It takes the PTA run around 62 seconds to compute the calculations that start at slow time which is a multiple of h (steps 1 through 5 in section 2.7). It takes the fine theory run around 8314 seconds to evolve the fine equation starting at slow time nh to slow time $(n+1)h$, where n is a positive integer. Thus, we could achieve a speedup of 134. We expect that the speedup will increase if we decrease the value of ϵ.

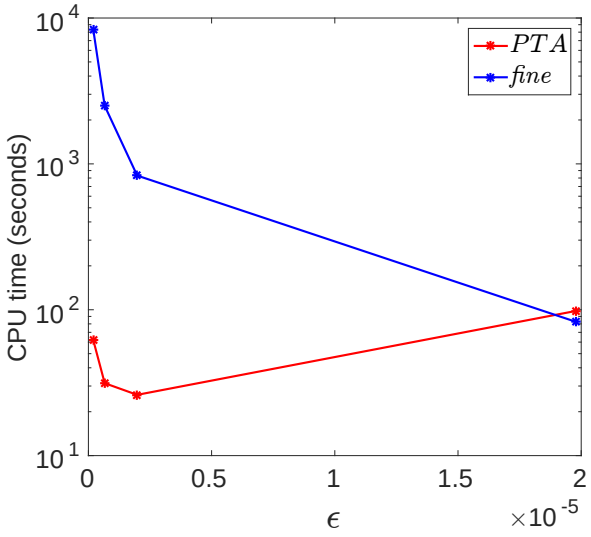

Figure 2.15: *Example II Case 2: Compute time comparison for simulations spanning* $t = 0.25$ *to* $t = 0.5$.

Fig.2.15 shows the comparison between the time taken by the fine and the PTA runs for simulations spanning $t = 0.25$ to $t = 0.5$ with $\Delta = 0.05$.

The speedup in compute time is given by the following polynomial:

$$S(\epsilon) = 164.34 - 1.62 \times 10^8\, \epsilon + 5.23 \times 10^{13}\, \epsilon^2 - 2.25 \times 10^{18} \epsilon^3. \tag{2.9.5}$$

The function $S(\epsilon)$ is an interpolation of the computationally obtained data to a cubic polynomial. We used the datapoint of $\epsilon = 1.98 \times 10^{-7}$ and obtained $S(1.98 \times 10^{-7}) = 134$. This speedup corresponds to an accuracy of 0.026% error. As ϵ is decreased and approaches zero, the asymptotic value of S is 164.

2.10 Example III: Relaxation oscillations of oscillators

This is a variation of the classical relaxation oscillation example(see, e.g., [Art02]). Consider the four-dimensional system

$$\begin{aligned}
\frac{dx}{dt} &= z \\
\frac{dy}{dt} &= \frac{1}{\epsilon}(-x + y - y^3) \\
\frac{dz}{dt} &= \frac{1}{\epsilon}(w + (z - y)(\frac{1}{8} - w^2 - (z - y)^2)) \\
\frac{dw}{dt} &= \frac{1}{\epsilon}(-(z - y) + w(\frac{1}{8} - w^2 - (z - y)^2)).
\end{aligned} \tag{2.10.1}$$

Notice that the (z, w) coordinates oscillate around the point $(y, 0)$ (in the (z, w)-space), with oscillations that converge to a circular limit cycle of radius $\frac{1}{\sqrt{8}}$. The coordinates (x, y) follow the classical relaxation oscillations pattern (for the fun of it, we replaced y in the slow equation by z, whose average in the limit is y). In particular, the limit dynamics of the y-coordinate moves slowly along the stable branches of the curve $0 = -x + y - y^3$, with

discontinuities at $x = -\frac{2}{3\sqrt{3}}$ and $x = \frac{2}{3\sqrt{3}}$. In turn, these discontinuities carry with them discontinuities of the oscillations in the (z, w) coordinates. The goal of the computation is to follow the limit behaviour, including the discontinuities of the oscillations.

2.10.1 Discussion

The slow dynamics, or the load, in the example is the x-variable. Its value does not determine the limit invariant measure in the fast dynamics, which comprises a point y and a limit circle in the (z, w)-coordinates. A slow observable that will determine the limit invariant measure is the y-coordinate. However, this observable does go through periodic discontinuities.

2.10.2 Results

We see in Fig. 2.16 that the y-coordinate moves slowly along the stable branches of the curve $0 = -x + y - y^3$ which is evident from the high density of points in these branches of the curve as can be seen in Fig. 2.16. There are also two discontinuities at $x = -\frac{2}{3\sqrt{3}}$ and $x = \frac{2}{3\sqrt{3}}$. The pair (z, w) oscillates around $(y, 0)$ in circular limit cycle of radius $\frac{1}{\sqrt{8}}$.

In Fig. 2.17, we see that the average of z and y which are given by the y-coordinate in the plot, are the same which acts as a verification that our scheme works correctly. Also, average of w is 0 as expected.

Since there is a jump in the evolution of the measure at the discontinuities (of the Young measure), the observable value obtained using extrapolation rule is not able to follow this jump. However, the observable values obtained using the guess for fine initial conditions at the next jump could follow the discontinuity. This is the principal computational demonstration of this example.

Fig. 2.19 shows the working of the PTA scheme when there is a discontinuity in the Young measure. We obtain the initial guess at time $t + h - \Delta$ by extrapolating the closest point

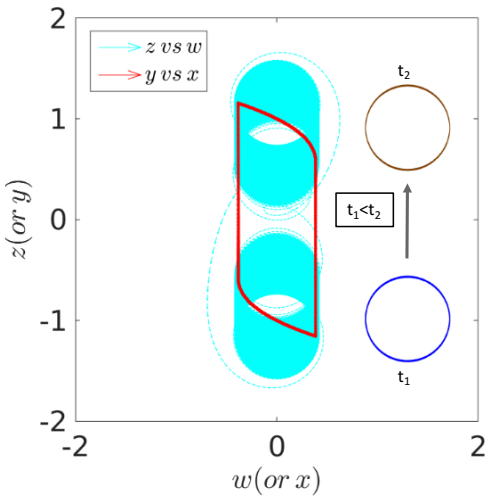

Figure 2.16: *Trajectory of* (2.10.1). *The vertical branches of the y vs x curve correspond to very fast move on the fast time scale. The blue curve shows the portion of the phase portrait of the z vs w trajectory obtained around time* t_1 *while the brown curve shows the portion around a later time* t_2.

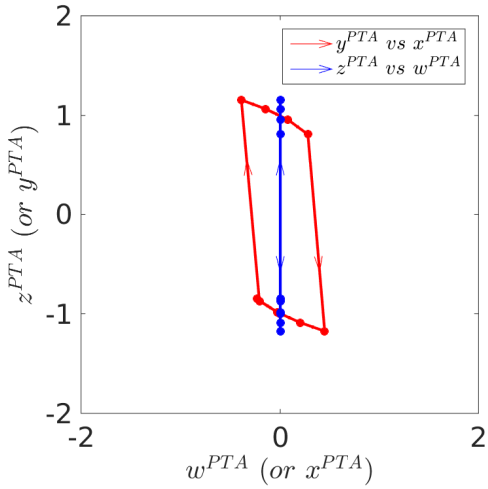

Figure 2.17: *PTA result. The portion with the arrows correspond to very rapid evolution on the slow time scale.*

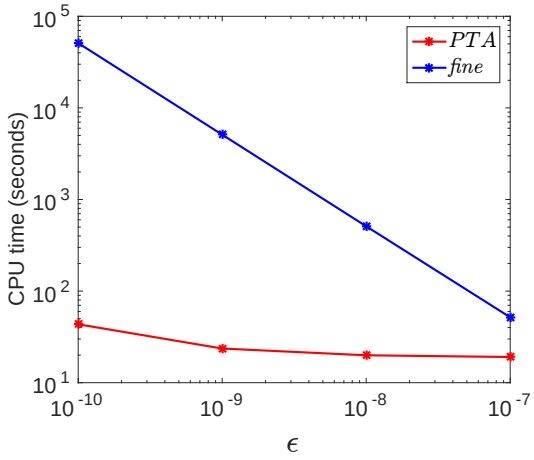

Figure 2.18: *Example III - Compute time comparison for simulations spanning* $t = 0.2$ *to* $t = 0.4$.

projection at time $t - h - \Delta$ of a point on the measure at time $t - \Delta$. The details of the procedure are mentioned in Step 3 of section 2.7. When there is a discontinuity in the Young measure, the results of the slow observables obtained using coarse evolution (Point 6)

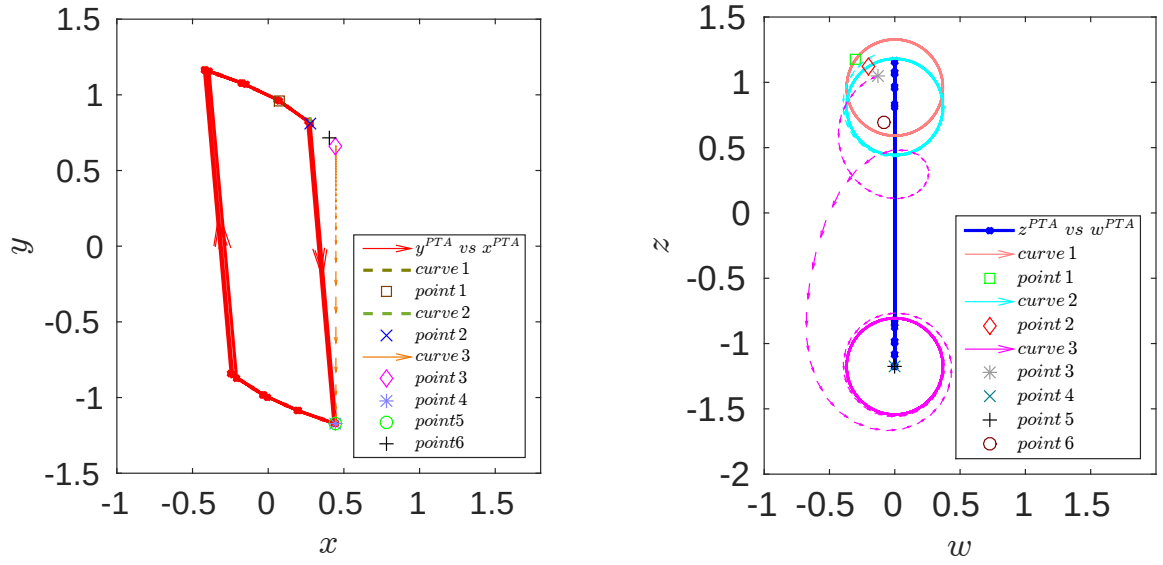

(a) (b)

Figure 2.19: *This figure shows how PTA scheme predicts the correct values of slow observables when there is a discontinuity in the Young measure. Part (a) shows the details for y vs x. The denotations of the different points mentioned here are provided in Step 3 of Section 2.7. Curve 1 is the set of all points in support of the measure at time $t-h-\Delta$. The point $x^{cp}_{t-h-\Delta}$ is given by point 1 in the figure (we obtain Curve 1 and point 1 using the details mentioned in Step 3 of Section 2.7). Curve 1 reduces to a point near point 1, so it is not visible in the figure. Curve 2 is the set of all points in support of the measure at time $t-\Delta$. The point $x^{arb}_{t-\Delta}$ is given by point 2 (we obtain Curve 2 and point 2 using the details mentioned in Step 3 of Section 2.7). Curve 2 reduces to a point very close to point 2, so it is not visible. Point 3 is the initial guess for time $t+h-\Delta$ which we calculate using the details in Step 3 of Section 2.7. Curve 3 is the set of all points in support of the measure at time $t+h-\Delta$. The slow observable value at time $t+h-\Delta$ obtained from the fine run is point 4. Point 5 is the slow observable value obtained from the PTA run using the details in Step 4 of Section 2.7. Point 6 corresponds to slow observable values obtained solely by using the coarse evolution equation without using the initial guess at time $t+h-\Delta$ (using Step 2 of Section 2.7). Part (b) shows the corresponding details for z vs w. In this figure, we see that Curve 1 and Curve 2 do not reduce to a point.*

is unable to follow the discontinuity. But when the fine run is initiated at the initial guess at time $t+h-\Delta$ which is given by Point 3 in the figure, the PTA scheme is able to follow the jump in the measure and we obtain the correct slow observable values (Point 5) which is very close to the slow observable value obtained from the fine run (Point 4).

Savings in computer time The speedup in compute time as a function of ϵ for $\Delta = 0.01$,

is given by the following polynomial :

$$S(\epsilon) = 1.29 \times 10^3 - 1.19 \times 10^{12}\,\epsilon + 1.17 \times 10^{20}\,\epsilon^2 - 1.05 \times 10^{27}\,\epsilon^3. \tag{2.10.2}$$

The function $S(\epsilon)$ is an interpolation of the computationally obtained data to a cubic polynomial. We used the datapoint of $\epsilon = 10^{-10}$ for this problem and obtained $S(10^{-10}) = 1.17 \times 10^3$. This speedup corresponds to an accuracy of 4.33% error. As we futher decrease ϵ and it approaches zero, the asymptotic value of S becomes 1.29×10^3.

Remark As a practical matter, it seems advantageous to set $\epsilon = 0$ in (2.7.4) for the computations of $R^m_{t-\Delta}$ in (2.7.5) and R^m_t in (2.7.3). Related to this, when the value of ϵ is decreased, calculating the slow variable value ($v(t+h)$ in (2.7.7)) using Simpson's rule as described in *Remark* in Appendix A.4 reduces T^{cpu}_{PTA} considerably and improves the speedup $S(\epsilon)$.

2.11 Discussion

The focus of this chapter has been the precise definition and demonstration of a computational tool to probe slow time-scale behavior of rapidly evolving microscopic dynamics, whether oscillatory or exponentially decaying to a manifold of slow variables, or containing both behaviors. A prime novelty of our approach is in the introduction of a general family of observables (H-observables) that is universally available, and a practical computational scheme that covers cases where the invariant measures may not be uniquely determined by the slow variables in play, and one that allows the tracking of slow dynamics even at points of discontinuity of the Young measure. We have solved three model problems that nevertheless contain most of the complications of averaging complex multiscale temporal dynamics. It can be hoped that the developed tool is of substantial generality for attacking real-world practical problems related to understanding and engineering complex microscopic dynamics in relatively simpler terms.

Chapter 3

An approach to plasticity without phenomenology

3.1 Introduction

We aim to develop and demonstrate a predictive computational tool for microstructure-sensitive design of metallic components subjected to mechanical stress and deformation. This will be achieved by coupling of a coarse graining scheme for nonlinear ODE called PTA, which has been described in detail in Chapter 2, with a PDE based model of meso-macroscopic dislocation mediated crystal plasticity [AR06, Ach11a]. The challenge will be the computation of the plastic strength and associated microstructure at the meso and macroscale *at realistic time scales*, directly from the underlying motion of crystal defects, without using constitutive assumptions. The PDE based theory (Mesoscale Field Dislocation Mechanics) contains well-defined place-holders for microscopic dislocation dynamics based input. These inputs will be prescribed by a carefully designed coupling, on the 'slow' time-scale of meso-macro response, with time-averaged response of 'fast', local (on the macroscopic scale) Discrete Dislocation dynamics (DD) simulations.

The rationale behind using a coupled approach instead of a completely DD based approach is the vast separation in time-scales between plasticity applications that operate at quasi-static loading rates and DD. Thus, it would be impractical to reach appreciable strains using DD alone. Therefore, we aim to apply a modern theory for singularly perturbed ODE systems to generate inputs for MFDM from DD. The approach does not involve postulating constitutive assumptions beyond those in DD methodology and macroscopic elastic response.

We will see that we have been able to obtain the stress-strain response of macroscopic samples at realistic loading rates up to appreciable values of strain, without using any phenomenlogical assumptions (except for thermal activation which is not part of the adopted microscopic model, i.e. DD), and with significant speedup in compute time. This would not be possible using conventional DD alone. However, the limitation of the work is that the dislocation content that is allowed to be mobile does not grow in density. Ideally, the mobile dislocations should grow in density and some of them should become sessile. Moreover, the excess/GND/polar dislocation velocity is almost negligible. These limitations are caused because we do not allow, in this first approximation, increase in mobile density in DD boxes in tune with the GND magnitudes suggested from MFDM. In reality, both the mobile dislocation density and the polar dislocation velocity should evolve and be coupled to the evolution of the microstructure and results of MFDM beyond the local stress (e.g. evolving polar density).

3.1.1 Literature review

Plastic deformation of metals depends primarily on the motion and interaction of dislocations. A main goal of crystal plasticity is to develop continuum constitutive relations from the underlying dynamics of a system of discrete dislocations. A statistical approach for the kinetic evolution of idealized dislocation systems on a single slip system in 2-d has been developed. Groma [Gro97] derived a continuum description for a system of straight parallel

dislocations from the equations of motion of individual dislocations. However, to get a closed set of equations, short range dislocation-dislocation interaction was neglected in this work and dislocation-dislocation interactions were only described by long-range terms. El-Azab [EA00, EA06] developed a continuum description of the dynamics of a system of curved dislocation in 3D using a different statistical mechanics framework. This work suffers from an inadequate accounting, at the mesoscale, of the connectedness of dislocation lines. Groma, Zaiser and Csikor [GCZ03] demonstrated the influence of short range dislocation-dislocation correlations by a local flow stress which scales like the square root of dislocation density and a plastic strain gradient term, introduced on an ad-hoc basis, motivated by spatial correlations of 2-d straight discrete dislocation distributions at equilibrium.

Hochrainer et al. [HSZG14] developed Continuum Dislocation Dynamics (CDD) which consists of solving a complicated set of evolution equations of internal variables for each slip system. This system is derived, by averaging over the line direction variable, from a kinetic theory like description for line direction and curvature probability density functions ([HSZG14]). The evolution equations for these density functions, i.e. the microscopic dynamics, are *postulated*, much like in the kinetic theory of gases, *without being derived from discrete dislocation dynamics*; thus such a model accounts for dislocation interactions in an approximate manner, much like the restrictions posed by collision operator approximations in the kinetic theory of gases, and such approximations taking into account dislocation interactions, even in the most rudimentary ways, has not appeared in the so-called 'kinematically-closed' versions of CDD. CDD also does not include physics of dislocation interactions on different slip systems and out of plane motion of dislocations.

Yasin, Zbib and Khaleed [YZK01] developed a numerical model coupling 3D discrete dislocation dynamics with a continuum finite element model in which the plastic strain rate is obtained from DD. However they do not develop the theoretical and computational infrastructure for averaging in time, so their coupled theory in effect operates at the time scale

of DD. Using the superposition principle, dislocation-surface interactions are computed numerically which are shown to have effects on the results. Zbib, Rubia and Bulatov [ZRB02] used a similar hybrid continuum-discrete framework to investigate a wide range of small scale plasticity phenomena such as formation of deformation bands and surface distortions under dynamic loading conditions. Groh and Zbib [GZ09] reviewed the use of dislocation dynamics to replace the constitutive equations in continuum plasticity models. They also addressed issues related to image stresses when dislocations exist in in finite volumes.

Lemarchand [LDK01] proposed the Discrete-Continuum Model (DCM) which is similar to the approach followed by Zbib et. al. ([YZK01], [ZRB02]) in the sense that it uses a coupled DD-finite element approach in which DD is used as a substitute for the constitutive form used in usual finite element frameworks, while the finite element code is used to test the conditions of mechanical equilibrium. However, the difference in this approach from Zbib et. al. ([YZK01], [ZRB02]) is that the stress at the Gauss points of the finite element mesh are interpolated to the midpoint of the dislocation segments to solve for the motion of dislocation segments. This is different from the approach in Zbib et. al. ([YZK01], [ZRB02]) in which the dislocation-dislocation interaction is computed for all dislocations present in the same element to obtain a homogenized internal stress, while the stress induced by dislocation segments not present in the same element is obtained using a multipole expansion.

Acharya and Roy [AR06] proposed Phenomenological Mesoscale Field Dislocation Mechanics (PMFDM) to study initial-boundary value problem of small-scale plasticity. It is obtained by space-time averaging of the equations of Field Dislocation Mechanics (FDM). This involves phenomenologically specifying some space-time averaged inputs from the finer scale model (FDM), which includes a model of plastic strain rate due to dislocations which are averaged out (statistically stored dislocations or SSDs). The resulting coarse model has only one extra material parameter over and above macroscopic continuum plasticity. Finite-element based computational predictions of this theory are presented in [AR06, PDA11, AA19],

where size effects, strong inhomogeneity in simple shear of plastically constrained grains and non-locality in elastic straining leading to Bauschinger effect are demonstrated.

The problem of coupling dislocation-dynamics with a nonlinear continuum theory of plasticity relies in determining the minimum physical set of variable averages (in space and time) to be used in the continuum theory and still be able to correctly capture the micromechanics of plastic deformation. In general, given a large volume V, we decompose it into sub-volumes V_i where dislocation dynamics (DD) is solved in each sub-volume (in this case each dislocation dynamics simulation represents a Gauss point in the large domain). Spatial and time-averages hence need to be computed to couple DD simulations to continuum theory. A simpler case to consider is when we assume that the large domain is composed of only one sub-volume (in this case the DD simulation is considered to be the only Gauss point) and we ignore the spatial-averaging. The steps of computing time-averages are further explained in the next section. The main thing to understand is that we will generally be interested in time-averages of nonlinear state functions and this is not the same thing as evaluating the state functions on time-averages of the state itself.

3.2 PTA for DD simulation

The framework and implementation of a scheme called Practical Time Averaging (PTA) which is used to coarse-grain nonlinear ordinary differential equations in time is discussed in detail in Chapter 2. Here, we discuss why this scheme is relevant for coarse graining DD simulations in time and then lay out the framework of its application. But before that, we present a brief description of DD.

3.2.1 Discrete Dislocation Dynamics

Discrete Dislocation Dynamics (DD) refers to the collective dynamics of dislocation ensembles which is used to predict plastic properties of materials. The goal of DD is to evolve a dislocation configuration based on the local stress. This includes self-stress of the loop, the stress due to other loops and other sources of stress, including externally applied stress. The Cauchy stress tensor due to a dislocation loop [Esh57] is given by

$$\sigma_{ij} = C_{ijkl}(u_{k,l} - \beta^P_{kl}) = S_{ijkl}\boldsymbol{R} * \alpha_{kl},$$

where C is the fourth order, possibly anisotropic tensor of spatially constant linear elastic moduli, $\boldsymbol{u}$ is the displacement field due to the dislocation loop, β^P is the plastic distortion tensor, $\boldsymbol{S}$ is a linear differential operator acting on the Euclidean distance $\boldsymbol{R}$ (given by $\boldsymbol{R} = \boldsymbol{x} - \boldsymbol{x}'$, where $\boldsymbol{x}$ is the point where the stress field is being calculated and $\boldsymbol{x}'$ is a point on the dislocation loop), $\boldsymbol{\alpha}$ is the dislocation density tensor and the symbol $*$ indicates convolution in three dimensional space. The force acting on a dislocation segment of infinitesimal length $d\ell$ due to the stress field is given by $df_k = \epsilon_{kjm}\sigma_{ji}b_i d\ell_m$ and is called the *Peach-Köehler* force ([PK50]).

The velocity field $\boldsymbol{w}$ is defined on the dislocation curves, and discretely on the nodes that discretize the curves. It is obtained by the solution of the following:

$$\oint_{\mathcal{L}} \Big[\tilde{w}_i B_{ij} w_j + \tilde{\lambda_2}\epsilon_{ijk} w_i b_j \hat{\xi_k}\Big] d\ell = \oint_{\mathcal{L}} \Big[\tilde{w}_i \Big(\frac{1}{\theta}\epsilon_{ijk} T_{jm} b_m \hat{\xi_k} - \lambda_2 \epsilon_{ijk} b_j \hat{\xi_k}\Big)\Big] d\ell, \tag{3.2.1}$$

which must be satisfied for arbitrary variations $\tilde{w_i}$ and $\tilde{\lambda_2}$ [PMC+14]. Here, $\boldsymbol{T}$ is the Cauchy stress tensor, $\boldsymbol{b}$ is the Burgers vector of the dislocation loop, $\boldsymbol{\xi}$ is the unit tangent to the dislocation line, $\boldsymbol{B}$ is a positive definite tensor subject to Onsager's symmetry relations, $\boldsymbol{\epsilon}$ is the third order alternating tensor, λ_2 is the chemical force preventing climb, $\mathcal{L}$ is the closed line bounding any surface spanned by the dislocation loop during its motion, θ is the

absolute temperature and $d\ell$ is the length of infinitesimal segment of $\mathcal{L}$.

The position of each node p is updated as

$$\boldsymbol{x}_p(t + \Delta t) = \boldsymbol{x}_p(t) + \boldsymbol{w}_p(t)\Delta t,$$

where t is the current time and Δt is the DD time step.

3.2.2 Thermal activation

Discrete Dislocation Dynamics is described in Section 3.2.1. However, when we use DD, we face a problem which is described next. The local plastic distortion rate $\boldsymbol{L}^p_{seg}$ produced by the motion of a dislocation segment is given by $\boldsymbol{L}^p_{seg} = \frac{\boldsymbol{b}}{A} \otimes (\hat{\boldsymbol{l}} \times \boldsymbol{V})$, where $\boldsymbol{b}$ is the Burgers vector, A is the core cross-section area, $\hat{\boldsymbol{l}}$ is the line direction and $\boldsymbol{V}$ is the velocity of the segment. If a single straight dislocation running from one boundary to another of the DD simulation box is considered and its motion is unimpeded and only driven by the applied stress, then this stress determines the magnitude of $\boldsymbol{V}$ in the expression for $\boldsymbol{L}^p_{seg}$. The value of $|\boldsymbol{L}^p_{seg}|$ due to such a segment, at an applied stress of 10 MPa/s, is around $10^{11} s^{-1}$, which is extremely high.

In order to approach realistic magnitudes of strain rates under slow loading, let the DD box be populated with many straight mobile and sessile dislocation segments running from boundary to boundary of the box (as shown in Fig. 3.2). The setup and its justification are provided later in Section 3.3.2. The mobile segments move and intersect with the sessile segments and such an intersection is called a junction (to be precise, it should be called a sessile junction because this type of junction does not move). The volume averaged plastic distortion rate is given by $\boldsymbol{L}^p_{avg} = \frac{1}{B_x} \sum \boldsymbol{L}^{p,i}_{seg}\, l_i\ A_i$, where l_i and A_i are the length of the segment and area of core cross section (see Fig. 3.1) of dislocation segment i respectively, and $\boldsymbol{L}^{p,i}_{seg}$ is the local plastic strain rate (defined as $\boldsymbol{L}^p_{seg}$ above) produced by dislocation

segment i. When the dislocations are moving freely, the volume averaging reduces the magnitude of the volume averaged plastic distortion rate to around $10^3 s^{-1}$. However, even at very realistic, practical values of applied stress, the configuration gets stuck, i.e. there is no dislocation motion and $|\boldsymbol{L}^p_{avg}|$ is found to vanish. This is due to the high sessile density and low mean spacing between obstacles, so that the applied stress necessary for the mobile segments to break past barriers (the junctions formed at the intersection of mobile and sessile segments) is much higher than the applied stress. So, $|\boldsymbol{L}^p_{avg}|$ is 0 or $10^3 s^{-1}$, and nothing in between.

Therefore, we implement thermal activation of obstacles by breaking junctions (intersection of mobile and sessile dislocation segments) randomly in time to reduce the time averaged value of $|\boldsymbol{L}^p_{avg}|$. This is not a part of conventional DD explained in Section 3.2.1 but is an important constitutive assumption in our approach, based in the modeling of reality. A dislocation is an arrangement of an atomic configuration that is constantly jiggling and when there is substantial temperature - i.e. kinetic energy of atomic motion - coordinated motions can happen for a dislocation to break past barriers. This can be addressed more fundamentally using Molecular Dynamics. Next, we discuss the implementation of thermal activation in our work.

The breaking time, t_b, of a junction is the elapsed time between its formation and its breaking. In the absence of a fundamental characterization of thermal activation from MD, we adopt a very simple functional form for t_b:

$$t_b = f\ a, \tag{3.2.2}$$

where a is the maximum breaking time (in the results presented in Section 3.3.3 and Section 3.5.5, a was set as $10^{-3}\ s$) and f is a fraction generated using a uniformly distributed floating point random number generator. The corresponding attempt frequency of junction breaking may be defined as $\frac{1}{a}$.

With thermal activation enabled (with an attempt frequency of $10^3 s^{-1}$), the time-averaged value of $|\boldsymbol{L}^p_{avg}|$ comes out as $10^{-2} s^{-1}$. It is important to note that the timescale set by the time-averaged value of $|\boldsymbol{L}^p_{avg}|$ (i.e. $10^2\, s^{-1}$) is not directly related to (and orders of magnitude larger) than the timescale set by t_b, and the achieved overall strain rates in the simulations are a truly *emergent* feature of our work that allows us to simulate realistic slow loading rate regimes of behavior.

3.2.3 Application of PTA for coarse-graining DD simulation

The framework of PTA is described in Section 2.2, where we state that PTA can be applied to understand the behavior of equations of the form given by (2.2.2), which have a separation of fast and slow dynamics governed by the small parameter ϵ (which is defined as the ratio of the time period of the fast and the slow dynamics). The problem of studying the slow behavior of DD also has a separation into fast and slow dynamics. The fast dynamics is the evolution of the dislocation segments, whose characteristic time period T_f is set by the drag, which is in the order of *nanoseconds*. The time period of slow dynamics is governed by the applied loading, which typically ranges between 1 to $1000s$. Hence there is a vast separation in time scale of the fast and slow evolution (the parameter $\epsilon = \frac{T_f}{T_s} \approx \frac{10^{-9}}{10^3} = 10^{-12}$), which justifies the application of PTA to this problem in order to study the slow time scale behavior of the fast dynamics (i.e.DD). The DD equations can be posed on the slow time-scale t (corresponding to the time-scale of applied loading) as

$$\begin{aligned} \epsilon \frac{d\boldsymbol{X}}{dt}(t) &= H(\boldsymbol{X}; l) \\ \frac{dl}{dt} &= L(l), \end{aligned} \tag{3.2.3}$$

where $\boldsymbol{X}$ is a n-dimensional vector of position of the segments/nodes. Here, n is assumed to be fixed for now although, as we will discuss in Section 3.2.5, the number of degrees of freedom (dofs) in DD is not fixed. H is a function of the state, L is the loading program

employed and $l(t)$ represents the load (corresponding to the magnitude of the applied stress) on the DD box. The evolution of a single dislocation loop is given by (3.2.1). The evolution of a system of dislocation loops can be posed in the form of (3.2.3), where the function H is composed of the forces experienced by the segments and is composed of the contributions from the rhs of (3.2.1) corresponding to the segments comprising each dislocation loop in the system.

Note that the slow time-scale is related to the fast time-scale σ through

$$t = \epsilon\,\sigma,\ 0 < \epsilon = \frac{T_f}{T_s} \ll 1.$$

The fast time equation, obtained by changing the time scale to $\sigma = \frac{t}{\epsilon}$, is

$$\frac{d\boldsymbol{X}}{d\sigma}(\sigma) = H(\boldsymbol{X}; l). \tag{3.2.4}$$

The general form of H-observables is defined by equation (2.5.4) of Section 2.5 in Chapter 2. Here, we define H-observables of the form

$$\overline{\Lambda}(t) = \int_{t-\Delta}^{t} \int_{\mathbb{R}^N} \Lambda(\gamma)\mu_{t,l(t),\boldsymbol{X}^0}(d\gamma). \tag{3.2.5}$$

The function Λ is a general state function of $\boldsymbol{X}$, l is the applied load and the nondimensional time interval Δ is an interval in the slow time-scale t, and is defined as $\Delta := \frac{\Delta^*}{T_s}$, where Δ^* is a fraction of the slow characteristic time, T_s. The choice of the state function is critical in the initialization of the microstructure after each time step on the slow time-scale. The Young measure $\mu_{(.)}$ was introduced in Section 2.4 of Chapter 2. It is a probability measure-valued map whose values are invariant measures of the fast time equation (3.2.4). In (3.2.5), $\mu_{t,l(t),\boldsymbol{X}^0}$ denotes Young measure at time t, with applied load $l(t)$, starting from initial state $\boldsymbol{X}^0$.

The evolution of $\overline{\Lambda}$ is given by

$$\frac{d\overline{\Lambda}}{dt} = \frac{1}{\Delta}\left(\int_{\mathbb{R}^N} \Lambda(\gamma)\mu_{t+\Delta,l(t+\Delta),\boldsymbol{X}^0}(d\gamma) - \int_{\mathbb{R}^N} \Lambda(\gamma)\mu_{t,l(t),\boldsymbol{X}^0}(d\gamma)\right), \tag{3.2.6}$$

where the Young measures are approximated as averages of M Dirac masses at M values of $\boldsymbol{X}$, i.e.,

$$\mu_{t,l(t),\boldsymbol{X}^0} \approx \frac{1}{M}\sum_{i=1}^{M} \delta(\boldsymbol{X}^{l(t),\boldsymbol{X}^0}(\sigma_i)). \tag{3.2.7}$$

Here, σ_i are the discrete time instants in the fast run with the load $l(t)$ fixed. M is chosen to be large for the averages to converge. The reasoning for arriving at Eq. (3.2.6) is given in Section 2.5 of Chapter 2 (in the discussion before (2.5.5)).

3.2.4 Examples of Λ functions

Here we discuss a few choices of state functions Λ specific to DD and their evolution.

1. Let $\Lambda(\boldsymbol{X}; l) = \boldsymbol{X}_n$, where n counts segments or nodes in the representation of dislocations and $\boldsymbol{X}$ without an index means the whole array of positions of segments/nodes. The initial state of $\boldsymbol{X}$ at any time t on the slow time-scale is given by $\boldsymbol{X}^0(t)$, while the load at time t is given by $l(t)$. Some possible choices of $\boldsymbol{X}^0(t+\Delta)$ are the states and average of states from previous run, at time t. Then:

$$\overline{\dot{\boldsymbol{X}}_n}(t) = \frac{1}{\Delta}\left(\int_{\mathbb{R}^N} \boldsymbol{X}_n(\gamma)\mu_{t+\Delta,l(t+\Delta),\boldsymbol{X}^0(t+\Delta)}(d\gamma) - \int_{\mathbb{R}^N} \boldsymbol{X}_n(\gamma)\mu_{t,l(t),\boldsymbol{X}^0(t)}(d\gamma)\right),$$

2. Let $\Lambda(\boldsymbol{X}; l) = l^{\boldsymbol{x}}(\boldsymbol{X}(\sigma), l(\sigma))$ be the total line length per unit volume of the dislocations present in the DD box at point $\boldsymbol{x}$ and at time σ, then:

$$\overline{\dot{l^{\boldsymbol{x}}}}(t) = \frac{1}{\Delta}\left(\int_{\mathbb{R}^N} l^{\boldsymbol{x}}(\gamma)\mu_{t+\Delta,l(t+\Delta),\boldsymbol{X}^0(t+\Delta)}(d\gamma) - \int_{\mathbb{R}^N} l^{\boldsymbol{x}}(\gamma)\mu_{t,l(t),\boldsymbol{X}^0(t)}(d\gamma)\right).$$

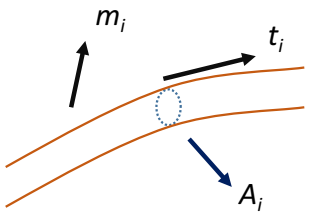

Figure 3.1: *Dislocation segment modeled as cylindrical tube*

Here:

$$l^{\boldsymbol{x}} = \frac{1}{|B_{\boldsymbol{x}}|}\int_{B_{\boldsymbol{x}}} \boldsymbol{\alpha} : \boldsymbol{\alpha}\; dB_{\boldsymbol{x}} = \frac{1}{|B_{\boldsymbol{x}}|}\sum_i \boldsymbol{\alpha}_i : \boldsymbol{\alpha}_i\; l_i A_i,$$

where dislocation segments are modeled as cylindrical tubes as shown in Fig. 3.1. Here, $\boldsymbol{\alpha}_i$ is the dislocation density tensor, B_x is the cube centered around spatial point $\boldsymbol{x}$, and A_i is the core area of the segment i, $\boldsymbol{m_i}$ is unit Burgers vector direction, $\boldsymbol{t_i}$ is the unit line direction, and $\boldsymbol{\alpha}_i$ is the contribution to the dislocation density tensor due to segment i. Using the fact that $\boldsymbol{\alpha}_i = \frac{|\boldsymbol{b}_i|}{A_i}\boldsymbol{m}^i \otimes \boldsymbol{t}^i$, the expression $\frac{1}{|B_x|}\sum_i \boldsymbol{\alpha}_i : \boldsymbol{\alpha}_i\; l_i A_i = \frac{1}{|B_x|}\sum_i \frac{|\boldsymbol{b}_i|^2}{A_i^2} l_i A_i = \frac{1}{|B_x|}\sum_i \frac{|\boldsymbol{b}_i|^2}{|\boldsymbol{b}_i|^4} l_i |\boldsymbol{b}_i|^2 = \frac{1}{|B_x|}\sum_i l_i$, which shows that l^x is the total dislocation line length per unit volume, i.e. the total dislocation density.

3. The plastic strain rate of a microscopic dislocation segment is given by $\boldsymbol{\alpha} \times \boldsymbol{V}$ (a detailed explanation is provided in [Ach11b]). The average plastic strain rate, denoted by $\boldsymbol{L}^p$, gives the rate of the plastic slip distortion tensor $\boldsymbol{U}^p$:

$$\dot{\boldsymbol{U}}^{p,\boldsymbol{x}}(t) = \boldsymbol{L}^{p,\boldsymbol{x}}(,t),$$

for a spatial point $\boldsymbol{x}$. If τ_i is the resolved shear stress on segment i,

$$(\boldsymbol{\alpha} \times \boldsymbol{V})^x(\mathbf{X}(\sigma), l(\sigma)) = \frac{1}{B_x}\sum_i \frac{\tau^i\; |\boldsymbol{b}_i|}{B}\boldsymbol{m}^i \otimes \boldsymbol{n}^i \frac{|\boldsymbol{b}_i|}{A_i}\; l_i A_i = \frac{1}{B_x}\sum_i \frac{\tau^i\; |\boldsymbol{b}_i|^2\; l_i}{B}\boldsymbol{m}^i \otimes \boldsymbol{n}^i \tag{3.2.8}$$

$$\overline{\dot{\boldsymbol{L}^{p,\boldsymbol{x}}}}(t) = \overline{\dot{(\boldsymbol{\alpha}\times\boldsymbol{V})^{\boldsymbol{x}}}}(t) = \frac{1}{\Delta}\left(\int_{\mathbb{R}^N}(\boldsymbol{\alpha}\times\boldsymbol{V})^{\boldsymbol{x}}(\gamma)\mu_{t+\Delta,l(t+\Delta),\boldsymbol{X}^0(t+\Delta)}(d\gamma) - \int_{\mathbb{R}^N}(\boldsymbol{\alpha}\times\boldsymbol{V})^{\boldsymbol{x}}(\gamma)\mu_{t,l(t),\boldsymbol{X}^0(t)}(d\gamma)\right). \tag{3.2.9}$$

4. Let $\boldsymbol{V}^{\boldsymbol{x}}(\mathbf{X}(\sigma),l(\sigma))$ be the volume-averaged dislocation velocity around $\boldsymbol{x}$, defined as

$$\boldsymbol{V}^{\boldsymbol{x}} = \frac{1}{|B_{\boldsymbol{x}}|}\sum_i \frac{\tau_i}{B}\left\{(\boldsymbol{T}\boldsymbol{m_i})\times\boldsymbol{t_i}\right\}_{//} l_i A_i, \tag{3.2.10}$$

where // represents projection to slip plane and one needs to adjust for cross-slipping segments. Then:

$$\overline{\dot{\boldsymbol{V}^{\boldsymbol{x}}}}(t) = \frac{1}{\Delta}\left(\int_{\mathbb{R}^N}\boldsymbol{V}^{\boldsymbol{x}}(\gamma)\mu_{t+\Delta,l(t+\Delta),\boldsymbol{X}^0}(d\gamma) - \int_{\mathbb{R}^N}\boldsymbol{V}^{\boldsymbol{x}}(\gamma)\mu_{t,l(t),\boldsymbol{X}^0}(d\gamma)\right). \tag{3.2.11}$$

3.2.5 Modification of PTA in application to DD

Everything explained in the previous sections (Section 3.2.3 and 3.2.4) are for fixed number of dofs. However, the number of dofs in DD is not fixed. PTA is applicable to ode systems while DD is not an ode system (because of the non-fixed number of dofs). Thus, the notion of a measure, as defined in Section 2.4 of Chapter 2 and which is used to define the coarse variable in (2.5.4) in Section 2.5 of Chapter 2, does not apply directly in the case of DD. However, the running time average, as defined in (2.7.3) in Section 2.7 of Chapter 2, survives and can be determined.

The application of PTA to DD does not include every step in the PTA algorithm described in Section 2.7 in Chapter 2. In particular, there are two main exclusions:

- The closest point projection of a fixed point in the state space with respect to the measure at a previous time in the slow time-scale (as outlined in Step 3 of Section 2.7), in order to obtain the fine initial conditions, is not determined. This is because the

microstructure involved in the DD simulations has non-fixed number of dofs. Instead, the final microstructure of the previous run (at time $t - h' + \Delta$) is used as the initial condition for the current run (at time t).

- The criteria of accepting the measure as outlined in Step 4 in Section 2.7 is relaxed as this constraint is too hard, especially for the coarse variable $\boldsymbol{L}^p$. Instead, the value of the coarse variable obtained from the extrapolation rule is accepted, unless there is a jump (as per Step 4 above).

These exclusions significantly weaken the power of the coarse graining scheme we employ in comparison to PTA, but, unfortunately, this is the price that has to be paid for the application to DD.

3.3 Coarse graining DD simulations in time

In this section, we consider a single DD box and apply the algorithm to coarse-grain DD simulations in time, in order to obtain the stress-strain response of the box at slow loading rates. We describe the algorithm of applying PTA in this case, describe the setup and then present results.

3.3.1 Algorithm

We define

$$R_t^m(t') := \frac{1}{t'} \int_t^{t+t'} m(\tau) d\tau. \tag{3.3.1}$$

where m is a state function. Some examples of m are the total dislocation density, ρ and the volume-averaged plastic distortion rate, $\boldsymbol{L}^p$. We denote the converged value of $R_t^m(t')$, upto some specified tolerance value, as $R_{t,conv}^m$.

Given at time $t - h'$: predicted density $\rho_{pred}(t - h')$, rate of change of density $\dot{\rho}(t - h')$, predicted plastic distortion rate $\boldsymbol{L}^p_{pred}(t - h')$, rate of change of plastic distortion rate $\dot{\boldsymbol{L}}^p(t - h')$.

The evolution equation in the model is for $\dot{\boldsymbol{L}}^p$ (as given by (3.2.9)). Usually, the evolution equation is for plastic strain $\boldsymbol{U}^p$. However, in our case, only $\boldsymbol{L}^p$ can be defined as a state variable but not $\boldsymbol{U}^p$.

We know the step size: h' and the loading rate: $L(t) = c_1$, where c_1 is a constant. The initial loading is $l(0) = 0$. Δ is a fraction of the time period of the slow time-scale, T_s (which can be obtained as $\frac{1}{c_1}$).
Also given is the predicted density at time t:

$$\rho_{pred}(t) = \rho_{pred}(t - h') + \dot{\rho}(t - h')h',$$

and the predicted plastic distortion rate at time t:

$$\boldsymbol{L}^p_{pred}(t) = \boldsymbol{L}^p_{pred}(t - h') + \dot{\boldsymbol{L}}^p(t - h')h'.$$

The tolerance for convergence of R^ρ_t and $R^\rho_{t+\Delta}$ is denoted as tol_ρ while the tolerance for convergence of $R^{\boldsymbol{L}^p}_t$ and $R^{\boldsymbol{L}^p}_{t+\Delta}$ is denoted as $tol_{\boldsymbol{L}^p}$. The maximum allowed value of $|\dot{\boldsymbol{L}}^p|$ is given by the threshold $|\dot{\boldsymbol{L}}^p_{max}|$, and if $|\dot{\boldsymbol{L}}^p| > |\dot{\boldsymbol{L}}^p_{max}|$, a jump in $\boldsymbol{L}^p$ is said to have occurred at time t.

We need to obtain: $\dot{\rho}(t)$, $\dot{\boldsymbol{L}}^p(t)$.

The steps are:

1. We use the microstructure obtained at the end of $t - h' + \Delta$ and apply stress $l(t)$ and run DD till $R^\rho_t(t')$ and $R^{\boldsymbol{L}^p}_t(t')$ converge (upto tolerance of tol_ρ and $tol_{\boldsymbol{L}^p}$ respectively) and hence, we obtain $R^\rho_{t,conv}$ and $R^{\boldsymbol{L}^p}_{t,conv}$.

2. With the same microstructure as at the end of Step 1 and with stress $l(t+\Delta)$, we run DD till we obtain $R^{\rho}_{t+\Delta,conv}$ and $R^{\boldsymbol{L}^p}_{t+\Delta,conv}$.

3. We obtain $\dot{\boldsymbol{L}}^p(t)$ from $R^{\boldsymbol{L}^p}_{t,conv}$ and $R^{\boldsymbol{L}^p}_{t+\Delta,conv}$ as $\dot{\boldsymbol{L}}^p(t) = \frac{1}{\Delta}(R^{\boldsymbol{L}^p}_{t+\Delta,conv} - R^{\boldsymbol{L}^p}_{t,conv})$.

4. If $|\dot{\boldsymbol{L}}^p(t)| > |\dot{\boldsymbol{L}}^p_{max}|$, as mentioned above, a jump in $\boldsymbol{L}^p$ is said to have occurred at time t. We take final state (of the dislocation system) at time $t+\Delta$ as the initial state and go back to Step 1 and repeat all the steps.

5. If $|R^{\boldsymbol{L}^p}_{t,conv}| > |R^{\boldsymbol{L}^p}_{t+\Delta,conv}|$, we do not accept $R^{\boldsymbol{L}^p}_{t,conv}$ as the converged value of $R^{\boldsymbol{L}^p}_{t}$. In this case, we keep running the time-average $R^{\boldsymbol{L}^p}_{t}$, till $|R^{\boldsymbol{L}^p}_{t}| \leq |R^{\boldsymbol{L}^p}_{t+\Delta,conv}|$, in which case we accept $R^{\boldsymbol{L}^p}_{t,conv} = R^{\boldsymbol{L}^p}_{t}$. If $|R^{\boldsymbol{L}^p}_{t}| > |R^{\boldsymbol{L}^p}_{t+\Delta,conv}|$ after running the time-average $R^{\boldsymbol{L}^p}_{t}$ for a very long period of time (t' in (3.3.1) is large enough so that there is essentially negligible change in the value of $R^{\boldsymbol{L}^p}_{t}$ with increasing t', so that $|R^{\boldsymbol{L}^p}_{t}| \leq |R^{\boldsymbol{L}^p}_{t+\Delta,conv}|$ is unlikely to be true in this case), we accept $R^{\boldsymbol{L}^p}_{t,conv} = R^{\boldsymbol{L}^p}_{t}$.

6. The current time step h is subjected to the following time step control:

$$|\boldsymbol{L}^p(t)| \leq \frac{0.002}{h}$$

7. We store $\dot{\rho}(t)$ and $\dot{\boldsymbol{L}}^p(t)$. We repeat steps 1 to 4 but now at time $t+h$.

3.3.2 DD simulation setup

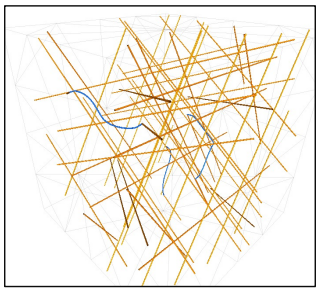

Figure 3.2: *DD simulation box*

We use the library *MODEL* (Mechanics of Defect Evolution Library) [PMC+14] to run the DD simulations. We generate a microstructure with a specified value of mobile and sessile density of dislocation segments. The mobile and sessile segments run from boundary to boundary of the DD simulation box (a representative image of such a box is shown in Fig. 3.2). The mobile segments form junctions with the sessile segments, which act as pinning points, around which they expand. The sessile segment density is much larger than the mobile segment density and the sessile segments essentially act as obstacles to the motion of the mobile segments.

The sessile segments are constructed as Lomer Cottrell (LC) locks, therefore their Burgers vector do not lie in their glide plane. However, majority of sessile segments in FCC crystals do not have this property (i.e. their Burgers vector lie in their slip plane). Therefore, a more physically appropriate case is when the Burgers vector of the sessile segments lie in the slip plane. We have presented results for that case as well, to show that such simulations can be performed.

The preference for using LC locks in this thesis is not fundamental but is related to the limitation of the version of *MODEL* that was used when this work was started.

3.3.2.1 Construction of initial microstructure

We populate the domain with mobile and sessile segments as follows: we assume a certain target density of mobile and sessile segments denoted by ρ_m and ρ_s respectively (with $\rho_s \gg \rho_m$). We insert the mobile density ρ_m in the ratio of the Schmid factor of the slip system i (denoted as $f_{s,i}$), i.e. the target mobile density of slip system i is $\rho_{m,i} = \rho_m \frac{|f_{s,i}|}{\Sigma_{k=1}^{N}|f_{s,k}|}$, where N is the total number of slip systems in the crystal. The Schmid factor of slip system i is calculated as

$$f_{s,i} = \frac{\boldsymbol{b}_i \cdot (\boldsymbol{\sigma}_e \boldsymbol{n}_i)}{|\boldsymbol{\sigma}_e|}, \tag{3.3.2}$$

where $\boldsymbol{\sigma}_e$ is the externally applied stress and $\boldsymbol{b}_i$ and $\boldsymbol{n}_i$ are the Burgers vector and slip plane normal of slip system i. The reason behind this kind of insertion is that segments in slip systems with small Schmid factor are expected to move less compared to those belonging to slip systems with higher Schmid factor, and hence their contribution to the coarse variables $\boldsymbol{L}^p$ and $\boldsymbol{V}$ will be less.

To insert segment n (which lies in slip system i), we construct a candidate segment as follows. We choose a random point $\boldsymbol{P}_{0,n}$ in the domain and then construct a ray from this point along a direction $\boldsymbol{d}_n$, which lies in the slip plane and is rotated at an angle θ_n from the Burgers vector $\boldsymbol{b}_i$ of its slip system, till it intersects the boundary at point $\boldsymbol{P}_{1,n}$. We also construct a ray from $\boldsymbol{P}_{0,n}$ in the opposite direction $-\boldsymbol{d}_n$ till it intersects the boundary at point $\boldsymbol{P}_{2,n}$. In this way, a candidate segment with end points on the boundary, given by $\boldsymbol{P}_{1,n}$ and $\boldsymbol{P}_{2,n}$ is constructed. If the density of the candidate segment is very close to $\rho_{m,i}$ (up to a specified tolerance), it is inserted as segment n, otherwise the process of finding a candidate segment is repeated until a suitable candidate is obtained.

We construct another segment $n+1$ from another random point $\boldsymbol{P}_{0,n+1}$ using the approach mentioned above, which belongs to the same slip system and is on the same slip plane but has opposite line direction. Thus, we have two segments which have the same density and belong to the same slip system and are on the same slip plane but have opposite line directions. This is to ensure that the net mobile dislocation density is very close to 0. Similarly, we construct a pair of segments on the other slip systems.

After this, we construct a number of sessile segments of total density ρ_s distributed isotropically across all slip systems and with zero net dislocation density i.e. every segment constructed has a corresponding segment in the same slip system at a different position and with same density but opposite line direction. Thus, the constructed microstructure is given by the mobile and sessile target densities ρ_m and ρ_s and a set of pairs $\{\boldsymbol{s}_n, \theta_n\}$ describing the mobile segments.

3.3.2.2 Reinsertion of segments

As the system of dislocation segments evolves, some mobile segments exit the box, leading to a reduction in the density of mobile segments. To compensate for this, there is a possibility of reinsertion of segments. The reinsertion should be in tune with the GND density $\overline{\boldsymbol{\alpha}}$ suggested by the MFDM-DD coupled strategy we are proposing and whose field equations are provided in (4.3.2) and the averaged total dislocation density $\overline{\rho}$ (whose evolution equation is derived in Chapter 4), where the microscopic total dislocation density is defined in Chapter 4 as $\rho := \boldsymbol{\alpha} : \boldsymbol{\alpha}$; the field equation for $\overline{\rho}$ has to be solved as an additional evolution equation in MFDM-DD coupling, thus augmenting its current structure. These descriptors will act as feedback for the initialization of the DD microstructure at discrete time steps.

However, in the results that we present in the next sections, reinsertion of segments is not done.

3.3.3 Results

We present the results of coarse graining DD simulations in time for two types of loading. Please note that unlike the coupling problem of DD with MFDM, which can be performed under both load and displacement control, as will be presented later in Section 3.5.5, the problem of coarse-graining DD simulations over a box in time can only be performed under load control, since only stress can be applied to the DD box using MODEL and not displacement boundary conditions.

3.3.3.1 Uniaxial tension

We consider a cubic box and apply tensile loading (traction boundary condition) in the y-direction (t_{22} loading). The orientation matrix represents the transformation rule between components of any vector on the crystal basis and the global basis and its components are

given by $A_{ki} = \boldsymbol{e}_k \cdot \hat{\boldsymbol{e}}_i$, where $\{\boldsymbol{e}_i\}$ and $\{\hat{\boldsymbol{e}}_i\}$ are the orthonormal global and crystal bases respectively. Suppose we know a set of orthonormal crystallographic directions $\{\mathbf{C}_j\}$ that coincide with the global basis vectors. Then, we can show that the orientation matrix has as rows the components of the basis given by the crystallographic directions $\{\mathbf{C}_j\}$ expressed in the crystal basis. We use the symmetric double slip orientation described in [Pie83] in which the crystal is rotated such that the crystallographic direction $\frac{1}{\sqrt{2}}[0\bar{1}1]$ is along the global X axis and the crystalllographic direction $\frac{1}{\sqrt{6}}[211]$ is along the global Y axis. Hence, the orientation matrix comes out as

$$A = \begin{bmatrix} 0 & -\frac{1}{\sqrt{2}} & \frac{1}{\sqrt{2}} \\ \frac{2}{\sqrt{6}} & \frac{1}{\sqrt{6}} & \frac{1}{\sqrt{6}} \\ -\frac{1}{\sqrt{3}} & \frac{1}{\sqrt{3}} & \frac{1}{\sqrt{3}} \end{bmatrix}.$$

We choose $\rho_m = 5 \times 10^{12} m^{-2}$ and $\rho_s = 2 \times 10^{14} m^{-2}$. We insert mobile segments in two slip systems, called the primary and the conjugate slip systems are $[101](11\bar{1})$ and $[110](1\bar{1}1)$ respectively (see Fig. 3.3).

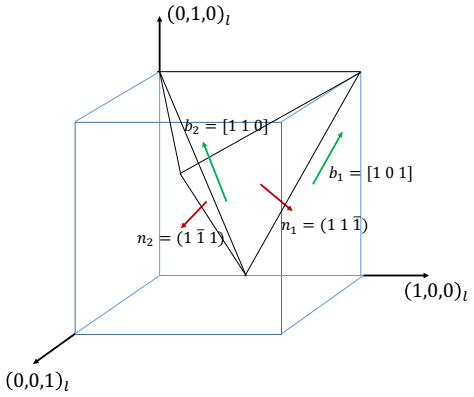

Figure 3.3: *Rotated Thompson tetrahedron of the crystal in tension, the primary and conjugate slip systems are given by* $\{\boldsymbol{b}_1, \boldsymbol{n}_1\}$ *and* $\{\boldsymbol{b}_2, \boldsymbol{n}_2\}$ *respectively. The fixed laboratory axes are marked with subscript* l.

All simulation parameters are provided in Table 3.1.

Name	Physical definition	Values
E	Young's modulus	$110\ GPa$
μ	shear modulus	$48\ GPa$
b	Burgers vector	$2.55 \times 10^{-10} m$
B	Drag	$2.32 \times 10^{-5} Pa.s$
A	Box size	$4000\, b$
Δ^*	time interval in t^*	$0.1s$
$\lvert e_1 \rvert$	tolerance for convergence for ρ_x	10^{-2}
$\lvert e_2 \rvert$	tolerance for convergence for L_x^p	3×10^{-2}
L	loading rate	$1\ MPa/s$
ρ_m	Mobile density	$5 \times 10^{12}\ m^{-2}$
ρ_s	Sessile density	$2 \times 10^{14}\ m^{-2}$

Table 3.1: Simulation parameters for the problem of coarse graining DD simulations in time.

The following are the results obtained in this setting:

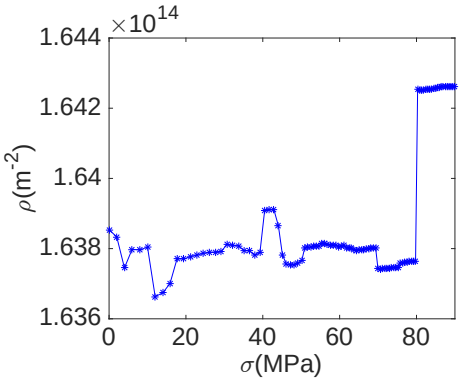

Figure 3.4: *Evolution of* ρ

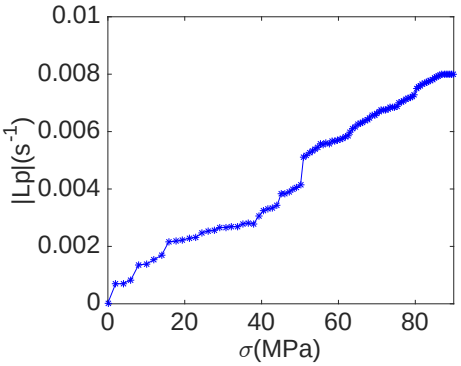

Figure 3.5: *Evolution of* $\boldsymbol{L}^p$

Figure 3.4 shows how ρ evolves with increasing stress. It increases as the mobile segments form junctions with the sessile segments around which they expand and grow in length. Figure 3.5 shows that $\boldsymbol{L}^p$ is increased with increasing stress. The plastic strain norm ϵ_p is obtained by integrating $|\boldsymbol{L}^p|$ in time, i.e. $\boldsymbol{\epsilon}_p(t) = \int_0^t |\boldsymbol{L}^p(t')| dt'$. The plastic strain components, which are also called the directional plastic strain, are obtained as $\epsilon_{p,ij} = \int_0^t (L^p)_{ij}^{sym}(t') dt'$, where $(\boldsymbol{L}^p)^{sym} = \frac{1}{2}(\boldsymbol{L}^p + (\boldsymbol{L}^p)^T)$ is the symmetric part of $\boldsymbol{L}^p$. The stress-strain profile is shown in Figure 3.6. In Figure 3.7, the directional plastic strain $\epsilon_{p,22}$ stays positive with increasing stress as it should. This is not guaranteed to happen since we do not have a

primary slip plane in this case. However, our algorithm can robustly predict the correct direction of $\epsilon_{p,22}$.

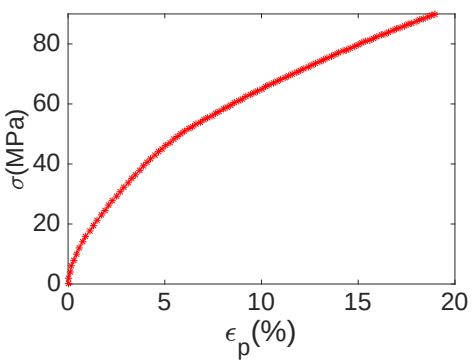

Figure 3.6: *Stress-strain profile*

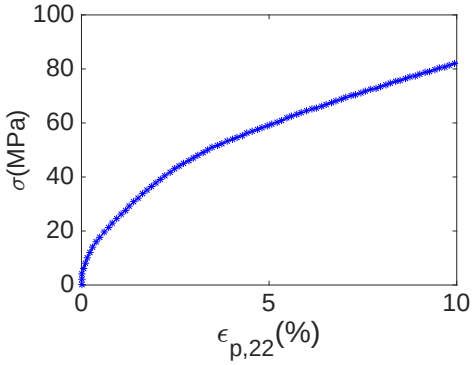

Figure 3.7: *Stress vs* $\epsilon_{p,22}$

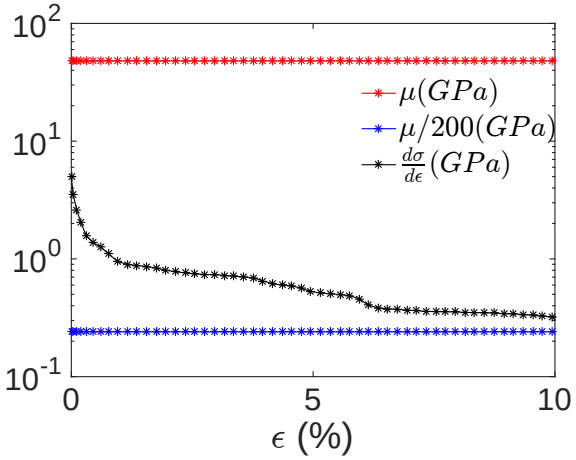

Figure 3.8: *Tangent modulus*

The total strain ϵ is determined as $\epsilon = \frac{\sigma}{\mu} + \epsilon_p$, where $\frac{\sigma}{\mu}$ is the elastic strain. The slope of the stress versus total strain curve is shown in Figure 3.8 and it is approximately $\frac{\mu}{200}$, which is the slope that we expect to see in Stage II hardening [KM03] (we expect Stage II hardening behavior as we start with a high density of sessile segments). We see that we are able to reach appreciable values of strain at realistic loading rates, at which experiments can be performed on macroscopic samples to study their plastic response. Performing simulations at these loading rates using DD simulations alone, for the given domain size and dislocation density, is very expensive and practically impossible.

The speedup in compute time, S, of conventional DD to PTA is obtained as follows. The compute time t_{DD}^{cpu} to run DD up to a time t_{DD} on the slow time-scale is determined. The compute time t_{PTA}^{cpu} to run PTA up to a time t_{PTA}, which is chosen to be the slow time at $\epsilon_p = 10\%$, is also determined. Then, the speedup in compute time, S, is obtained as $S = \left(\frac{t_{DD}^{cpu}}{t_{DD}}\right) \div \left(\frac{t_{PTA}^{cpu}}{t_{PTA}}\right)$. The value of S is around 5000 for this loading case.

3.3.3.2 Simple shear

We consider the same setting as in uniaxial tension but apply shear loading (traction boundary condition) in t_{12} direction. We rotate the crystal such that the crystallographic direction $[1\bar{1}1]$ lies along the global Y axis and the slip direction $[011]$ lies along the global X direction. Therefore, the orientation matrix (an explanation of how to construct it is provided in Appendix B) is

$$A = \begin{bmatrix} 0 & \frac{1}{\sqrt{2}} & \frac{1}{\sqrt{2}} \\ -\frac{1}{\sqrt{3}} & \frac{1}{\sqrt{3}} & -\frac{1}{\sqrt{3}} \\ -\frac{2}{\sqrt{6}} & -\frac{1}{\sqrt{6}} & \frac{1}{\sqrt{6}} \end{bmatrix}.$$

In this case also, we insert segments on two slip systems and the primary and conjugate slip systems are chosen as $[011](1\bar{1}1)$ and $[\bar{1}01](1\bar{1}1)$ respectively. The former is the primary slip system as after rotation, its normal is along the global Y axis and we shear along its slip direction (global X axis). The rotated crystal is shown in Fig. 3.9.

The results are presented below:

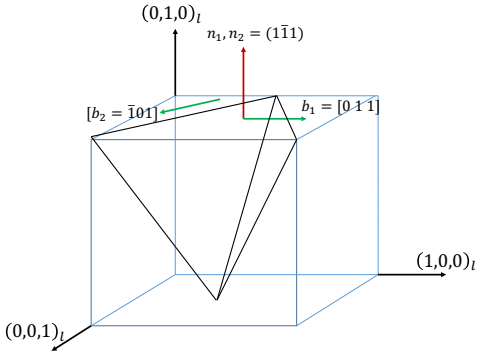

Figure 3.9: *Rotated Thompson tetrahedron of the crystal in shear, the primary and conjugate slip systems are given by* $\{\boldsymbol{b}_1, \boldsymbol{n}_1\}$ *and* $\{\boldsymbol{b}_2, \boldsymbol{n}_2\}$ *respectively. The fixed laboratory axes are marked with subscript* l*.*

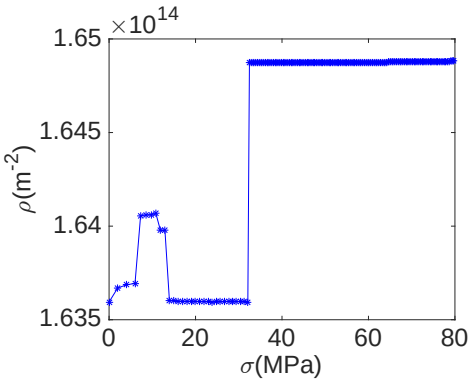

Figure 3.10: *Evolution of* ρ

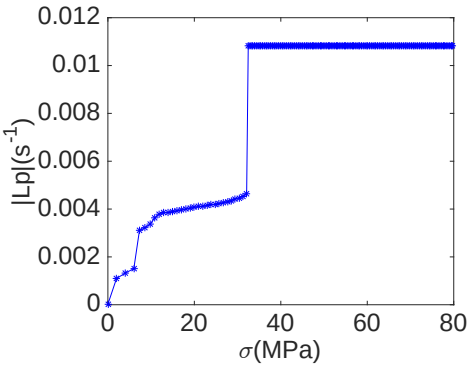

Figure 3.11: *Evolution of* $\boldsymbol{L}^p$

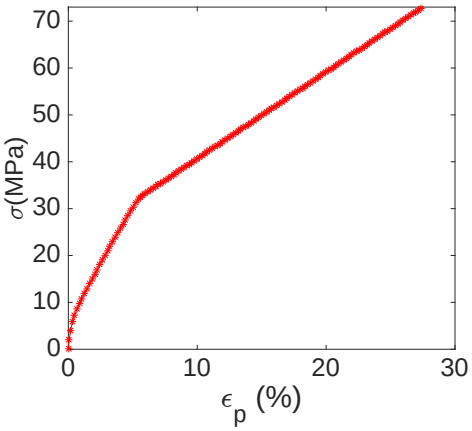

Figure 3.12: *Stress-strain profile*

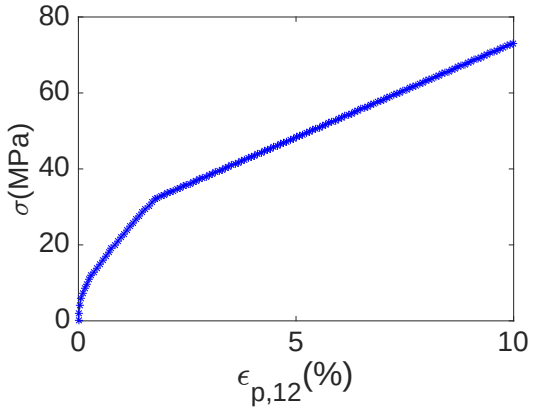

Figure 3.13: *Stress vs* $\epsilon_{p,12}$

These results follow a similar trend as in the uniaxial loading case presented in Section

3.3.3.1. We see in Figure 3.10 that dislocation density ρ increases with stress. The definition of plastic strain norm ϵ_p, directional plastic strain $\epsilon_{p,ij}$ and the total strain ϵ are provided in the previous section (Section 3.3.3.1). In Figure 3.13, we see that the directional plastic strain strain $\epsilon_{p,12}$ remains positive with increasing stress, as it is supposed to. In Figure 3.14, the slope of the stress-total strain curve (Figure 3.14) comes close to $\frac{\mu}{200}$, which is the slope we observe in Stage II hardening. The speedup in compute time, S, defined in Section 3.3.3.1, is around 2000.

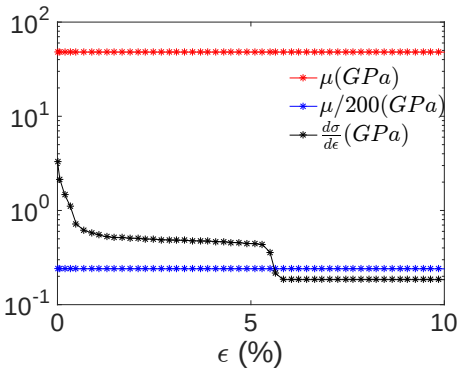

Figure 3.14: *Tangent modulus*

3.4 DD-continuum plasticity coupling

All the discussions in the previous sections were for DD simulations in one box. Now we think of many boxes being part of a larger domain in which we want to do regular plasticity calculations and couple this with a larger plasticity calculation in the body, in which equilibrium equations are solved. The pde-based theory which represents time averaged Dislocation Dynamics is MFDM (which stands for Mesoscale Field Dislocation Mechanics). However, phenomenological constitutive assumptions will be replaced with time averaged inputs from DD, which are obtained using the framework of PTA as outlined in Section 3.2.3 and Section 3.2.4. Next, we describe MFDM , its algorithm and the changes we have made in the current work in order to replace the constitutive assumptions with inputs from Dislocation

Dynamics.

3.4.1 MFDM

The theory of MFDM ([AR06]) involves the evolution of the following system of pdes:

$$\dot{\overline{\boldsymbol{\alpha}}} = -curl\ (\overline{\boldsymbol{\alpha}} \times \overline{\boldsymbol{V}} + \boldsymbol{L}^p) \tag{3.4.1}$$

$$curl\overline{\boldsymbol{\chi}} = \overline{\boldsymbol{\alpha}}$$

$$div\overline{\boldsymbol{\chi}} = 0 \tag{3.4.2}$$

$$div(grad\,\dot{\overline{\boldsymbol{z}}}) = div(\overline{\boldsymbol{\alpha}} \times \overline{\boldsymbol{V}} + \boldsymbol{L}^p) \tag{3.4.3}$$

$$\overline{\boldsymbol{T}} = \boldsymbol{C} : (grad(\overline{\boldsymbol{u}} - \overline{\boldsymbol{z}}) + \overline{\boldsymbol{\chi}}$$

$$div\overline{\boldsymbol{T}} = 0. \tag{3.4.4}$$

The tensor $\boldsymbol{\alpha}$ is the dislocation density tensor, $\boldsymbol{V}$ is the dislocation velocity vector, $\boldsymbol{C}$ is the fourth-order, possibly anisotropic, tensor of linear elastic moduli, and $\boldsymbol{u}$ is the total displacement vector, $\boldsymbol{\chi}$ is the incompatible part of the elastic distortion tensor, $\boldsymbol{u} - \boldsymbol{z}$ is a vector field whose gradient is the compatible part of the elastic distortion tensor and $\boldsymbol{T}$ is the symmetric stress tensor. The slipping distortion tensor $\boldsymbol{S}$ is $\boldsymbol{\alpha} \times \boldsymbol{V} + \boldsymbol{L}^p$.

In the specific model of PMFDM (where P stands for Phenomenological), $\boldsymbol{L}^p$ and $\boldsymbol{V}$ are specified using phenomenological constitutive assumptions as mentioned in [AR06].

3.4.1.1 Algorithm of PMFDM

We describe here the algorithm of (P)MFDM. Let BC and IC be the abbreviation for *Boundary Condition* and *Initial Condition* respectively.

Step 1:

BC : $\boldsymbol{z}$ constrained to prevent rigid body motion; $\boldsymbol{\chi}\mathbf{n} = 0$, where $\boldsymbol{n}$ is the outward unit normal at the boundary surface,

IC : $\boldsymbol{\alpha}_0$ is prescribed.

Solve for $\boldsymbol{\chi}_0$. Solve for $\boldsymbol{z}$ and the initial state of stress due to $\boldsymbol{\alpha}_0$.

Step 2 :

In case a problem of ECDD needs to be solved for the distribution $\boldsymbol{\alpha}_0$ with applied displacement and/or traction boundary conditions, impose displacement and traction BCs as per the physical problem we are trying to solve. Superpose the initial state of stress due to $\boldsymbol{\alpha}_0$ with the stress due to displacement and traction BCs. This is done by solving the MFDM problem with $\boldsymbol{V}$ and $\boldsymbol{L}^p$ set to $\mathbf{0}$.

Step 3 : Now initialize the MFDM problem.
IC: $\boldsymbol{u}, \boldsymbol{z}, \boldsymbol{\alpha}$ and $\boldsymbol{\chi}$ to be retrieved from the previous step results.
BC: $\boldsymbol{\chi}\mathbf{n} = 0$ at the boundary, which implies that the incompatible part of $\boldsymbol{U}^e$ is $\mathbf{0}$ if $\boldsymbol{\alpha} = \mathbf{0}$.
$\boldsymbol{z}$ is to be specified at one point to get a unique solution.
The BC on $\boldsymbol{\alpha}$ can be specified in two ways, which are called the *constrained* and *unconstrained* cases. In the *constrained* case, the body is plastically constrained on the boundaries and dislocations cannot exit the body, but can only move in a tangential direction at the boundary. The BC for this case is $(\boldsymbol{\alpha} \times \boldsymbol{V} + \boldsymbol{L}^p) \times \boldsymbol{n} = 0$ on the boundary. A less restrictive BC which corresponds to the *unconstrained* case is the imposition of the dislocation flux $\boldsymbol{\alpha}(\boldsymbol{V} \cdot \boldsymbol{n})$ on the inflow points on the boundary (where $\boldsymbol{V} \cdot \boldsymbol{n} = 0$), along with the specification of $\boldsymbol{L}^p \times \boldsymbol{n}$ on the entire boundary. This condition allows the free exit of GNDs at the outflow points.

The time step at the first increment is $\Delta t^0 = \Delta t_{step}$, where Δt_{step} is the prescribed time step for Step 4. The total time of the simulation is T_s.

The steps are as follows. For every time increment k (while $t^k < T_s$),

1. Set the current time as $t^k = t^{k-1} + \Delta t^{k-1}$. Set the current time step as $\Delta t^k = \Delta t^{k-1}$.

2. Impose displacement and/or traction boundary condition.

For all Gauss points,

3. Calculate $\boldsymbol{L}^{p,k}$ and $\boldsymbol{V}^k$ using $\boldsymbol{T}^k$ using constitutive assumptions mentioned in [AR06]. It is here that phenomenology enters MFDM.

4. Solve $\boldsymbol{\alpha}$ equation (3.4.1) for $\boldsymbol{\alpha}^{k+1}$: $\boldsymbol{\alpha}^{k+1} = \boldsymbol{\alpha}^k - \Delta t^k curl(\boldsymbol{\alpha}^{k+1} \times \boldsymbol{V}^k + \boldsymbol{L}^{p,k})$.

5. Solve $\boldsymbol{\chi}$ equation (3.4.2) for $\boldsymbol{\chi}^{k+1}$: $\boldsymbol{\alpha}^{k+1} = curl\boldsymbol{\chi}^{k+1}$ and $div\boldsymbol{\chi}^{k+1} = 0$.

6. Solve z equation (3.4.3) for $\boldsymbol{z}^{k+1}$: $div(grad\ \dot{\boldsymbol{z}}^k) = div(\boldsymbol{\alpha}^{k+1} \times \boldsymbol{V}^k + \boldsymbol{L}^{pk})$.

7. Solve $\boldsymbol{u}$ equations (3.4.4) for $\boldsymbol{u}^{k+1}$: $div\boldsymbol{T}^{k+1} = 0$, $\boldsymbol{T}^{k+1} = \mathbf{C} : \boldsymbol{U}^{e(k+1)}$, $\boldsymbol{u}^{e(k+1)} = grad(\boldsymbol{u}^{k+1} - \boldsymbol{z}^{k+1}) + \boldsymbol{\chi}^{k+1}$. Special algorithms are required to solve the MFDM equations (steps 3 through 6 above). These algorithms can be found in [RA05].

8. Calculate $\boldsymbol{L}^{p,k+1}$ and $\boldsymbol{V}^{k+1}$ using $\boldsymbol{T}^{k+1}$.

9. The numerical stability condition is given by:

$$\Delta t^k \leq min_{gp}\Big(\frac{0.002}{|\boldsymbol{\alpha}^k \times \boldsymbol{V}^k| + \dot{\gamma}^k}, f\frac{d}{|\boldsymbol{V}|}\Big),\ f \sim 0.1 \tag{3.4.5}$$

where gp is the set of all Gauss points in the sample and d is a minimum element edge length. This reflects a conservative choice between a Courant condition and a maximum bound of 0.2% on the plastic strain increment.

If Δt^k does not satisfy

$$\Delta t^k <= min_{gp}\left(\frac{0.002}{|\boldsymbol{\alpha}^{k+1} \times \boldsymbol{V}^{k+1}| + \dot{\gamma}^{k+1}}, f\frac{d}{|\boldsymbol{V}^{k+1}|}\right),$$

then it is likely that the computed state at increment $k+1$ gives rise to a large plastic strain rate and the increment from k to $k+1$ should be done with a smaller time step to have better control on the evolution. Therefore, as a preemptive measure, set it as

$$\Delta t^k = min_{gp}\left(\frac{0.002}{|\boldsymbol{\alpha}^{k+1} \times \boldsymbol{V}^{k+1}| + \dot{\gamma}^{k+1}}, f\frac{d}{|\boldsymbol{V}^{k+1}|}\right).$$

Then reinitialize the increment k and go to Item 1 of Step 4. This process of rerunning the increment is called *cutback*.

10. If it happens that $\Delta t^k < \Delta t_{step}$ and $min_{gp}\left(\frac{0.002}{|\boldsymbol{\alpha}^k \times \boldsymbol{V}^k| + \dot{\gamma}^k}, f\frac{d}{\boldsymbol{V}}\right) \geq \Delta t^k$ (where gp is the set of all Gauss points in the sample) for two consectutive steps, then double Δt^k. This increases the time step when plastic strain rate reduces.

3.5 DD-MFDM coupling

The constitutive equations to obtain $\boldsymbol{L}^p$ and $\boldsymbol{V}$ are mentioned in [AR06]. Here, we aim to obtain them using PTA. The values of the plastic distortion rate, $\boldsymbol{L}^p$ and the polar dislocation velocity, $\boldsymbol{V}$ at every Gauss point in FEM should be obtained using (3.2.9) and (3.2.11) respectively using the value of the stress, $\boldsymbol{T}$, at the Gauss point. We divide the domain into $n \times n$ blocks. For example, in Fig. 3.15, the domain is divided into 5×5 blocks. Each block is a collection of a number of FEM elements that are used in the solution of the MFDM equations. Please note that the thickness of the block is the same as the thickness of the sample, which implies a state of plane stress.

Every block contains a DD box of a fixed size in which DD simulations are performed. The stress that is used as input to perform the DD simulation in each block is the volume average of the stress obtained from the solution of the MFDM equations, over the block. The size of the block, denoted by B, is therefore called the *stress averaging* size. Let the entire domain be denoted by Ω and the set of all points that lie within block i be denoted as Ω_i. The

averaged stress for block r is denoted as $\langle \boldsymbol{T} \rangle_r^B$, and is given by

$$\langle \boldsymbol{T} \rangle_r^B = \frac{\int_{\Omega_r} T dv}{|\Omega_r|}, \tag{3.5.1}$$

where $|\Omega_r| := B \times B \times a$, where a is the thickness of the block/sample. The *stress averaging* size B plays a crucial role in convergence of the solution. It will be shown later in section 3.5.5 that there is most likely a limiting in-plane *stress averaging* size of $5\mu m$ for a DD box of size $1\mu m$, for which there is a converged solution.

Since the size of the block remains fixed for the results in Section 3.5.5 (except for the convergence studies in Section 3.5.5.1.1), the superscript B in $\langle \boldsymbol{T} \rangle_r^B$ is dropped from here onwards for notational convenience.

Finally, after running the DD simulations for block r using $\langle \boldsymbol{T} \rangle_r$ at time t and $t + \Delta$ (where Δ is a fraction of time period of slow time-scale T_s), we obtain measures of the plastic strain rate and dislocation velocity for that block, which we denote as $\boldsymbol{L}_r^p$ and $\overline{\boldsymbol{V}}_r$ respectively.

The characteristic function of block i is given by

$$\chi^i(\boldsymbol{x}) = \begin{cases} 1, & \text{if} \quad \boldsymbol{x} \in \Omega_i \\ 0, & \text{if} \quad \boldsymbol{x} \notin \Omega_i \end{cases}$$

Define $\tilde{\boldsymbol{L}}^p(\boldsymbol{x})$ by

$$\tilde{\boldsymbol{L}}^p(\boldsymbol{x}) = \sum_{i=1}^{N_B} \overline{\boldsymbol{L}}_i^p \chi^i(\boldsymbol{x}), \quad x \in \Omega$$

where N_B is the total number of blocks.

3.5.1 Obtaining $\boldsymbol{L}^p$, $\overline{\boldsymbol{V}}$ at Gauss point of element

Let the characteristic function of block i is given by

$$\chi^i(\boldsymbol{x}) = \begin{cases} 1, & \text{if} \quad \boldsymbol{x} \in \Omega_i \\ 0, & \text{if} \quad \boldsymbol{x} \notin \Omega_i \end{cases}$$

Define $\widetilde{\boldsymbol{L}}^p(\boldsymbol{x})$ by

$$\widetilde{\boldsymbol{L}}^p(\boldsymbol{x}) = \sum_{i=1}^{N_B} \boldsymbol{L}_i^p \chi^i(\boldsymbol{x}), \quad x \in \Omega$$

where N_B is the total number of blocks.

The field $\widetilde{\boldsymbol{L}}^p$ is discontinuous across blocks. To obtain a (C^0) continuous field in Ω, we perform the following operations. We obtain an L^2 projection of $\widetilde{\boldsymbol{L}}^p$ on the finite dimensional space, $C^{0,B}$, formed by the linear span of globally continuous, piecewise smooth finite element shape functions corresponding to a FE mesh for Ω, *comprising the blocks* of size B (the MFDM calculations involve another finer FE mesh that further discretizes the blocks). This projection, after discretization, gives the values of the plastic strain rate at the nodes of the blocks. Each block, in turn, contains many elements for the MFDM calculations, and we interpolate using the isoparametric shape functions for the blocks and for the elements within them to obtain the value of $\boldsymbol{L}^p$ at the MFDM elemental Gauss points.

The above operations can be stated as follows. Define

$$\widehat{\boldsymbol{L}}^p := \underset{\boldsymbol{L} \in C^{0,B}(\Omega)}{\operatorname{argmin}} \int_\Omega \frac{1}{2} |\boldsymbol{L} - \widetilde{\boldsymbol{L}}^p|^2 dv.$$

To keep the debauch of indices to a minimum in what follows, we rename $\widehat{\boldsymbol{L}}^p := \boldsymbol{A}$. The

above definition translates to the following discrete statement:

$$\sum_{R=1}^{\mathsf{N}}\sum_{Q=1}^{\mathsf{N}}\delta A_{ij}^{R}\Big[\int_{\Omega_i} N^R\delta_{ik}\delta_{jl}N^Q dv\Big]A_{kl}^{Q}=\sum_{R=1}^{\mathsf{N}}\delta A_{ij}^{R}\int_{\Omega_i} N^R\delta_{ik}\delta_{jl}\widetilde{\boldsymbol{L}}_{kl}^{p}dv.$$

(note that p is not an index). Here $\delta\boldsymbol{A}^R$ is a test function and R and Q are indices representing nodes of the $n\times n$ 'block' FE mesh with N^R and N^Q denote global shape functions of the mesh. N denotes the total number of nodes of the block mesh. This results in a linear solve for the nodal values of $\boldsymbol{A}$ on the block FE mesh.

With the nodal values of $\boldsymbol{A}$ determined so that it is a globally continuous function on the domain, we now determine the values of this continuous function at the Gauss points of the finite elements comprising the FEM mesh for the MFDM calculations (where $\boldsymbol{A}$ is needed as an input). This is done as follows. Let M be a node of element e that is contained in block r, whose isoparametric coordinate (with respect to the containing block r that is an element of the block-FE solve) is denoted as $\xi_{e,M}^{r}$. Then $\boldsymbol{A}$ at node M of element e can be obtained as $\boldsymbol{A}_{e,M,r}=\sum_{Q=1}^{N^v}\boldsymbol{A}^Q N^Q(\xi_{e,M}^{r})$, where N^v is the number of nodes on a block (e.g. 8 for a hexahedral brick element). Finally, $\boldsymbol{L}^p$ at Gauss point I of element e in block r can be obtained as $\boldsymbol{L}_{e,I,r}^{p}=\sum_{K=1}^{N^v}\boldsymbol{A}_{e,K,r}N^K(\xi_I^e)$, where K is a node of element e (see Fig. 3.15) and ξ_I^e is the isoparametric coordinate of Gauss point I in element e (and we have made the (non-essential) assumption that the each element of the block-mesh and MFDM-mesh have the same number of nodes).

We obtain the polar dislocation velocity at the Gauss point I of element e, of block r, $\overline{\boldsymbol{V}}_{e,I,r}$ in the same way.

3.5.2 Ensuring non-negative dissipation

Let the $\boldsymbol{L}^p$ and $\boldsymbol{V}$ (we revert here to dropping overhead bars) obtained at a Gauss point of an element (for MFDM calculations) as described above be denoted as $\boldsymbol{L}_{gp}^{p}$ and $\boldsymbol{V}_{gp}$, respectively.

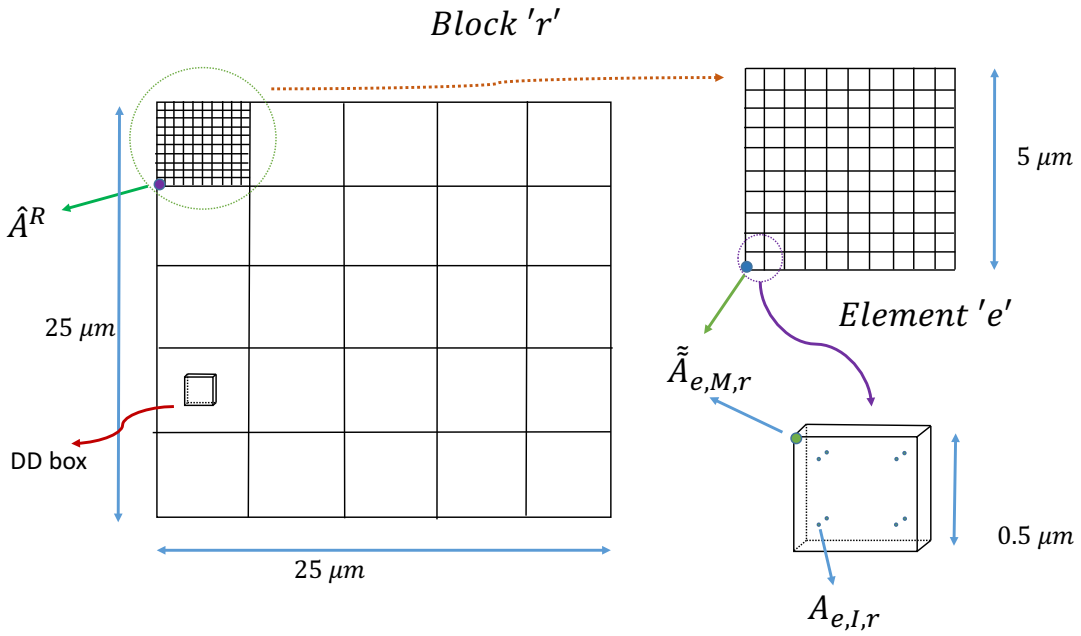

Figure 3.15: *This figure shows the decomposition of the domain of size* 25 *micron into* 5×5 *blocks. Each block contains a DD box. Each block also consists of a number of elements* (10×10 *in this figure).*

In order to ensure that the dissipation is non-negative , we redefine the $\boldsymbol{L}^p$ and $\boldsymbol{V}$ as

1. If $\boldsymbol{T} : \boldsymbol{L}^p_{gp} = d$ and $d < 0$, we take the component of $\boldsymbol{L}^p_{gp}$ given by

$$\boldsymbol{L}^p = \boldsymbol{L}^p_{gp} - d\frac{\boldsymbol{T}}{|\boldsymbol{T}|^2}. \tag{3.5.2}$$

2. If $\beta = \boldsymbol{V}_{gp} \cdot (\boldsymbol{XT\alpha}) < 0$, we take the component of $\boldsymbol{V}_{gp}$ given by

$$\boldsymbol{V} = \boldsymbol{V}_{gp} - \beta\frac{\boldsymbol{XT\alpha}}{|\boldsymbol{XT\alpha}|^2}. \tag{3.5.3}$$

Here, $\boldsymbol{T}$ and $\boldsymbol{\alpha}$ are the stress and the dislocation density tensor at the Gauss point respectively, while $\boldsymbol{X}$ is the third order alternating tensor. The dissipation resulting from the components of $\boldsymbol{L}^p$ and $\boldsymbol{V}$ given by (3.5.2) and (3.5.3) is 0, which can be verified by taking an inner product of (3.5.2) and (3.5.3) with $\boldsymbol{T}$ and $\boldsymbol{XT\alpha}$, respectively. These $\boldsymbol{L}^p$ and $\boldsymbol{V}$ are

used to solve the MFDM equations which is described in detail in Section 3.5.4.

Next, we discuss the basic ideas behind the current work of coupling MFDM with DD and the necessary modifications that we made to the PMFDM algorithm in order to enable them.

3.5.3 Key changes in DD-MFDM coupling

In order to get a measure at a particular time t, the fast dynamics, which is DD in this case, has to be run long enough (over a period t' on the slow time-scale), till the running time average of the state function converges, see (3.3.1)). During this period, many junctions will be formed and broken. The period t' should be much smaller than the interval Δ^* (a fraction of time period of slow time-scale T_s; the state functions of DD are averaged with respect to the Young measure over the interval $\Delta = \frac{\Delta^*}{T_s}$ to generate coarse variables, see (3.2.5)), due to the vast separation in the time-scale of the fast and the slow dynamics. Therefore, it is reasonable to say that $a \ll t' \ll \Delta^*$ and we fix Δ^* as $\Delta^* = n\ a$, where n is a positive integer.

Suppose the MFDM time step at increment k, given by Δt^k in Section 3.4.1.1, is denoted as h^*, and given by $h^* = m\ \Delta^*$, where m is a positive integer (for the results presented in Section 3.5.5, m was set as 10). This implies the condition $\Delta^* \ll h^*$, which is a necessary constraint for the application of PTA (see Section 2.6 in Chapter 2).

The above discussion can be summarized as the following constraint:

$$a \ll \Delta^* \ll h^*. \tag{3.5.4}$$

The MFDM system evolves in a stable way when the plastic strain increment is less than a

threshold of 0.2% in a given time increment, which is stated as

$$h^* \leq \frac{0.002}{|\boldsymbol{\alpha} \times \boldsymbol{V}| + |\boldsymbol{L}^p|}. \tag{3.5.5}$$

Equations (3.4.5) and (3.5.4) have to be always satisfied and form the constraints of the DD-MFDM coupling problem. However, when $|\boldsymbol{L}^p|$ is high, such that

$$\frac{0.002}{|\boldsymbol{\alpha} \times \boldsymbol{V}| + |\boldsymbol{L}^p|} \leq \Delta^*, \tag{3.5.6}$$

for one or more blocks, (3.5.5) and (3.5.6), when combined together, may violate (3.5.4). For instance, if $\Delta^* = 0.01\ s$ and $|\boldsymbol{\alpha} \times \boldsymbol{V}| + |\boldsymbol{L}^p| = 0.03\ s^{-1}$, (3.5.6) is satisfied and $h^* \leq 0.0067 < \Delta^*$ by (3.5.5). Thus, (3.5.4) is violated. In such situations, since h^* is free to choose, we explicitly set it as $h^* = \Delta^*$. When $\boldsymbol{L}^p$ is high, it is physically expected that the local flow stress either stays fixed or decreases. Based on this, we assume that the local stress at time t and $t + \Delta^*$ are same, which implies $\dot{\boldsymbol{L}}^p = 0$ and $\dot{\boldsymbol{V}} = 0$ by (3.2.9). When such a plastic instability happens at any point, we declare that the system has reached a *limit* load and do not allow the external loading to increase, i.e., $L = 0$ in (3.2.3) (we consider that the simulation is performed in a sophisticated loading apparatus).

However, if $\dot{\boldsymbol{L}}^p$ following (3.2.9) is such that it reduces $|\boldsymbol{L}^p|$ to a value such that (3.5.6) is not true, $\boldsymbol{L}^p$ is allowed to evolve using $\dot{\boldsymbol{L}}^p$ for that block. If it happens at any time that none of the blocks satisfy (3.5.6), then the system is no longer in the state of *limit* load. In that case, the loading rate is set back to the prescribed non-zero value for the problem. Hence, the system is allowed to get out of the *limit* load condition in a consistent manner.

We next discuss the modifications to the PMFDM algorithm in order to incorporate the above changes.

3.5.4 Modifications in algorithm for DD-MFDM coupling

Based on the discussion in the previous subsection, we have implemented the following changes in DD-MFDM coupling. For every time increment k:

1. Instead of calculating $\boldsymbol{L}^{p,k}$ and $\boldsymbol{V}^k$ from $\boldsymbol{T}^k$ using constitutive assumptions in item 3 of step 4 of the PMFDM algorithm presented in Section 3.4.1.1, we obtain them as follows:

   (a) For each block r, obtain the averaged stress $\overline{\boldsymbol{T}}^k_r$. Next, we pass the stress $\hat{\boldsymbol{T}}^k_{r,t} = \langle \boldsymbol{T} \rangle^k_r$ and $\hat{\boldsymbol{T}}^k_{r,t+\Delta} = \langle \boldsymbol{T} \rangle^k_r + \frac{\Delta}{\Delta t^{k-1}}(\langle \boldsymbol{T} \rangle^k_r - \langle \boldsymbol{T} \rangle^{k-1}_r)$ to run PTA at block r. Here, t is the time on the slow time-scale at the current increment k.

   (b) If $|\hat{\boldsymbol{T}}^k_{r,t}|$ and $|\hat{\boldsymbol{T}}^k_{r,t+\Delta}|$ are close to each other ($|\hat{\boldsymbol{T}}^k_{r,t+\Delta} - \hat{\boldsymbol{T}}^k_{r,t}|$ is less than a threshold, which was found to be around 0.5 MPa), the numerator on the rhs of (3.2.9) (which gives $\boldsymbol{L}^p$) becomes very small and DD cannot resolve it, which is a *limitation* of DD. In that case, since $\hat{\boldsymbol{T}}^k_{r,t+\Delta}$ is the only variable we are free to modify, we change it, while keeping $\hat{\boldsymbol{T}}^k_{r,t}$ fixed, such that the difference is 0.5 MPa. It is obtained as: $mag = \frac{0.5}{|\hat{\boldsymbol{T}}^k_{r,t+\Delta} - \hat{\boldsymbol{T}}^k_{r,t}|}$, if $mag > 1$, $\hat{\boldsymbol{T}}^k_{r,t+\Delta} = \hat{\boldsymbol{T}}^k_{r,t} + mag\ (\hat{\boldsymbol{T}}^k_{r,t+\Delta} - \hat{\boldsymbol{T}}^k_{r,t})$.

   (c) Obtain $\dot{\boldsymbol{L}}^{p,k}_r$ and $\dot{\overline{\boldsymbol{V}}}^k_r$ using PTA (using (3.2.9) and (3.2.11) respectively).

   (d) If $mag > 1$, then scale $\dot{\boldsymbol{L}}^{p,k}_r$ and $\dot{\overline{\boldsymbol{V}}}^k_r$ down by mag i.e. $\dot{\boldsymbol{L}}^{p,k}_r = \frac{\dot{\boldsymbol{L}}^{p,k}_r}{mag}$ and $\dot{\overline{\boldsymbol{V}}}^k_r = \frac{\dot{\overline{\boldsymbol{V}}}^k_r}{mag}$. This is because ideally $\dot{\boldsymbol{L}}^{p,k}_r$ should be generated from $\hat{\boldsymbol{T}}^k_{r,t}$ and $\hat{\boldsymbol{T}}^k_{r,t+\Delta}$ using PTA as per Step 1c above. However, due to the restriction imposed by DD on the minimum threshold of the difference $|\hat{\boldsymbol{T}}^k_{r,t+\Delta} - \hat{\boldsymbol{T}}^k_{r,t}|$, the value of $\hat{\boldsymbol{T}}^k_{r,t+\Delta}$ was modified in order to scale up the difference to 0.5 MPa, as outlined in Step 1b. Thus, the resulting $\dot{\boldsymbol{L}}^{p,k}_r$ must be scaled down such that it corresponds to the original stress difference between $\hat{\boldsymbol{T}}^k_{r,t+\Delta}$ and $\hat{\boldsymbol{T}}^k_{r,t}$.

   (e) Obtain $\boldsymbol{L}^{p,k}_{gp}$ and $\boldsymbol{V}^k_{gp}$ at Gauss points of elements in block r from $\boldsymbol{L}^{p,k}_r$ and $\overline{\boldsymbol{V}}^k_r$ using the procedure described in Section 3.5.1.

(f) Modify $\boldsymbol{L}^{p,k}$ and $\boldsymbol{V}^k$ using (3.5.2) and (3.5.3) respectively, to ensure non-negative dissipation at every Gauss point.

2. We check if the *limit* load has been reached by checking if $\frac{0.002}{|\boldsymbol{\alpha}^k \times \boldsymbol{V}^k| + |\boldsymbol{L}_r^{p,k}|} \leq \Delta^*$ (equation (3.5.6)) at any block r. If yes, we set the loading rate L to 0, otherwise we keep it at the prescribed value for the problem. We also set $h^* = \Delta^*$ and set $\dot{\boldsymbol{L}}_r^{p,k}$ for block r. The justification for these assignments is provided in Section 3.5.3. This also implies that $\dot{\boldsymbol{L}}_r^{p,k} = 0$ and $\dot{\overline{\boldsymbol{V}}}_r^k = 0$, following the argument surrounding (3.5.6).

   However, if (3.5.6) is satisfied and $\frac{0.002}{|\boldsymbol{\alpha}^{k+1} \times \boldsymbol{V}^{k+1}| + |\boldsymbol{L}_r^{p,k} + \dot{\boldsymbol{L}}_r^{p,k}\,\Delta^*|} < \Delta^*$, the value of $\dot{\boldsymbol{L}}_r^{p,k}$ and $\dot{\overline{\boldsymbol{V}}}_r^k$ are used to evolve $\boldsymbol{L}_r^{p,k}$ and $\overline{\boldsymbol{V}}_r^k$ respectively.

   If (3.5.6) is not satisfied for any block, the system is no more in the state of *limit* load and we set the loading rate l back to the prescribed value for the problem.

3. The term $\dot{\gamma}^k$ in the numerical stability constraint of PMFDM (3.4.5) is replaced by $|\boldsymbol{L}^{p,k}|$ in the numerical stability constraint (3.5.5) of the DD-MFDM coupled problem.

4. An additional stress-based time step control is placed due to the introduction of DD in the MFDM problem. It is implemented as follows. Compute $|\hat{\boldsymbol{T}}_{r,t}^{k+1} - \hat{\boldsymbol{T}}_{r,t}^k|$, if it is greater than a threshold (assumed to be 3 MPa), then reduce Δt^k, calculated using Point 2 above, by half, and rerun the current increment. If in this process, Δt^k comes out less than Δ^*, then put $\Delta t^k = \Delta^*$. Restricting the value of $|\hat{\boldsymbol{T}}_{r,t}^{k+1} - \hat{\boldsymbol{T}}_{r,t}^k|$ to within a threshold by reducing the time step has been found to make the evolution of the DD-MFDM coupled problem more stable, as the DD microstructure is not subjected to high variation in the applied stress that goes into the PTA calculation, between consecutive time steps.

Remark. There is only stress-coupling between DD and MFDM in this first exercise. The DD microstructure can also be coupled to other descriptors, like the GND density predicted by MFDM. More importantly, an additional equation in MFDM for the averaged dislocation

density, which is derived in Chapter 4, should be evolved and the density in the DD box should be adjusted in tune with that prediction.

3.5.5 Results and discussion

In this section, we present results on the

- convergence
- orientation effect
- rate effect
- effect of initial DD microstructure

for the DD-MFDM coupled problem under load and displacement control.

Following the discussion in Section 3.3.2, there are two cases into which the results can be categorized:

- **Case 1** The sessile segments are constructed as Lomer Cottrell (LC) locks, with their Burgers vector out of the slip plane.
- **Case 2** The sessile segments are constructed such that their Burgers vector lie in the slip plane.

Most of the results presented in this Section correspond to Case 1, while a few results for Case 2 have also been presented. The justification for the preference of Case 1 in this thesis has been provided in Section 3.3.2.

3.5.5.1 Case 1: Load Control

We apply two load cases of simple shear and uniaxial tension. The boundary conditions for the two loading cases are as follows. Standard displacement boundary condition to prevent

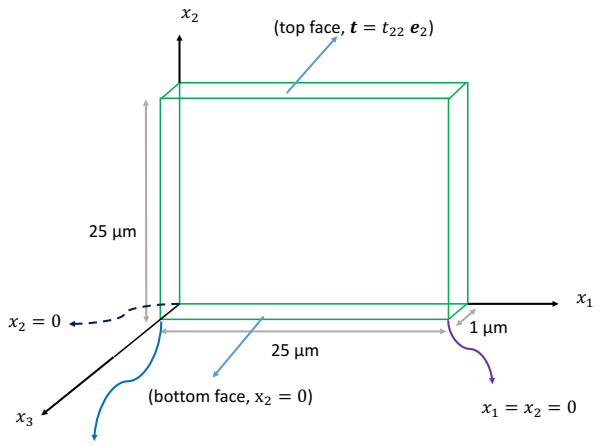

Figure 3.16: *Boundary conditions for uniaxial tension*

rigid body motion is applied. For uniaxial tension, we apply the traction $\boldsymbol{t} = t_{22}\boldsymbol{e}_2$ on the top face and keep the bottom face fixed in the Y direction ($x_2 = 0$), as shown in Fig. 3.16. For the shear problem, we apply the traction $\boldsymbol{t} = t_{12}\boldsymbol{e}_2$ and $\boldsymbol{t} = t_{12}\boldsymbol{e}_1$ on the top and right face respectively, and $\boldsymbol{t} = -t_{12}\boldsymbol{e}_1$ and $\boldsymbol{t} = -t_{12}\boldsymbol{e}_2$ on the left and bottom faces respectively. The load (t_{12} for the shear problem and t_{22} for the tension problem) depends on the loading rate l, which is set as $1MPa/s$ unless the *limit* load is reached, in which case it is set to 0. All simulation details are mentioned in Table 3.1 in Section 3.3.3.

3.5.5.1.1 Convergence We choose a $25\mu m \times 25\mu m \times 1\mu m$ sample and divide it into 2500 elements each of size $0.5\mu m \times 0.5\mu m \times 1\mu m$. As introduced and explained in Section 3.4, we divide the domain into 5×5, 7×7 and 10×10 blocks with *stress averaging* size of $5\mu m$, $3.5\mu m$ and $2.5\mu m$ respectively. We perform DD simulations in each such block (in parallel).

The stress strain curves for the $25\mu m$ size in tension for *stress averaging* size of $5\mu m$, $3.5\mu m$ and $2.5\mu m$ are shown in Fig. 3.17. We also did a run with domain size of $400\mu m \times 400\mu m \times 1\mu m$ in tension with *stress averaging* sizes of $80\mu m$ and $40\mu m$ and the stress strain curves are shown in Fig. 3.18. The relative error of the stress strain response is calculated as $e(\epsilon) = \frac{|\sigma_{10\times10}(\epsilon) - \sigma_{5\times5}(\epsilon)|}{|\sigma_{10\times10}(\epsilon)|} \times 100$, where $\sigma_{10\times10}(\epsilon)$ and $\sigma_{5\times5}(\epsilon)$ are the stresses corresponding to

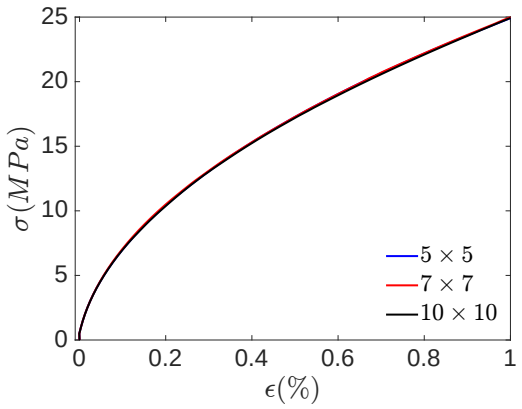

Figure 3.17: *Convergence in stress-strain response for 25 micron sample in tension for different* stress averaging *sizes*

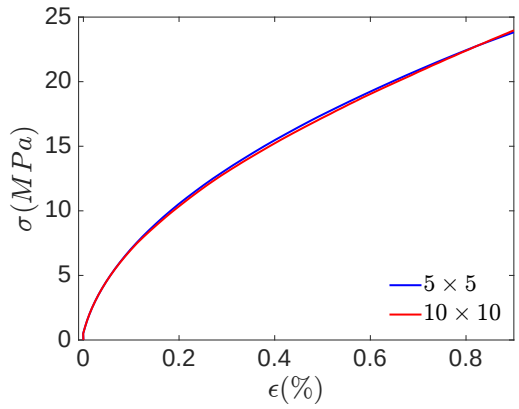

Figure 3.18: *Stress-strain response for 400 micron sample in shear for different* stress averaging *sizes*

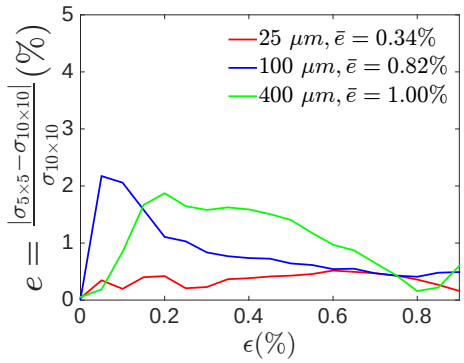

Figure 3.19: *Relative error*

strain ϵ, for runs with 10×10 and 5×5 blocks respectively, as shown in Fig. 3.17 and Fig. 3.18. The relative error is shown in Fig. 3.19 and it decreases as the sample size reduces (which is evident from the average relative error, $\bar{e}$) and in turn the *stress averaging* size, with an *stress averaging* size of $5\mu m$ or less being very accurate, with $\bar{e}$ of only 0.32%. Based on these results, we think that *stress averaging* size of $5\mu m$ for a $1\mu m$ DD box shows convergence.

3.5.5.1.2 Microstructure, rate and orientation effects The initial state of DD for the simulation is refererred as the initial DD microstructure. The state of the sample obtained from solving the MFDM system is simply called the microstructure. Here, we discuss about

the details of the microstructure and various effects that we observe.

1. **Microstructure** We see the variation of the norm of the dislocation density tensor ($|\boldsymbol{\alpha}|/b$) and the norm of the deviatoric stress, referred to as J_2 here, across the domain for a 25 micron size with 5×5 processors in uniaxial tension in Fig. 3.20 and Fig. 3.21 respectively. For the shear case, we see the dislocation density and stress in Fig. 3.22 and Fig. 3.23 respectively. We see that both the dislocation density and stress profiles are heterogeneous at high levels of strain.

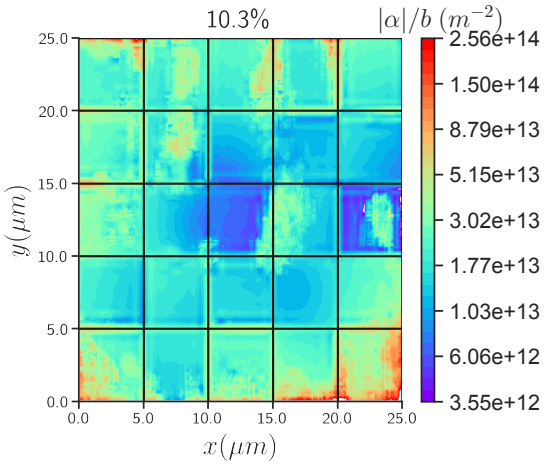

Figure 3.20: $|\boldsymbol{\alpha}|$ *for* 25 *micron sample in uniaxial tension with* 5×5 *blocks at* 10.3% *strain*

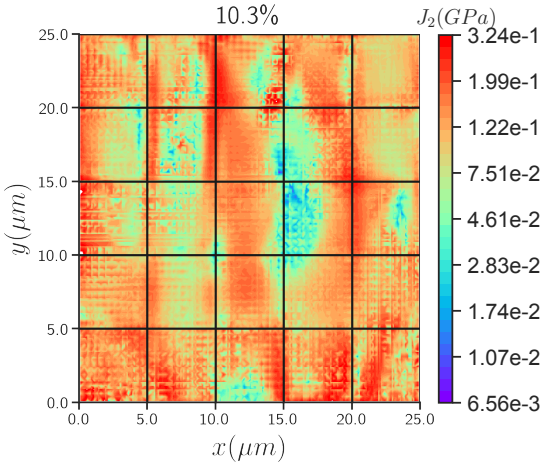

Figure 3.21: J_2 *for* 25 *micron sample in uniaxial tension with* 5×5 *blocks at* 10.3% *strain*

2. **Orientation effects** We see in Fig.3.24 that the stress-strain profile for the 25 μm sample is harder for uniaxial tension as compared to simple shear. This is expected, as in the shear case, we have dislocation segments in the primary plane which have a higher Schmid factor, while in the tension case, we have segments in planes which have smaller Schmid factor. The ratio of the sum of the Schmid factors of the active slip systems (denoted as $f_{s,i}$ and defined in (3.3.2)) is 1.84. The ratio of the stress response of the uniaxial tension and simple shear as shown in Fig. 3.24 lies between 1.99 and 2.31 with a mean of 2.13. Thus, the difference in the response between the two orientations is in accord with the prediction of the Schmid factor. However, it is

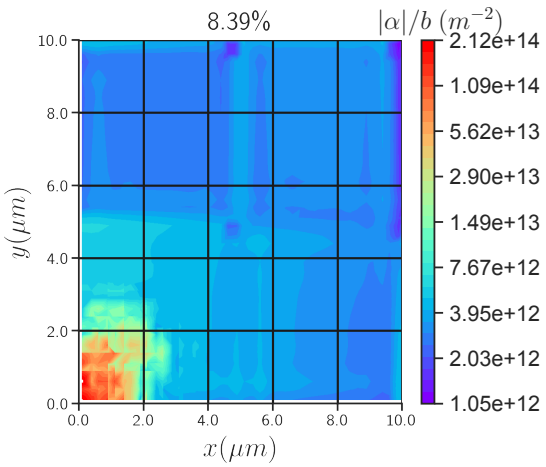

Figure 3.22: $|\boldsymbol{\alpha}|$ *for* 25 *micron sample in simple shear with* 5×5 *blocks at* 8.39% *strain*

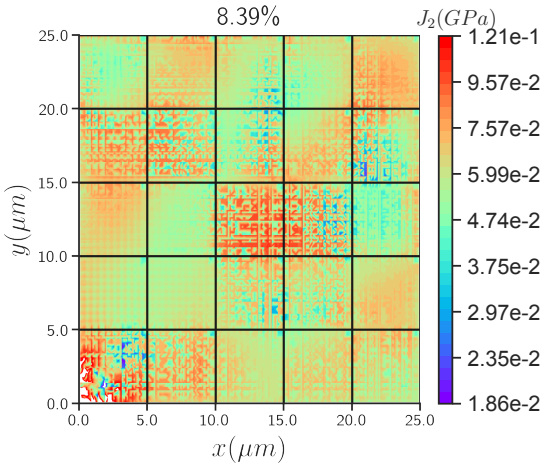

Figure 3.23: J_2 *for* 25 *micron sample in simple shear with* 5×5 *blocks at* 8.39% *strain*

to be noted that this is an emergent behavior and there is no ad-hoc *assumption* made here.

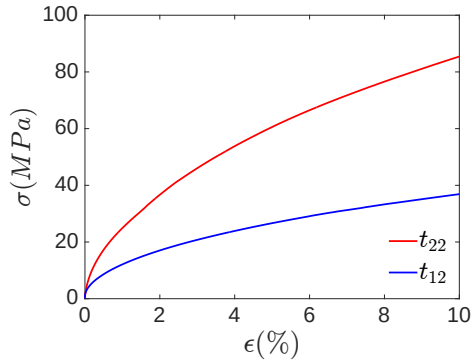

Figure 3.24: *Orientation effect: stress-strain response for* 25 *micron sample in uniaxial tension* (t_{22}) *and simple shear* (t_{12}) *under load control*

3. **Rate effects** With the reduction of loading rate, the stress-strain response becomes softer in both tension and shear (as shown in Fig. 3.25 for a 25 *micron* sample), as expected, because there is more time for plasticity to happen. The response is appreciably rate dependent for the loading rate of 1 MPa/s and the nominal mobile and sessile dislocation densities (of $1.51 \times 10^{12}\ m^{-2}$ and $1.63 \times 10^{14}\ m^{-2}$ respectively) involved. Rate independence is explored later.

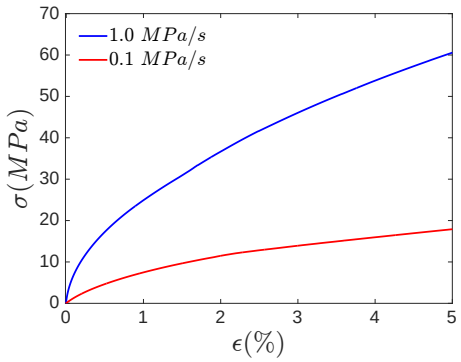

Figure 3.25: *Rate effect: stress-strain response for* 25 *micron sample in uniaxial tension under load control at different rates*

4. **Effect of different initial DD microstructure** We run a number of simulations with different initial DD microstructures and then take the average of the stress-strain response obtained from these runs. The results are presented in Fig. 3.26.

   The response varies with the choice of the initial DD microstructure. In general, for the same ρ^s, an increase in ρ^m leads to a softer stress strain response. This is expected as more mobile density means more generation of plastic strain, and hence the curve is supposed to be softer.

   The layout (configuration of the dislocation segments) of the initial DD microstructure also appears to be very important in determining the response of the sample. However, in reality, for macroscopic samples of size greater than 100 μm, the layout of the initial microstructure does not play such an important role. Thus, this is a limitation of our strategy. One way to address this is to add macroscopic descriptors in MFDM, which will act as sources of feedback, based on which the evolution of the DD microstructure can be controlled.

3.5.5.2 Case 1: Displacement Control

We also perform the simulation for the 25 *micron* sample with displacement control. Standard displacement boundary condition to prevent rigid body motion is applied. However,

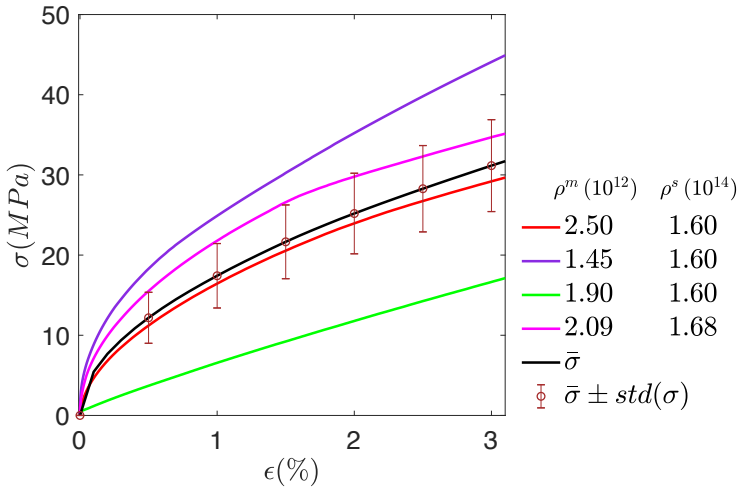

Figure 3.26: *Stress-strain response for* 25 *micron sample in uniaxial tension with different initial microstructure described by their mobile and sessile densities, their average given by* $\bar{\sigma}$ *and the upper and lower bounds given by* $\bar{\sigma} + std(\sigma)$ *and* $\bar{\sigma} - std(\sigma)$ *respectively, where* $std(\sigma)$ *is the standard deviation of the stress across all the different initial microstructures. The units of* ρ^m *and* ρ^s *is* m^{-2}.

instead of applying the traction $\boldsymbol{t} = t_{22}\boldsymbol{e}_2$ on the top face as shown in Fig. 3.16, we apply displacement boundary condition on the top face corresponding to uniaxial tension $\boldsymbol{x} = x_2\boldsymbol{e}_2$ and the bottom face is kept fixed in the Y direction. The *current* load x_2 depends on the strain rate s unless it is set to 0 when the *limit* load is reached. However, one point of difference in the displacement control case from the load control case is that when the load is kept fixed in the load control case, deformation still happens and we are supplying energy to the system, which is not true when we keep the displacement fixed in the displacement control case. The goal is to be able to run simulations for very slow loading rates upto appreciable values of strain.

The stress-strain response depends on the ratio of mobile segment density (ρ^m) to sessile segment density (ρ^s). In general, for a particular value of applied strain rate, there appears to exist an approximate ratio $r = \frac{\rho^s}{\rho^m}$, for which the simulations can be performed upto large values of strain, without the occurrence of a collapse (vanishing of the reaction force) in the stress-strain response. For example, we used two microstructures with ρ^m and ρ^s mentioned in Fig. 3.27 (ρ^m and ρ^s are in units of m^{-2} here and in the results mentioned

later). The ratio r comes out to be 590.28 and 625 respectively for the two microstructures. Using a ratio of this order for the initial microstructure, the simulations could be performed with an applied strain rate of $s = 10^{-4}/s$, without a collapse. The response corresponding to $\rho^m = 2.82 \times 10^{11}\, m^{-2}$ and $\rho^s = 1.7 \times 10^{14}\, m^{-2}$ shows a drop in stress from a strain of 0.07% to a strain of 0.17%. The drop in stress at very small strains is a common feature of responses for uniaxial tension using displacement control (see Fig. 3.30 and Fig. 3.31). At small strains and high values of stress, there is increased motion of dislocations, leading to a rise in the plastic strain rate, which causes the drop in stress. This follows with a rise in stress till a strain of 0.63%, which is caused by the internal stress fields which affect the Peach-Koehler forces acting on the segments and slows their motion.

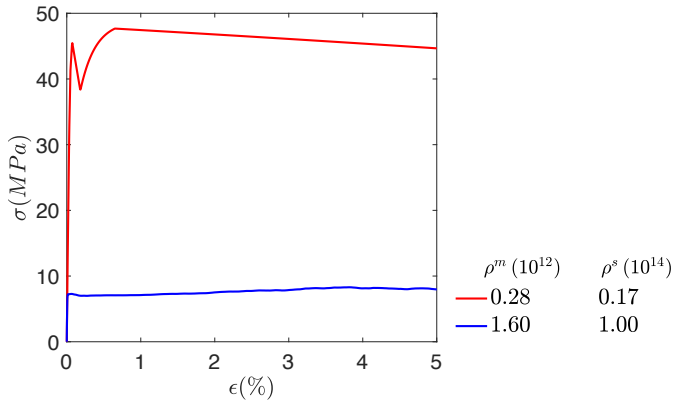

Figure 3.27: *Stress-strain response for* 25 *micron sample in uniaxial tension under displacement control at applied strain rate of* $s = 10^{-4}/s$.

Next, we discuss about the microstructure details, orientation and rate effect and the effect of different initial DD microstructures under displacement control.

1. **Microstructure** We see the variation of the norm of dislocation density tensor ($|\boldsymbol{\alpha}|/b$) and the stress (J_2) across the domain for a 25 micron size with 5×5 processors in uniaxial tension for an applied strain rate of $s = 10^{-4}/s$ in Fig. 3.28 and Fig. 3.29 respectively (the stress-strain curve for this run is shown in Fig. 3.27). We see that both the dislocation density and stress profiles are very heterogeneous at high levels of strain.

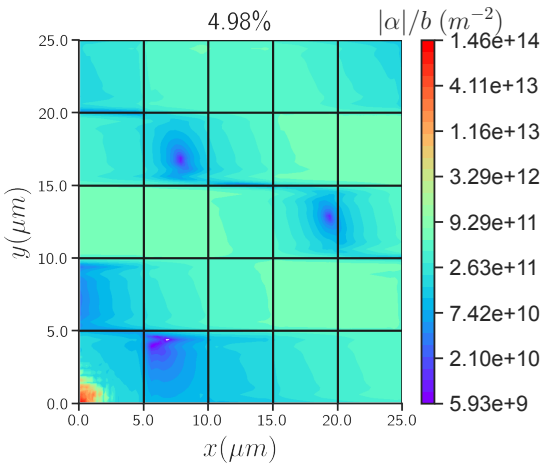

Figure 3.28: $|\boldsymbol{\alpha}|$ *for* 25 *micron sample in uniaxial tension with* 5×5 *processors at* 4.98% *strain*

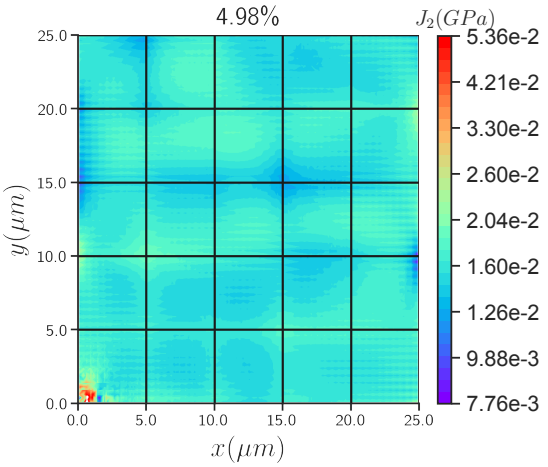

Figure 3.29: J_2 *for* 25 *micron sample in uniaxial tension with* 5×5 *processors at* 4.98% *strain*

2. **Orientation effects** We see in Fig. 3.30 that the stress-strain profile for the 25 μm sample is harder and has higher yield stress (the value of stress at which the slope reduces significantly from the initial slope of the elastic response) for uniaxial tension as compared to simple shear. This is expected, as in the shear case, we have dislocation segments in the primary plane which have a higher Schmid factor, while in the tension case, we have segments in planes which have smaller Schmid factor. The ratio of the sum of the Schmid factors of the active slip systems (denoted as $f_{s,i}$ and defined by (3.3.2)) is 1.84. The ratio of the stress strain response of the uniaxial tension and simple shear, as shown in Fig. 3.30, lies between 2.87 and 3.49, for strain higher than 1 % (which is maximum value of strain at which the response for both the loading cases show yielding).

3. **Rate effects** We see in Fig. 3.31 that with the reduction of loading rate, the stress-strain response becomes softer and has a lower yield stress in uniaxial tension. This is expected, as for lower strain rate, there is more time for plastic deformation to happen. The response is rate dependent for a loading rate of $10^{-3}/s$ and mobile and sessile dislocation densities of $3.73 \times 10^{11}\ m^{-2}$ and $1.67 \times 10^{14}\ m^{-2}$ respectively.

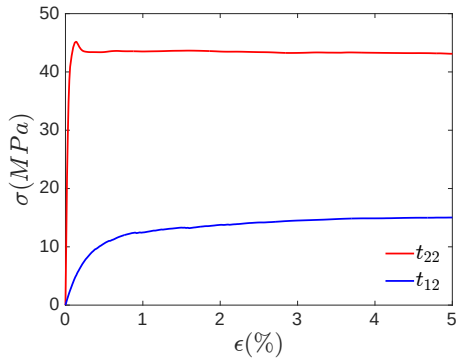

Figure 3.30: *Orientation effect: stress-strain response for* 25 *micron sample in uniaxial tension* (t_{22}) *and simple shear* (t_{12}) *under displacement control*

The response is harder for $s = 10^{-4}/s$ (Fig. 3.32) compared to $s = 2 \times 10^{-5}/s$ for $\rho^s = 1.7 \times 10^{14}\ m^{-2}$. However, for $\rho^s = 10^{15}\ m^{-2}$, the response is rate independent for $s = 10^{-4}/s$ compared to $s = 2 \times 10^{-5}/s$, till a strain of 0.2%. For higher strains, the response for $s = 2 \times 10^{-5}/s$ is harder compared to that for $s = 10^{-4}/s$. The response for $s = 2 \times 10^{-5}/s$ shows Stage I hardening till a strain of 0.2 %. Then it rises steeply till a strain of 0.35 %, which is characteristic of Stage II hardening. The average slope of the stress-strain curve in this part is 17.71 GPa, which is much higher than $\frac{\mu}{200} = 0.24$ GPa (where μ is the shear modulus, whose value has been provided in Table 3.1), which is the slope observed in Stage II hardening in macroscopic samples.

This follows with a decrease in the slope (Stage III hardening). It is observed that ρ^m does not appreciably increase (while ρ^s is fixed), so the hardening is not caused by an increase in the density of dislocation segments. This strongly implies that the internal stress field affects the Peach-Koehler force acting on the segments and causes the hardening.

4. **Effect of different initial microstructure** We run a number of simulations with different initial microstructures and then take the average of the stress-strain response obtained from these runs.

   The results are presented in Fig. 3.33. We see that there the response varies with the

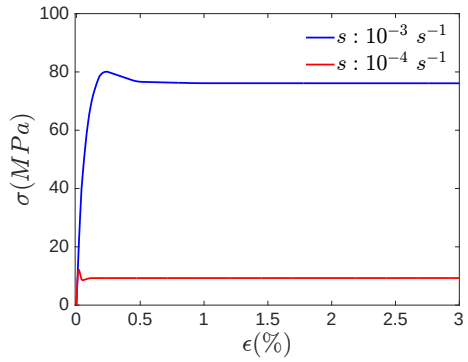

Figure 3.31: *Rate effect: stress-strain response for* 25 *micron sample in uniaxial tension under displacement control at different rates*

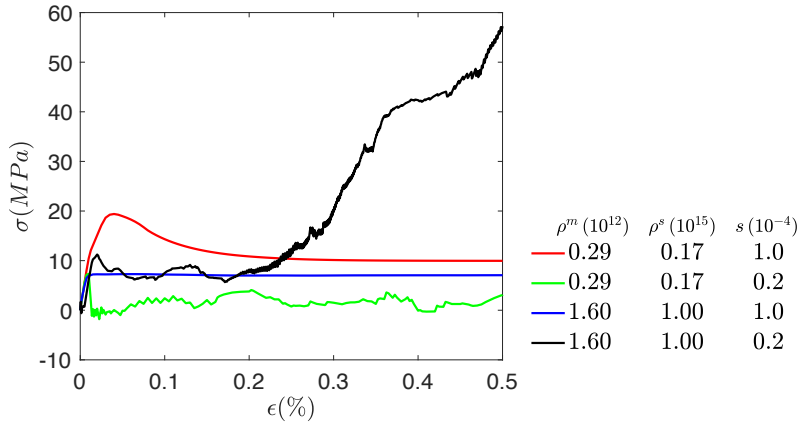

Figure 3.32: *Rate effect: stress-strain response for* 25 *micron sample in uniaxial tension under displacement control at different rates. The strain rate* s *is in units of* s^{-1}.

choice of the initial DD microstructure. In general, for the same ρ^s, higher the ρ^m, the softer the stress strain response is. This is expected as more mobile density means more generation of plastic strain, and hence the curve is supposed to be softer.

Remark It has been demonstrated in many experiments that at the micron and sub-micron scales, the sample size dramatically affects the strength, as seen in uniaxial tension experiments on a wide range of single-crystal nano and micro pillars (for review, see [USD09, KGMW10]). The stress-strain curves for Ni microcompression samples having diameters in the 20 μm to 40 μm range are similar to those for bulk samples, while samples less than 20 μm show distinct variations in the stress-strain curves [UDFN04]. [KGDP08] reported size effects in Cu single crystals of size less than 8 μm

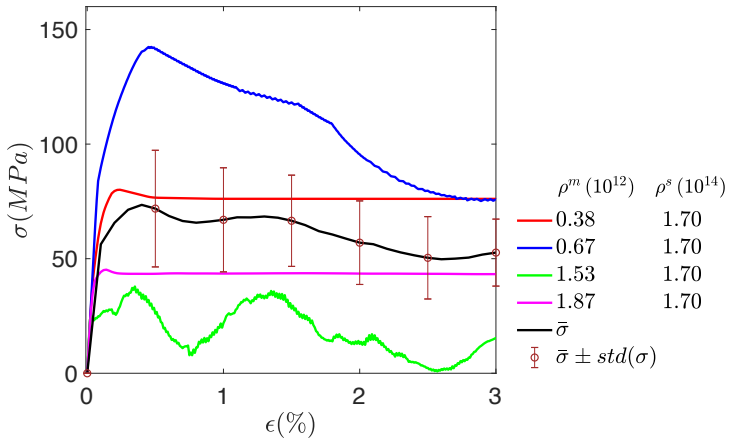

Figure 3.33: *Stress-strain response for* 25 *micron sample in uniaxial tension with different initial microstructure described by their mobile and sessile densities, their average given by* $\bar{\sigma}$ *and the upper and lower bounds given by* $\bar{\sigma} + std(\sigma)$ *and* $\bar{\sigma} - std(\sigma)$*, where* $std(\sigma)$ *is the standard deviation of the stress across all the different initial microstructures.*

in tension, while [JBG10] showed strong size effect in Cu nanopillars in compression. Some other crystalline materials whose size effect for samples less than 10 μm in diameter have been reported are Au [GON05] and Al [NN08]. [HS04] reported size effect in stress-strain curves of nanoscale Al and Au films with microelectromechanical systems (MEMS) based uniaxial tensile testing technique.

Our results for sample size of 25 μm also show high variation in the stress-strain response, which depends on the initial microstructure (see Fig. 3.33). Whether such variation ceases to exist in our simulations for bulk samples needs to be further explored.

5. **Initial yield** In Fig. 3.30, the intial yield stress (the value of stress at which the response deviates from being elastic) of the response corresponding to uniaxial tension is approximately 35 MPa while that for simple shear is approximately 10 MPa. Thus, the ratio between the yield stresses for the two cases is around 3.5. The ratio of the Schmid factors corresponding to the primary planes of the orientations for these two loading cases (as described in Section 3.3.3.1 and 3.3.3.2 respectively) is 2.45. This is a prediction of the coupled DD-MFDM strategy, without any ad-hoc *assumption* put

in by hand.

3.5.5.3 Case 2

In this case, the Burgers vector of the sessile segments lie in the slip plane. Thus, this is a more physically appropriate case. We present some results for this case to show how it compares with Case 1.

The stress strain response of a 25 μm sample in uniaxial tension, under load control, at loading rates of 1 MPa/s and 0.1 MPa/s is shown in Fig. 3.34. Case 1 is represented as $\boldsymbol{b}^s \cdot \boldsymbol{n} \neq 0$. Case 2 is represented as $\boldsymbol{b}^s \cdot \boldsymbol{n} = 0$.

The stress strain response of a 25 μm sample in uniaxial tension, under displacement control, at a strain rate of 10^{-3} s^{-1} is shown in Fig. 3.35.

This important physical idealization appears to suggest (as evident in Fig. 3.34 and Fig. 3.35) that the response is harder when the Burgers vector of the sessile segments lie in the slip plane, when compared to the case where they lie outside the slip plane. The Burgers vector distribution of the sessile segments affect the Peach-Koehler force driving the motion of each segment, thus affecting the overall plasticity in the block. These preliminary results suggest that, even after averaging, this is a significant effect.

3.5.6 Speedup

The speedup in compute time for a single Gauss point case, for a $1\mu m$ DD box, as mentioned in Section 3.3.3, is around 1000. So, for a 25 μm sample, the speedup is around

$$\frac{25}{1} \times \frac{25}{1} \times 1000 = 6.25 \times 10^5.$$

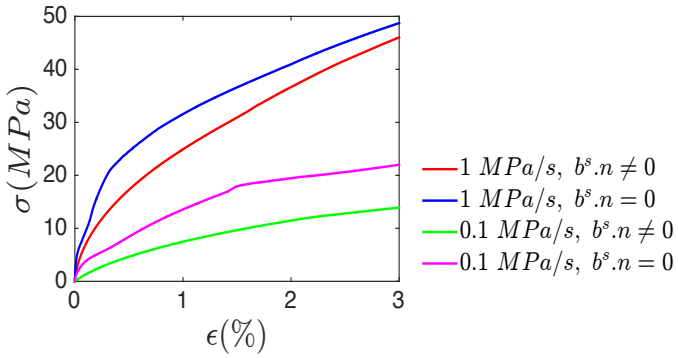

Figure 3.34: *Stress strain response of a 25 micron sample in uniaxial tension at different loading rates under load control for Case 1* ($\boldsymbol{b}^s \cdot \boldsymbol{n} \neq 0$) *and Case 2* ($\boldsymbol{b}^s \cdot \boldsymbol{n} = 0$).

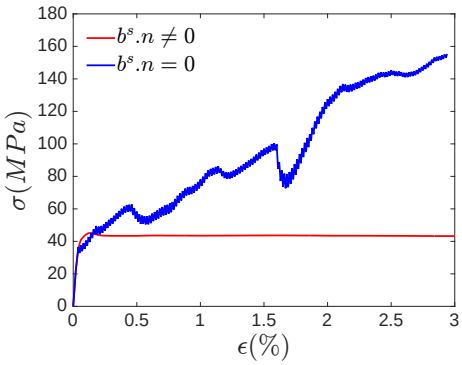

Figure 3.35: *Stress strain response of a 25 micron sample in uniaxial tension at strain rate of* 10^{-3} s^{-1} *under displacement control for Case 1* ($\boldsymbol{b}^s \cdot \boldsymbol{n} \neq 0$) *and Case 2* ($\boldsymbol{b}^s \cdot \boldsymbol{n} = 0$).

This is a very conservative estimate since we are not considering the interactions that would exist between these 1 μm boxes throughout the sample of 25 μm. But even for such a conservative estimate, the speedup is very high when compared to conventional DD, which shows the advantage of our DD-MFDM coupling strategy.

3.6 Discussion

A novel concurrent, multiscale approach to meso/macroscale plasticity has been implemented using a carefully designed coupling of MFDM with space-time averaged inputs from DD simulations. We have been able to obtain the stress strain response at *realistic* slow loading rates for large sample sizes and with significant speedup in compute time (around 10^5 using a conservative estimate), which shows the advantage of our coupled approach compared to conventional DD.

We have been able to show the strong dependence of the results on: (i) the orientation of the microstructure (for the two loading cases of simple shear and uniaxial tension) (ii) the loading rate (iii) the ratio of mobile to sessile segment density. We have been able to show

these effects for both load and displacement controlled simulations. We have also suggested that there is a limiting *stress averaging* size of 5 μm for which we get converged results for a DD box of 1 μm. Moreover, we are able to demonstrate the collective behavior of dislocations under the action of internal stress. The effect of internal stresses, which control the *Peach-Köehler* forces acting on the segments and affect their motion, is visible in the stress-strain responses that we presented.

The only constitutive assumption used in this coupled strategy is a simplified adaptation of the thermal activation of dislocation motion past obstacles [KM03], which is described in Section 3.2.2. However, the order of the timescale set by the plastic strain rate obtained in our simulations is very different from the timescale set by the junction breaking time.

We point out the (current) limitations of our approach. These are

- The dislocation content that is allowed to be mobile does not grow in density to the extent that is observed in reality. In a well annealed crystal, the total dislocation density grows by around 8 orders of magnitude and a large fraction of the mobile segments becomes sessile. Our simulations are currently incapable of representing such growth of the dislocation density. To account for this deficiency, we adopt the physical picture of [KM03]) and work with an a-priori assumption of a sessile distribution of dislocations in each DD box and a separate mobile population, the latter being allowed to evolve and grow (or diminish), with full interaction within itself as well as with the sessile population.

- The polar dislocation velocity is negligible.

- The response is highly dependent on the configuration of the segments in the initial DD microstructure. In reality, for macroscopic samples, it is generally observed that the response does not vary so much based on the state of the initial microstructure. Whether our simulations bear out this expectation for larger sample sizes needs to be explored. A difficulty associated with performing our simulations for large sample sizes

is the computational expense. However, this is not a fundamental difficulty but a practical one, which can be addressed with more sophisticated parallelization algorithms and implementation than this first effort.

Immediate partial remedial measures for these limitations are expected to be the accounting of the mobile density in DD boxes in accord with the averaged dislocation density $\overline{\rho}$ (whose evolution is derived in Chapter 4) and the GND density $\overline{\boldsymbol{\alpha}}$ suggested by MFDM, in the coupled DD-MFDM strategy. These descriptors will act as feedback for the initialization of the DD microstructure at discrete time steps.

Chapter 4

A formal hierarchy of governing equations by averaging dislocation dynamics in real space and time

4.1 Introduction

This section is concerned with the formal derivation of governing field equations of increasingly detailed space-time averaged behavior of microscopic dislocation dynamics. The microscopic dislocation dynamics is posed as a system of pde, capable of representing the dynamics of a collection of possibly tangled smooth curves representing dislocation core cylinders, each core cylinder movable by a combination of glide and climb due to the action of a vectorial velocity field. The velocity field is determined, following well-accepted notions, purely from the dislocation density field (with the possibly tangled web of core cylinders viewed simply as appropriate smooth localizations in space of the dislocation density field), and the (nonlinear crystal elastic) stress field in the body; even when linear elasticity is used, the point-wise Burgers vector direction and line direction (information built into the dislocation density

field) are adequate to describe the motion of edge segments, and the motion of screws are restricted to within a geometrically defined set of planes. In any case a resolution into slip system dislocation densities is not essential (cf. [ZCA13]). This pde system is adequate for representing the plasticity of the constituent material when atomic length scales are resolved - we refer to this system as Field Dislocation Mechanics (FDM). We are interested in obtaining the implications of this model when the resolved length (and time) scales are much coarser, i.e. we are interested in obtaining some information on the nature of the governing evolution equations for increasingly detailed descriptions of averaged behavior of this microscopic system, appropriate for coarser-length and time scales. We emphasize that the derived averaged equations represent exact, but non-closed, statements of evolution of the defined average variables, without any compromise on the inherent kinematic constraints of the microscopic system(e.g. the connectedness of the dislocation lines represented by the solenoidal property of the microscopic dislocation density field).

The above line of inquiry was initiated in [AR06, AC12]; as will be shown in this chapter, the exact equations of evolution become exceedingly complex and cumbersome and it was suggested in [AR06] that closure assumptions be made at a relatively lower level to maintain tractability (while allowing for the inclusion of all that is known in the physics-based phenomenological modeling of plastic deformation and strength, e.g. [KAA75]) and refining the description as required for greater fidelity. We will refer to this approach as the MFDM (Mesoscale Field Dislocation Mechanics) approach to plasticity.

In the Continuum Dislocation Dynamics (CDD) framework of Hochrainer and collaborators [HZG07, Hoc16, MZ18], models are developed based on a kinetic theory-like framework, starting from the assumption that a fundamental statement for the evolution of a number density function on the space of dislocation segment positions and orientations is available at the microscopic level. This *microscopic* governing equation is non-closed even if one knows completely the rules of physical evolution of individual dislocations segments of connected

lines; one would need to study the behavior of an ensemble of dislocation dynamics evolutions to define, and then also only in principle, the evolution of such a number density function (cf. [HZG07, Sec 3.1, 5]) - this detail is built into the state-space velocity function introduced in [HZG07], which cannot be simply defined by a well-accepted statement like the Peach-Köhler force for a segment of a real-space description of a dislocation line. Furthermore, Equations (7) and (11) of [HZG07], the fundamental statement of evolution governing the number density function (a 'collective' quantity), are postulated without fundamental justification. This is in contrast to FDM where the *fundamental justification for the statement of microscopic dynamics* is the integral statement of conservation of Burgers vector, a physically observed fact (which does not imply a conservation of the 'number' of dislocations, whether loops or otherwise, as stated in [HZG07, Sec. 4], and as demonstrated in exercises related to annihilation and nucleation [GAM15]); then, the equations of MFDM follow strictly from FDM on averaging, without any further assumptions. Returning to CDD, on making various assumptions for tractability, the theory produces (non-closed) statements of evolution for the averaged dislocation density (akin to the mesoscale Nye tensor field), the total dislocation density (similar to an appropriate sum of the averaged Nye tensor density) and, these densities being defined as physical scalars, and an associated curvature density field. Closure assumptions are made to cut off infinite hierarchies, which is standard for averaging based on nonlinear 'microscopic equations', and further closure assumptions for constitutive statements are made based on standard thermodynamic arguments [Hoc16].

The model in [XEA15] belongs to the same mathematical class as MFDM but with more complicated constitutive structure related to multiple-slip behavior [DAS16]. It assumes geometrically linear kinematics for the total deformation coupled to a system of stress-dependent, nonlinear transport equations for vector-valued slip-system dislocation densities. These slip system density transport equations involve complicated, phenomenological constitutive assumptions related to cross-slip, and the authors of [XEA15] promote the point of view that dislocation patterning is related to the modeling of slip system dislocation densities

and cross-slip. An attempt to understand emergence of microstructure in 1-d setting was made in [DAS16], and in 3-d and finite deformation setting was made in [AA19]. They concluded that in all likelihood, such complexity is not essential for the emergence of dislocation microstructure in this family of models.

Despite *postulating* fundamental microscopic statements, making closure assumptions of their own, and making ad-hoc choices of cutting off the infinite hierarchy of their equations, the CDD authors have criticized the MFDM approach as inadequate for describing the plasticity of metals [HZG07, Hoc16, MZ18]. The authors of [XEA15] have criticized MFDM for using a phenomenological approach and for the lack of resolution into slip systems in order to model cross slip. One goal of this chapter is to show that the criticisms leveled against the MFDM approach in [SHZG11, XEA15, MZ18] are unfounded.

The MFDM approach starts from a well-accepted fundamental microscopic dynamical statement (unlike CDD), and produces an exact hierarchy of equations for any desired level of detail in the coarse description as an implication of this fundamental microscopic dynamics. Extending the work in [AC12], this paper explicitly shows that while the MFDM approach can easily accommodate descriptors like slip system dislocation densities and define precise hierarchies of evolution equations for them, such an enterprise comes at a significant cost in complexity and tractability of the resulting model, and shows the exact nature of phenomenology and gross approximation that would necessarily be inherent in any proposed formalism for coarse-grained dislocation dynamics (e.g., [SHZG11, XEA15]) that does not consider head-on the question of averaging the stress-coupled interaction-related dynamics of dislocations.

This chapter is organized as follows. In Section 4.2, we apply the averaging procedure utilized in [Bab97] to generate an infinite hierarchy of nonlinear coarse equations corresponding to a fine dynamics, which (essentially) cannot be solved. In Section 4.3, we apply the averaging procedure to derive the coarse evolution of averaged total dislocation density and

demonstrate, using a simple example, that the averaged dislocation density of an expanding circular loop increases. In Section 4.3.2, we present a refined description of the variables with respect to individual slip systems, reflective of a crystal plasticity description and present the coarse evolution of these variables, namely the averaged dislocation density tensor and the averaged total dislocation density. In order to do so, we define a characteristic function, which indicates whether any given position has a dislocation of a particular slip system. We show how the coarse evolution of these variables are very cumbersome and hence, why it is reasonable to close the infinite hierarchy of non-closed system of equations at a low level. It is also important to generate lower level closure assumptions that account for the *stress coupled* dynamics of dislocations. Such work is currently in progress ([CPZ$^+$]).

4.2 Hierarchy of averaged equations for nonlinear microscopic equations: the basic idea

In this section, we will utilize an averaging procedure used in the literature for multiphase flows (see [Bab97]). For a microscopic field f given as a function of space and time, the mesoscopic space-time-averaged field $\bar{f}$ [AR06, AC12] is given as

$$\bar{f}(\boldsymbol{x},t) = \frac{1}{\int_{I(t)}\int_{\Omega(\boldsymbol{x})} w(\boldsymbol{x}-\boldsymbol{x}',t-t')d\boldsymbol{x}'dt'} \int_{\Im}\int_{B} w(\boldsymbol{x}-\boldsymbol{x}',t-t')f(\boldsymbol{x}',t')d\boldsymbol{x}'dt', \qquad (4.2.1)$$

where B is the body and I a sufficiently large interval of time. In the above, $\Omega(\boldsymbol{x})$ is a bounded region within the body around the point $\boldsymbol{x}$ with linear dimension of the order of the spatial resolution of the macroscopic model we seek, and $I(t)$ is a bounded interval in I containing t. The weighting function w is non-dimensional, assumed to be smooth in the variables $\boldsymbol{x}$, $\boldsymbol{x}'$, t, t' and, for fixed $\boldsymbol{x}$ and t, have support (i.e. to be non-zero) only in $\Omega(\boldsymbol{x}) \times I(t)$ when viewed as a function of $(\boldsymbol{x}', t')$.

The one-dimensional analogue of (4.2.1) is

$$\partial_{t'} f = F(f, \partial_{x'} f), \tag{4.2.2}$$

where x' is the spatial coordinate and t' is time and f is a function of x' and t'. We call the system given by equation (4.2.2) as the fine scale system.

We aim to understand the macroscopic evolution of the fine dynamics (4.2.2) in terms of averaged (coarse) variables. To do so, the averaging operator (4.2.1) is applied to both sides of (4.2.2), which results in the following:

$$\frac{\partial}{\partial t}\overline{f}(x,t) = \overline{F(f, \partial_{x'} f)}(x,t). \tag{4.2.3}$$

We denote $A_0 := \overline{f}$ and $A_{01} := \partial_t A_0 = \overline{F}$. The fluctuation of function f is defined as:

$$\Sigma^f(x', t', x, t) := f(x', t') - \overline{f}(x,t). \tag{4.2.4}$$

The average of the product (p) of two variables f and g is given by

$$\begin{aligned}
\overline{f(p)g} =& \overline{\{\bar{f} + (f - \bar{f})\}(p)\{\bar{g} + (g - \bar{g})\}} \\
=& \overline{\bar{f}(p)\bar{g} + \bar{f}(p)(g - \bar{g}) + (f - \bar{f})(p)\bar{g} + (f - \bar{f})(p)(g - \bar{g})} \\
=& \overline{f}(p)\overline{g} + \bar{f}(p)\overline{\Sigma^g} + \bar{g}(p)\overline{\Sigma^f} + \overline{\Sigma^f(p)\Sigma^g} \\
=& \overline{f}(p)\overline{g} + \overline{\Sigma^f(p)\Sigma^g},
\end{aligned} \tag{4.2.5}$$

so that

$$\overline{f(p)g} - \bar{f}(p)\bar{g} = \overline{f(p)g - \bar{f}(p)\bar{g}} = \overline{\Sigma^f(p)\Sigma^g}.$$

Here, f and g can be scalar, vector or tensor valued. Some examples of the product (p) are

scalar multiplication, vector inner product, tensor inner product, cross product of a tensor with a vector etc. For example, if f and g are scalar and (p) is the scalar multiplication operator,

$$\overline{fg} = \overline{f}\,\overline{g} + \overline{\Sigma^f \Sigma^g}. \tag{4.2.6}$$

Using (4.2.5), we obtain the average of product of three variables as

$$\begin{aligned}\overline{f(p)g(p)h} =& \overline{f}(p)\overline{g(p)h} + \overline{\Sigma^f(p)\Sigma^{g(p)h}} = \overline{f}(p)\{\overline{g}(p)\overline{h} + \overline{\Sigma^g(p)\Sigma^h}\} + \overline{\Sigma^f(p)\Sigma^{g(p)h}} \\ =& \overline{f}(p)\overline{g}(p)\overline{h} + \overline{f}(p)\overline{\Sigma^g(p)\Sigma^h} + \overline{\Sigma^f(p)\Sigma^{g(p)h}}.\end{aligned} \tag{4.2.7}$$

Similarly, for f, g and h scalars and (p) the scalar multiplication operator,

$$\overline{fgh} = \overline{f}\,\overline{g}\,\overline{h} + \overline{f}\,\overline{\Sigma^g\,\Sigma^h} + \overline{\Sigma^f\,\Sigma^{g\,h}}. \tag{4.2.8}$$

Equations (4.2.6), (4.2.7) and (4.2.8) show that the *averages of products of two or more variables are not the products of their averages.*

It can be shown using (4.2.2), (4.2.3) and (4.2.4) that

$$\partial_{tt}A_0 = \partial_t A_{01} = \overline{\partial_2 F \partial_1 F}\partial_x A_0 + \overline{\partial_2 F \partial_2 F}\partial_{xx}A_0 + A_{011} + \overline{\Sigma^{(\partial_2 F \partial_1 F)}\Sigma^{(\partial_{x'}f)}} + \overline{\Sigma^{(\partial_2 F \partial_2 F)}\Sigma^{(\partial_{x'x'}f)}}, \tag{4.2.9}$$

where $A_{011} := \overline{\partial_1 F F}$.

Thus, in the coarse evolution of $\bar{F}$, new terms (e.g. $\overline{\partial_2 F \partial_1 F}$) emerge and therefore, it is necessary to augment (4.2.9) with coarse evolution equations of the new terms (that appear

on the rhs of (4.2.9)), namely the following:

$$\begin{aligned}
\partial_t \left(\overline{\partial_2 F \partial_1 F}\right) &= G_1 \\
\partial_t \left(\overline{\partial_2 F \partial_2 F}\right) &= G_2 \\
\partial_t \left(\overline{\Sigma^{(\partial_2 F \partial_1 F)} \Sigma^{(\partial_{x'} f)}}\right) &= G_3 \\
\partial_t \left(\overline{\Sigma^{(\partial_2 F \partial_2 F)} \Sigma^{(\partial_{x'x'} f)}}\right) &= G_4,
\end{aligned} \tag{4.2.10}$$

where G_i ($i = 1$ to 4) are functionals of the state. In general, these functionals cannot be expressed as functionals of the independent fields of the averaged model, such relations being referred to as 'closure' relations.

The functionals G_i can be generated by applying the averaging operator (4.2.1) to the fine scale equations and decomposing the average of product of functions in the fine scale into product of their averages and their associated fluctuation terms. For example, the coarse evolution of $\overline{\partial_2 F \partial_1 F}$ (which is given by G_1 above) is

$$\begin{aligned}
\partial_t \left(\overline{\partial_2 F \partial_1 F}\right) &= \overline{\partial_t' \left(\partial_2 F \partial_1 F\right)} = \overline{\partial_t' \left(\partial_2 F\right) \partial_1 F + \partial_2 F \partial_t' \left(\partial_1 F\right)} \\
&= \overline{H(\partial_1 F) + (\partial_2 F) M} = \overline{H \partial_1 F} + \overline{M \partial_2 F} + \overline{\Sigma^{H} \Sigma^{\partial_1 F}} + \overline{\Sigma^{M} \Sigma^{\partial_2 F}},
\end{aligned}$$

where $H = \partial_t' \left(\partial_2 F\right)$ and $M = \partial_t' \left(\partial_1 F\right)$. Thus, new terms appear in the coarse evolution of the term $\overline{\partial_2 F \partial_1 F}$, and similarly for the other terms in (4.2.10). In this manner, we can generate an infinite hierarchy of nonlinear coarse equations corresponding to the fine dynamics (4.2.2). Solution of such an infinite system is not possible.

It is therefore necessary to close the equations at a desired level, which means to use physics based assumptions for the necessary terms instead of solving their exact evolution equation (for example, in equation (4.2.10) above, we might use closure assumptions for the functionals G_i on the rhs). Morever, even if the system was finite but large and could be solved (in principle), approximating solutions to nonlinear systems of pde is by no means a trivial

task, so that it is definitely better to shift the focus from generating large formal hierarchies of nonlinear pde to generating controlled, with respect to accuracy, closure assumptions to maintain tractability.

4.3 Models of MFDM with varying coarse descriptors

The model of FDM [Ach01, Ach03, Ach04] represents the dynamics of a collection of dislocation lines at the atomic length scale. The field equations of FDM are as follows:

$$\begin{aligned}
&\dot{\boldsymbol{\alpha}} = -curl(\boldsymbol{\alpha} \times \boldsymbol{V}) \\
&curl\boldsymbol{\chi} = \boldsymbol{\alpha} \\
&div\boldsymbol{\chi} = 0 \\
&div(grad\dot{\boldsymbol{z}}) = div(\boldsymbol{\alpha} \times \boldsymbol{V} + \boldsymbol{L}^p) \\
&div(\boldsymbol{C} : \{grad\boldsymbol{u} - \boldsymbol{z} + \boldsymbol{\chi}\}) = 0.
\end{aligned} \tag{4.3.1}$$

The tensor $\boldsymbol{\alpha}$ is the dislocation density tensor, $\boldsymbol{V}$ is the dislocation velocity vector, $\boldsymbol{C}$ is the fourth-order, possibly anisotropic, tensor of linear elastic moduli, $\boldsymbol{u}$ is the total displacement vector, $\boldsymbol{\chi}$ is the incompatible part of the elastic distortion tensor, and $\boldsymbol{u} - \boldsymbol{z}$ is a vector field whose gradient is the compatible part of the elastic distortion tensor. Upon application of the averaging operator (4.2.1) defined in Section 4.2 to both sides of (4.3.1), we have the following system of averaged equations

$$\begin{aligned}
&\dot{\overline{\boldsymbol{\alpha}}} = -curl(\overline{\boldsymbol{\alpha}} \times \overline{\boldsymbol{V}} + \boldsymbol{L}^p) \\
&curl\overline{\boldsymbol{\chi}} = \overline{\boldsymbol{\alpha}} \\
&div\overline{\boldsymbol{\chi}} = 0 \\
&div(grad\dot{\overline{\boldsymbol{z}}}) = div(\overline{\boldsymbol{\alpha}} \times \overline{\boldsymbol{V}} + \boldsymbol{L}^p)
\end{aligned}$$

$$div(\overline{\boldsymbol{C}} : \{grad(\overline{\boldsymbol{u}} - \overline{\boldsymbol{z}}) + \overline{\boldsymbol{\chi}}\}) = 0 \tag{4.3.2}$$

[AR06]. The system (4.3.2) is called *Mesoscale Field Dislocation Mechanics*. Here, $\boldsymbol{L}^p$ is defined as

$$\boldsymbol{L}^p := \overline{\boldsymbol{\alpha} \times \boldsymbol{V}} - \overline{\boldsymbol{\alpha}} \times \overline{\boldsymbol{V}}, \tag{4.3.3}$$

and it represents the strain rate produced by 'statistically stored dislocations'. It follows from (4.2.5) that $\boldsymbol{L}^p$ is the average of the cross product of the fluctuation of $\boldsymbol{\alpha}$ and $\boldsymbol{V}$ (which means $\boldsymbol{L}^p = \overline{\Sigma^{\boldsymbol{\alpha}} \times \Sigma^{\boldsymbol{V}}}$). Consider a uniformly expanding square loop. Since $\boldsymbol{\alpha} = \boldsymbol{b} \otimes \hat{\boldsymbol{l}}$, where $\boldsymbol{b}$ is the Burgers vector density per unit area and $\hat{\boldsymbol{l}}$ is the line direction at each point of the loop and $\boldsymbol{b}$ remains uniform along the loop, and both $\hat{\boldsymbol{l}}$ and $\boldsymbol{V}$ change sign going from one side of the square loop to the opposite side, both $\overline{\boldsymbol{\alpha}} = \boldsymbol{0}$ and $\overline{\boldsymbol{V}} = \boldsymbol{0}$. However, $\boldsymbol{\alpha} \times \boldsymbol{V}$ is identical for opposite sides of the loop and does not cancel out and hence, $\boldsymbol{L}^p \neq \boldsymbol{0}$.

4.3.1 Isotropic MFDM

We consider as descriptors of the system the averaged total dislocation density ρ and the plastic distortion rate $\boldsymbol{L}^p$, which are commonly used in the literature (also see [AC12]).

- The evolution equation for **averaged total dislocation density**, $\overline{\rho^l}$. The total dislocation density is defined as

$$\rho := \boldsymbol{\alpha} : \boldsymbol{\alpha}. \tag{4.3.4}$$

  Suppose we have many dislocation segments in a box of volume V. We see that $\frac{\int_V \rho dv}{V} = \frac{\sum_i \boldsymbol{\alpha}_i : \boldsymbol{\alpha}_i \; l_i A_i}{V}$, where $\boldsymbol{\alpha}_i$, l_i and A_i (which is assumed to be $|\boldsymbol{b}_i|^2$ up to a constant) are the dislocation density tensor, line length and cross section area of segment

i respectively. We also have that $\boldsymbol{\alpha}_i = \frac{|\boldsymbol{b}_i|\boldsymbol{m}_i \otimes \boldsymbol{t}_i}{A_i}$, where $\boldsymbol{b}_i$, $\boldsymbol{m}_i$ and $\boldsymbol{t}_i$ are the Burgers vector, Burgers vector direction and the line direction of segment i. Therefore, $\frac{\sum_i \boldsymbol{\alpha}_i : \boldsymbol{\alpha}_i \ l_i A_i}{V} = \frac{1}{V}\sum_i \frac{|\boldsymbol{b}_i|^2}{A_i^2} l_i A_i = \frac{1}{V}\sum_i \frac{|\boldsymbol{b}_i|^2}{|\boldsymbol{b}_i|^4} l_i |\boldsymbol{b}_i|^2 = \frac{1}{V}\sum_i l_i$, which is the averaged dislocation density in the box. Since ρ is the microscopic total dislocation density, $\frac{\int_V \rho dv}{V}$ is ρ averaged over V, which gives the averaged dislocation density of the box. This acts as a verification that ρ is indeed the total dislocation density.

The space-time averaged total dislocation density $\overline{\rho}$ is given by

$$\overline{\rho} = \overline{\boldsymbol{\alpha}} : \overline{\boldsymbol{\alpha}} + \overline{\Sigma^{\boldsymbol{\alpha}} : \Sigma^{\boldsymbol{\alpha}}}. \tag{4.3.5}$$

This follows from (4.2.5) and shows that the average of the total dislocation density contains average terms as well as averages of fluctuations. We can interpret this using Fig. 4.1 in which we see that the averaging box has many loops which are inside the box and there are some loops which are not entirely contained inside the box. Since the Burgers vector is uniform over a loop, the average dislocation density $(\boldsymbol{b} \otimes \hat{\boldsymbol{l}})$ due to the loops which are contained in the box is $\mathbf{0}$ since the average of the line direction $\hat{\boldsymbol{l}}$ over the loop cancels out. The only contribution to the first term on the rhs of (4.3.5) is from the loops which are not entirely contained in the averaging box. If our averaging box has a very large length scale, then most loops will be contained inside the box and as such, $\overline{\boldsymbol{\alpha}} \approx \mathbf{0}$ and the main contribution to the averaged total dislocation density will come from the average of the fluctuation term given by the second term on the rhs of (4.3.5). The evolution of such fluctuation terms, as discussed in Section 4.2, will be given by other pde, which will themselves be non-closed, as they will contain other fluctuation terms. This will generate an infinite hierarchy of non-closed cumbersome pde, as will be shown next.

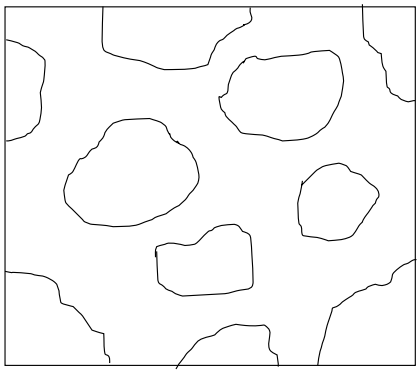

Figure 4.1: *Dislocation loops in averaging box*

The evolution of $\overline{\rho}$ is given by

$$\begin{aligned}\dot{\overline{\rho}} = &- grad\ \overline{\rho} \cdot \overline{\boldsymbol{V}} - 2\ \overline{\rho}\ div\overline{\boldsymbol{V}} + 2\ \overline{\boldsymbol{\alpha}} : (div\overline{\boldsymbol{\alpha}} \otimes \overline{\boldsymbol{V}}) + 2\ \overline{\boldsymbol{\alpha}} : \{\overline{\boldsymbol{\alpha}}\ grad\overline{\boldsymbol{V}}\} - \overline{\Sigma^{grad\rho} \cdot \Sigma^{\boldsymbol{V}}} \\ &- 2\overline{\Sigma^{\rho}\Sigma^{divV}} + 2\ \overline{\boldsymbol{\alpha}} : (\overline{\Sigma^{div\boldsymbol{\alpha}} \otimes \Sigma^{\boldsymbol{V}}}) + 2\overline{\Sigma^{\boldsymbol{\alpha}} : \Sigma^{div\boldsymbol{\alpha}\otimes\boldsymbol{V}}} + 2\ \overline{\boldsymbol{\alpha}} : \overline{\Sigma^{\boldsymbol{\alpha}}\ \Sigma^{grad\boldsymbol{V}}} \\ &+ 2\ \overline{\Sigma^{\boldsymbol{\alpha}} : \Sigma^{\boldsymbol{\alpha}}\ grad\boldsymbol{V}}. \end{aligned} \tag{4.3.6}$$

The derivation of (4.3.6) is given in Appendix C.1. As the averaging length scale becomes large, the RHS of (4.3.6) is dominated by the averages of the fluctuation terms.

Example: Circular dislocation loop

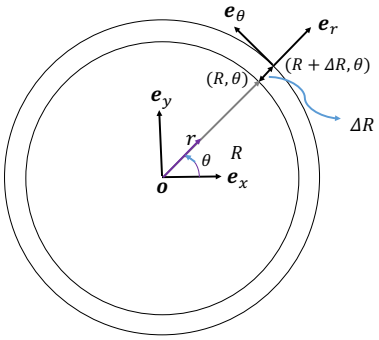

Figure 4.2: *Top view of a uniformly expanding loop of radius R and width ΔR.*

The evolution equation for ρ (as derived in Appendix C.1 and given by (C.1.2)) is

$$\dot{\rho} = -grad\rho \cdot \boldsymbol{V} - 2\rho(divV) + 2\boldsymbol{\alpha} : (div\boldsymbol{\alpha} \otimes \boldsymbol{V}) + 2\boldsymbol{\alpha} : \{\boldsymbol{\alpha}\, gradV\}$$

Application of the averaging operator (4.2.1) to the above results in the following:

$$\dot{\overline{\rho}} = -\overline{grad\rho \cdot \boldsymbol{V}} - \overline{2\rho(divV)} + \overline{2\boldsymbol{\alpha} : (div\boldsymbol{\alpha} \otimes \boldsymbol{V})} + \overline{2\boldsymbol{\alpha} : \{\boldsymbol{\alpha}\, gradV\}}. \tag{4.3.7}$$

We aim to understand the evolution of $\overline{\rho}$ for the case of a circular dislocation loop of inner radius R, width ΔR (see Fig. 4.2) and thickness t. The area of cross section of the loop is $A = \Delta R.\, t$, which is assumed to be b^2, where b is the magnitude of the Burgers vector $\boldsymbol{b}$. The radial unit vector is $\boldsymbol{e}_r = cos\theta \boldsymbol{e}_x + sin\theta \boldsymbol{e}_y$, while the tangential unit vector is $\boldsymbol{e}_\theta = -sin\theta \boldsymbol{e}_x + cos\theta \boldsymbol{e}_y$. Let us assume that its velocity has the same magnitude for all points (r, θ, z) of the loop (where z is the spatial coordinate along the thickness) and points radially outwards. Hence, the velocity is given by $\boldsymbol{V} = v(r)\ \boldsymbol{e}_r$, where $v(r) = \tilde{v}H(r - R) - \tilde{v}H(r - (R + \Delta R))$. Let the averaging domain be a circular plate of radius L and thickness H, where $L \gg R$ and $H \gg t$.

We have

$$\begin{aligned}
\overline{\boldsymbol{V}} =& \frac{1}{\pi L^2 H} \int_{\theta=0}^{\theta=2\pi} \int_{r=0}^{r=L} \int_{z=-\frac{t}{2}}^{\frac{t}{2}} v(r)\boldsymbol{e}_r r dr d\theta dz \\
=& \frac{t}{\pi L^2 H} \int_{\theta=0}^{\theta=2\pi} \int_{r=0}^{r=L} \{\tilde{v}H(r - R) - \tilde{v}H(r - (R + \Delta R))\}\{cos\theta \boldsymbol{e}_x + sin\theta \boldsymbol{e}_y\} r dr d\theta \\
=& \frac{\tilde{v}t}{\pi L^2 H} \Big[\int_R^{R+\Delta R} r\ dr \Big] \Big[\Big(\int_{\theta=0}^{\theta=2\pi} cos\theta \Big) \boldsymbol{e}_x + \Big(\int_{\theta=0}^{\theta=2\pi} sin\theta \Big) \boldsymbol{e}_y \Big] \\
=& \frac{\tilde{v}t}{\pi L^2 H} \left[\frac{r^2}{2} \right]_R^{R+\Delta R} \Big[\{sin2\pi - sin0\} \boldsymbol{e}_x + \{cos2\pi - cos0\} \boldsymbol{e}_y \Big] \\
=& \frac{\tilde{v}t}{\pi L^2 H}\ \Delta R\ (2R + \Delta R)\ \boldsymbol{0} = \boldsymbol{0}
\end{aligned} \tag{4.3.8}$$

Also,

$$\begin{aligned}
\overline{\boldsymbol{\alpha}} =& \frac{1}{\pi L^2 H}\int_{\theta=0}^{\theta=2\pi}\int_{r=0}^{r=L}\int_{z=-\frac{t}{2}}^{\frac{t}{2}} \frac{\boldsymbol{b}}{A}\otimes\hat{\boldsymbol{l}} r dr d\theta dz = \frac{t}{\pi L^2 H b^2}\int_{\theta=0}^{\theta=2\pi}\int_{r=0}^{r=L}\boldsymbol{b}\otimes\boldsymbol{e}_\theta r dr d\theta \\
=& \frac{t}{\pi L^2 H b^2}\int_{\theta=0}^{\theta=2\pi}\int_{r=0}^{r=L}\boldsymbol{b}\otimes\{-sin\theta\boldsymbol{e}_x + cos\theta\boldsymbol{e}_y\} r dr d\theta \\
=& \frac{t}{\pi L^2 H b^2}\boldsymbol{b}\otimes\Big[\int_R^{R+\Delta R} r\ dr\Big]\Big[\Big(\int_{\theta=0}^{\theta=2\pi} -sin\theta\Big)\boldsymbol{e}_x + \Big(\int_{\theta=0}^{\theta=2\pi} cos\theta\Big)\boldsymbol{e}_y\Big] \\
=& \frac{t}{\pi L^2 H b^2}\boldsymbol{b}\otimes\Big[\frac{r^2}{2}\Big]_R^{R+\Delta R}\ \Big[\{cos2\pi - cos0\}\boldsymbol{e}_x - \{sin2\pi - sin0\}\boldsymbol{e}_y\Big] \\
=& \frac{t}{\pi L^2 H b^2}\boldsymbol{b}\otimes\{\Delta R.(2R+\Delta R).\boldsymbol{0}\} = \frac{2R+\Delta R}{\pi L^2 H}\boldsymbol{b}\otimes\boldsymbol{0} = \boldsymbol{0}.
\end{aligned} \tag{4.3.9}$$

Moreover,

$$\begin{aligned}
grad\boldsymbol{V} &= \frac{\partial V_r}{\partial r}\boldsymbol{e}_r\otimes\boldsymbol{e}_r + \frac{V_r}{r}\boldsymbol{e}_\theta\otimes\boldsymbol{e}_\theta \\
\implies div\boldsymbol{V} &= grad\boldsymbol{V} : \boldsymbol{I} = \frac{\partial v(r)}{\partial r} + \frac{v(r)}{r} \\
&= \tilde{v}\delta(r-R) - \tilde{v}\ \delta(r-(R+\Delta R)) + \frac{\tilde{v}\ [H(r-R) - H(r-(R+\Delta r))]}{r}
\end{aligned}$$

Hence,

$$\begin{aligned}
\overline{div(\boldsymbol{V})} &= \frac{1}{\pi L^2}\int_{\theta=0}^{\theta=2\pi}\int_{r=0}^{r=L}\int_{z=-\frac{t}{2}}^{\frac{t}{2}} grad(\boldsymbol{V}) r dr d\theta dz \\
&= \frac{\tilde{v}t}{\pi L^2 H}\int_{\theta=0}^{\theta=2\pi}\int_{r=0}^{r=L}\Big\{\tilde{v}\ \delta(r-R) - \tilde{v}.\delta(r-(R+\Delta R)) \\
&\qquad + \frac{\tilde{v}\ [H(r-R) - H(r-(R+\Delta r))]}{r}\Big\} r dr d\theta \\
&= \frac{\tilde{v}t}{\pi L^2 H}[R-(R+\Delta R)].(2\pi) + \frac{\tilde{v}t}{\pi L^2 H}\Big\{\int_R^{R+\Delta R} dr\Big\}.(2\pi) \\
&= -\frac{\tilde{v}t}{\pi L^2 H}.\Delta R.(2\pi) + \frac{\tilde{v}t}{\pi L^2 H}.\Delta R.(2\pi) = 0
\end{aligned} \tag{4.3.10}$$

We also note that $\overline{div\boldsymbol{V}} = div\overline{\boldsymbol{V}} = div\boldsymbol{0} = 0$. We also have

$$\begin{aligned}\rho =& \boldsymbol{\alpha} : \boldsymbol{\alpha} = \frac{\boldsymbol{b}}{A} \otimes \hat{\boldsymbol{l}} : \frac{\boldsymbol{b}}{A} \otimes \hat{\boldsymbol{l}} = \frac{1}{A^2}(\boldsymbol{b} \cdot \boldsymbol{b})(\hat{\boldsymbol{l}} \cdot \hat{\boldsymbol{l}}) = \frac{b^2}{b^2.b^2}.(1) = \frac{1}{b^2} \\ \implies & grad\rho = \frac{\partial \rho}{\partial r}\boldsymbol{e}_r + \frac{1}{r}\frac{\partial \rho}{\partial \theta}\hat{\boldsymbol{e}}_\theta = 0 + 0 = 0. \end{aligned} \tag{4.3.11}$$

We have that

$$\begin{aligned} div\boldsymbol{\alpha} =& \frac{\partial \boldsymbol{\alpha}}{\partial r}\boldsymbol{e}_r + \frac{1}{r}\frac{\partial \boldsymbol{\alpha}}{\partial \theta}\boldsymbol{e}_\theta \\ =& \frac{\partial(\frac{\boldsymbol{b}}{A} \otimes \hat{\boldsymbol{l}})}{\partial r}\boldsymbol{e}_r + \frac{1}{r}\frac{\partial(\frac{\boldsymbol{b}}{A} \otimes \hat{\boldsymbol{l}})}{\partial \theta}\boldsymbol{e}_\theta \\ =& \frac{1}{b^2}\boldsymbol{b} \otimes \frac{\partial \hat{\boldsymbol{l}}}{\partial r}\boldsymbol{e}_r + \frac{1}{rb^2}\boldsymbol{b} \otimes \frac{\partial \hat{\boldsymbol{l}}}{\partial \theta}\boldsymbol{e}_\theta \end{aligned}$$

Noting that $\hat{\boldsymbol{l}} = \boldsymbol{e}_\theta$ and hence, $\frac{\partial \hat{\boldsymbol{l}}}{\partial r} = 0$ and $\frac{\partial \hat{\boldsymbol{l}}}{\partial \theta} = -\boldsymbol{e}_r$, we have

$$div\boldsymbol{\alpha} = \frac{1}{b^2}\boldsymbol{b} \otimes (0.\boldsymbol{e}_r) - \frac{1}{rb^2}(\boldsymbol{b} \otimes \boldsymbol{e}_r)\boldsymbol{e}_\theta = 0 - \frac{\boldsymbol{b}}{rb^2}\boldsymbol{e}_r \cdot \boldsymbol{e}_\theta = 0 + 0 = 0. \tag{4.3.12}$$

Also,

$$\begin{aligned} \boldsymbol{\alpha} : [\boldsymbol{\alpha}\ grad\boldsymbol{V}] &= \frac{\boldsymbol{b}}{A} \otimes \hat{\boldsymbol{l}} : [(\frac{\boldsymbol{b}}{A} \otimes \hat{\boldsymbol{l}})\ grad\boldsymbol{V}] = \frac{1}{A^2}(\boldsymbol{b} \otimes \hat{\boldsymbol{l}}) : \left[\boldsymbol{b} \otimes [grad\boldsymbol{V}]^T\ \hat{\boldsymbol{l}}\right] \\ &= \frac{1}{b^4}(\boldsymbol{b} \cdot \boldsymbol{b})\ (\hat{\boldsymbol{l}} \cdot [grad\boldsymbol{V}]^T\ \hat{\boldsymbol{l}}) \end{aligned}$$

Since $\hat{\boldsymbol{l}} = \boldsymbol{e}_\theta$,

$$\begin{aligned} \boldsymbol{\alpha} : [\boldsymbol{\alpha}\ grad\boldsymbol{V}] &= \frac{1}{b^4}(\boldsymbol{b} \cdot \boldsymbol{b})\ \left[\boldsymbol{e}_\theta \cdot \left(\frac{\partial V_r}{\partial r}\boldsymbol{e}_r \otimes \boldsymbol{e}_r + \frac{V_r}{r}\boldsymbol{e}_\theta \otimes \boldsymbol{e}_\theta\right)\ \boldsymbol{e}_\theta\right] \\ &= \frac{b^2}{b^4}\ \left[\boldsymbol{e}_\theta \cdot \frac{v(r)}{r}\boldsymbol{e}_\theta\right] = \frac{1}{b^2}\ \frac{v(r)}{r} \end{aligned}$$

Therefore,

$$\begin{aligned}\overline{\boldsymbol{\alpha} : [\boldsymbol{\alpha}\ grad\boldsymbol{V}]} &= \frac{1}{\pi L^2 H}\int_{\theta=0}^{\theta=2\pi}\int_{r=0}^{r=L}\int_{z=-\frac{t}{2}}^{\frac{t}{2}}\frac{1}{b^2}\ \frac{v}{r}rdrd\theta dz \\ &= \frac{t}{\pi L^2 H.b^2}\int_{\theta=0}^{\theta=2\pi}\int_{r=0}^{r=L}\tilde{v}\{H(r-R)-\tilde{v}H(r-(R+\Delta r))\}drd\theta \\ &= \frac{t}{\pi L^2 Hb^2}\Big\{\int_{r=R}^{r=R+\Delta R}\tilde{v}dr\Big\}2\pi = \frac{\tilde{v}t}{\pi L^2 Hb^2}.\Delta R.(2\pi) \\ &= \frac{2\tilde{v}}{L^2 H} \end{aligned} \tag{4.3.13}$$

Substituting the results from (4.3.8), (4.3.10), (4.3.11), (4.3.12) and (4.3.13) in (4.3.7), we get

$$\begin{aligned}\dot{\bar{\rho}} =& -\overline{0\cdot\boldsymbol{V}} - \frac{2}{b^2}\overline{divV} + \overline{2\boldsymbol{\alpha} : (\boldsymbol{0}\otimes\boldsymbol{V})} + \frac{2\tilde{v}}{L^2 H} = 0+0+0+\frac{2\tilde{v}}{L^2 H} \\ =& \frac{2\tilde{v}}{L^2 H}. \end{aligned} \tag{4.3.14}$$

Since $\tilde{v} > 0$ for an expanding loop, this shows that $\dot{\bar{\rho}} > 0$. This is justified because as shown before, $\bar{\rho}$ give the averaged line length and therefore it has to increase for an expanding loop.

- The evolution equation for **plastic distortion rate**, $\boldsymbol{L}^p$

  There are many quantities whose evolution are governed by the average of the fluctuation terms. For example, the evolution of $\boldsymbol{L}^p$ defined by (4.3.3) and obtained using (4.2.5) is

$$\begin{aligned}\dot{\boldsymbol{L}}^p &= \overline{\dot{\boldsymbol{\alpha}}\times\boldsymbol{V}} - \dot{\overline{\boldsymbol{\alpha}}}\times\overline{\boldsymbol{V}} - \overline{\boldsymbol{\alpha}}\times\dot{\overline{\boldsymbol{V}}} \\ &= \dot{\overline{\boldsymbol{\alpha}}}\times\overline{\boldsymbol{V}} + \overline{\boldsymbol{\alpha}}\times\dot{\overline{\boldsymbol{V}}} + \overline{\Sigma^{\dot{\boldsymbol{\alpha}}}\times\Sigma^{\boldsymbol{V}} + \Sigma^{\boldsymbol{\alpha}}\times\Sigma^{\dot{\boldsymbol{V}}}} - \dot{\overline{\boldsymbol{\alpha}}}\times\overline{\boldsymbol{V}} - \overline{\boldsymbol{\alpha}}\times\dot{\overline{\boldsymbol{V}}} \\ &= \overline{\Sigma^{-curl(\boldsymbol{\alpha}\times\boldsymbol{V})}\times\Sigma^{\boldsymbol{V}} + \Sigma^{\boldsymbol{\alpha}}\times\Sigma^{\dot{\boldsymbol{V}}}}. \end{aligned} \tag{4.3.15}$$

  This shows that the evolution of $\boldsymbol{L}^p$ is governed by the sum of the averages of the

fluctuation terms.

For the example of an expanding circular loop, using the results from (4.3.20) and (4.3.8) and the fact that $\hat{\boldsymbol{l}} = \boldsymbol{e}_\theta$,

$$\begin{aligned}
\boldsymbol{L}^p =& \overline{\boldsymbol{\alpha} \times \boldsymbol{V}} - \overline{\boldsymbol{\alpha}} \times \overline{\boldsymbol{V}} = \overline{(\frac{\boldsymbol{b}}{A} \otimes \hat{\boldsymbol{l}}) \times \boldsymbol{V}} - 0 \times 0 \\
=& \overline{\frac{v}{b^2} \boldsymbol{b} \otimes (\boldsymbol{e}_\theta \times \boldsymbol{e}_r)} = \overline{-\frac{v}{b^2} \boldsymbol{b} \otimes \boldsymbol{e}_z} \\
=& \frac{1}{\pi L^2 H} \int_{\theta=0}^{\theta=2\pi} \int_{r=0}^{r=L} \int_{z=-\frac{t}{2}}^{\frac{t}{2}} -\frac{v}{b^2} \boldsymbol{b} \otimes \boldsymbol{e}_z r dr d\theta dz \\
=& -\frac{t}{\pi L^2 H.b^2} \boldsymbol{b} \otimes \boldsymbol{e}_z \int_{\theta=0}^{\theta=2\pi} \int_{r=0}^{r=L} v r dr d\theta \\
=& -\frac{t}{\pi L^2 H.b^2} \boldsymbol{b} \otimes \boldsymbol{e}_z \int_{\theta=0}^{\theta=2\pi} \int_{r=0}^{r=L} \tilde{v}\{H(r-R) - \tilde{v}H(r-(R+\Delta r))\} r dr d\theta \\
=& -\frac{t}{\pi L^2 H.b^2} \boldsymbol{b} \otimes \boldsymbol{e}_z \Big\{ \int_{r=R}^{r=R+\Delta R} \tilde{v} r dr \Big\} 2\pi \\
=& -\frac{\tilde{v}t}{\pi L^2 H.b^2} \boldsymbol{b} \otimes \boldsymbol{e}_z \left[\frac{r^2}{2}\right]_R^{R+\Delta R} .2\pi = -\frac{2\tilde{v}t\{\Delta R.(2R+\Delta R)\}}{\pi L^2 H.b^2} \boldsymbol{b} \otimes \boldsymbol{e}_z \\
\implies |\boldsymbol{L}^p| =& -\frac{2\tilde{v}t.\Delta R.(2R+\Delta R)}{L^2 H.b^2}.b = -\frac{2\tilde{v}.(2R+\Delta R).b}{L^2 H}, \qquad (4.3.16)
\end{aligned}$$

where $\boldsymbol{e}_z = \boldsymbol{e}_r \times \boldsymbol{e}_\theta$. From (4.3.14) and (4.3.16), we observe that both $\dot{\bar{\rho}}$ and $|\boldsymbol{L}^p|$, for the case of a uniformly expanding circular loop, are proportional to $\tilde{v}$, and hence, $\dot{\bar{\rho}}$ is proportional to $|\boldsymbol{L}^p|$. This observation is in agreement with classical theory which states that $\dot{\bar{\rho}}$ (where the averaged line length $\bar{\rho}$ is a measure of the strength of the material) is proportional to $|\boldsymbol{L}^p|$. However, in classical theory, strength of a material cannot decrease whereas $\bar{\rho}$ can decrease in our case.

4.3.2 Crystal Plasticity MFDM

Conventional crystal plasticity involves resolution of the system of evolution equations into individual slip systems and superposing the effect of plastic strain on different slip systems. Motivated by the work in [AC12] to evaluate what is involved in working with the evolution

of slip-system level coarse variables (as proposed in [SHZG11, XEA15], but using ad-hoc equations of mesoscopic evolution as discussed in Section 4.1), we consider a refined description, in which we define state variables with respect to individual slip system and derive their evolution. The state variables that describe this model are:

- $\boldsymbol{\alpha}$
- $\boldsymbol{a}^l := \chi^l \boldsymbol{\alpha}$ (4.3.17a)
- $\rho^l := \chi^l \, \boldsymbol{\alpha} : \boldsymbol{\alpha}$ (4.3.17b)

Here, $\boldsymbol{\alpha}$ is the dislocation density tensor, $\chi^l(\boldsymbol{x}, t)$ is the characteristic function of dislocations of slip system l (with normal $\boldsymbol{n}^l$ and slip direction $\boldsymbol{b}^l$) at position $\boldsymbol{x}$ and $\boldsymbol{a}^l$ and ρ^l are the dislocation density tensor and total dislocation density respectively, corresponding to slip system l.

The characteristic function $\chi^l(\boldsymbol{x}, t)$ indicates whether the point $\boldsymbol{x}$ at time t is occupied by a dislocation of slip system l. We denote the exponential operator as $e(.)$. The characteristic function can be approximated as

$$\chi^l(\boldsymbol{x}, t) \approx e\left(-\left(\frac{|\boldsymbol{\alpha}\boldsymbol{n}^l|}{c_1}\right)^m\right) \; e\left(-\left(\frac{||\tilde{\boldsymbol{b}}^l.\tilde{\boldsymbol{\alpha}}\tilde{\boldsymbol{\alpha}}^T.\tilde{\boldsymbol{b}}^l|-1|}{c_2}\right)^n\right), \tag{4.3.18}$$

where

$$\begin{aligned} \tilde{\boldsymbol{b}}^l &= \frac{\boldsymbol{b}}{|\boldsymbol{b}|} \\ \tilde{\boldsymbol{\alpha}} &= \frac{\boldsymbol{\alpha}}{|\boldsymbol{\alpha}|} \end{aligned} \tag{4.3.19}$$

and c_1 and c_2 are very small positive constants and m and n are very large positive constants. For a dislocation to belong to slip system l, it must satisfy $\boldsymbol{\alpha} \cdot \boldsymbol{n}^l = 0$ (as $\boldsymbol{\alpha} \cdot \boldsymbol{n}^l = (\boldsymbol{b} \otimes \hat{\boldsymbol{l}}) \cdot \boldsymbol{n}^l = (\hat{\boldsymbol{l}} \cdot \boldsymbol{n}^l)\boldsymbol{b} = 0.\boldsymbol{b} = 0$, where $\boldsymbol{b}$ and $\hat{\boldsymbol{l}}$ are the Burgers vector and line direction of the dislocation

respectively). In that case, the first term on the rhs of (4.3.18), $e\left(-\left(\frac{|\boldsymbol{\alpha}\boldsymbol{n}^l|}{c_1}\right)^m\right)$, is 1 as $\frac{|\boldsymbol{\alpha}\boldsymbol{n}^l|}{c_1} = 0$. Otherwise (when $\boldsymbol{\alpha}\cdot\boldsymbol{n}^l \neq 0$), the first term $e\left(-\left(\frac{|\boldsymbol{\alpha}\boldsymbol{n}^l|}{c_1}\right)^m\right)$ is approximately 0, since c_1 is a small positive constant and m is a very large positive constant. Moreover, if the Burgers vector $\boldsymbol{b}$ of the dislocation coincides with $\boldsymbol{b}^l$, the term $|\tilde{\boldsymbol{b}}^l.\tilde{\boldsymbol{\alpha}}\tilde{\boldsymbol{\alpha}}^T.\tilde{\boldsymbol{b}}^l| = 1$. Hence, in that case, the second term on the rhs of (4.3.18) is 1, since $\left(\frac{||\tilde{\boldsymbol{b}}^l.\tilde{\boldsymbol{\alpha}}\tilde{\boldsymbol{\alpha}}^T.\tilde{\boldsymbol{b}}^l|-1|}{c_2}\right) = 0$. Otherwise, it is approximately 0, since c_2 is a small positive constant and n is a very large positive constant. Thus, the first term decides whether the dislocation is in the slip plane of the slip system, while the second term decides whether it has the same Burgers vector as the slip system. Only when both of these are true, we have $\chi^l = 1$. Otherwise, we have $\chi^l \approx 0$.

An implied assumption in the definition of the characteristic function and the slip system variables is that a particular spatial location is occupied at any instant by a dislocation of a single slip system, which excludes the proper accounting of junctions in the definition of the slip system variables, even though the microscopic dynamics does not involve any such exclusion.

4.3.3 The coarse variables

We are interested in understanding the plastic behavior of metals at a length scale which is much coarser than the atomic length scale and at a time scale comparable to real life load applications (which is much larger compared to the time scale of the motion of dislocations, set by the drag). Therefore, we are interested in the averaged theory of the microscopic dynamics, which involves the evolution of the coarse variables corresponding to the variables defined in (4.3.17), which are $\overline{\boldsymbol{\alpha}}$, $\overline{\boldsymbol{a}^l}$ and $\overline{\rho^l}$. In order to do so, we also need to know the evolution of the averaged characteristic function $\overline{\boldsymbol{\chi}^l}$, since χ^l appears on the rhs of their evolution equations (4.3.17). In this Section, we derive the evolution of these coarse variables. Corresponding brackets have been marked with the same color to make the equations look more readable. The primary averaged variables have been marked in blue, to show how

much of the rhs is known in terms of them. We also define the following variables to make the equations look more readable and compact:

$$P := \frac{|\boldsymbol{\alpha} \boldsymbol{n}^l|}{c_1}$$
$$Q := \frac{||\tilde{\boldsymbol{b}}^l . \tilde{\boldsymbol{\alpha}} \tilde{\boldsymbol{\alpha}}^T . \tilde{\boldsymbol{b}}^l| - 1|}{c_2}$$
$$p := |\tilde{\boldsymbol{b}}^l . \tilde{\boldsymbol{\alpha}} \tilde{\boldsymbol{\alpha}}^T . \tilde{\boldsymbol{b}}^l| - 1.$$

4.3.3.1 The evolution equation for averaged dislocation density, $\overline{\boldsymbol{\alpha}}$

The evolution of $\overline{\boldsymbol{\alpha}}$ (following [AR06]) is given by

$$\dot{\overline{\boldsymbol{\alpha}}} = -curl(\overline{\boldsymbol{\alpha}} \times \overline{\boldsymbol{V}} + \boldsymbol{L}^p). \tag{4.3.20}$$

4.3.3.2 The evolution equation for the averaged characteristic function, $\overline{\chi^l}$, for slip system l

$\overline{\chi^l}$ is obtained by applying the averaging operator (4.2.1) to (4.3.18). Its evolution equation is

$$\begin{aligned}
\dot{\overline{\chi^l}} =& \frac{m}{c_2} \overline{e(-P^m)}\ \overline{e(-Q^n)}\ \overline{P^{m-1}} \left[-\overline{\boldsymbol{\alpha}} \boldsymbol{n}^l \cdot \{curl(\overline{\boldsymbol{\alpha}} \times \overline{\boldsymbol{V}} + \boldsymbol{L}^p) \boldsymbol{n}^l\} \right] \\
& - \frac{n}{c_2} \overline{e(-P^m)}\ \overline{e(-Q^n)}\ \overline{Q^{n-1}}\ \overline{sgn(|p|-1)}\ \overline{sgn(p)} \\
& \tilde{\boldsymbol{b}}^l \cdot \Bigg\{ \Bigg(-curl(\overline{\boldsymbol{\alpha}} \times \overline{\boldsymbol{V}} + \boldsymbol{L}^p)\ \overline{\left(\frac{1}{\boldsymbol{\alpha}}\right)} - \overline{\boldsymbol{\alpha}} : curl(\overline{\boldsymbol{\alpha}} \times \overline{\boldsymbol{V}} + \boldsymbol{L}^p)\ \overline{\left(\frac{1}{|\boldsymbol{\alpha}|^3}\right)} \Bigg)\ \overline{\tilde{\boldsymbol{\alpha}}^T} \\
& \quad + \overline{\tilde{\boldsymbol{\alpha}}} \Bigg((-curl(\overline{\boldsymbol{\alpha}} \times \overline{\boldsymbol{V}} + \boldsymbol{L}^p))^T\ \overline{\left(\frac{1}{\boldsymbol{\alpha}}\right)} - \overline{\boldsymbol{\alpha}} : curl(\overline{\boldsymbol{\alpha}} \times \overline{\boldsymbol{V}} + \boldsymbol{L}^p) \overline{\left(\frac{1}{|\boldsymbol{\alpha}|^3}\right)} \Bigg) \Bigg\} \cdot \tilde{\boldsymbol{b}}^l \\
& - m \Bigg\{ \overline{e(-P^m)}\ \overline{e(-Q^n)}\ \overline{P^{m-1}} \Bigg(\overline{\Sigma^{\boldsymbol{\alpha}\boldsymbol{n}^l} \cdot \Sigma^{-curl(\boldsymbol{\alpha} \times \boldsymbol{V})\boldsymbol{n}^l}} \overline{\left(\frac{1}{|\boldsymbol{\alpha}\boldsymbol{n}^l|}\right)}
\end{aligned}$$

$$
\begin{aligned}
&\qquad\qquad + \overline{\textstyle\sum^{-(\boldsymbol{\alpha}\boldsymbol{n}^l)\cdot(curl(\boldsymbol{\alpha}\times\boldsymbol{V})\boldsymbol{n}^l)\ \sum^{\frac{1}{|\boldsymbol{\alpha}\boldsymbol{n}^l|}}}} \Big) \\
&\quad + \overline{\textstyle\sum^{e(-P^m)\ e(-Q^n)}\ \overline{P^{m-1}}} \Big(-\frac{1}{c_1}\Big(\overline{\boldsymbol{\alpha}}\boldsymbol{n}^l \cdot \{curl(\overline{\boldsymbol{\alpha}}\times\overline{\boldsymbol{V}} + \boldsymbol{L}^p)\boldsymbol{n}^l\} \\
&\quad + \overline{\textstyle\sum \boldsymbol{\alpha}\boldsymbol{n}^l \cdot \sum^{-curl(\boldsymbol{\alpha}\times\boldsymbol{V})}\boldsymbol{n}^l}\Big)\overline{\Big(\frac{1}{|\boldsymbol{\alpha}\boldsymbol{n}^l|}\Big)} + \overline{\textstyle\sum^{-(\boldsymbol{\alpha}\boldsymbol{n}^l)\cdot(curl(\boldsymbol{\alpha}\times\boldsymbol{V})\boldsymbol{n}^l)\ \sum^{\frac{1}{|\boldsymbol{\alpha}\boldsymbol{n}^l|}}}} \Big) \\
&\quad + \overline{\textstyle\sum^{e(-P^m)\ e(-Q^n)}\ \sum P^{m-1}} \Big(-\frac{1}{c_1}\Big(\overline{\boldsymbol{\alpha}}\boldsymbol{n}^l \cdot \{curl(\overline{\boldsymbol{\alpha}}\times\overline{\boldsymbol{V}} + \boldsymbol{L}^p)\boldsymbol{n}^l\} \\
&\quad + \overline{\textstyle\sum \boldsymbol{\alpha}\boldsymbol{n}^l \cdot \sum^{-curl(\boldsymbol{\alpha}\times\boldsymbol{V})}\boldsymbol{n}^l}\Big)\overline{\Big(\frac{1}{|\boldsymbol{\alpha}\boldsymbol{n}^l|}\Big)} + \overline{\textstyle\sum^{-(\boldsymbol{\alpha}\boldsymbol{n}^l)\cdot(curl(\boldsymbol{\alpha}\times\boldsymbol{V})\boldsymbol{n}^l)\ \sum^{\frac{1}{|\boldsymbol{\alpha}\boldsymbol{n}^l|}}}} \Big) \Big\} \\
&- \frac{n}{c_2}\Big[\overline{e(-P^m)}\ \overline{e(-Q^n)}\ \overline{Q^{n-1}} \\
&\quad \overline{sgn(|p|-1)}\ \overline{sgn(p)}\ \tilde{\boldsymbol{b}}^l \cdot \Big\{ \Big(\overline{\textstyle\sum^{-curl(\boldsymbol{\alpha}\times\boldsymbol{V})}\sum^{\frac{1}{|\boldsymbol{\alpha}|}}} \\
&\quad + \Big[\Big\{ \Big(\overline{\textstyle\sum^{\boldsymbol{\alpha}} : \sum^{-curl(\boldsymbol{\alpha}\times\boldsymbol{V})}} \Big) \overline{\Big(\frac{1}{|\boldsymbol{\alpha}|^3}\Big)} \\
&\quad + \overline{\textstyle\sum^{-\boldsymbol{\alpha}:curl(\boldsymbol{\alpha}\times\boldsymbol{V})}\sum^{\frac{1}{|\boldsymbol{\alpha}|^3}}} \Big\}\overline{\boldsymbol{\alpha}} + \overline{\textstyle\sum^{\frac{-\boldsymbol{\alpha}:curl(\boldsymbol{\alpha}\times\boldsymbol{V})}{|\boldsymbol{\alpha}|^3}}\sum\boldsymbol{\alpha}} \Big] \Big)\ \overline{\tilde{\boldsymbol{\alpha}}^T} \\
&\quad + \overline{\tilde{\boldsymbol{\alpha}}} \Big(\overline{\textstyle\sum^{-(curl(\boldsymbol{\alpha}\times\boldsymbol{V}))^T}\sum^{\frac{1}{|\boldsymbol{\alpha}|}}} \\
&\qquad + \Big[\Big\{ \Big(\overline{\textstyle\sum^{\boldsymbol{\alpha}} : \sum^{-(curl(\boldsymbol{\alpha}\times\boldsymbol{V}))^T}} \Big) \overline{\Big(\frac{1}{|\boldsymbol{\alpha}|^3}\Big)} \\
&\qquad + \overline{\textstyle\sum^{-\boldsymbol{\alpha}:(curl(\boldsymbol{\alpha}\times\boldsymbol{V}))}\sum^{\frac{1}{|\boldsymbol{\alpha}|^3}}} \Big\}\overline{\boldsymbol{\alpha}^T} + \overline{\textstyle\sum^{\frac{-\boldsymbol{\alpha}:(curl(\boldsymbol{\alpha}\times\boldsymbol{V}))}{|\boldsymbol{\alpha}|^3}}\sum\boldsymbol{\alpha}^T} \Big] \Big) \Big\}\tilde{\boldsymbol{b}}^l \\
&\quad + \overline{sgn(|p|-1)}\ \Big(\overline{\textstyle\sum^{sgn(p)}\sum^{\tilde{\boldsymbol{b}}^l\cdot\Big[\Big(-\frac{curl(\boldsymbol{\alpha}\times\boldsymbol{V})}{|\boldsymbol{\alpha}|}-\Big(\frac{\boldsymbol{\alpha}:curl(\boldsymbol{\alpha}\times\boldsymbol{V})}{|\boldsymbol{\alpha}|^3}\Big)\ \boldsymbol{\alpha}\Big)\tilde{\boldsymbol{\alpha}}^T}} \\
&\qquad\qquad \overline{+\tilde{\boldsymbol{\alpha}}\Big(-\frac{\{curl(\boldsymbol{\alpha}\times\boldsymbol{V})\}^T}{|\boldsymbol{\alpha}|}-\Big(\frac{\boldsymbol{\alpha}:\{curl(\boldsymbol{\alpha}\times\boldsymbol{V})\}}{|\boldsymbol{\alpha}|^3}\Big)\ \boldsymbol{\alpha}^T\Big)\Big]\tilde{\boldsymbol{b}}^l} \Big) \\
&\quad + \overline{\textstyle\sum^{sgn(|p|-1)}} \Big(\overline{\textstyle\sum^{sgn(p)\ \tilde{\boldsymbol{b}}^l\cdot\Big[\Big(-\frac{curl(\boldsymbol{\alpha}\times\boldsymbol{V})}{|\boldsymbol{\alpha}|}-\Big(\frac{\boldsymbol{\alpha}:curl(\boldsymbol{\alpha}\times\boldsymbol{V})}{|\boldsymbol{\alpha}|^3}\Big)\ \boldsymbol{\alpha}\Big)\tilde{\boldsymbol{\alpha}}^T}} \\
&\qquad\qquad \overline{+\tilde{\boldsymbol{\alpha}}\Big(-\frac{\{curl(\boldsymbol{\alpha}\times\boldsymbol{V})\}^T}{|\boldsymbol{\alpha}|}-\Big(\frac{\boldsymbol{\alpha}:\{curl(\boldsymbol{\alpha}\times\boldsymbol{V})\}}{|\boldsymbol{\alpha}|^3}\Big)\ \boldsymbol{\alpha}^T\Big)\Big]\tilde{\boldsymbol{b}}^l} \Big)
\end{aligned}
$$

$$
\begin{aligned}
&+\overline{\textstyle\sum^{e(-P^m)\ e(-Q^n)}}\ \overline{Q^{n-1}}\\
&\overline{sgn(|p|-1)}\ \overline{sgn(p)}\ \tilde{\boldsymbol{b}}^l\cdot\Bigg\{\Bigg(\Big\{-curl(\overline{\boldsymbol{\alpha}}\times\overline{\boldsymbol{V}}+\boldsymbol{L}^p)\ \overline{\Big(\frac{1}{\boldsymbol{\alpha}}\Big)}+\overline{\textstyle\sum^{-curl(\boldsymbol{\alpha}\times\boldsymbol{V})\sum\frac{1}{|\boldsymbol{\alpha}|}}}\Big\}\\
&+\Big[\Big\{\Big(-\overline{\boldsymbol{\alpha}}:curl(\overline{\boldsymbol{\alpha}}\times\overline{\boldsymbol{V}}+\boldsymbol{L}^p)+\overline{\textstyle\sum\boldsymbol{\alpha}:\sum^{-curl(\boldsymbol{\alpha}\times\boldsymbol{V})}}\Big)\overline{\Big(\frac{1}{|\boldsymbol{\alpha}|^3}\Big)}\\
&+\overline{\textstyle\sum^{-\boldsymbol{\alpha}:curl(\boldsymbol{\alpha}\times\boldsymbol{V})\sum\frac{1}{|\boldsymbol{\alpha}|^3}}}\Big\}\overline{\boldsymbol{\alpha}}+\overline{\textstyle\sum^{\frac{-\boldsymbol{\alpha}:curl(\boldsymbol{\alpha}\times\boldsymbol{V})}{|\boldsymbol{\alpha}|^3}\sum\boldsymbol{\alpha}}}\Big]\Bigg)\ \overline{\tilde{\boldsymbol{\alpha}}^T}\\
&+\overline{\tilde{\boldsymbol{\alpha}}}\Bigg(\Big\{(-curl(\overline{\boldsymbol{\alpha}}\times\overline{\boldsymbol{V}}+\boldsymbol{L}^p))^T\ \overline{\Big(\frac{1}{\boldsymbol{\alpha}}\Big)}+\overline{\textstyle\sum^{-(curl(\boldsymbol{\alpha}\times\boldsymbol{V}))^T\sum\frac{1}{|\boldsymbol{\alpha}|}}}\Big\}\\
&\quad+\Big[\Big\{\Big(-\overline{\boldsymbol{\alpha}}:(curl(\overline{\boldsymbol{\alpha}}\times\overline{\boldsymbol{V}}+\boldsymbol{L}^p))+\overline{\textstyle\sum\boldsymbol{\alpha}^T:\sum^{-(curl(\boldsymbol{\alpha}\times\boldsymbol{V})^T)}}\Big)\overline{\Big(\frac{1}{|\boldsymbol{\alpha}|^3}\Big)}\\
&\quad+\overline{\textstyle\sum^{-\boldsymbol{\alpha}:(curl(\boldsymbol{\alpha}\times\boldsymbol{V}))\sum\frac{1}{|\boldsymbol{\alpha}|^3}}}\Big\}\overline{\boldsymbol{\alpha}^T}+\overline{\textstyle\sum^{\frac{-\boldsymbol{\alpha}:(curl(\boldsymbol{\alpha}\times\boldsymbol{V}))}{|\boldsymbol{\alpha}|^3}\sum\boldsymbol{\alpha}^T}}\Big]\Bigg)\Bigg\}\tilde{\boldsymbol{b}}^l\\
&+\overline{sgn(|p|-1)}\ \overline{\Bigg(\textstyle\sum^{sgn(p)\sum^{\tilde{\boldsymbol{b}}^l\cdot\Big[\Big(-\frac{curl(\boldsymbol{\alpha}\times\boldsymbol{V})}{|\boldsymbol{\alpha}|}-\Big(\frac{\boldsymbol{\alpha}:curl(\boldsymbol{\alpha}\times\boldsymbol{V})}{|\boldsymbol{\alpha}|^3}\Big)\ \boldsymbol{\alpha}\Big)\tilde{\boldsymbol{\alpha}}^T}}\\
&\qquad\overline{+\tilde{\boldsymbol{\alpha}}\Big(-\frac{\{curl(\boldsymbol{\alpha}\times\boldsymbol{V})\}^T}{|\boldsymbol{\alpha}|}-\Big(\frac{\boldsymbol{\alpha}:\{curl(\boldsymbol{\alpha}\times\boldsymbol{V})\}}{|\boldsymbol{\alpha}|^3}\Big)\ \boldsymbol{\alpha}^T\Big)\Big]\tilde{\boldsymbol{b}}^l}\Bigg)}\\
&+\overline{\textstyle\sum^{sgn(|p|-1)}\Bigg(\sum^{sgn(p)\ \tilde{\boldsymbol{b}}^l\cdot\Big[\Big(-\frac{curl(\boldsymbol{\alpha}\times\boldsymbol{V})}{|\boldsymbol{\alpha}|}-\Big(\frac{\boldsymbol{\alpha}:curl(\boldsymbol{\alpha}\times\boldsymbol{V})}{|\boldsymbol{\alpha}|^3}\Big)\ \boldsymbol{\alpha}\Big)\tilde{\boldsymbol{\alpha}}^T}}\\
&\qquad\overline{+\tilde{\boldsymbol{\alpha}}\Big(-\frac{\{curl(\boldsymbol{\alpha}\times\boldsymbol{V})\}^T}{|\boldsymbol{\alpha}|}-\Big(\frac{\boldsymbol{\alpha}:\{curl(\boldsymbol{\alpha}\times\boldsymbol{V})\}}{|\boldsymbol{\alpha}|^3}\Big)\ \boldsymbol{\alpha}^T\Big)\Big]\tilde{\boldsymbol{b}}^l}\Bigg)}\\
&+\overline{\textstyle\sum^{e(-P^m)\ e(-Q^n)}\ \sum Q^{n-1}}\\
&\overline{sgn(|p|-1)}\ \overline{sgn(p)}\ \tilde{\boldsymbol{b}}^l\cdot\Bigg\{\Bigg(\Big\{-curl(\overline{\boldsymbol{\alpha}}\times\overline{\boldsymbol{V}}+\boldsymbol{L}^p)\ \overline{\Big(\frac{1}{\boldsymbol{\alpha}}\Big)}+\overline{\textstyle\sum^{-curl(\boldsymbol{\alpha}\times\boldsymbol{V})\sum\frac{1}{|\boldsymbol{\alpha}|}}}\Big\}\\
&+\Big[\Big\{\Big(-\overline{\boldsymbol{\alpha}}:curl(\overline{\boldsymbol{\alpha}}\times\overline{\boldsymbol{V}}+\boldsymbol{L}^p)+\overline{\textstyle\sum\boldsymbol{\alpha}:\sum^{-curl(\boldsymbol{\alpha}\times\boldsymbol{V})}}\Big)\overline{\Big(\frac{1}{|\boldsymbol{\alpha}|^3}\Big)}\\
&+\overline{\textstyle\sum^{-\boldsymbol{\alpha}:curl(\boldsymbol{\alpha}\times\boldsymbol{V})\sum\frac{1}{|\boldsymbol{\alpha}|^3}}}\Big\}\overline{\boldsymbol{\alpha}}+\overline{\textstyle\sum^{\frac{-\boldsymbol{\alpha}:curl(\boldsymbol{\alpha}\times\boldsymbol{V})}{|\boldsymbol{\alpha}|^3}\sum\boldsymbol{\alpha}}}\Big]\Bigg)\ \overline{\tilde{\boldsymbol{\alpha}}^T}\\
&+\overline{\tilde{\boldsymbol{\alpha}}}\Bigg(\Big\{(-curl(\overline{\boldsymbol{\alpha}}\times\overline{\boldsymbol{V}}+\boldsymbol{L}^p))^T\ \overline{\Big(\frac{1}{\boldsymbol{\alpha}}\Big)}+\overline{\textstyle\sum^{-(curl(\boldsymbol{\alpha}\times\boldsymbol{V}))^T\sum\frac{1}{|\boldsymbol{\alpha}|}}}\Big\}
\end{aligned}
$$

$$
\begin{aligned}
&+\Big[\Big\{\Big(-\overline{\boldsymbol{\alpha}}:(curl(\overline{\boldsymbol{\alpha}}\times\overline{\boldsymbol{V}}+\boldsymbol{L}^p))+\overline{\Sigma\boldsymbol{\alpha}^T:\Sigma^{-(curl(\boldsymbol{\alpha}\times\boldsymbol{V})^T)}}\Big)\overline{\Big(\frac{1}{|\boldsymbol{\alpha}|^3}\Big)}\\
&+\overline{\Sigma^{-\boldsymbol{\alpha}:(curl(\boldsymbol{\alpha}\times\boldsymbol{V}))}\Sigma\frac{1}{|\boldsymbol{\alpha}|^3}}\Big\}\overline{\boldsymbol{\alpha}^T}+\overline{\Sigma^{\frac{-\boldsymbol{\alpha}:(curl(\boldsymbol{\alpha}\times\boldsymbol{V}))}{|\boldsymbol{\alpha}|^3}}\Sigma\boldsymbol{\alpha}^T}\Big]\Big)\Big\}\tilde{\boldsymbol{b}}^l\\
&+\overline{sgn(|p|-1)}\Bigg(\overline{\Sigma^{sgn(p)}\Sigma^{\tilde{\boldsymbol{b}}^l\cdot\Big[\Big(-\frac{curl(\boldsymbol{\alpha}\times\boldsymbol{V})}{|\boldsymbol{\alpha}|}-\Big(\frac{\boldsymbol{\alpha}:curl(\boldsymbol{\alpha}\times\boldsymbol{V})}{|\boldsymbol{\alpha}|^3}\Big)\ \boldsymbol{\alpha}\Big)\tilde{\boldsymbol{\alpha}}^T}}\\
&\qquad\overline{+\tilde{\boldsymbol{\alpha}}\Big(-\frac{\{curl(\boldsymbol{\alpha}\times\boldsymbol{V})\}^T}{|\boldsymbol{\alpha}|}-\Big(\frac{\boldsymbol{\alpha}:\{curl(\boldsymbol{\alpha}\times\boldsymbol{V})\}}{|\boldsymbol{\alpha}|^3}\Big)\ \boldsymbol{\alpha}^T\Big)\Big]\tilde{\boldsymbol{b}}^l}\Bigg)\\
&+\overline{\Sigma sgn(|p|-1)}\Bigg(\overline{\Sigma^{sgn(p)\ \tilde{\boldsymbol{b}}^l\cdot\Big[\Big(-\frac{curl(\boldsymbol{\alpha}\times\boldsymbol{V})}{|\boldsymbol{\alpha}|}-\Big(\frac{\boldsymbol{\alpha}:curl(\boldsymbol{\alpha}\times\boldsymbol{V})}{|\boldsymbol{\alpha}|^3}\Big)\ \boldsymbol{\alpha}\Big)\tilde{\boldsymbol{\alpha}}^T}}\\
&\qquad\overline{+\tilde{\boldsymbol{\alpha}}\Big(-\frac{\{curl(\boldsymbol{\alpha}\times\boldsymbol{V})\}^T}{|\boldsymbol{\alpha}|}-\Big(\frac{\boldsymbol{\alpha}:\{curl(\boldsymbol{\alpha}\times\boldsymbol{V})\}}{|\boldsymbol{\alpha}|^3}\Big)\ \boldsymbol{\alpha}^T\Big)\Big]\tilde{\boldsymbol{b}}^l}\Bigg)\Bigg]\\
&-m\ \overline{\Sigma e(-P^m)\ e(-Q^n)\ P^{m-1}\ \Sigma\Big(\frac{(\boldsymbol{\alpha}\boldsymbol{n}^l)\cdot(-curl(\boldsymbol{\alpha}\times\boldsymbol{V})^T)\boldsymbol{n}^l}{c_1|\boldsymbol{\alpha}\boldsymbol{n}^l|}\Big)}\\
&-n\ \Bigg(\overline{\Sigma e(-P^m)\ e(-Q^n)\ Q^{n-1}}\\
&\qquad\overline{\Sigma^{\frac{1}{c_2}sgn(p)\ \tilde{\boldsymbol{b}}^l\cdot\Big[\Big\{-\frac{curl(\boldsymbol{\alpha}\times\boldsymbol{V})}{|\boldsymbol{\alpha}|}+\Big(\frac{\boldsymbol{\alpha}:curl(\boldsymbol{\alpha}\times\boldsymbol{V})}{|\boldsymbol{\alpha}|^3}\Big)\ \boldsymbol{\alpha}\Big\}\tilde{\boldsymbol{\alpha}}^T+\tilde{\boldsymbol{\alpha}}\Big\{-\frac{\{curl(\boldsymbol{\alpha}\times\boldsymbol{V})\}^T}{|\boldsymbol{\alpha}|}+\Big(\frac{\boldsymbol{\alpha}:\{curl(\boldsymbol{\alpha}\times\boldsymbol{V})\}}{|\boldsymbol{\alpha}|^3}\Big)\ \boldsymbol{\alpha}^T\Big\}\Big]\tilde{\boldsymbol{b}}^l}\Bigg).
\end{aligned}
\tag{4.3.21}
$$

The derivation of (4.3.21) is given in Appendix C.2.

4.3.3.3 The evolution equation for the averaged dislocation density tensor, $\overline{\boldsymbol{a}^l}$, for slip system l

$\overline{\boldsymbol{a}^l}$ is obtained by applying the averaging operator (4.2.1) to (4.3.17a). Its evolution equation is

$$
\begin{aligned}
\dot{\overline{\boldsymbol{a}^l}}=&\frac{m}{c_2}\ \overline{\boldsymbol{\alpha}}\ \overline{e(-P^m)}\ \overline{e(-Q^n)}\ \overline{P^{m-1}}\ \Big[-\overline{\boldsymbol{\alpha}}\boldsymbol{n}^l\cdot\{curl(\overline{\boldsymbol{\alpha}}\times\overline{\boldsymbol{V}}+\boldsymbol{L}^p)\boldsymbol{n}^l\}\Big]\\
&-\frac{n}{c_2}\ \overline{\boldsymbol{\alpha}}\ \overline{e(-P^m)}\ \overline{e(-Q^n)}\ \overline{Q^{n-1}}\ \overline{sgn(|p|-1)}\ \overline{sgn(p)}
\end{aligned}
$$

$$\tilde{\boldsymbol{b}}^l \cdot \Bigg\{ \Bigg(-curl(\overline{\boldsymbol{\alpha}} \times \overline{\boldsymbol{V}} + \boldsymbol{L}^p) \, \overline{\left(\frac{1}{\boldsymbol{\alpha}}\right)} - \overline{\boldsymbol{\alpha}} : curl(\overline{\boldsymbol{\alpha}} \times \overline{\boldsymbol{V}} + \boldsymbol{L}^p) \, \overline{\left(\frac{1}{|\boldsymbol{\alpha}|^3}\right)} \Bigg) \, \overline{\tilde{\boldsymbol{\alpha}}^T}$$

$$+ \overline{\tilde{\boldsymbol{\alpha}}} \Bigg((-curl(\overline{\boldsymbol{\alpha}} \times \overline{\boldsymbol{V}} + \boldsymbol{L}^p))^T \, \overline{\left(\frac{1}{\boldsymbol{\alpha}}\right)} - \overline{\boldsymbol{\alpha}} : curl(\overline{\boldsymbol{\alpha}} \times \overline{\boldsymbol{V}} + \boldsymbol{L}^p) \overline{\left(\frac{1}{|\boldsymbol{\alpha}|^3}\right)} \Bigg) \Bigg\} \cdot \tilde{\boldsymbol{b}}^l$$

$$- curl\{\overline{\boldsymbol{a}^l} \times (\overline{\chi^l} \, \overline{\boldsymbol{V}})\} + 2 \, \overline{\chi^l} \, (\overline{\boldsymbol{\alpha}} \times \overline{\boldsymbol{V}})[\boldsymbol{X}(grad \overline{\chi^l})]$$

$$- m\overline{\boldsymbol{\alpha}} \Bigg\{ \overline{e(-P^m)} \, \overline{e(-Q^n)} \, \overline{P^{m-1}} \Bigg(\overline{\Sigma^{\boldsymbol{\alpha}\boldsymbol{n}^l \, \cdot \, \Sigma^{-curl(\boldsymbol{\alpha}\times\boldsymbol{V})\boldsymbol{n}^l}}} \overline{\left(\frac{1}{|\boldsymbol{\alpha}\boldsymbol{n}^l|}\right)}$$

$$+ \overline{\Sigma^{-(\boldsymbol{\alpha}\boldsymbol{n}^l)\cdot(curl(\boldsymbol{\alpha}\times\boldsymbol{V})\boldsymbol{n}^l) \; \Sigma^{\frac{1}{|\boldsymbol{\alpha}\boldsymbol{n}^l|}}}} \Bigg)$$

$$+ \overline{\Sigma^{e(-P^m) \; e(-Q^n)} \; \overline{P^{m-1}}} \Bigg(-\frac{1}{c_1} \Big(\overline{\boldsymbol{\alpha}}\boldsymbol{n}^l \cdot \{curl(\overline{\boldsymbol{\alpha}} \times \overline{\boldsymbol{V}} + \boldsymbol{L}^p)\boldsymbol{n}^l\}$$

$$+ \overline{\Sigma^{\boldsymbol{\alpha}\boldsymbol{n}^l \, \cdot \, \Sigma^{-curl(\boldsymbol{\alpha}\times\boldsymbol{V})\boldsymbol{n}^l}}} \Big) \overline{\left(\frac{1}{|\boldsymbol{\alpha}\boldsymbol{n}^l|}\right)} + \overline{\Sigma^{-(\boldsymbol{\alpha}\boldsymbol{n}^l)\cdot(curl(\boldsymbol{\alpha}\times\boldsymbol{V})\boldsymbol{n}^l) \; \Sigma^{\frac{1}{|\boldsymbol{\alpha}\boldsymbol{n}^l|}}}} \Bigg)$$

$$+ \overline{\Sigma^{e(-P^m) \; e(-Q^n)} \; \Sigma^{P^{m-1}}} \Bigg(-\frac{1}{c_1} \Big(\overline{\boldsymbol{\alpha}}\boldsymbol{n}^l \cdot \{curl(\overline{\boldsymbol{\alpha}} \times \overline{\boldsymbol{V}} + \boldsymbol{L}^p)\boldsymbol{n}^l\}$$

$$+ \overline{\Sigma^{\boldsymbol{\alpha}\boldsymbol{n}^l \, \cdot \, \Sigma^{-curl(\boldsymbol{\alpha}\times\boldsymbol{V})\boldsymbol{n}^l}}} \Big) \overline{\left(\frac{1}{|\boldsymbol{\alpha}\boldsymbol{n}^l|}\right)} + \overline{\Sigma^{-(\boldsymbol{\alpha}\boldsymbol{n}^l)\cdot(curl(\boldsymbol{\alpha}\times\boldsymbol{V})\boldsymbol{n}^l) \; \Sigma^{\frac{1}{|\boldsymbol{\alpha}\boldsymbol{n}^l|}}}} \Bigg) \Bigg\}$$

$$- \frac{n}{c_2} \overline{\boldsymbol{\alpha}} \Bigg[\overline{e(-P^m)} \, \overline{e(-Q^n)} \, \overline{Q^{n-1}}$$

$$\overline{sgn(|p|-1)} \, \overline{sgn(p)} \, \tilde{\boldsymbol{b}}^l \cdot \Bigg\{ \Bigg(\overline{\Sigma^{-curl(\boldsymbol{\alpha}\times\boldsymbol{V})\Sigma^{\frac{1}{|\boldsymbol{\alpha}|}}}}$$

$$+ \Bigg[\Bigg\{ \Big(\overline{\Sigma^{\boldsymbol{\alpha}} : \Sigma^{-curl(\boldsymbol{\alpha}\times\boldsymbol{V})}} \Big) \overline{\left(\frac{1}{|\boldsymbol{\alpha}|^3}\right)}$$

$$+ \overline{\Sigma^{-\boldsymbol{\alpha}:curl(\boldsymbol{\alpha}\times\boldsymbol{V})\Sigma^{\frac{1}{|\boldsymbol{\alpha}|^3}}}} \Bigg\} \overline{\boldsymbol{\alpha}} + \overline{\Sigma^{\frac{-\boldsymbol{\alpha}:curl(\boldsymbol{\alpha}\times\boldsymbol{V})}{|\boldsymbol{\alpha}|^3}\Sigma\boldsymbol{\alpha}}} \Bigg] \Bigg) \, \overline{\tilde{\boldsymbol{\alpha}}^T}$$

$$+ \overline{\tilde{\boldsymbol{\alpha}}} \Bigg(\overline{\Sigma^{-(curl(\boldsymbol{\alpha}\times\boldsymbol{V}))^T\Sigma^{\frac{1}{|\boldsymbol{\alpha}|}}}}$$

$$+ \Bigg[\Bigg\{ \Big(\overline{\Sigma^{\boldsymbol{\alpha}} : \Sigma^{-(curl(\boldsymbol{\alpha}\times\boldsymbol{V}))^T}} \Big) \overline{\left(\frac{1}{|\boldsymbol{\alpha}|^3}\right)}$$

$$+ \overline{\Sigma^{-\boldsymbol{\alpha}:(curl(\boldsymbol{\alpha}\times\boldsymbol{V}))\Sigma^{\frac{1}{|\boldsymbol{\alpha}|^3}}}} \Bigg\} \overline{\boldsymbol{\alpha}^T} + \overline{\Sigma^{\frac{-\boldsymbol{\alpha}:(curl(\boldsymbol{\alpha}\times\boldsymbol{V}))}{|\boldsymbol{\alpha}|^3}\Sigma\boldsymbol{\alpha}^T}} \Bigg] \Bigg) \Bigg\} \tilde{\boldsymbol{b}}^l$$

$$
\begin{aligned}
&+\overline{sgn(|p|-1)}\ \overline{\left(\sum^{sgn(p)}\sum^{\tilde{\boldsymbol{b}}^l\cdot\left[\left(-\frac{curl(\boldsymbol{\alpha}\times\boldsymbol{V})}{|\boldsymbol{\alpha}|}-\left(\frac{\boldsymbol{\alpha}:curl(\boldsymbol{\alpha}\times\boldsymbol{V})}{|\boldsymbol{\alpha}|^3}\right)\ \boldsymbol{\alpha}\right)\tilde{\boldsymbol{\alpha}}^T\right.}\right.}\\
&\qquad\overline{\left.\left.+\tilde{\boldsymbol{\alpha}}\left(-\frac{\{curl(\boldsymbol{\alpha}\times\boldsymbol{V})\}^T}{|\boldsymbol{\alpha}|}-\left(\frac{\boldsymbol{\alpha}:\{curl(\boldsymbol{\alpha}\times\boldsymbol{V})\}}{|\boldsymbol{\alpha}|^3}\right)\ \boldsymbol{\alpha}^T\right)\right]\tilde{\boldsymbol{b}}^l\right)}\\
&+\overline{\sum^{sgn(|p|-1)}\left(\sum^{sgn(p)\ \tilde{\boldsymbol{b}}^l\cdot\left[\left(-\frac{curl(\boldsymbol{\alpha}\times\boldsymbol{V})}{|\boldsymbol{\alpha}|}-\left(\frac{\boldsymbol{\alpha}:curl(\boldsymbol{\alpha}\times\boldsymbol{V})}{|\boldsymbol{\alpha}|^3}\right)\ \boldsymbol{\alpha}\right)\tilde{\boldsymbol{\alpha}}^T\right.}\right.}\\
&\qquad\overline{\left.\left.+\tilde{\boldsymbol{\alpha}}\left(-\frac{\{curl(\boldsymbol{\alpha}\times\boldsymbol{V})\}^T}{|\boldsymbol{\alpha}|}-\left(\frac{\boldsymbol{\alpha}:\{curl(\boldsymbol{\alpha}\times\boldsymbol{V})\}}{|\boldsymbol{\alpha}|^3}\right)\ \boldsymbol{\alpha}^T\right)\right]\tilde{\boldsymbol{b}}^l\right)}\\
&+\overline{\sum e(-P^m)\ e(-Q^n)}\ \overline{Q^{n-1}}\\
&\quad\overline{sgn(|p|-1)}\ \overline{sgn(p)}\ \tilde{\boldsymbol{b}}^l\cdot\left\{\left(\left\{-curl(\overline{\boldsymbol{\alpha}}\times\overline{\boldsymbol{V}}+\boldsymbol{L}^p)\ \overline{\left(\frac{1}{\boldsymbol{\alpha}}\right)}+\overline{\sum^{-curl(\boldsymbol{\alpha}\times\boldsymbol{V})}\sum^{\frac{1}{|\boldsymbol{\alpha}|}}}\right\}\right.\right.\\
&\quad+\left[\left\{\left(-\overline{\boldsymbol{\alpha}}:curl(\overline{\boldsymbol{\alpha}}\times\overline{\boldsymbol{V}}+\boldsymbol{L}^p)+\overline{\Sigma^{\boldsymbol{\alpha}}:\Sigma^{-curl(\boldsymbol{\alpha}\times\boldsymbol{V})}}\right)\overline{\left(\frac{1}{|\boldsymbol{\alpha}|^3}\right)}\right.\right.\\
&\quad\left.\left.+\overline{\sum^{-\boldsymbol{\alpha}:curl(\boldsymbol{\alpha}\times\boldsymbol{V})}\sum^{\frac{1}{|\boldsymbol{\alpha}|^3}}}\right\}\overline{\boldsymbol{\alpha}}+\overline{\sum^{\frac{-\boldsymbol{\alpha}:curl(\boldsymbol{\alpha}\times\boldsymbol{V})}{|\boldsymbol{\alpha}|^3}}\Sigma^{\boldsymbol{\alpha}}}\right]\Bigg)\ \overline{\tilde{\boldsymbol{\alpha}}^T}\\
&\quad+\overline{\tilde{\boldsymbol{\alpha}}}\left(\left\{(-curl(\overline{\boldsymbol{\alpha}}\times\overline{\boldsymbol{V}}+\boldsymbol{L}^p))^T\ \overline{\left(\frac{1}{\boldsymbol{\alpha}}\right)}+\overline{\Sigma^{-(curl(\boldsymbol{\alpha}\times\boldsymbol{V}))^T}\sum^{\frac{1}{|\boldsymbol{\alpha}|}}}\right\}\right.\\
&\qquad+\left[\left\{\left(-\overline{\boldsymbol{\alpha}}:(curl(\overline{\boldsymbol{\alpha}}\times\overline{\boldsymbol{V}}+\boldsymbol{L}^p))+\overline{\Sigma^{\boldsymbol{\alpha}^T}:\Sigma^{-(curl(\boldsymbol{\alpha}\times\boldsymbol{V})^T)}}\right)\overline{\left(\frac{1}{|\boldsymbol{\alpha}|^3}\right)}\right.\right.\\
&\qquad\left.\left.\left.+\ \overline{\Sigma^{-\boldsymbol{\alpha}:(curl(\boldsymbol{\alpha}\times\boldsymbol{V}))}\sum^{\frac{1}{|\boldsymbol{\alpha}|^3}}}\right\}\overline{\boldsymbol{\alpha}^T}+\overline{\Sigma^{\frac{-\boldsymbol{\alpha}:(curl(\boldsymbol{\alpha}\times\boldsymbol{V}))}{|\boldsymbol{\alpha}|^3}}\Sigma^{\boldsymbol{\alpha}^T}}\right]\right)\Bigg\}\tilde{\boldsymbol{b}}^l\\
&+\overline{sgn(|p|-1)}\ \overline{\left(\sum^{sgn(p)}\sum^{\tilde{\boldsymbol{b}}^l\cdot\left[\left(-\frac{curl(\boldsymbol{\alpha}\times\boldsymbol{V})}{|\boldsymbol{\alpha}|}-\left(\frac{\boldsymbol{\alpha}:curl(\boldsymbol{\alpha}\times\boldsymbol{V})}{|\boldsymbol{\alpha}|^3}\right)\ \boldsymbol{\alpha}\right)\tilde{\boldsymbol{\alpha}}^T\right.}\right.}\\
&\qquad\overline{\left.\left.+\tilde{\boldsymbol{\alpha}}\left(-\frac{\{curl(\boldsymbol{\alpha}\times\boldsymbol{V})\}^T}{|\boldsymbol{\alpha}|}-\left(\frac{\boldsymbol{\alpha}:\{curl(\boldsymbol{\alpha}\times\boldsymbol{V})\}}{|\boldsymbol{\alpha}|^3}\right)\ \boldsymbol{\alpha}^T\right)\right]\tilde{\boldsymbol{b}}^l\right)}\\
&+\overline{\sum^{sgn(|p|-1)}\left(\sum^{sgn(p)\ \tilde{\boldsymbol{b}}^l\cdot\left[\left(-\frac{curl(\boldsymbol{\alpha}\times\boldsymbol{V})}{|\boldsymbol{\alpha}|}-\left(\frac{\boldsymbol{\alpha}:curl(\boldsymbol{\alpha}\times\boldsymbol{V})}{|\boldsymbol{\alpha}|^3}\right)\ \boldsymbol{\alpha}\right)\tilde{\boldsymbol{\alpha}}^T\right.}\right.}\\
&\qquad\overline{\left.\left.+\tilde{\boldsymbol{\alpha}}\left(-\frac{\{curl(\boldsymbol{\alpha}\times\boldsymbol{V})\}^T}{|\boldsymbol{\alpha}|}-\left(\frac{\boldsymbol{\alpha}:\{curl(\boldsymbol{\alpha}\times\boldsymbol{V})\}}{|\boldsymbol{\alpha}|^3}\right)\ \boldsymbol{\alpha}^T\right)\right]\tilde{\boldsymbol{b}}^l\right)}\\
&+\overline{\sum e(-P^m)\ e(-Q^n)\ \sum Q^{n-1}}
\end{aligned}
$$

$$
\begin{aligned}
&\overline{sgn(|p|-1)}\ \overline{sgn(p)}\ \tilde{\boldsymbol{b}}^l \cdot \Bigg\{ \Bigg(\Big\{ -curl(\overline{\boldsymbol{\alpha}} \times \overline{\boldsymbol{V}} + \boldsymbol{L}^p)\ \overline{\left(\frac{1}{\boldsymbol{\alpha}}\right)} + \overline{\Sigma^{-curl(\boldsymbol{\alpha}\times\boldsymbol{V})} \Sigma^{\frac{1}{|\boldsymbol{\alpha}|}}} \Big\} \\
&+ \Big[\Big\{ \Big(-\overline{\boldsymbol{\alpha}} : curl(\overline{\boldsymbol{\alpha}} \times \overline{\boldsymbol{V}} + \boldsymbol{L}^p) + \overline{\Sigma \boldsymbol{\alpha} : \Sigma^{-curl(\boldsymbol{\alpha}\times\boldsymbol{V})}} \Big) \overline{\left(\frac{1}{|\boldsymbol{\alpha}|^3}\right)} \\
&+ \overline{\Sigma^{-\boldsymbol{\alpha}:curl(\boldsymbol{\alpha}\times\boldsymbol{V})} \Sigma^{\frac{1}{|\boldsymbol{\alpha}|^3}}} \Big\} \overline{\boldsymbol{\alpha}} + \overline{\Sigma^{\frac{-\boldsymbol{\alpha}:curl(\boldsymbol{\alpha}\times\boldsymbol{V})}{|\boldsymbol{\alpha}|^3}} \Sigma \boldsymbol{\alpha}} \Big] \Bigg)\ \overline{\tilde{\boldsymbol{\alpha}}^T} \\
&+ \overline{\tilde{\boldsymbol{\alpha}}} \Bigg(\Big\{ (-curl(\overline{\boldsymbol{\alpha}} \times \overline{\boldsymbol{V}} + \boldsymbol{L}^p))^T\ \overline{\left(\frac{1}{\boldsymbol{\alpha}}\right)} + \overline{\Sigma^{-(curl(\boldsymbol{\alpha}\times\boldsymbol{V}))^T \Sigma^{\frac{1}{|\boldsymbol{\alpha}|}}}} \Big\} \\
&\quad + \Big[\Big\{ \Big(-\overline{\boldsymbol{\alpha}} : (curl(\overline{\boldsymbol{\alpha}} \times \overline{\boldsymbol{V}} + \boldsymbol{L}^p)) + \overline{\Sigma \boldsymbol{\alpha}^T : \Sigma^{-(curl(\boldsymbol{\alpha}\times\boldsymbol{V})^T)}} \Big) \overline{\left(\frac{1}{|\boldsymbol{\alpha}|^3}\right)} \\
&\quad + \overline{\Sigma^{-\boldsymbol{\alpha}:(curl(\boldsymbol{\alpha}\times\boldsymbol{V}))\Sigma^{\frac{1}{|\boldsymbol{\alpha}|^3}}}} \Big\} \overline{\boldsymbol{\alpha}^T} + \overline{\Sigma^{\frac{-\boldsymbol{\alpha}:(curl(\boldsymbol{\alpha}\times\boldsymbol{V}))}{|\boldsymbol{\alpha}|^3}} \Sigma \boldsymbol{\alpha}^T} \Big] \Bigg) \Bigg\} \tilde{\boldsymbol{b}}^l \\
&+ \overline{sgn(|p|-1)}\ \overline{\Bigg(\Sigma^{sgn(p)} \Sigma^{\tilde{\boldsymbol{b}}^l \cdot \Big[\left(-\frac{curl(\boldsymbol{\alpha}\times\boldsymbol{V})}{|\boldsymbol{\alpha}|} - \left(\frac{\boldsymbol{\alpha}:curl(\boldsymbol{\alpha}\times\boldsymbol{V})}{|\boldsymbol{\alpha}|^3} \right) \boldsymbol{\alpha} \right) \tilde{\boldsymbol{\alpha}}^T} \\
&\qquad \overline{+ \tilde{\boldsymbol{\alpha}} \left(-\frac{\{curl(\boldsymbol{\alpha}\times\boldsymbol{V})\}^T}{|\boldsymbol{\alpha}|} - \left(\frac{\boldsymbol{\alpha}:\{curl(\boldsymbol{\alpha}\times\boldsymbol{V})\}}{|\boldsymbol{\alpha}|^3} \right) \boldsymbol{\alpha}^T \right) \Big] \tilde{\boldsymbol{b}}^l} \Bigg)} \\
&+ \overline{\Sigma^{sgn(|p|-1)} \Bigg(\Sigma^{sgn(p)\ \tilde{\boldsymbol{b}}^l \cdot \Big[\left(-\frac{curl(\boldsymbol{\alpha}\times\boldsymbol{V})}{|\boldsymbol{\alpha}|} - \left(\frac{\boldsymbol{\alpha}:curl(\boldsymbol{\alpha}\times\boldsymbol{V})}{|\boldsymbol{\alpha}|^3} \right) \boldsymbol{\alpha} \right) \tilde{\boldsymbol{\alpha}}^T} \\
&\qquad \overline{+ \tilde{\boldsymbol{\alpha}} \left(-\frac{\{curl(\boldsymbol{\alpha}\times\boldsymbol{V})\}^T}{|\boldsymbol{\alpha}|} - \left(\frac{\boldsymbol{\alpha}:\{curl(\boldsymbol{\alpha}\times\boldsymbol{V})\}}{|\boldsymbol{\alpha}|^3} \right) \boldsymbol{\alpha}^T \right) \Big] \tilde{\boldsymbol{b}}^l} \Bigg) \Bigg] \\
&- m\overline{\boldsymbol{\alpha}}\ \overline{\Sigma e(-P^m)\ e(-Q^n)\ P^{m-1}\ \Sigma^{\left(\frac{(\boldsymbol{\alpha}\boldsymbol{n}^l)\cdot(-curl(\boldsymbol{\alpha}\times\boldsymbol{V})^T)\boldsymbol{n}^l}{c_1|\boldsymbol{\alpha}\boldsymbol{n}^l|} \right)}} \\
&- n\overline{\boldsymbol{\alpha}}\ \overline{\Bigg(\Sigma e(-P^m)\ e(-Q^n)\ Q^{n-1} \\
&\qquad \overline{\Sigma^{\frac{1}{c_2} sgn(p)\ \tilde{\boldsymbol{b}}^l \cdot \Big[\Big\{ -\frac{curl(\boldsymbol{\alpha}\times\boldsymbol{V})}{|\boldsymbol{\alpha}|} + \left(\frac{\boldsymbol{\alpha}:curl(\boldsymbol{\alpha}\times\boldsymbol{V})}{|\boldsymbol{\alpha}|^3} \right) \boldsymbol{\alpha} \Big\} \tilde{\boldsymbol{\alpha}}^T + \tilde{\boldsymbol{\alpha}} \Big\{ -\frac{\{curl(\boldsymbol{\alpha}\times\boldsymbol{V})\}^T}{|\boldsymbol{\alpha}|} + \left(\frac{\boldsymbol{\alpha}:\{curl(\boldsymbol{\alpha}\times\boldsymbol{V})\}}{|\boldsymbol{\alpha}|^3} \right) \boldsymbol{\alpha}^T \Big\} \Big] \tilde{\boldsymbol{b}}^l}} \Bigg) \Bigg] \\
&- m\ \overline{\Sigma e(-P^m)\ e(-Q^n)\ P^{m-1}\ \Sigma^{\left(\frac{(\boldsymbol{\alpha}\boldsymbol{n}^l)\cdot(-curl(\boldsymbol{\alpha}\times\boldsymbol{V})^T)\boldsymbol{n}^l}{c_1|\boldsymbol{\alpha}\boldsymbol{n}^l|} \right)}} \\
&- n\ \overline{\Bigg(\Sigma e(-P^m)\ e(-Q^n)\ Q^{n-1}}
\end{aligned}
$$

$$\overline{\sum^{\frac{1}{c_2}sgn(p)\ \tilde{\boldsymbol{b}}^l\cdot\left[\left\{-\frac{curl(\boldsymbol{\alpha}\times\boldsymbol{V})}{|\boldsymbol{\alpha}|}+\left(\frac{\boldsymbol{\alpha}:curl(\boldsymbol{\alpha}\times\boldsymbol{V})}{|\boldsymbol{\alpha}|^3}\right)\ \boldsymbol{\alpha}\right\}\tilde{\boldsymbol{\alpha}}^T+\tilde{\boldsymbol{\alpha}}\left\{-\frac{\{curl(\boldsymbol{\alpha}\times\boldsymbol{V})\}^T}{|\boldsymbol{\alpha}|}+\left(\frac{\boldsymbol{\alpha}:\{curl(\boldsymbol{\alpha}\times\boldsymbol{V})\}}{|\boldsymbol{\alpha}|^3}\right)\ \boldsymbol{\alpha}^T\right\}\right]\tilde{\boldsymbol{b}}^l}\Bigg)$$

$$+\sum\Bigg[-m\ e(-P^m)e(-Q^n)P^{m-1}\left(\frac{(\boldsymbol{\alpha}\boldsymbol{n}^l)\cdot(-curl(\boldsymbol{\alpha}\times\boldsymbol{V})^T)\boldsymbol{n}^l}{c_1|\boldsymbol{\alpha}\boldsymbol{n}^l|}\right)-\frac{n}{c_2}\ e(-P^m)e(-Q^n)Q^{n-1}\cdot$$

$$\overline{\left(sgn(p)\ \tilde{\boldsymbol{b}}^l\cdot\left[\left\{-\frac{curl(\boldsymbol{\alpha}\times\boldsymbol{V})}{|\boldsymbol{\alpha}|}+\left(\frac{\boldsymbol{\alpha}:curl(\boldsymbol{\alpha}\times\boldsymbol{V})}{|\boldsymbol{\alpha}|^3}\right)\ \boldsymbol{\alpha}\right\}\tilde{\boldsymbol{\alpha}}^T+\tilde{\boldsymbol{\alpha}}\left\{-\frac{\{curl(\boldsymbol{\alpha}\times\boldsymbol{V})\}^T}{|\boldsymbol{\alpha}|}+\left(\frac{\boldsymbol{\alpha}:\{curl(\boldsymbol{\alpha}\times\boldsymbol{V})\}}{|\boldsymbol{\alpha}|^3}\right)\ \boldsymbol{\alpha}^T\right\}\right]\tilde{\boldsymbol{b}}^l\right)}\Bigg]_{\sum\boldsymbol{\alpha}}$$

$$-curl\left(\overline{\Sigma\boldsymbol{a}^l\times\Sigma(\chi^l\boldsymbol{V})}\right)+2\ \overline{\chi^l}\ \overline{\Sigma\boldsymbol{\alpha}\times\Sigma\boldsymbol{V}}[\boldsymbol{X}(grad\overline{\chi^l})]+2\ \overline{\Sigma\chi^l\ \Sigma\boldsymbol{\alpha}\times\boldsymbol{V}}[\boldsymbol{X}(grad\overline{\chi^l})]$$

$$+2\ \overline{\Sigma\chi^{l(\boldsymbol{\alpha}\times\boldsymbol{V})}\ \Sigma^{\boldsymbol{X}(grad_{x'}\chi^l)}}-curl(\overline{\boldsymbol{a}^l}\times\overline{\Sigma\chi^l\,\Sigma\boldsymbol{V}}),\qquad(4.3.22)$$

where P,Q and p are defined in Section 4.3.3. The derivation of (4.3.22) is given in Appendix C.3. The merit of (4.3.22) is that it shows what the exact evolution equation of $\overline{\boldsymbol{a}^l}$ should be (cf. [XEA15]). It is cumbersome, to say the least and, moreover, contains fluctuation terms whose evolution are given by other pde, resulting in an 'unsolvable' infinite hierarchy.

4.3.3.4 The evolution equation for the averaged total dislocation density, $\overline{\rho^l}$, for slip system l

$\overline{\rho^l}$ is obtained by applying the averaging operator (4.2.1) to (4.3.17b). Its evolution is given by

$$\dot{\overline{\rho^l}}=2\ \frac{m}{c_2}\overline{\rho}\ \overline{e(-P^m)}\ \overline{e(-Q^n)}\ \overline{P^{m-1}}\ \Big[-\overline{\boldsymbol{\alpha}}\boldsymbol{n}^l\cdot\{curl(\overline{\boldsymbol{\alpha}}\times\overline{\boldsymbol{V}}+\boldsymbol{L}^p)\boldsymbol{n}^l\}\Big]$$

$$-2\frac{n}{c_2}\ \overline{\rho}\ \overline{e(-P^m)}\ \overline{e(-Q^n)}\ \overline{Q^{n-1}}\ \overline{sgn(|p|-1)}\ \overline{sgn(p)}$$

$$\tilde{\boldsymbol{b}}^l\cdot\Bigg\{\Bigg(-curl(\overline{\boldsymbol{\alpha}}\times\overline{\boldsymbol{V}}+\boldsymbol{L}^p)\ \overline{\left(\frac{1}{\boldsymbol{\alpha}}\right)}-\overline{\boldsymbol{\alpha}}:curl(\overline{\boldsymbol{\alpha}}\times\overline{\boldsymbol{V}}+\boldsymbol{L}^p)\ \overline{\left(\frac{1}{|\boldsymbol{\alpha}|^3}\right)}\Bigg)\ \overline{\tilde{\boldsymbol{\alpha}}^T}$$

$$+\overline{\tilde{\boldsymbol{\alpha}}}\Bigg((-curl(\overline{\boldsymbol{\alpha}}\times\overline{\boldsymbol{V}}+\boldsymbol{L}^p))^T\ \overline{\left(\frac{1}{\boldsymbol{\alpha}}\right)}-\overline{\boldsymbol{\alpha}}:curl(\overline{\boldsymbol{\alpha}}\times\overline{\boldsymbol{V}}+\boldsymbol{L}^p)\overline{\left(\frac{1}{|\boldsymbol{\alpha}|^3}\right)}\Bigg)\Bigg\}\cdot\tilde{\boldsymbol{b}}^l$$

$$+\overline{\chi^l}\Big[-grad\ \overline{\rho}\cdot\overline{\boldsymbol{V}}-2\ \overline{\rho}\ div\overline{\boldsymbol{V}}+2\ \overline{\boldsymbol{\alpha}}:(div\overline{\boldsymbol{\alpha}}\otimes\overline{\boldsymbol{V}})+2\ \overline{\boldsymbol{\alpha}}:\{\overline{\boldsymbol{\alpha}}\ grad\overline{\boldsymbol{V}}\}\Big]$$

$$
\begin{aligned}
&-2m\overline{\rho}\Big\{\ \overline{e(-P^m)}\ \overline{e(-Q^n)}\ \overline{P^{m-1}}\ \Big(\overline{\Sigma^{\boldsymbol{\alpha}\boldsymbol{n}^l}\cdot\Sigma^{-curl(\boldsymbol{\alpha}\times\boldsymbol{V})\boldsymbol{n}^l}}\,\overline{\Big(\frac{1}{|\boldsymbol{\alpha}\boldsymbol{n}^l|}\Big)}\\
&\qquad\qquad+\overline{\Sigma^{-(\boldsymbol{\alpha}\boldsymbol{n}^l)\cdot(curl(\boldsymbol{\alpha}\times\boldsymbol{V})\boldsymbol{n}^l)}\ \Sigma^{\frac{1}{|\boldsymbol{\alpha}\boldsymbol{n}^l|}}}\Big)\\
&\quad+\overline{\Sigma^{e(-P^m)}\ e(-Q^n)}\ \overline{P^{m-1}}\ \Big(-\frac{1}{c_1}\Big(\overline{\boldsymbol{\alpha}}\boldsymbol{n}^l\cdot\{curl(\overline{\boldsymbol{\alpha}}\times\overline{\boldsymbol{V}}+\boldsymbol{L}^p)\boldsymbol{n}^l\}\\
&\quad+\overline{\Sigma\boldsymbol{\alpha}\boldsymbol{n}^l\cdot\Sigma^{-curl(\boldsymbol{\alpha}\times\boldsymbol{V})\boldsymbol{n}^l}}\Big)\overline{\Big(\frac{1}{|\boldsymbol{\alpha}\boldsymbol{n}^l|}\Big)}+\overline{\Sigma^{-(\boldsymbol{\alpha}\boldsymbol{n}^l)\cdot(curl(\boldsymbol{\alpha}\times\boldsymbol{V})\boldsymbol{n}^l)}\ \Sigma^{\frac{1}{|\boldsymbol{\alpha}\boldsymbol{n}^l|}}}\Big)\\
&\quad+\overline{\Sigma^{e(-P^m)}\ e(-Q^n)}\ \overline{\Sigma^{P^{m-1}}}\ \Big(-\frac{1}{c_1}\Big(\overline{\boldsymbol{\alpha}}\boldsymbol{n}^l\cdot\{curl(\overline{\boldsymbol{\alpha}}\times\overline{\boldsymbol{V}}+\boldsymbol{L}^p)\boldsymbol{n}^l\}\\
&\quad+\overline{\Sigma\boldsymbol{\alpha}\boldsymbol{n}^l\cdot\Sigma^{-curl(\boldsymbol{\alpha}\times\boldsymbol{V})\boldsymbol{n}^l}}\Big)\overline{\Big(\frac{1}{|\boldsymbol{\alpha}\boldsymbol{n}^l|}\Big)}+\overline{\Sigma^{-(\boldsymbol{\alpha}\boldsymbol{n}^l)\cdot(curl(\boldsymbol{\alpha}\times\boldsymbol{V})\boldsymbol{n}^l)}\ \Sigma^{\frac{1}{|\boldsymbol{\alpha}\boldsymbol{n}^l|}}}\Big)\Big\}\\
&-2\frac{n}{c_2}\overline{\rho}\Big[\overline{e(-P^m)}\ \overline{e(-Q^n)}\ \overline{Q^{n-1}}\\
&\quad\overline{sgn(|p|-1)}\ \overline{sgn(p)}\ \tilde{\boldsymbol{b}}^l\cdot\Big\{\Big(\overline{\Sigma^{-curl(\boldsymbol{\alpha}\times\boldsymbol{V})}\Sigma^{\frac{1}{|\boldsymbol{\alpha}|}}}\\
&\quad+\Big[\Big\{\Big(\overline{\Sigma^{\boldsymbol{\alpha}}:\Sigma^{-curl(\boldsymbol{\alpha}\times\boldsymbol{V})}}\Big)\overline{\Big(\frac{1}{|\boldsymbol{\alpha}|^3}\Big)}\\
&\quad+\overline{\Sigma^{-\boldsymbol{\alpha}:curl(\boldsymbol{\alpha}\times\boldsymbol{V})}\Sigma^{\frac{1}{|\boldsymbol{\alpha}|^3}}}\Big\}\overline{\boldsymbol{\alpha}}+\overline{\Sigma^{\frac{-\boldsymbol{\alpha}:curl(\boldsymbol{\alpha}\times\boldsymbol{V})}{|\boldsymbol{\alpha}|^3}}\Sigma^{\boldsymbol{\alpha}}}\Big]\Big)\ \overline{\tilde{\boldsymbol{\alpha}}^T}\\
&\quad+\overline{\tilde{\boldsymbol{\alpha}}}\ \Big(\overline{\Sigma^{-(curl(\boldsymbol{\alpha}\times\boldsymbol{V}))^T\Sigma^{\frac{1}{|\boldsymbol{\alpha}|}}}}\\
&\qquad+\Big[\Big\{\Big(\overline{\Sigma^{\boldsymbol{\alpha}}:\Sigma^{-(curl(\boldsymbol{\alpha}\times\boldsymbol{V}))^T}}\Big)\overline{\Big(\frac{1}{|\boldsymbol{\alpha}|^3}\Big)}\\
&\qquad+\overline{\Sigma^{-\boldsymbol{\alpha}:(curl(\boldsymbol{\alpha}\times\boldsymbol{V}))\Sigma^{\frac{1}{|\boldsymbol{\alpha}|^3}}}}\Big\}\overline{\boldsymbol{\alpha}^T}+\overline{\Sigma^{\frac{-\boldsymbol{\alpha}:(curl(\boldsymbol{\alpha}\times\boldsymbol{V}))}{|\boldsymbol{\alpha}|^3}\Sigma\boldsymbol{\alpha}^T}}\Big]\Big)\Big\}\tilde{\boldsymbol{b}}^l\\
&\quad+\overline{\overline{sgn(|p|-1)}\ \Big(\Sigma^{sgn(p)}\Sigma^{\tilde{\boldsymbol{b}}^l\cdot\Big[\Big(-\frac{curl(\boldsymbol{\alpha}\times\boldsymbol{V})}{|\boldsymbol{\alpha}|}-\Big(\frac{\boldsymbol{\alpha}:curl(\boldsymbol{\alpha}\times\boldsymbol{V})}{|\boldsymbol{\alpha}|^3}\Big)\ \boldsymbol{\alpha}\Big)\tilde{\boldsymbol{\alpha}}^T}}\\
&\qquad\qquad\overline{+\tilde{\boldsymbol{\alpha}}\Big(-\frac{\{curl(\boldsymbol{\alpha}\times\boldsymbol{V})\}^T}{|\boldsymbol{\alpha}|}-\Big(\frac{\boldsymbol{\alpha}:\{curl(\boldsymbol{\alpha}\times\boldsymbol{V})\}}{|\boldsymbol{\alpha}|^3}\Big)\ \boldsymbol{\alpha}^T\Big)\Big]\tilde{\boldsymbol{b}}^l}\Big)}\\
&\quad+\overline{\Sigma^{sgn(|p|-1)}\Big(\Sigma^{sgn(p)\ \tilde{\boldsymbol{b}}^l\cdot\Big[\Big(-\frac{curl(\boldsymbol{\alpha}\times\boldsymbol{V})}{|\boldsymbol{\alpha}|}-\Big(\frac{\boldsymbol{\alpha}:curl(\boldsymbol{\alpha}\times\boldsymbol{V})}{|\boldsymbol{\alpha}|^3}\Big)\ \boldsymbol{\alpha}\Big)\tilde{\boldsymbol{\alpha}}^T}}
\end{aligned}
$$

$$
\overline{+\tilde{\boldsymbol{\alpha}}\left(-\frac{\{curl(\boldsymbol{\alpha}\times\boldsymbol{V})\}^T}{|\boldsymbol{\alpha}|}-\left(\frac{\boldsymbol{\alpha}:\{curl(\boldsymbol{\alpha}\times\boldsymbol{V})\}}{|\boldsymbol{\alpha}|^3}\right)\ \boldsymbol{\alpha}^T\right)\Big]\tilde{\boldsymbol{b}}^l}\Bigg)
$$

$$
+\ \overline{\Sigma^{e(-P^m)}\ e(-Q^n)}\ \overline{Q^{n-1}}
$$

$$
\overline{sgn(|p|-1)}\ \overline{sgn(p)}\ \tilde{\boldsymbol{b}}^l\cdot\Bigg\{\Bigg(\Big\{-curl(\overline{\boldsymbol{\alpha}}\times\overline{\boldsymbol{V}}+\boldsymbol{L}^p)\ \overline{\left(\frac{1}{\boldsymbol{\alpha}}\right)}+\overline{\Sigma^{-curl(\boldsymbol{\alpha}\times\boldsymbol{V})}\Sigma^{\frac{1}{|\boldsymbol{\alpha}|}}}\Big\}
$$

$$
+\Big[\Big\{\Big(-\overline{\boldsymbol{\alpha}}:curl(\overline{\boldsymbol{\alpha}}\times\overline{\boldsymbol{V}}+\boldsymbol{L}^p)+\overline{\Sigma^{\boldsymbol{\alpha}}:\Sigma^{-curl(\boldsymbol{\alpha}\times\boldsymbol{V})}}\Big)\overline{\left(\frac{1}{|\boldsymbol{\alpha}|^3}\right)}
$$

$$
+\overline{\Sigma^{-\boldsymbol{\alpha}:curl(\boldsymbol{\alpha}\times\boldsymbol{V})}\Sigma^{\frac{1}{|\boldsymbol{\alpha}|^3}}}\Big\}\overline{\boldsymbol{\alpha}}+\overline{\Sigma^{\frac{-\boldsymbol{\alpha}:curl(\boldsymbol{\alpha}\times\boldsymbol{V})}{|\boldsymbol{\alpha}|^3}}\Sigma^{\boldsymbol{\alpha}}}\Big]\Bigg)\ \overline{\tilde{\boldsymbol{\alpha}}^T}
$$

$$
+\overline{\tilde{\boldsymbol{\alpha}}}\Bigg(\Big\{(-curl(\overline{\boldsymbol{\alpha}}\times\overline{\boldsymbol{V}}+\boldsymbol{L}^p))^T\ \overline{\left(\frac{1}{\boldsymbol{\alpha}}\right)}+\overline{\Sigma^{-(curl(\boldsymbol{\alpha}\times\boldsymbol{V}))^T}\Sigma^{\frac{1}{|\boldsymbol{\alpha}|}}}\Big\}
$$

$$
+\Big[\Big\{\Big(-\overline{\boldsymbol{\alpha}}:(curl(\overline{\boldsymbol{\alpha}}\times\overline{\boldsymbol{V}}+\boldsymbol{L}^p))+\overline{\Sigma^{\boldsymbol{\alpha}^T}:\Sigma^{-(curl(\boldsymbol{\alpha}\times\boldsymbol{V})^T)}}\Big)\overline{\left(\frac{1}{|\boldsymbol{\alpha}|^3}\right)}
$$

$$
+\ \overline{\Sigma^{-\boldsymbol{\alpha}:(curl(\boldsymbol{\alpha}\times\boldsymbol{V}))}\Sigma^{\frac{1}{|\boldsymbol{\alpha}|^3}}}\Big\}\overline{\boldsymbol{\alpha}^T}+\overline{\Sigma^{\frac{-\boldsymbol{\alpha}:(curl(\boldsymbol{\alpha}\times\boldsymbol{V}))}{|\boldsymbol{\alpha}|^3}}\Sigma^{\boldsymbol{\alpha}^T}}\Big]\Bigg)\Bigg\}\tilde{\boldsymbol{b}}^l
$$

$$
+\overline{sgn(|p|-1)}\ \Bigg(\overline{\Sigma^{sgn(p)}\Sigma^{\tilde{\boldsymbol{b}}^l\cdot\left[\left(-\frac{curl(\boldsymbol{\alpha}\times\boldsymbol{V})}{|\boldsymbol{\alpha}|}-\left(\frac{\boldsymbol{\alpha}:curl(\boldsymbol{\alpha}\times\boldsymbol{V})}{|\boldsymbol{\alpha}|^3}\right)\ \boldsymbol{\alpha}\right)\tilde{\boldsymbol{\alpha}}^T\right.}}
$$

$$
\left.\overline{+\tilde{\boldsymbol{\alpha}}\left(-\frac{\{curl(\boldsymbol{\alpha}\times\boldsymbol{V})\}^T}{|\boldsymbol{\alpha}|}-\left(\frac{\boldsymbol{\alpha}:\{curl(\boldsymbol{\alpha}\times\boldsymbol{V})\}}{|\boldsymbol{\alpha}|^3}\right)\ \boldsymbol{\alpha}^T\right)\Big]\tilde{\boldsymbol{b}}^l}\Bigg)
$$

$$
+\overline{\Sigma^{sgn(|p|-1)}\Bigg(\Sigma^{sgn(p)\ \tilde{\boldsymbol{b}}^l\cdot\left[\left(-\frac{curl(\boldsymbol{\alpha}\times\boldsymbol{V})}{|\boldsymbol{\alpha}|}-\left(\frac{\boldsymbol{\alpha}:curl(\boldsymbol{\alpha}\times\boldsymbol{V})}{|\boldsymbol{\alpha}|^3}\right)\ \boldsymbol{\alpha}\right)\tilde{\boldsymbol{\alpha}}^T\right.}}
$$

$$
\left.\overline{+\tilde{\boldsymbol{\alpha}}\left(-\frac{\{curl(\boldsymbol{\alpha}\times\boldsymbol{V})\}^T}{|\boldsymbol{\alpha}|}-\left(\frac{\boldsymbol{\alpha}:\{curl(\boldsymbol{\alpha}\times\boldsymbol{V})\}}{|\boldsymbol{\alpha}|^3}\right)\ \boldsymbol{\alpha}^T\right)\Big]\tilde{\boldsymbol{b}}^l}\Bigg)
$$

$$
+\ \overline{\Sigma^{e(-P^m)}\ e(-Q^n)}\ \overline{\Sigma^{Q^{n-1}}}
$$

$$
\overline{sgn(|p|-1)}\ \overline{sgn(p)}\ \tilde{\boldsymbol{b}}^l\cdot\Bigg\{\Bigg(\Big\{-curl(\overline{\boldsymbol{\alpha}}\times\overline{\boldsymbol{V}}+\boldsymbol{L}^p)\ \overline{\left(\frac{1}{\boldsymbol{\alpha}}\right)}+\overline{\Sigma^{-curl(\boldsymbol{\alpha}\times\boldsymbol{V})}\Sigma^{\frac{1}{|\boldsymbol{\alpha}|}}}\Big\}
$$

$$
+\Big[\Big\{\Big(-\overline{\boldsymbol{\alpha}}:curl(\overline{\boldsymbol{\alpha}}\times\overline{\boldsymbol{V}}+\boldsymbol{L}^p)+\overline{\Sigma^{\boldsymbol{\alpha}}:\Sigma^{-curl(\boldsymbol{\alpha}\times\boldsymbol{V})}}\Big)\overline{\left(\frac{1}{|\boldsymbol{\alpha}|^3}\right)}
$$

$$
+\overline{\Sigma^{-\boldsymbol{\alpha}:curl(\boldsymbol{\alpha}\times\boldsymbol{V})}\Sigma^{\frac{1}{|\boldsymbol{\alpha}|^3}}}\Big\}\overline{\boldsymbol{\alpha}}+\overline{\Sigma^{\frac{-\boldsymbol{\alpha}:curl(\boldsymbol{\alpha}\times\boldsymbol{V})}{|\boldsymbol{\alpha}|^3}}\Sigma^{\boldsymbol{\alpha}}}\Big]\Bigg)\ \overline{\tilde{\boldsymbol{\alpha}}^T}
$$

$$
\begin{aligned}
&+\overline{\tilde{\boldsymbol{\alpha}}}\Bigg(\Big\{(-curl(\overline{\boldsymbol{\alpha}}\times\overline{\boldsymbol{V}}+\boldsymbol{L}^p))^T\ \overline{\left(\frac{1}{\boldsymbol{\alpha}}\right)}+\overline{\Sigma^{-(curl(\boldsymbol{\alpha}\times\boldsymbol{V}))^T\Sigma\frac{1}{|\boldsymbol{\alpha}|}}}\Big\}\\
&\quad+\Bigg[\Big\{\Big(-\overline{\boldsymbol{\alpha}}:(curl(\overline{\boldsymbol{\alpha}}\times\overline{\boldsymbol{V}}+\boldsymbol{L}^p))+\overline{\Sigma\boldsymbol{\alpha}^T:\Sigma^{-(curl(\boldsymbol{\alpha}\times\boldsymbol{V})^T)}}\Big)\overline{\left(\frac{1}{|\boldsymbol{\alpha}|^3}\right)}\\
&\quad+\overline{\Sigma^{-\boldsymbol{\alpha}:(curl(\boldsymbol{\alpha}\times\boldsymbol{V}))\Sigma\frac{1}{|\boldsymbol{\alpha}|^3}}}\Big\}\overline{\boldsymbol{\alpha}^T}+\overline{\Sigma^{\frac{-\boldsymbol{\alpha}:(curl(\boldsymbol{\alpha}\times\boldsymbol{V}))}{|\boldsymbol{\alpha}|^3}\Sigma\boldsymbol{\alpha}^T}}\Bigg]\Bigg)\Bigg\}\tilde{\boldsymbol{b}}^l\\
&+\overline{sgn(|p|-1)}\ \overline{\Bigg(\Sigma^{sgn(p)}\Sigma^{\tilde{\boldsymbol{b}}^l\cdot\Big[\Big(-\frac{curl(\boldsymbol{\alpha}\times\boldsymbol{V})}{|\boldsymbol{\alpha}|}-\Big(\frac{\boldsymbol{\alpha}:curl(\boldsymbol{\alpha}\times\boldsymbol{V})}{|\boldsymbol{\alpha}|^3}\Big)\ \boldsymbol{\alpha}\Big)\tilde{\boldsymbol{\alpha}}^T}\\
&\qquad\overline{+\tilde{\boldsymbol{\alpha}}\Big(-\frac{\{curl(\boldsymbol{\alpha}\times\boldsymbol{V})\}^T}{|\boldsymbol{\alpha}|}-\Big(\frac{\boldsymbol{\alpha}:\{curl(\boldsymbol{\alpha}\times\boldsymbol{V})\}}{|\boldsymbol{\alpha}|^3}\Big)\ \boldsymbol{\alpha}^T\Big)\Big]\tilde{\boldsymbol{b}}^l}\Bigg)}\\
&+\overline{\Sigma^{sgn(|p|-1)}\Bigg(\Sigma^{sgn(p)\ \tilde{\boldsymbol{b}}^l\cdot\Big[\Big(-\frac{curl(\boldsymbol{\alpha}\times\boldsymbol{V})}{|\boldsymbol{\alpha}|}-\Big(\frac{\boldsymbol{\alpha}:curl(\boldsymbol{\alpha}\times\boldsymbol{V})}{|\boldsymbol{\alpha}|^3}\Big)\ \boldsymbol{\alpha}\Big)\tilde{\boldsymbol{\alpha}}^T}\\
&\qquad\overline{+\tilde{\boldsymbol{\alpha}}\Big(-\frac{\{curl(\boldsymbol{\alpha}\times\boldsymbol{V})\}^T}{|\boldsymbol{\alpha}|}-\Big(\frac{\boldsymbol{\alpha}:\{curl(\boldsymbol{\alpha}\times\boldsymbol{V})\}}{|\boldsymbol{\alpha}|^3}\Big)\ \boldsymbol{\alpha}^T\Big)\Big]\tilde{\boldsymbol{b}}^l}\Bigg)\Bigg]}\\
&-2m\overline{\rho}\ \overline{\Sigma^{e(-P^m)}\ e(-Q^n)\ P^{m-1}\ \Sigma^{\left(\frac{(\boldsymbol{\alpha}\boldsymbol{n}^l)\cdot(-curl(\boldsymbol{\alpha}\times\boldsymbol{V})^T)\boldsymbol{n}^l}{c_1|\boldsymbol{\alpha}\boldsymbol{n}^l|}\right)}}\\
&-2n\overline{\rho}\ \overline{\Bigg(\Sigma^{e(-P^m)}\ e(-Q^n)\ Q^{n-1}}\\
&\qquad\overline{\Sigma^{\frac{1}{c_2}sgn(p)\ \tilde{\boldsymbol{b}}^l\cdot\Big[\Big\{-\frac{curl(\boldsymbol{\alpha}\times\boldsymbol{V})}{|\boldsymbol{\alpha}|}+\Big(\frac{\boldsymbol{\alpha}:curl(\boldsymbol{\alpha}\times\boldsymbol{V})}{|\boldsymbol{\alpha}|^3}\Big)\ \boldsymbol{\alpha}\Big\}\tilde{\boldsymbol{\alpha}}^T+\tilde{\boldsymbol{\alpha}}\Big\{-\frac{\{curl(\boldsymbol{\alpha}\times\boldsymbol{V})\}^T}{|\boldsymbol{\alpha}|}+\Big(\frac{\boldsymbol{\alpha}:\{curl(\boldsymbol{\alpha}\times\boldsymbol{V})\}}{|\boldsymbol{\alpha}|^3}\Big)\ \boldsymbol{\alpha}^T\Big\}\Big]\tilde{\boldsymbol{b}}^l}\Bigg)}\\
&-m\ \overline{\Sigma^{e(-P^m)}\ e(-Q^n)\ P^{m-1}\ \Sigma^{\left(\frac{(\boldsymbol{\alpha}\boldsymbol{n}^l)\cdot(-curl(\boldsymbol{\alpha}\times\boldsymbol{V})^T)\boldsymbol{n}^l}{c_1|\boldsymbol{\alpha}\boldsymbol{n}^l|}\right)}}\\
&-n\ \overline{\Bigg(\Sigma^{e(-P^m)}\ e(-Q^n)\ Q^{n-1}}\\
&\qquad\overline{\Sigma^{\frac{1}{c_2}sgn(p)\ \tilde{\boldsymbol{b}}^l\cdot\Big[\Big\{-\frac{curl(\boldsymbol{\alpha}\times\boldsymbol{V})}{|\boldsymbol{\alpha}|}+\Big(\frac{\boldsymbol{\alpha}:curl(\boldsymbol{\alpha}\times\boldsymbol{V})}{|\boldsymbol{\alpha}|^3}\Big)\ \boldsymbol{\alpha}\Big\}\tilde{\boldsymbol{\alpha}}^T+\tilde{\boldsymbol{\alpha}}\Big\{-\frac{\{curl(\boldsymbol{\alpha}\times\boldsymbol{V})\}^T}{|\boldsymbol{\alpha}|}+\Big(\frac{\boldsymbol{\alpha}:\{curl(\boldsymbol{\alpha}\times\boldsymbol{V})\}}{|\boldsymbol{\alpha}|^3}\Big)\ \boldsymbol{\alpha}^T\Big\}\Big]\tilde{\boldsymbol{b}}^l}\Bigg)}\\
&+2\ \overline{\Sigma\Bigg[-m\ e(-P^m)e(-Q^n)P^{m-1}\Big(\frac{(\boldsymbol{\alpha}\boldsymbol{n}^l)\cdot(-curl(\boldsymbol{\alpha}\times\boldsymbol{V})^T)\boldsymbol{n}^l}{c_1|\boldsymbol{\alpha}\boldsymbol{n}^l|}\Big)-\frac{n}{c_2}\ e(-P^m)e(-Q^n)Q^{n-1}\cdot}\\
&\qquad\overline{\Big(sgn(p)\ \tilde{\boldsymbol{b}}^l\cdot\Big[\Big\{-\frac{curl(\boldsymbol{\alpha}\times\boldsymbol{V})}{|\boldsymbol{\alpha}|}+\Big(\frac{\boldsymbol{\alpha}:curl(\boldsymbol{\alpha}\times\boldsymbol{V})}{|\boldsymbol{\alpha}|^3}\Big)\ \boldsymbol{\alpha}\Big\}\tilde{\boldsymbol{\alpha}}^T+\tilde{\boldsymbol{\alpha}}\Big\{-\frac{\{curl(\boldsymbol{\alpha}\times\boldsymbol{V})\}^T}{|\boldsymbol{\alpha}|}+\Big(\frac{\boldsymbol{\alpha}:\{curl(\boldsymbol{\alpha}\times\boldsymbol{V})\}}{|\boldsymbol{\alpha}|^3}\Big)\ \boldsymbol{\alpha}^T\Big\}\Big]\tilde{\boldsymbol{b}}^l\Big)\Bigg]_{\Sigma^\rho}}
\end{aligned}
$$

$$
\begin{aligned}
&- \overline{\chi^l}\Big[\overline{\Sigma^{grad\rho}\cdot\Sigma^{\boldsymbol{V}}} - 2\overline{\Sigma^{\rho}\Sigma^{divV}} + 2\,\overline{\boldsymbol{\alpha}} : (\overline{\Sigma^{div\boldsymbol{\alpha}}\otimes\Sigma^{\boldsymbol{V}}}) \\
&\qquad + 2\overline{\Sigma^{\boldsymbol{\alpha}} : \Sigma^{div\boldsymbol{\alpha}\otimes\boldsymbol{V}}} + 2\,\overline{\boldsymbol{\alpha}} : \overline{\Sigma^{\boldsymbol{\alpha}}\ \Sigma^{grad\boldsymbol{V}}} + 2\,\overline{\Sigma^{\boldsymbol{\alpha}} : \Sigma^{\boldsymbol{\alpha}}\ grad\boldsymbol{V}}\Big] \\
&+ \overline{\Sigma\chi^l\Sigma\Big[-grad\rho\cdot\boldsymbol{V} - 2\rho(divV) + 2\boldsymbol{\alpha}:(div\boldsymbol{\alpha}\otimes\boldsymbol{V}) + 2\boldsymbol{\alpha}:\{\boldsymbol{\alpha}\,gradV\}\Big]},
\end{aligned}
\tag{4.3.23}
$$

where P,Q and p are defined in Section 4.3.3. The derivation of (4.3.23) is given in Appendix C.4. The equation (4.3.23) is the exact evolution equation of $\overline{\rho^l}$. The same remarks as to the practicality of this exact equation as in Section 4.3.3.3 applies.

Remark In the evolution equations for $\bar{\boldsymbol{\alpha}}$ (4.3.20), $\bar{\boldsymbol{a}}^l$ (4.3.22) and $\bar{\rho}^l$ (4.3.23), the plastic distortion rate $\boldsymbol{L}^p$ appears. It is defined in (4.3.3) and is a fluctuation term ($\boldsymbol{L}^p = \overline{\Sigma^{\boldsymbol{\alpha}}\times\Sigma^{\boldsymbol{V}}}$). As shown in Section 4.2, the hierarchy can involve equations of evolution for the fluctuations. We derived the evolution equation for $\boldsymbol{L}^p$ in (4.3.15) which is as follows:

$$
\dot{\boldsymbol{L}}^p = \overline{\Sigma^{-curl(\boldsymbol{\alpha}\times\boldsymbol{V})}\times\Sigma^{\boldsymbol{V}} + \Sigma^{\boldsymbol{\alpha}}\times\Sigma^{\dot{\boldsymbol{V}}}}.
$$

The $\boldsymbol{L}^p$ for a uniformly expanding circular loop was obtained in Section 4.3.1 and is given by (4.3.16). However, this was possible due to the drastic assumption of uniform velocity (of same magnitude pointing radially outward) at all points of the loop. In reality, the value of the local velocity is difficult to obtain without consideration of the microscopic DD problem, as it depends on the Peach-Koehler force acting on the dislocation segments, which is a function of the internal stresses. This makes it essentially impossible to define an evolution equation for $\boldsymbol{L}^p$ in realistic situations without some sort of 'on-the-fly' coupling to local DD calculations. The coupled DD-MFDM strategy that is described and implemented in Chapter 3 defines evolution equations for $\boldsymbol{L}^p$ using appropriate time averaging of Discrete Dislocation Dynamics is a first demonstration towards achieving exactly this goal for realistic applied loading rates.

4.4 Conclusion

We stated some descriptors of the microscopic dynamics and obtained the evolution of the coarse variables generated from such descriptors. The coarse variables give an idea of the averaged behavior of the system at a much coarser length and time scale. We see that the evolution of the total dislocation density (4.3.6) contains the averages of fluctuations, and hence is exact but not closed. We considered a refined description in which we resolved the dynamics into slip systems. We see that the evolution of the dislocation density tensor (4.3.22) and the total dislocation density (4.3.23) of any particular slipsystem is extremely cumbersome, which shows the limitations of such a refined description. The evolution equations of the coarse variables involve many average terms, average of fluctuation terms and their partial derivatives, all of which have their own evolution given by other pdes. Thus, we get an infinite hierarchy of non-linear non-closed coarse evolution pdes, which cannot be solved for all practical purposes. The CDD framework [HZG07, Hoc16, SZ15] *postulates* fundamental microscopic statements and uses closure assumptions of their own to cut off the infinite hierarchy of equations. In contrast, MFDM (4.3.2), which follows by averaging the equations of FDM (4.3.1) in space and time, is based on the fundamental statement of the conservation of Burgers vector (which is a physically observed fact). While cumbersome, one could try to work with these exact equations if they were known in full detail. If this is not the case, the justifications for using such infinite hierarchies is scarce. It is much more reasonable, and important to focus on closure assumptions generated from constitutive, stress coupled interation dynamics and their averaging at a lower level, about which such 'kinematic' infinite hierarchies say nothing. In previous works [AR06], the system is closed using physics-based phenomenological modeling at the lowest level of the hierarchy as a trade-off with practicality. Currently, work is in progress [CPZ$^+$] to replace the constitutive *phenomenological* assumptions in MFDM with inputs obtained by appropriate time averaging of a fine-scale model (Discrete Dislocation Dynamics). The details of the work has

been presented in Chapter 3.

Chapter 5

Conclusion

A novel approach to meso/macroscale plasticity has been implemented using a carefully designed coupling of MFDM with space-time averaged inputs from DD simulations. It does not involve postulating constitutive assumptions beyond those embodied in DD methodology. In order to achieve this, we used a rigorous mathematic theory involving Young Measures for averaging of nonlinear ODE response and its practical implementation which we call Practical Time Averaging (PTA). The first part of the thesis demonstrates the application of PTA using three illustrative examples to probe the slow time scale behavior of rapidly evolving microscopic dynamics, including both oscillatory and exponentially decaying behavior. Our scheme is also able to cover cases where there is a discontinuity in the Young measure, thereby demonstrating its robustness.

In the second part, we used PTA to couple MFDM with DD. The coupled approach is implemented using a hybrid computational tool that utilizes both MPI and OpenMP parallelizations. We have been able to show the strong dependence of the results on: (i) the orientation of the microstructure (for the two loading cases of simple shear and uniaxial tension) (ii) the loading rate (iii) the ratio of mobile to sessile segment density. We have been able to show these effects for both load and displacement controlled simulations. The

simulations have been performed at slow, *realistic* loading rates for large sample sizes and with huge speedup in compute time (around 10^5 using a conservative estimate), which shows the advantage of our coupled approach compared to conventional DD. However, a limitation of the work is that the dislocation density does not grow. In a well annealed crystal, the total dislocation density grows by around 8 orders of magnitude and our simulations are incapable of representing such growth of the dislocation density. The polar dislocation velocity is almost negligible, when both of these quantities should be coupled to the evolution of the microstructure. The strategies for addressing these limitations have been provided in Section 3.6 of Chapter 3.

Appendix A

A.1 Verlet Integration

The implementation of Verlet scheme that we used in Example II to integrate the fine equation (A.2.3) is as follows [San16]:

$$
\begin{aligned}
x_1(\sigma+\Delta\sigma) &= x_1(\sigma) + \Delta\sigma\, y_1(\sigma) + \frac{1}{2}\Delta\sigma^2\,\frac{dy_1}{d\sigma}\\
x_2(\sigma+\Delta\sigma) &= x_2(\sigma) + \Delta\sigma\, y_2(\sigma) + \frac{1}{2}\Delta\sigma^2\,\frac{dy_2}{d\sigma}\\
\hat{y_1}(\sigma+\Delta\sigma) &= y_1(\sigma) + \frac{1}{2}\Delta\sigma\left(\frac{dy_1}{d\sigma} + a_1\left\{x_1(\sigma+\Delta\sigma), y_1(\sigma) + \Delta\sigma\frac{dy_1}{d\sigma}, y_2(\sigma) + \Delta\sigma\frac{dy_2}{d\sigma}, w_1(\sigma)\right\}\right)\\
\hat{y_2}(\sigma+\Delta\sigma) &= y_2(\sigma) + \frac{1}{2}\Delta\sigma\left(\frac{dy_2}{d\sigma} + a_2\left\{x_2(\sigma+\Delta\sigma), y_1(\sigma) + \Delta\sigma\frac{dy_1}{d\sigma}, y_2(\sigma) + \Delta\sigma\frac{dy_2}{d\sigma}, w_2(\sigma)\right\}\right)\\
y_1(\sigma+\Delta\sigma) &= y_1(\sigma) + \frac{1}{2}\Delta\sigma\left(\frac{dy_1}{d\sigma} + a_1\left\{x_1(\sigma+\Delta\sigma), \hat{y_1}(\sigma+\Delta\sigma), \hat{y_2}(\sigma+\Delta\sigma), w_1(\sigma)\right\}\right)\\
y_2(\sigma+\Delta\sigma) &= y_2(\sigma) + \frac{1}{2}\Delta\sigma\left(\frac{dy_2}{d\sigma} + a_2\left\{x_2(\sigma+\Delta\sigma), \hat{y_1}(\sigma+\Delta\sigma), \hat{y_2}(\sigma+\Delta\sigma), w_2(\sigma)\right\}\right).
\end{aligned}
\tag{A.1.1}
$$

Here $a_1(x_1, y_1, y_2, w_1) = \frac{dy_1}{d\sigma}$ and $a_2(x_2, y_1, y_2, w_2) = \frac{dy_2}{d\sigma}$ where $\frac{dy_1}{d\sigma}$ and $\frac{dy_2}{d\sigma}$ are given by (A.2.3).

A.2 Example II: Derivation of system of equations

Two massless springs and masses m_1 and m_2 are connected through a dashpot damper, and each is attached to two bars, or walls, that may move very slowly, compared to possible oscillations of the springs. The system is described in Fig. 2.8 of Section 2.9.

Let the springs constants be k_1 and k_2 respectively, and let η be the dashpot constant. Denote by x_1 and x_2, and by w_1 and w_2, the displacements from equilibrium positions of the masses of the springs and the positions of the two walls. We agree here that all positive displacements are toward the right. We think of the movement of the two walls as being external to the system, determined by a "slow" differential equation. The movement of the springs, however, will be "fast", which we model as singularly perturbed. Let m_{w_1} and m_{w_2} be the masses of the left and the right walls respectively. The displacements x_1, x_2, w_1 and w_2 have physical dimensions of length. The spring constants k_1 and k_2 have physical dimensions of force per unit length while m_1 and m_2 have physical dimensions of mass. In view of the assumptions just made, a general form of the dynamics of the system is given by following set of equations:

$$\begin{aligned} m_1\frac{d^2x_1}{dt^{*2}} &= -k_1(x_1-w_1)+\eta\left(\frac{dx_2}{dt^*}-\frac{dx_1}{dt^*}\right)\\ m_2\frac{d^2x_2}{dt^{*2}} &= -k_2(x_2-w_2)-\eta\left(\frac{dx_2}{dt^*}-\frac{dx_1}{dt^*}\right)\\ m_{w_1}\frac{d^2w_1}{dt^{*2}} &= k_1(x_1-w_1)+R_1\\ m_{w_2}\frac{d^2w_2}{dt^{*2}} &= k_2(x_2-w_2)+R_2, \end{aligned} \tag{A.2.1}$$

where R_1 and R_2 incorporate the reaction forces on the left and right walls respectively due to their prescribed motion. We agree that forces acting toward the right are being considered positive. We make the assumption that $m_{w_1} = m_{w_2} = 0$. The time scale t^* is a time scale with physical dimensions of time. In our calculations, however, we address a

simplified version, of first order equations, that can be obtained from the previous set by appropriately specifying what the forces on the system are:

$$\begin{aligned}
\frac{dx_1}{dt^*} &= y_1 \\
\frac{dy_1}{dt^*} &= -\frac{k_1}{m_1}(x_1 - w_1) + \frac{\eta}{m_1}(y_2 - y_1) \\
\frac{dx_2}{dt^*} &= y_2 \\
\frac{dy_2}{dt^*} &= -\frac{k_2}{m_2}(x_2 - w_2) - \frac{\eta}{m_2}(y_2 - y_1) \\
\frac{dw_1}{dt^*} &= L_1(w_1) \\
\frac{dw_2}{dt^*} &= L_2(w_2).
\end{aligned} \tag{A.2.2}$$

The motion of the walls are determined by the functions $L_1(w_1)$ and $L_2(w_2)$. In the derivations that follow, we use the form $L_1(w_1) = c_1$ and $L_2(w_2) = c_2$, with $c_1 = 0$ and c_2 being a constant. The terms c_1 and c_2 have physical dimensions of velocity.

We define a coarse time period, T_s, in terms of the applied loading rate as $T_s = \frac{const}{L_2}$. Hence, $T_s c_2$ is a constant which is independent of the value of T_s. The fine time period, T_f, is defined as the smaller of the periods of the two spring mass systems. We then define the *non-dimensional* slow and fast time scales as $t = \frac{t^*}{T_s}$ and $\sigma = \frac{t^*}{T_f}$, respectively. The parameter ϵ is given by $\epsilon = \frac{T_f}{T_s}$. Then the dynamics on the slow time-scale is given by (2.9.1) in Section 2.9. The dynamics on the fast time-scale is written as:

$$\begin{aligned}
\frac{dx_1}{d\sigma} &= T_f\, y_1 \\
\frac{dy_1}{d\sigma} &= -T_f \left(\frac{k_1}{m_1}(x_1 - w_1) - \frac{\eta}{m_1}(y_2 - y_1) \right) \\
\frac{dx_2}{d\sigma} &= T_f\, y_2
\end{aligned}$$

$$\begin{aligned}
\frac{dy_2}{d\sigma} &= -T_f\left(\frac{k_2}{m_2}(x_2 - w_2) + \frac{\eta}{m_2}(y_2 - y_1)\right)\\
\frac{dw_1}{d\sigma} &= \epsilon\, T_s\, L_1(w_1)\\
\frac{dw_2}{d\sigma} &= \epsilon\, T_s\, L_2(w_2).
\end{aligned} \tag{A.2.3}$$

Remark A special case of (2.9.1) is when $c_1 = 0$ and $c_2 = 0$. This represents the unforced system i.e. the walls remain fixed. Then (2.9.1) is modified to:

$$\dot{\mathbf{x}} = \mathbf{B}\mathbf{x}, \tag{A.2.4}$$

where $\mathbf{x} = (x_1, y_1, x_2, y_2)^T$. The overhead dot represent time derivatives w.r.t. t. The matrix $\mathbf{B}$ is given by

$$\mathbf{B} = T_s \begin{pmatrix} 0 & 1 & 0 & 0 \\ -\frac{k_1}{m_1} & -\frac{\eta}{m_1} & 0 & \frac{\eta}{m_1} \\ 0 & 0 & 0 & 1 \\ 0 & \frac{\eta}{m_2} & -\frac{k_2}{m_2} & -\frac{\eta}{m_2} \end{pmatrix}.$$

A.3 Example II: Case 1 - Validity of commonly used approximations

The mechanical system (2.9.1) can be written in the form

$$\begin{aligned}
\left(\frac{T_i}{T_s}\right)^2 \mathbf{A}_1 \frac{d^2\mathbf{x}}{dt^2} + \left(\frac{T_\nu}{T_s}\right) \mathbf{A}_2 \frac{d\mathbf{x}}{dt} + \mathbf{A}_3\mathbf{x} &= \frac{\mathbf{F}}{k}\\
\frac{d\mathbf{w}}{dt} &= \mathbf{L}(\mathbf{w}),
\end{aligned} \tag{A.3.1}$$

where $t = \frac{t^*}{T_s}$ where t^* is dimensional time and T_s is a time-scale of loading defined below, $T_i^2 = \frac{m}{k}$, $T_\nu = \frac{D}{k}$ (the mass m, damping D and stiffness k have physical dimensions of $mass$, $\frac{Force \times time}{length}$ and $\frac{Force}{Length}$ respectively), $\mathbf{x}$ and $\mathbf{w}$ are displacements with physical units

of *length*, $\mathbf{L}$ is a function, *independent of* T_s, with physical units of *length* , and $\mathbf{A}_1$, $\mathbf{A}_2$ and $\mathbf{A}_3$ are non-dimensional matrices. In this notation, $\frac{T_i}{T_s} = \epsilon$. In the examples considered, $\mathbf{L} = \tilde{\mathbf{c}} = T_s\mathbf{c}$, where $\mathbf{c}$ has physical dimensions of *velocity* and is assumed given in the form $\mathbf{c} = \frac{\tilde{\mathbf{c}}}{T_s}$ thus serving to define T_s; $\tilde{\mathbf{c}}$ has dimensions of *length*.

Necessary conditions for the application of the Tikhonov framework are that $\frac{T_i}{T_s} \to 0$, $\frac{T_\nu}{T_s} \to 0$ as $T_s \to \infty$. Those for the quasi-static assumption, commonly used in solid mechanics when loading rates are small, are that $\frac{T_i}{T_s} \to 0$ and $\frac{T_\nu}{T_s} \approx 1$ as $T_s \to \infty$.

In our example, we have $m = 1kg$,$k = 2 \times 10^7 N/m$, $D = 5 \times 10^3 Ns/m$ and $T_s = 100s$. Hence $\frac{T_i}{T_s} = 2.24 \times 10^{-6}$ and $\frac{T_\nu}{T_s} = 2.5 \times 10^{-6}$, and the damping is not envisaged as variable as $T_s \to \infty$, which shows that the quasi-static approximation is not applicable.

Nevertheless, due to the common use of the quasi-assumption under slow loading in solid mechanics (which amounts to setting $\epsilon\frac{dy_1}{dt} = 0$, $\epsilon\frac{dy_2}{dt} = 0$ in (2.9.1)), we record the quasi-static solution as well.

The Tikhonov framework It is easy to see that under the conditions in Case 1, when the walls do not move, all solutions tend to an equilibrium (that may depend on the position of the walls). Indeed, the only way the energy will not be dissipated is when $y_1(t) = y_2(t)$ along time intervals, a not sustainable situation. Thus, we are in the classical Tikhonov framework, and, as we already noted toward the end of the introduction of Chapter 2, the limit solution will be of the form of steady-state equilibrium of the springs, moving on the manifold of equilibria determined by the load, namely the walls. Computing the equilibria in (2.9.1) (equivalently (A.2.2)) is straightforward. Indeed, for fixed (w_1,w_2) we get

$$\begin{aligned} x_1 &= w_1, \quad x_2 = w_2 \\ y_1 &= 0, \qquad y_2 = 0. \end{aligned} \tag{A.3.2}$$

Under the assumption that $L_1 = 0$ and $L_2 = c_2$ we get

$$\begin{aligned} w_1(t) &= 0 \\ w_2(t) &= c_2 T_s t. \end{aligned} \tag{A.3.3}$$

Plugging the dynamics (A.3.3) in (A.3.2) yields the limit dynamics of the springs. The real world approximation for ϵ small would be a fast movement toward the equilibrium set (i.e., a boundary layer which has damped oscillations), then an approximation of (A.3.2)-(A.3.3). Our computations in Section 2.9.2 corroborate this claim.

Solutions to (2.9.1) seem to suggest that this is one example where the limit solution (A.3.2)-(A.3.3) is attained by a sequence of solutions of (2.9.1) as $\epsilon \to 0$ or $T_s \to \infty$ in a 'strong' sense (i.e. not in the 'weak' sense of averages); e.g. for small $\epsilon > 0$, y_2 takes the value c_2 in the numerical calculations and this, when measured in units of slow time-scale T_s (note that y has physical dimensions of velocity), yields $T_s c_2$ which equals the value of the (non-dimensional) time rates of w_2 and x_2 corresponding to the limit solution (A.3.2)-(A.3.3); of course, $c_2 \to 0$ as $T_s \to \infty$, by definition, and therefore $y_2 \to 0$ as well. Thus, the kinetic energy and potential energy evaluated from the limit solution (A.3.2)-(A.3.3), i.e. 0 respectively, are a good approximation of the corresponding values from the actual solution for a specific value of small $\epsilon > 0$, as given in Sec. 2.9.2.

The quasi-static assumption We solve the system of equations:

$$\begin{aligned} -k_1(x_1 - w_1) + \eta(y_2 - y_1) &= 0 \\ -k_2(x_2 - w_2) - \eta(y_2 - y_1) &= 0 \\ y_1 &= \frac{1}{T_s}\frac{dx_1}{dt} \\ y_2 &= \frac{1}{T_s}\frac{dx_2}{dt}. \end{aligned} \tag{A.3.4}$$

We assume the left wall to be fixed and the right wall to be moving at a constant velocity of magnitude c_2, so that $w_1 = 0$ and $w_2 = c_2\, T_s\, t$. This results in

$$\frac{dx_1}{dt} + \frac{k_1 T_s}{\eta(1+\frac{k_1}{k_2})} x_1 = \frac{c_2 T_s}{1+\frac{k_1}{k_2}}. \tag{A.3.5}$$

Solving for x_1 and using (A.3.4), we get the following solution

$$\begin{aligned} x_1 &= \frac{c_2\eta}{k_1} + \alpha\, e^{-\beta T_s t}, \quad y_1 = -\alpha\, \beta e^{-\beta T_s t}, \\ x_2 &= c_2 T_s t - \frac{c_2\eta}{k_2} - \frac{k_1}{k_2}\alpha e^{-\beta T_s t}, \quad y_2 = c_2 - \frac{k_1}{k_2}\alpha\beta e^{-\beta T_s t}, \end{aligned} \tag{A.3.6}$$

where α is a constant of integration and $\beta = \frac{k_1}{\eta(1+\frac{k_1}{k_2})}$.

Remark. The solution of the unforced system given by (A.2.4) in Appendix A.2 is of the form

$$\mathbf{x}(t) = \sum_{i=1}^{4} Q_i e^{\lambda_i t} \mathbf{V}_i, \tag{A.3.7}$$

where λ_i and $\mathbf{V}_i$ are the eigenvalues and eigenvectors of $\mathbf{B}$ respectively. Using the values provided in Table 2.1 to construct $\mathbf{B}$, we find that λ_i and $\mathbf{V}_i$ are complex. The general real-valued solution to the system can be written as $\sum_{i=1}^{4} \psi_i e^{\gamma_i t} \mathbf{M}_i(t)$ where

$\xi = 2.58 \times 10^5$	$j=1$	$j=2$	$j=3$	$j=4$
γ_j	-6.17×10^5	-1.22×10^5	-5.63×10^3	-5.63×10^3
$\mathbf{M}_{1,j}(t)$	0.0001	-0.8732	-0.0001	0.4873
$\mathbf{M}_{2,j}(t)$	0.0006	-0.7486	-0.0005	0.6630
$\mathbf{M}_{3,j}(t)$	$-0.0001\ cos(\xi t) - 0.0003\ sin(\xi t)$	$-0.6812\ cos(\xi t) + 0.1818\ sin(\xi t)$	$-0.0003\ sin(\xi t)$	$-0.7092\ cos(\xi t)$
$\mathbf{M}_{4,j}(t)$	$0.0003\ cos(\xi t) - 0.0001\ sin(\xi t)$	$-0.1818\ cos(\xi t) + 0.6812\ sin(\xi t)$	$0.0003\ cos(\xi t)$	$-0.7092\ sin(\xi t)$

We see that all the real (time-dependent) modes $\mathbf{M}_i(t)$ are decaying. Moreover, none of the modes describe the dashpot as being undeformed i.e. $\mathbf{M}_{i,1}(t) = \mathbf{M}_{i,3}(t)$ and $\mathbf{M}_{i,2}(t) = \mathbf{M}_{i,4}(t)$ (where $\mathbf{M}_{i,j}(t)$ is the j^{th} row of the mode $\mathbf{M}_i(t)$). Therefore, solution $\mathbf{x}$(t) goes to rest when t becomes large and the initial transient dies.

A.4 Example II: Case 2 - Closed-form Solution

We can convert (2.9.1) to the following:

$$\begin{pmatrix} \ddot{x_1} \\ \ddot{x_2} \end{pmatrix} + \alpha {T_s}^2 \begin{pmatrix} x_1 \\ x_2 \end{pmatrix} + T_s \begin{pmatrix} \frac{\eta}{m_1} & -\frac{\eta}{m_1} \\ -\frac{\eta}{m_2} & \frac{\eta}{m_2} \end{pmatrix} \begin{pmatrix} \dot{x_1} \\ \dot{x_2} \end{pmatrix} = \begin{pmatrix} \alpha\, w_1 \\ \alpha\, w_2 \end{pmatrix}, \tag{A.4.1}$$

where $\alpha = \frac{k_1}{m_1} = \frac{k_2}{m_2}$ and w_1 and w_2 are defined as :

$$\begin{aligned} w_1(t) &= 0 \\ w_2(t) &= c_2\, T_s\, t. \end{aligned} \tag{A.4.2}$$

The overhead dots represent time derivatives w.r.t. t. The above equation is of the form:

$$\ddot{\mathbf{x}} + \alpha\, {T_s}^2\, \mathbf{x} + T_s \mathbf{A} \dot{\mathbf{x}} = \mathbf{g}(t), \tag{A.4.3}$$

with the general solution

$$x_1 = C_1 cos(\sqrt{\alpha} T_s t) + C_2 sin(\sqrt{\alpha} T_s t) - \frac{m_2}{m_1} C_3 e^{-p_1 T_s t} - \frac{m_2}{m_1} C_4 e^{-p_2 T_s t} + \frac{\eta c_2}{k_1}, \tag{A.4.4a}$$

$$x_2 = C_1 cos(\sqrt{\alpha} T_s t) + C_2 sin(\sqrt{\alpha} T_s t) + C_3 e^{-p_1 T_s t} + C_4 e^{-p_2 T_s t} + c_2\ T_s\ t - \frac{\eta c_2}{k_2}, \tag{A.4.4b}$$

where $p_1 = \frac{\eta(m_1+m_2)+\sqrt{\eta^2(m_1+m_2)^2-4\alpha m_1^2 m_2^2}}{2m_1 m_2}$ and $p_2 = \frac{\eta(m_1+m_2)-\sqrt{\eta^2(m_1+m_2)^2-4\alpha m_1^2 m_2^2}}{2m_1 m_2}$. In the computational results in Section 2.9.2 and 2.9.3, we found that $p_1, p_2 > 0$.

Imposing initial conditions ${x_1}^0$ and ${x_2}^0$ on displacement and ${v_1}^0$ and ${v_2}^0$ on velocity of the two masses m_1 and m_2 respectively, we obtain

C_1	$\frac{m_1 {x_1}^0 + m_2 {x_2}^0}{m_1+m_2}$
C_2	$\frac{m_1 {v_1}^0 + m_2 {v_2}^0 - c_2 m_2}{\sqrt{\alpha}(m_1+m_2)}$
C_3	$\frac{c_2\eta m_1 p_2 + c_2\eta m_2 p_2 - \alpha c_2 m_1 m_2 - \alpha m_1 m_2 p_2 {x_1}^0 + \alpha m_1 m_2 p_2 {x_2}^0}{\alpha m_2(m_1+m_2)(p_1-p_2)}$
C_4	$\frac{c_2\eta m_1 p_1 + c_2\eta m_2 p_1 - \alpha c_2 m_1 m_2 - \alpha m_1 m_2 p_1 {x_1}^0 + \alpha m_1 m_2 p_1 {x_2}^0}{\alpha m_2(m_1+m_2)(p_1-p_2)}$

The *closed-form average kinetic energy* (K^{cf}), *closed-form average potential energy* (P^{cf})and *closed-form average reaction force* (R_2^{cf}) are

$$\begin{aligned} K^{cf}(t) &= \frac{1}{\Delta}\int_{t-\Delta}^{t}\left(\frac{1}{2}m_1 y_1(s)^2 + \frac{1}{2}m_2 y_2(s)^2\right)ds \\ P^{cf}(t) &= \frac{1}{\Delta}\int_{t-\Delta}^{t}\left(\frac{1}{2}k_1 x_1(s)^2 + \frac{1}{2}k_2\left(x_2(s)-w_2(s)\right)^2\right)ds \\ R_2^{cf}(t) &= \frac{1}{\Delta}\int_{t-\Delta}^{t}\left(-k_2\left(\left(x_2(s)-w_2(s)\right)\right)ds, \end{aligned} \tag{A.4.5}$$

where $x_1(s)$ and $x_2(s)$ can be substituted from (A.4.4) and $y_1(s) = \frac{1}{T_s}\frac{dx_1}{ds}$ and $y_2(s) = \frac{1}{s}\frac{dx_2}{ds}$.

Non-dimensionalization Let us denote

$$m_{max} = \max_i \; m(x_\epsilon(\sigma_i), l_\epsilon(\sigma_i)),$$

where $m(x_\epsilon(\sigma_i), l_\epsilon(\sigma_i))$ is given in (2.7.3) and (2.7.5). Please note that i is chosen such that there is no effect of the initial transient. Using (2.9.2) and computational results in Case 2.4 in Section 2.9.3, we find that

$$K_{max} = \frac{1}{2}C_1^2(k_1+k_2), \quad P_{max} = \frac{1}{2}C_1^2(k_1+k_2), \quad R_{2,max} = C_1 k_2.$$

We introduce the following non-dimensional variables:

$$\tilde{K}^{cf} = \frac{K^{cf}}{K_{max}}, \quad \tilde{P}^{cf} = \frac{P^{cf}}{P_{max}}, \quad \tilde{R_2}^{cf} = \frac{R_2^{cf}}{R_{2,max}}. \tag{A.4.6}$$

Henceforth, while referring to the dimensionless variables, we drop the overhead tilde for simplicity.

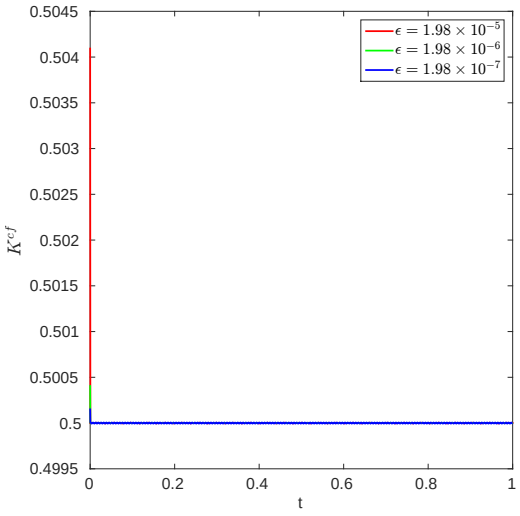

Figure A.1: K^{cf} *as a function of* t.

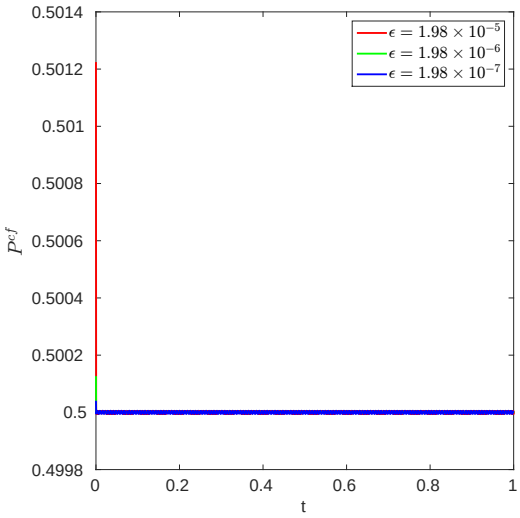

Figure A.2: P^{cf} *as a function of* t.

We evaluated (A.4.5) numerically (since the analytical expressions become lengthy) with 2×10^6 integration points over the interval $[t - \Delta, t]$ using Simpson's rule and we used 2000 discrete points for t. We substituted the values provided in Table 2.1. We repeated the calculations with 4×10^6 integration points over the interval $[t - \Delta, t]$ and 4000 discrete points for t, and found the results to be the same. We see in Fig. A.1 and Fig.A.2 that K^{cf} and P^{cf} oscillate around 0.5 with very small amplitude for different values of ϵ (recall that $\epsilon = \frac{T_f}{T_s}$ and we think of T_f being fixed with $T_s \to \infty$ to effect $\epsilon \to 0$). However, as we decrease ϵ, the amplitude of oscillations of R_2^{cf} decreases and it goes to zero for $\epsilon = 1.98 \times 10^{-7}$ as we see in Fig. A.3. We use these 'closed-form' results to compare with the PTA results in Section 2.9.2 and Section 2.9.3.

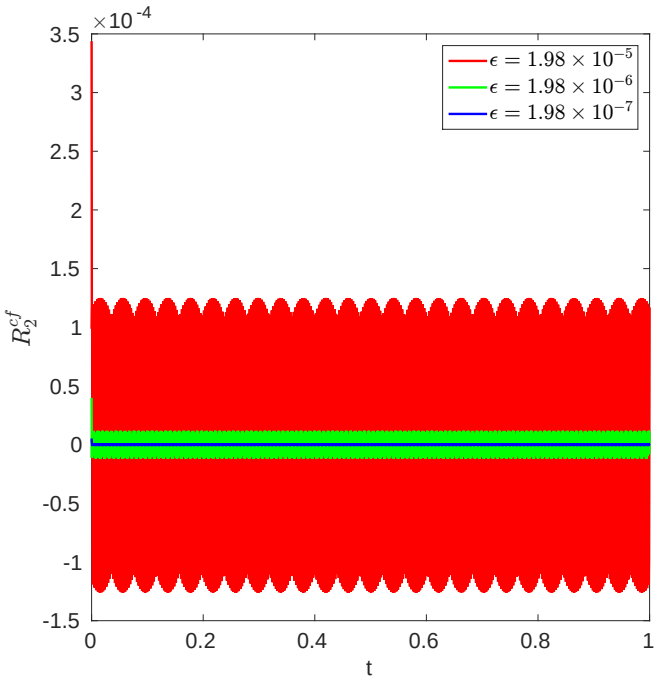

Figure A.3: R_2^{cf} *as a function of* t.

Remark The criteria for convergence of R_t^m (as mentioned in the discussion following (2.7.4) in Section 2.7) is discussed as follows. Let us denote

$$m_{I,t} = \frac{1}{I}\sum_{i=1}^{I} m(x_\epsilon(\sigma_i), l_\epsilon(\sigma_i)),$$

where $x_\epsilon(\sigma_i), l_\epsilon(\sigma_i)$ is defined in (2.7.4), $I \in \mathbb{Z}_+$ and $m(x_\epsilon(\sigma_i), l_\epsilon(\sigma_i))$ is non-dimensionalized $\forall i \in [1, I]$. Then, we say that $m_{I,t}$ has converged if

$$|\frac{m_{I-jk,t} - m_{I-pk,t}}{m_{I-pk,t}}| \leq tol_1^m, \tag{A.4.7}$$

$\forall j \in [0, p]$ where $p, k \in \mathbb{Z}_+$ and $p, k < I$ and tol_1^m is a specified value of tolerance (which is a small value generally around 10^{-2}). We declare $N_t = I$ (where N_t is defined in the discussion following (2.7.4)) and $R_t^m = m_{I,t}$. In situations where $m_{I-pk,t}$ becomes very small so that the convergence criteria in (A.4.7) cannot be practically implemented, we say that $m_{I,t}$ has

converged if

$$|m_{I-jk,t}| \leq tol_2^m, \tag{A.4.8}$$

$\forall j \in [0, p]$ and tol_2^m is a specified value of tolerance (generally around 10^{-5}).

Remark We used the Simpson's rule of numerical integration to obtain the value of the slow variable instead of using (2.7.7) to obtain the results in Section 2.9.2 and 2.9.3. The Simpson's rule of numerical integration for any function $f(t)$ over the interval $[a, b]$ where $a, b \in \mathbb{R}$ is

$$\int_a^b f(t)dt \approx \frac{\Delta t}{n}[f(t_0) + 4f(t_1) + 2f(t_2) + ... + 2f(t_{n-2}) + 4f(t_{n-1}) + f(t_n)],$$

where $\Delta t = \frac{b-a}{n}$, $n \in \mathbb{Z}_+$, n is even and $t_i = t_0 + i\Delta t$ for $i \in \mathbb{Z}$ and $i \leq n$. All the function evaluations at points with odd subscripts are multiplied by 4 and all the function evaluations at points with even subscripts (except for the first and last) are multiplied by 2. Since we are calculating the value of the slow variable v given by (2.7.1), the function $f(t)$ is given by R_t^m which is defined in (2.7.3), with $\epsilon = 0$ in (2.7.4). We chose $n = 2$ and calculated the values of $R^m_{t-\Delta+\frac{i}{n}\Delta}$ using (2.7.3) for $i = 0, 1, 2$. We obtained the fine initial conditions $x_{guess}(t - \Delta + \frac{i}{n}\Delta)$ as

$$x_{guess}(t - \Delta + \frac{i}{n}\Delta) = x^{arb}_{t-\Delta} + \frac{\left(x^{arb}_{t-\Delta} - x^{cp}_{t-h}\right)}{(h - \Delta)} \frac{i\Delta}{n},$$

where $x^{arb}_{\cdot}$ and $x^{cp}_{\cdot}$ are defined in Step 3 in Section 2.7.

Please note that we also used Simpson's rule to evaluate (A.4.5) with $n = 2 \times 10^6$ and the details of the calculation are mentioned in *Non-dimensionalization* in this Appendix above.

Remark To see the effect of the initial condition on the solution, we solve (A.2.4) in a

particular case using the values provided in Table 2.1 but with $k_2 = 2 \times 10^7 N/m$ and $c_2 = 0$. The general real-valued solution to the system can be written as $\sum_{i=1}^{4} \psi_i e^{\gamma_i t} \mathbf{M}_i(t)$ where

$\omega = 3.16 \times 10^5$	$j = 1$	$j = 2$	$j = 3$	$j = 4$
γ_j	-5.76×10^5	-1.73×10^5	0	0
$\mathbf{M}_{1,j}(t)$	0.0002	-0.8944	-0.0001	0.4472
$\mathbf{M}_{2,j}(t)$	0.0005	-0.8944	-0.0003	0.4421
$\mathbf{M}_{3,j}(t)$	$0.0002\ sin(\omega t)$	$-0.7071\ cos(\omega t)$	$0.0002\ sin(\omega t)$	$0.7071\ cos(\omega t)$
$\mathbf{M}_{4,j}(t)$	$-0.0002\ cos(\omega t)$	$0.7071\ sin(\omega t)$	$-0.0002\ cos(\omega t)$	$0.7071\ sin(\omega t)$

We see that while $\mathbf{M}_1(t)$ and $\mathbf{M}_2(t)$ are decaying real (time-dependent) modes, $\mathbf{M}_3(t)$ and $\mathbf{M}_4(t)$ are the non-decaying real (time-dependent) modes. Moreover, both $\mathbf{M}_3(t)$ and $\mathbf{M}_4(t)$ describe the dashpot as being undeformed i.e. $\mathbf{M}_{i,1}(t) = \mathbf{M}_{i,3}(t)$ and $\mathbf{M}_{i,2}(t) = \mathbf{M}_{i,4}(t)$ (where $\mathbf{M}_{i,j}(t)$ is the j^{th} row of the mode $\mathbf{M}_i(t)$). The solution $\mathbf{x}(t)$ described in (A.3.7) of Appendix A.3 can be written as

$$\mathbf{x}(t) = \sum_{i=1}^{4} \kappa_i \mathbf{M}_i(t), \tag{A.4.9}$$

where the coefficients κ_i are obtained from the initial condition $\mathbf{x}_0$ using

$$\kappa_i = \mathbf{x}_0 \cdot \mathbf{M}_i^d(0)$$

where $\mathbf{M}_i^d(t)$ are the dual basis of $\mathbf{M}_i(t)$.

Appendix B

The orientation matrix

The orientation matrix represents the transformation rule between components of any vector on the cyrstal basis and the global basis. Let the crystal basis be $\{\hat{e}_i\}$ and the global basis be $\{e_i\}$. Let both the crystal and global bases be orthonormal. Let $\boldsymbol{v} = c_i\ \hat{e}_i = g_i\ e_i$. Then $g_k = (e_k \cdot \hat{e}_i)\ c_i$. Then the orientation matrix $\boldsymbol{A}$ is given by $A_{ki} = e_k \cdot \hat{e}_i$.

However, suppose we do not know the crystal basis vectors in the global basis. Instead, suppose we know a set of orthonormal crystallographic directions $\{C_j\}$ (where $C_j = C_{ij}\hat{e}_i$ and C_{ij} are known by hypothesis), that coincide with the global basis vectors, i.e. $C_j = e_j$. Let $g_{kj}e_k = e_j$ which implies that $g_{kj} = \delta_{kj}$. Then, we have

$$\begin{aligned} C_j = e_j &\implies g_{kj}e_k = C_{ij}\hat{e}_i \\ &\implies g_{kj}e_k \cdot e_m = C_{ij}(\hat{e}_i \cdot e_m) \\ &\implies g_{mj} = (e_m \cdot \hat{e}_i)C_{ij} \\ &\implies g_{mj} = A_{mi}C_{ij} \\ &\implies g_{mj}C^{-1}_{jp} = A_{mp}. \end{aligned}$$

But $g_{mj} = \delta_{mj}$ which implies that $A_{mp} = C^{-1}_{mp}$. But the matrix $\boldsymbol{C}$ has for columns the

components of an orthonormal basis expressed on the basis $\{\hat{i}_i\}$. Thus, $\boldsymbol{C}$ is an orthogonal matrix and its transpose is its inverse. Then, $\boldsymbol{A}$ has as rows the components of the basis $\{C_j\}$ expressed in the crystal basis $\{\hat{e}_i\}$.

Appendix C

Derivation of evolution equations

C.1 Total dislocation density, ρ^l

From (4.3.4), we have

$$\rho = \boldsymbol{\alpha} : \boldsymbol{\alpha} \tag{C.1.1}$$

We differentiate (C.1.1) in time to get

$$\begin{aligned}
\dot{\rho} &= 2\ \boldsymbol{\alpha} : \dot{\boldsymbol{\alpha}} = -2\ \boldsymbol{\alpha} : curl(\boldsymbol{\alpha} \times \boldsymbol{V}) = -2\alpha_{ij}[curl(\boldsymbol{\alpha} \times \boldsymbol{V})]_{ij} \\
&= -2\alpha_{ij} e_{jmn} (\boldsymbol{\alpha} \times \boldsymbol{V})_{in,m} = -2\alpha_{ij} e_{jmn} e_{npq} (\alpha_{ip} V_q)_{,m} \\
&= -2(\delta_{jp}\delta_{mq} - \delta_{jq}\delta_{mp})[\alpha_{ij}\alpha_{ip,m} V_q + \alpha_{ij}\alpha_{ip} V_{q,m}] \\
&= -2[\alpha_{ij}\alpha_{ij,m} V_m + \alpha_{ij}\alpha_{ij} V_{m,m} - \alpha_{ij}\alpha_{im,m} V_j - \alpha_{ij}\alpha_{im} V_{j,m}] \\
&= -2\ [\frac{1}{2} grad(\boldsymbol{\alpha} : \boldsymbol{\alpha}) \cdot \boldsymbol{V} + \boldsymbol{\alpha} : \boldsymbol{\alpha}(divV) - \boldsymbol{\alpha} : (div\boldsymbol{\alpha} \otimes \boldsymbol{V}) - \boldsymbol{\alpha} : \{\boldsymbol{\alpha}\, gradV\}] \\
&= -2\ [\frac{1}{2} grad\rho \cdot \boldsymbol{V} + \rho(divV) - \boldsymbol{\alpha} : (div\boldsymbol{\alpha} \otimes \boldsymbol{V}) - \boldsymbol{\alpha} : \{\boldsymbol{\alpha}\, gradV\}] \\
&= -grad\rho \cdot \boldsymbol{V} - 2\rho(divV) + 2\boldsymbol{\alpha} : (div\boldsymbol{\alpha} \otimes \boldsymbol{V}) + 2\boldsymbol{\alpha} : \{\boldsymbol{\alpha}\, gradV\}
\end{aligned} \tag{C.1.2}$$

We apply the averaging operator (4.2.1) to both sides of (C.1.2) and use (4.2.4) to get

$$\dot{\overline{\rho}} = -grad\ \overline{\rho} \cdot \overline{\boldsymbol{V}} - 2\ \overline{\rho}\ div\overline{\boldsymbol{V}} - \overline{\Sigma^{grad\rho} \cdot \Sigma^{\boldsymbol{V}}} - \overline{\Sigma^{\rho}\Sigma^{divV}} + 2\ \overline{\boldsymbol{\alpha} : (div\boldsymbol{\alpha} \otimes \boldsymbol{V})} + 2\ \overline{\boldsymbol{\alpha} : \{\boldsymbol{\alpha}\ grad\boldsymbol{V}\}}. \tag{C.1.3}$$

Using (C.1.3) and the facts that

$$\overline{\boldsymbol{\alpha} : \{\boldsymbol{\alpha}\ grad\boldsymbol{V}\}} = \overline{\boldsymbol{\alpha}} : \{\overline{\boldsymbol{\alpha}}\ grad\overline{\boldsymbol{V}}\} + \overline{\boldsymbol{\alpha}} : \overline{\Sigma^{\boldsymbol{\alpha}}\ \Sigma^{grad\boldsymbol{V}}} + \overline{\Sigma^{\boldsymbol{\alpha}} : \Sigma^{\boldsymbol{\alpha}}\ grad\boldsymbol{V}}$$

$$\overline{\boldsymbol{\alpha} : (div\boldsymbol{\alpha} \otimes \boldsymbol{V})} = \overline{\boldsymbol{\alpha}} : (div\overline{\boldsymbol{\alpha}} \otimes \overline{\boldsymbol{V}}) + \overline{\boldsymbol{\alpha}} : (\overline{\Sigma^{div\boldsymbol{\alpha}} \otimes \Sigma^{\boldsymbol{V}}}) + \overline{\Sigma^{\boldsymbol{\alpha}} : \Sigma^{div\boldsymbol{\alpha} \otimes \boldsymbol{V}}},$$

we get the evolution of $\overline{\rho}$ as (4.3.6) in section 4.3.

C.2 The characteristic function, χ^l

We will use the following results in the derivation:

- If $\boldsymbol{f}$ is a vector, then

$$\dot{|\boldsymbol{f}|} = \frac{\boldsymbol{f} \cdot \dot{\boldsymbol{f}}}{|\boldsymbol{f}|}, \tag{C.2.1}$$

  which gives,

$$\dot{\overline{|\boldsymbol{f}|}} = \dot{\frac{\overline{\boldsymbol{f} \cdot \dot{\boldsymbol{f}}}}{|\boldsymbol{f}|}} = \dot{\overline{\boldsymbol{f} \cdot \dot{\boldsymbol{f}}}}.\overline{\frac{1}{|\boldsymbol{f}|}} + \overline{\Sigma^{\boldsymbol{f} \cdot \dot{\boldsymbol{f}}} \Sigma^{\frac{1}{|\boldsymbol{f}|}}} = \left(\dot{\overline{\boldsymbol{f}}} \cdot \dot{\overline{\boldsymbol{f}}} + \overline{\Sigma^{\boldsymbol{f}} \cdot \Sigma^{\dot{\boldsymbol{f}}}}\right).\overline{\frac{1}{|\boldsymbol{f}|}} + \overline{\Sigma^{\boldsymbol{f} \cdot \dot{\boldsymbol{f}}} \Sigma^{\frac{1}{|\boldsymbol{f}|}}}. \tag{C.2.2}$$

- If q is a scalar,

$$\dot{|q|} = sgn(q)\dot{q}, \tag{C.2.3}$$

which gives,

$$\overline{\dot{|q|}} = \overline{sgn(q)\ \dot{q}} = \overline{sgn(q)}\ \dot{\overline{q}} + \overline{\Sigma^{sgn(q)}\Sigma^{\dot{q}}}. \tag{C.2.4}$$

From (4.3.18), we have

$$\chi^l = e(-P^m)\ e(-Q^n), \tag{C.2.5}$$

where $P = \frac{|\boldsymbol{\alpha} \boldsymbol{n}^l|}{c_1}$ and $Q = \frac{||\tilde{\boldsymbol{b}}^l.\tilde{\boldsymbol{\alpha}}\tilde{\boldsymbol{\alpha}}^T.\tilde{\boldsymbol{b}}^l|-1|}{c_2}$. Taking time derivative of (C.2.5) and using (C.2.1) and (C.2.3), we have,

$$\begin{aligned}
\dot{\chi}^l =& - m\ e(-P^m)e(-Q^n)P^{m-1}\dot{P} - ne(-P^m)e(-Q^n)Q^{n-1}\dot{Q} \\
=& - m\ e(-P^m)e(-Q^n)P^{m-1}\left(\frac{(\boldsymbol{\alpha}\boldsymbol{n}^l)\cdot(-curl(\boldsymbol{\alpha}\times\boldsymbol{V})^T)\boldsymbol{n}^l}{c_1|\boldsymbol{\alpha}\boldsymbol{n}^l|}\right) \\
& - \frac{n}{c_2}\ e(-P^m)e(-Q^n)Q^{n-1}\Bigg[sgn(p)\ \tilde{\boldsymbol{b}}^l\cdot\Big[\Big\{-\frac{curl(\boldsymbol{\alpha}\times\boldsymbol{V})}{|\boldsymbol{\alpha}|} + (\frac{\boldsymbol{\alpha} : curl(\boldsymbol{\alpha}\times\boldsymbol{V})}{|\boldsymbol{\alpha}|^3})\ \boldsymbol{\alpha}\Big\}\tilde{\boldsymbol{\alpha}}^T \\
& + \tilde{\boldsymbol{\alpha}}\Big\{-\frac{\{curl(\boldsymbol{\alpha}\times\boldsymbol{V})\}^T}{|\boldsymbol{\alpha}|} + (\frac{\boldsymbol{\alpha} : \{curl(\boldsymbol{\alpha}\times\boldsymbol{V})\}}{|\boldsymbol{\alpha}|^3})\ \boldsymbol{\alpha}^T\Big\}\Big]\tilde{\boldsymbol{b}}^l\Bigg]
\end{aligned} \tag{C.2.6}$$

From (C.2.6), we have,

$$\begin{aligned}
\dot{\overline{\chi}}^l =& - m\ \overline{eP^m\ eQ^n\ P^{m-1}}\ \dot{\overline{P}} - m\overline{\Sigma^{eP^m\ eQ^n\ P^{m-1}\ \Sigma^{\dot{P}}}} - n\ \overline{eP^m\ eQ^n\ Q^{n-1}}\ \dot{\overline{Q}} - n\overline{\Sigma^{eP^m\ eQ^n\ Q^{n-1}\ \Sigma^{\dot{Q}}}} \\
=& - m\ \overline{eP^m\ eQ^n\ P^{m-1}}\ \dot{\overline{P}} - n\ \overline{eP^m\ eQ^n\ Q^{n-1}}\ \dot{\overline{Q}} - m\overline{\Sigma^{eP^m\ eQ^n\ P^{m-1}\ \Sigma^{\dot{P}}}} - n\overline{\Sigma^{eP^m\ eQ^n\ Q^{n-1}\ \Sigma^{\dot{Q}}}} \\
=& - m\Big(\ \overline{eP^m\ eQ^n}\ \overline{P^{m-1}} + \overline{\Sigma^{eP^m\ eQ^n\ \Sigma^{P^{m-1}}}}\Big)\ \dot{\overline{P}} - n\Big(\ \overline{eP^m\ eQ^n}\ \overline{Q^{n-1}} + \overline{\Sigma^{eP^m\ eQ^n\ \Sigma^{Q^{n-1}}}}\Big)\ \dot{\overline{Q}} \\
& - m\overline{\Sigma^{eP^m\ eQ^n\ P^{m-1}\ \Sigma^{\dot{P}}}} - n\overline{\Sigma^{eP^m\ eQ^n\ Q^{n-1}\ \Sigma^{\dot{Q}}}} \\
=& - m\Big(\ (\overline{eP^m}\ \overline{eQ^n} + \overline{\Sigma^{eP^m\ eQ^m}})\ \overline{P^{m-1}} + \overline{\Sigma^{eP^m\ eQ^n\ \Sigma^{P^{m-1}}}}\Big)\ \dot{\overline{P}} \\
& - n\Big(\ (\overline{eP^m}\ \overline{eQ^n} + \overline{\Sigma^{eP^m\ eQ^m}})\ \overline{Q^{n-1}} + \overline{\Sigma^{eP^m\ eQ^n\ \Sigma^{Q^{n-1}}}}\Big)\ \dot{\overline{Q}} \\
& - m\overline{\Sigma^{eP^m\ eQ^n\ P^{m-1}\ \Sigma^{\dot{P}}}} - n\overline{\Sigma^{eP^m\ eQ^n\ Q^{n-1}\ \Sigma^{\dot{Q}}}}
\end{aligned}$$

$$
\begin{aligned}
&= - m\Big(\overline{eP^m}\ \overline{eQ^n}\ \overline{P^{m-1}}\ \dot{\overline{P}} + \overline{\Sigma^{eP^m}\ eQ^m}\ \overline{P^{m-1}}\ \dot{\overline{P}} + \overline{\Sigma^{eP^m}\ eQ^n\ \Sigma^{P^{m-1}}}\ \dot{\overline{P}}\Big) \\
&\quad - n\Big(\overline{eP^m}\ \overline{eQ^n}\ \overline{Q^{n-1}}\ \dot{\overline{Q}} + \overline{\Sigma^{eP^m}\ eQ^m}\ \overline{Q^{n-1}}\ \dot{\overline{Q}} + \overline{\Sigma^{eP^m}\ eQ^n\ \Sigma^{Q^{n-1}}}\ \dot{\overline{Q}}\Big) \\
&\quad - m\ \overline{\Sigma^{eP^m}\ eQ^n\ P^{m-1}\ \Sigma^{\dot{P}}} - n\ \overline{\Sigma^{eP^m}\ eQ^n\ Q^{n-1}\ \Sigma^{\dot{Q}}}
\end{aligned} \tag{C.2.7}
$$

From the definition of P in the discussion following (C.2.5) and using (C.2.1),

$$
\dot{P} = \frac{P \cdot \dot{P}}{|P|} = \frac{1}{c_1} \frac{(\boldsymbol{\alpha}\ \boldsymbol{n}^l) \cdot (\dot{\boldsymbol{\alpha}}\ \boldsymbol{n}^l)}{|\boldsymbol{\alpha}\ \boldsymbol{n}^l|} = -\frac{1}{c_1} \frac{(\boldsymbol{\alpha}\ \boldsymbol{n}^l) \cdot \{curl(\boldsymbol{\alpha} \times \boldsymbol{V})\ \boldsymbol{n}^l\}}{|\boldsymbol{\alpha}\ \boldsymbol{n}^l|} \tag{C.2.8}
$$

Using (C.2.2),

$$
\begin{aligned}
\dot{\overline{P}} =& \frac{1}{c_1} \left(\overline{\boldsymbol{\alpha}\boldsymbol{n}^l} \cdot \dot{\overline{\boldsymbol{\alpha}\boldsymbol{n}^l}} + \overline{\Sigma^{\boldsymbol{\alpha}\boldsymbol{n}^l} \cdot \Sigma^{\dot{\boldsymbol{\alpha}}\boldsymbol{n}^l}} \right) \overline{\left(\frac{1}{|\boldsymbol{\alpha}\boldsymbol{n}^l|} \right)} + \overline{\Sigma^{(\boldsymbol{\alpha}\boldsymbol{n}^l)\cdot(\dot{\boldsymbol{\alpha}}\boldsymbol{n}^l)\ \Sigma^{\frac{1}{|\boldsymbol{\alpha}\boldsymbol{n}^l|}}}} \\
=& \frac{1}{c_1} \left((\overline{\boldsymbol{\alpha}}\boldsymbol{n}^l) \cdot (\dot{\overline{\boldsymbol{\alpha}}}\boldsymbol{n}^l) + \overline{\Sigma^{\boldsymbol{\alpha}\boldsymbol{n}^l} \cdot \Sigma^{\dot{\boldsymbol{\alpha}}\boldsymbol{n}^l}} \right) \overline{\left(\frac{1}{|\boldsymbol{\alpha}\boldsymbol{n}^l|} \right)} + \overline{\Sigma^{(\boldsymbol{\alpha}\boldsymbol{n}^l)\cdot(\dot{\boldsymbol{\alpha}}\boldsymbol{n}^l)\ \Sigma^{\frac{1}{|\boldsymbol{\alpha}\boldsymbol{n}^l|}}}} \\
=& -\frac{1}{c_1} \Big[\Big((\overline{\boldsymbol{\alpha}}\boldsymbol{n}^l) \cdot (curl(\boldsymbol{\alpha} \times \boldsymbol{V} + \boldsymbol{L}^p)\boldsymbol{n}^l) + \overline{\Sigma^{\boldsymbol{\alpha}\boldsymbol{n}^l} \cdot \Sigma^{\dot{\boldsymbol{\alpha}}\boldsymbol{n}^l}} \Big) \overline{\left(\frac{1}{|\boldsymbol{\alpha}\boldsymbol{n}^l|} \right)} \\
&+ \overline{\Sigma^{-(\boldsymbol{\alpha}\boldsymbol{n}^l)\cdot(curl(\boldsymbol{\alpha}\times\boldsymbol{V})\boldsymbol{n}^l)\ \Sigma^{\frac{1}{|\boldsymbol{\alpha}\boldsymbol{n}^l|}}}} \Big].
\end{aligned} \tag{C.2.9}
$$

From the definition of Q in the discussion following (C.2.5) and using (C.2.3) and denoting $p = \tilde{\boldsymbol{b}}^l \cdot \tilde{\boldsymbol{\alpha}}\tilde{\boldsymbol{\alpha}}^T\tilde{\boldsymbol{b}}^l$,

$$
\dot{Q} = \frac{1}{c_2}\ sgn(|p|{-}1)\ sgn(p)\ \dot{p} = \frac{1}{c_2}\ sgn(|p|{-}1)\ sgn(p)\ \tilde{\boldsymbol{b}}^l \cdot (\dot{\tilde{\boldsymbol{\alpha}}}\tilde{\boldsymbol{\alpha}}^T + \tilde{\boldsymbol{\alpha}}\dot{\tilde{\boldsymbol{\alpha}}}^T)\tilde{\boldsymbol{b}}^l \tag{C.2.10}
$$

Now,

$$
\begin{aligned}
\dot{\tilde{\boldsymbol{\alpha}}} &= \frac{\dot{\boldsymbol{\alpha}}}{|\boldsymbol{\alpha}|} + \left(\frac{\boldsymbol{\alpha} : \dot{\boldsymbol{\alpha}}}{|\boldsymbol{\alpha}|^3} \right)\ \boldsymbol{\alpha} = -\frac{curl(\boldsymbol{\alpha} \times \boldsymbol{V})}{|\boldsymbol{\alpha}|} - \left(\frac{\boldsymbol{\alpha} : curl(\boldsymbol{\alpha} \times \boldsymbol{V})}{|\boldsymbol{\alpha}|^3} \right)\ \boldsymbol{\alpha} \\
\dot{\widetilde{\boldsymbol{\alpha}}}^T &= -\frac{\{curl(\boldsymbol{\alpha} \times \boldsymbol{V})\}^T}{|\boldsymbol{\alpha}|} - \left(\frac{\boldsymbol{\alpha} : \{curl(\boldsymbol{\alpha} \times \boldsymbol{V})\}}{|\boldsymbol{\alpha}|^3} \right)\ \boldsymbol{\alpha}^T.
\end{aligned} \tag{C.2.11}
$$

Hence,

$$\begin{aligned}\dot{Q} =& sgn(|p|-1)\ sgn(p)\ \tilde{\boldsymbol{b}}^l \cdot \Big[\Big\{ -\frac{curl(\boldsymbol{\alpha}\times\boldsymbol{V})}{|\boldsymbol{\alpha}|} + (\frac{\boldsymbol{\alpha} : curl(\boldsymbol{\alpha}\times\boldsymbol{V})}{|\boldsymbol{\alpha}|^3})\ \boldsymbol{\alpha}\Big\}\tilde{\boldsymbol{\alpha}}^T \\ &+ \tilde{\boldsymbol{\alpha}}\Big\{ -\frac{\{curl(\boldsymbol{\alpha}\times\boldsymbol{V})\}^T}{|\boldsymbol{\alpha}|} + (\frac{\boldsymbol{\alpha} : \{curl(\boldsymbol{\alpha}\times\boldsymbol{V})\}}{|\boldsymbol{\alpha}|^3})\ \boldsymbol{\alpha}^T\Big\}\Big]\tilde{\boldsymbol{b}}^l. \end{aligned} \tag{C.2.12}$$

Using (C.2.12),

$$\begin{aligned}\dot{\overline{Q}} =& \frac{1}{c_2}\overline{sgn(|p|-1)\ sgn(p)\ \dot{p}} = \frac{1}{c_2}(\overline{sgn(|p|-1)}\ \overline{sgn(p)\ \dot{p}} + \overline{\Sigma^{sgn(|p|-1)}\Sigma^{sgn(p)\ \dot{p}}}) \\ =& \frac{1}{c_2}(\overline{sgn(|p|-1)}\ \overline{sgn(p)}\ \dot{\overline{p}} + \overline{sgn(|p|-1)}\ \overline{\Sigma^{sgn(p)}\ \Sigma^{\dot{p}}} + \overline{\Sigma^{sgn(|p|-1)\Sigma^{sgn(p)}\ \dot{p}}}). \end{aligned} \tag{C.2.13}$$

Using the definition of p in the discussion around (C.2.10) ,

$$\begin{aligned} \dot{p} =& \tilde{\boldsymbol{b}}^l \cdot (\dot{\tilde{\boldsymbol{\alpha}}}\tilde{\boldsymbol{\alpha}}^T + \tilde{\boldsymbol{\alpha}}\dot{\tilde{\boldsymbol{\alpha}}}^T)\tilde{\boldsymbol{b}}^l \\ \implies \dot{\overline{p}} =& \tilde{\boldsymbol{b}}^l \cdot (\dot{\overline{\tilde{\boldsymbol{\alpha}}}}\ \overline{\tilde{\boldsymbol{\alpha}}^T} + \overline{\tilde{\boldsymbol{\alpha}}}\ \dot{\overline{\tilde{\boldsymbol{\alpha}}^T}})\tilde{\boldsymbol{b}}^l \end{aligned} \tag{C.2.14}$$

From [AR06], we have

$$\dot{\overline{\boldsymbol{\alpha}}} = -curl(\overline{\boldsymbol{\alpha}}\times\overline{\boldsymbol{V}} + \boldsymbol{L}^p)$$

So,

$$\begin{aligned}\dot{\overline{\tilde{\boldsymbol{\alpha}}}} &= \Big(\dot{\overline{\boldsymbol{\alpha}}}\ \overline{\frac{1}{|\boldsymbol{\alpha}|}} + \overline{\Sigma^{\dot{\boldsymbol{\alpha}}}\Sigma^{\frac{1}{|\boldsymbol{\alpha}|}}}\Big) + \Big\{\Big(\overline{\frac{\boldsymbol{\alpha}:\dot{\boldsymbol{\alpha}}}{|\boldsymbol{\alpha}|^3}}\Big)\overline{\boldsymbol{\alpha}} + \overline{\Sigma^{\frac{\boldsymbol{\alpha}:\dot{\boldsymbol{\alpha}}}{|\boldsymbol{\alpha}|^3}}\Sigma^{\boldsymbol{\alpha}}}\Big\} \\ &= \Big(\dot{\overline{\boldsymbol{\alpha}}}\ \overline{\frac{1}{|\boldsymbol{\alpha}|}} + \overline{\Sigma^{\dot{\boldsymbol{\alpha}}}\Sigma^{\frac{1}{|\boldsymbol{\alpha}|}}}\Big) + \Big\{\Big(\overline{\frac{\boldsymbol{\alpha}:\dot{\boldsymbol{\alpha}}}{|\boldsymbol{\alpha}|^3}}\Big)\overline{\boldsymbol{\alpha}} + \overline{\Sigma^{\frac{\boldsymbol{\alpha}:\dot{\boldsymbol{\alpha}}}{|\boldsymbol{\alpha}|^3}}\Sigma^{\boldsymbol{\alpha}}}\Big\} \\ &= \Big(\dot{\overline{\boldsymbol{\alpha}}}\ \overline{\frac{1}{|\boldsymbol{\alpha}|}} + \overline{\Sigma^{\dot{\boldsymbol{\alpha}}}\Sigma^{\frac{1}{|\boldsymbol{\alpha}|}}}\Big) + \Big[\Big\{\Big(\overline{\boldsymbol{\alpha}} : \dot{\overline{\boldsymbol{\alpha}}} + \overline{\Sigma^{\boldsymbol{\alpha}} : \Sigma^{\dot{\boldsymbol{\alpha}}}}\Big)\overline{\frac{1}{|\boldsymbol{\alpha}|^3}} + \overline{\Sigma^{\boldsymbol{\alpha}:\dot{\boldsymbol{\alpha}}}\Sigma^{\frac{1}{|\boldsymbol{\alpha}|^3}}}\Big\}\overline{\boldsymbol{\alpha}} + \overline{\Sigma^{\frac{\boldsymbol{\alpha}:\dot{\boldsymbol{\alpha}}}{|\boldsymbol{\alpha}|^3}}\Sigma^{\boldsymbol{\alpha}}}\Big] \\ &= \Big(-curl(\overline{\boldsymbol{\alpha}}\times\overline{\boldsymbol{V}} + \boldsymbol{L}^p)\ \overline{\frac{1}{|\boldsymbol{\alpha}|}} + \overline{\Sigma^{-curl(\boldsymbol{\alpha}\times\boldsymbol{V})\Sigma^{\frac{1}{|\boldsymbol{\alpha}|}}}}\Big) + \Big[\Big\{\Big(-\overline{\boldsymbol{\alpha}} : curl(\overline{\boldsymbol{\alpha}}\times\overline{\boldsymbol{V}} + \boldsymbol{L}^p)\end{aligned}$$

$$+\overline{\Sigma^{\boldsymbol{\alpha}}:\Sigma^{-curl(\boldsymbol{\alpha}\times\boldsymbol{V})}}\Big)\overline{\frac{1}{|\boldsymbol{\alpha}|^3}}+\overline{\Sigma^{\boldsymbol{\alpha}:-curl(\boldsymbol{\alpha}\times\boldsymbol{V})}\Sigma^{\frac{1}{|\boldsymbol{\alpha}|^3}}}\Big\}\overline{\boldsymbol{\alpha}}+\overline{\Sigma^{\frac{-\boldsymbol{\alpha}:curl(\boldsymbol{\alpha}\times\boldsymbol{V})}{|\boldsymbol{\alpha}|^3}}\Sigma^{\boldsymbol{\alpha}}}\Bigg]. \tag{C.2.15}$$

Similarly, we can obtain $\overline{\dot{\tilde{\boldsymbol{\alpha}}^T}}=\frac{\boldsymbol{\alpha}^T}{|\boldsymbol{\alpha}|}$ by replacing $\boldsymbol{\alpha}$, $\dot{\boldsymbol{\alpha}}$, $\overline{\boldsymbol{\alpha}}$ and $\dot{\overline{\boldsymbol{\alpha}}}$ above with their respective transpose and obtain

$$\begin{aligned}\overline{\dot{\tilde{\boldsymbol{\alpha}}^T}}=&\Big((-curl(\overline{\boldsymbol{\alpha}}\times\overline{\boldsymbol{V}}+\boldsymbol{L}^p))^T\ \overline{\frac{1}{|\boldsymbol{\alpha}|}}+\overline{\Sigma^{-(curl(\boldsymbol{\alpha}\times\boldsymbol{V}))^T\Sigma^{\frac{1}{|\boldsymbol{\alpha}|}}}}\Big)+\Bigg[\Bigg\{\Big(-\overline{\boldsymbol{\alpha}}:(curl(\overline{\boldsymbol{\alpha}}\times\overline{\boldsymbol{V}}+\boldsymbol{L}^p))\\&+\overline{\Sigma^{\boldsymbol{\alpha}^T}:\Sigma^{-(curl(\boldsymbol{\alpha}\times\boldsymbol{V}))^T}}\Big)\overline{\frac{1}{|\boldsymbol{\alpha}|^3}}+\overline{\Sigma^{-\boldsymbol{\alpha}:(curl(\boldsymbol{\alpha}\times\boldsymbol{V}))\Sigma^{\frac{1}{|\boldsymbol{\alpha}|^3}}}}\Bigg\}\overline{\boldsymbol{\alpha}^T}+\overline{\Sigma^{\frac{-\boldsymbol{\alpha}:(curl(\boldsymbol{\alpha}\times\boldsymbol{V}))}{|\boldsymbol{\alpha}|^3}}\Sigma^{\boldsymbol{\alpha}^T}}\Bigg].\end{aligned} \tag{C.2.16}$$

Using (C.2.13), (C.2.14), (C.2.15) and (C.2.16), we get

$$\begin{aligned}\dot{\overline{Q}}=\frac{1}{c_2}\Bigg[&\overline{sgn(|p|-1)}\ \overline{sgn(p)}\ \tilde{\boldsymbol{b}}^l\cdot\Bigg\{\Big\{\Big\{-curl(\overline{\boldsymbol{\alpha}}\times\overline{\boldsymbol{V}}+\boldsymbol{L}^p)\ \overline{\Big(\frac{1}{\boldsymbol{\alpha}}\Big)}+\overline{\Sigma^{-curl(\boldsymbol{\alpha}\times\boldsymbol{V})\Sigma^{\frac{1}{|\boldsymbol{\alpha}|}}}}\Big\}\\&\Big[\Big\{\Big(-\overline{\boldsymbol{\alpha}}:curl(\overline{\boldsymbol{\alpha}}\times\overline{\boldsymbol{V}}+\boldsymbol{L}^p)+\overline{\Sigma^{\boldsymbol{\alpha}}:\Sigma^{-curl(\boldsymbol{\alpha}\times\boldsymbol{V})}}\Big)\overline{\Big(\frac{1}{|\boldsymbol{\alpha}|^3}\Big)}\Big\}\ \overline{\tilde{\boldsymbol{\alpha}}^T}\\&+\overline{\tilde{\boldsymbol{\alpha}}}\ \Big\{\Big\{(-curl(\overline{\boldsymbol{\alpha}}\times\overline{\boldsymbol{V}}+\boldsymbol{L}^p))^T\ \overline{\Big(\frac{1}{\boldsymbol{\alpha}}\Big)}+\overline{\Sigma^{-(curl(\boldsymbol{\alpha}\times\boldsymbol{V}))^T\Sigma^{\frac{1}{|\boldsymbol{\alpha}|}}}}\Big\}\\&\Big[\Big\{\Big(-\overline{\boldsymbol{\alpha}}:(curl(\overline{\boldsymbol{\alpha}}\times\overline{\boldsymbol{V}}+\boldsymbol{L}^p))+\overline{\Sigma^{\boldsymbol{\alpha}^T}:\Sigma^{-(curl(\boldsymbol{\alpha}\times\boldsymbol{V})^T)}}\Big)\overline{\Big(\frac{1}{|\boldsymbol{\alpha}|^3}\Big)}\Big\}\Bigg\}\tilde{\boldsymbol{b}}^l\\&+\overline{sgn(|p|-1)}\ \overline{\Sigma^{sgn(p)}\Sigma^{\tilde{\boldsymbol{b}}^l\cdot\Big[\Big(-\frac{curl(\boldsymbol{\alpha}\times\boldsymbol{V})}{|\boldsymbol{\alpha}|}-\Big(\frac{\boldsymbol{\alpha}:curl(\boldsymbol{\alpha}\times\boldsymbol{V})}{|\boldsymbol{\alpha}|^3}\Big)\ \boldsymbol{\alpha}\Big)\tilde{\boldsymbol{\alpha}}^T}}\\&\qquad\overline{+\tilde{\boldsymbol{\alpha}}\Big(-\frac{\{curl(\boldsymbol{\alpha}\times\boldsymbol{V})\}^T}{|\boldsymbol{\alpha}|}-\Big(\frac{\boldsymbol{\alpha}:\{curl(\boldsymbol{\alpha}\times\boldsymbol{V})\}}{|\boldsymbol{\alpha}|^3}\Big)\ \boldsymbol{\alpha}^T\Big)\Big]\tilde{\boldsymbol{b}}^l}\\&+\overline{\Sigma^{sgn(|p|-1)}\Sigma^{sgn(p)\ \tilde{\boldsymbol{b}}^l\cdot\Big[\Big(-\frac{curl(\boldsymbol{\alpha}\times\boldsymbol{V})}{|\boldsymbol{\alpha}|}-\Big(\frac{\boldsymbol{\alpha}:curl(\boldsymbol{\alpha}\times\boldsymbol{V})}{|\boldsymbol{\alpha}|^3}\Big)\ \boldsymbol{\alpha}\Big)\tilde{\boldsymbol{\alpha}}^T}}\\&\qquad\overline{+\tilde{\boldsymbol{\alpha}}\Big(-\frac{\{curl(\boldsymbol{\alpha}\times\boldsymbol{V})\}^T}{|\boldsymbol{\alpha}|}-\Big(\frac{\boldsymbol{\alpha}:\{curl(\boldsymbol{\alpha}\times\boldsymbol{V})\}}{|\boldsymbol{\alpha}|^3}\Big)\ \boldsymbol{\alpha}^T\Big)\Big]\tilde{\boldsymbol{b}}^l}\Bigg]\end{aligned} \tag{C.2.17}$$

Using (C.2.6), (C.2.9), (C.2.10), (C.2.14), (C.2.15) and (C.2.16), we get the evolution of $\overline{\chi^l}$

given by (4.3.21) in section 4.3.

C.3 Dislocation density tensor corresponding to slip system l, $\boldsymbol{a}^l$

Following (4.3.17), the dislocation density corresponding to slip system l is defined as

$$\boldsymbol{a}^l := \chi^l \boldsymbol{\alpha}. \tag{C.3.1}$$

We take time derivative of (C.3.1) to obtain

$$\begin{aligned} \dot{\boldsymbol{a}^l} &= \dot{\chi^l}\boldsymbol{\alpha} + \chi^l \dot{\boldsymbol{\alpha}} \\ &= \dot{\chi^l}\boldsymbol{\alpha} - \chi^l curl(\boldsymbol{\alpha} \times \boldsymbol{V}). \end{aligned} \tag{C.3.2}$$

Using the fact that $\chi^l \approx (\chi^l)^2$, since χ^l can (approximately) take either of the values 0 or 1, the second term on the right hand side above can be written as

$$\begin{aligned} \chi^l curl(\boldsymbol{\alpha} \times \boldsymbol{V}) =& \chi^l \{curl(\boldsymbol{\alpha} \times \boldsymbol{V})\}_{im} \approx (\chi^l)^2 e_{mjk} \{\boldsymbol{\alpha} \times \boldsymbol{V}\}_{ik,j} \\ =& e_{mjk} \{\chi^l \boldsymbol{\alpha} \times \chi^l \boldsymbol{V}\}_{ik,j} - e_{mjk} \{\boldsymbol{\alpha} \times \boldsymbol{V}\}_{ik} \frac{\partial {\chi^l}^2}{\partial \chi_{j'}} \\ =& \{curl(\chi^l \boldsymbol{\alpha} \times \chi^l \mathbf{V})\}_{im} - 2\{\boldsymbol{\alpha} \times \boldsymbol{V}\}_{ik} e_{mjk} \chi^l \frac{\partial \chi^l}{\partial \chi_{j'}} \\ =& \{curl(\boldsymbol{a}^l \times \boldsymbol{V}^l)\}_{im} - 2\ \chi^l\ \{\boldsymbol{\alpha} \times \boldsymbol{V}\}_{ik} [\boldsymbol{X}(grad_{x'} \chi^l)]_{km} \\ \Rightarrow \chi^l curl(\boldsymbol{\alpha} \times \boldsymbol{V}) =& curl(\boldsymbol{a}^l \times \boldsymbol{V}^l) - 2\ \chi^l (\boldsymbol{\alpha} \times \boldsymbol{V})[\boldsymbol{X}(grad_{x'} \chi^l)], \end{aligned} \tag{C.3.3}$$

where e_{mjk} is a component of the third-order alternating tensor $\boldsymbol{X}$ and its action on a tensor

$\boldsymbol{A}$ is given by $\{\boldsymbol{X}(\boldsymbol{A})\}_i = e_{ijk}A_{jk}$, while its action on a vector $\boldsymbol{N}$ is given by $\{\boldsymbol{X}(\boldsymbol{N})\}_{ij} = e_{ijk}N_k$.

Using (C.3.2) and (C.3.3) above, we have

$$\dot{\boldsymbol{a}^l} = \dot{\chi^l}\boldsymbol{\alpha} - curl(\boldsymbol{a}^l \times \boldsymbol{V}^l) + 2\ \chi^l(\boldsymbol{\alpha} \times \boldsymbol{V})[\boldsymbol{X}(grad_{x'}\chi^l)]. \tag{C.3.4}$$

We apply the averaging operator (4.2.1) to both sides of (C.3.4) to get

$$\dot{\overline{\boldsymbol{a}^l}} = \dot{\overline{\chi^l}}\ \overline{\boldsymbol{\alpha}} + \overline{\Sigma^{\dot{\chi}}\ \Sigma^{\boldsymbol{\alpha}}} - curl(\overline{\boldsymbol{a}^l} \times \overline{\boldsymbol{V}^l}) - curl\Big(\overline{\Sigma^{\boldsymbol{a}^l} \times \Sigma^{\boldsymbol{V}^l}}\Big) + \overline{2\chi^l(\boldsymbol{\alpha} \times \boldsymbol{V})[\boldsymbol{X}(grad_{x'}\chi^l)]} \tag{C.3.5}$$

We have

$$\begin{aligned}
&\overline{2\chi^l(\boldsymbol{\alpha} \times \boldsymbol{V})[\boldsymbol{X}(grad_{x'}\chi^l)]} = 2\ \overline{\chi^l(\boldsymbol{\alpha} \times \boldsymbol{V})}\ [\boldsymbol{X}(grad\overline{\chi^l})] + 2\ \overline{\Sigma^{\chi^l(\boldsymbol{\alpha}\times\boldsymbol{V})}\ \Sigma^{\boldsymbol{X}(grad_{x'}\chi^l)}} \\
&= 2\ \Big(\overline{\chi^l}\ \overline{\boldsymbol{\alpha} \times \boldsymbol{V}} + \overline{\Sigma^{\chi^l}\ \Sigma^{\boldsymbol{\alpha}\times\boldsymbol{V}}}\Big)\ [\boldsymbol{X}(grad\overline{\chi^l})] + 2\ \overline{\Sigma^{\chi^l(\boldsymbol{\alpha}\times\boldsymbol{V})}\ \Sigma^{\boldsymbol{X}(grad_{x'}\chi^l)}} \\
&= 2\ \overline{\chi^l}\ (\overline{\boldsymbol{\alpha}} \times \overline{\boldsymbol{V}})[\boldsymbol{X}(grad\overline{\chi^l})] + 2\ \overline{\chi^l}\ \overline{\Sigma^{\boldsymbol{\alpha}} \times \Sigma^{\boldsymbol{V}}}[\boldsymbol{X}(grad\overline{\chi^l})] + 2\ \overline{\Sigma^{\chi^l}\ \Sigma^{\boldsymbol{\alpha}\times\boldsymbol{V}}}[\boldsymbol{X}(grad\overline{\chi^l})] \\
&\quad + 2\ \overline{\Sigma^{\chi^l(\boldsymbol{\alpha}\times\boldsymbol{V})}\ \Sigma^{\boldsymbol{X}(grad_{x'}\chi^l)}}
\end{aligned}$$

Hence, using (C.3.5), we have

$$\begin{aligned}
\dot{\overline{\boldsymbol{a}^l}} =& \dot{\overline{\chi^l}}\ \overline{\boldsymbol{\alpha}} + \overline{\Sigma^{\dot{\chi}}\ \Sigma^{\boldsymbol{\alpha}}} - curl(\overline{\boldsymbol{a}^l} \times \overline{\boldsymbol{V}^l}) - curl\Big(\overline{\Sigma^{\boldsymbol{a}^l} \times \Sigma^{\boldsymbol{V}^l}}\Big) \\
&+ 2\ \overline{\chi^l}\ (\overline{\boldsymbol{\alpha}} \times \overline{\boldsymbol{V}})[\boldsymbol{X}(grad\overline{\chi^l})] + 2\ \overline{\chi^l}\ \overline{\Sigma^{\boldsymbol{\alpha}} \times \Sigma^{\boldsymbol{V}}}[\boldsymbol{X}(grad\overline{\chi^l})] + 2\ \overline{\Sigma^{\chi^l}\ \Sigma^{\boldsymbol{\alpha}\times\boldsymbol{V}}}[\boldsymbol{X}(grad\overline{\chi^l})] \\
&+ 2\ \overline{\Sigma^{\chi^l(\boldsymbol{\alpha}\times\boldsymbol{V})}\ \Sigma^{\boldsymbol{X}(grad_{x'}\chi^l)}}
\end{aligned} \tag{C.3.6}$$

Finally, we use (C.2.6) and (4.3.21) to obtain the evolution of $\overline{\boldsymbol{a}^l}$ as (4.3.22) in section 4.3.

C.4 Total dislocation density corresponding to slip system l, ρ^l

The total dislocation density corresponding to slip system l is defined in (4.3.17) and is given by

$$\rho^l := \chi^l \, \boldsymbol{\alpha} : \boldsymbol{\alpha} \approx (\chi^l)^2 \, \boldsymbol{\alpha} : \boldsymbol{\alpha}. \tag{C.4.1}$$

We differentiate (C.4.1) with respect to time to get

$$\dot{\rho^l} = 2\chi^l \, \dot{\chi^l} \, \boldsymbol{\alpha} : \boldsymbol{\alpha} + 2 \, (\chi^l)^2 \, \boldsymbol{\alpha} : \dot{\boldsymbol{\alpha}} \tag{C.4.2}$$

$$= 2\dot{\chi^l}\rho^l + \chi^l[2\boldsymbol{\alpha} : \dot{\boldsymbol{\alpha}}] = 2\dot{\chi^l}\rho^l + \chi^l\dot{\rho} \tag{C.4.3}$$

We apply the averaging operator (4.2.1) to both sides of (C.4.2) and use (4.2.4) to get the evolution of $\overline{\rho^l}$ as

$$\dot{\overline{\rho^l}} = 2\dot{\overline{\chi^l}}\overline{\rho} + 2\overline{\Sigma\dot{\chi^l}\Sigma\rho} + \overline{\rho^l}\dot{\overline{\rho}} + \overline{\Sigma\chi^l\Sigma\dot{\rho}} \tag{C.4.4}$$

Finally, using (C.2.6) and (4.3.21), we have the evolution equation for $\overline{\rho^l}$ as (4.3.23) in section 4.3.

Bibliography

[AA19] Rajat Arora and Amit Acharya. Dislocation pattern formation in finite deformation crystal plasticity. *International Journal of Solids and Structures*, 2019.

[AC12] Amit Acharya and S.Jonathan Chapman. Elementary observations on the averaging of dislocation mechanics: dislocation origin of aspects of anisotropic yield and plastic spin. *Procedia IUTAM*, 3:297–309, 2012.

[Ach01] Amit Acharya. A model of crystal plasticity based on the theory of continuously distributed dislocations. *Journal of the Mechanics and Physics of Solids*, 49(4):761 – 784, 2001.

[Ach03] Amit Acharya. Driving forces and boundary conditions in continuum dislocation mechanics. *Proceedings of the Royal Society of London. Series A: Mathematical, Physical and Engineering Sciences*, 459, 2003.

[Ach04] Amit Acharya. Constitutive analysis of finite deformation field dislocation mechanics. *Journal of the Mechanics and Physics of Solids*, 52(2):301 – 316, 2004.

[Ach07] Amit Acharya. On the choice of coarse variables for dynamics. *Multiscale Computational Engineering*, 5:483–489, 2007.

[Ach10] Amit Acharya. Coarse-graining autonomous ODE systems by inducing a separation of scales: practical strategies and mathematical questions. *Mathematics and Mechanics of Solids*, 15:342–352, 2010.

[Ach11a] Amit Acharya. Microcanonical entropy and mesoscale dislocation mechanics and plasticity. *Journal of Elasticity*, 104(1):23–44, 2011.

[Ach11b] Amit Acharya. Microcanonical entropy and mesoscale dislocation mechanics and plasticity. *Journal of Elasticity*, 104(1):23–44, Aug 2011.

[AET09a] Gil Ariel, Bjorn Engquist, and Richard Tsai. A multiscale method for highly oscillatory ordinary differential equations with resonance. *Mathematics of Computation*, 78(266):929–956, 2009.

[AET09b] Gil Ariel, Bjorn Engquist, and Richard Tsai. Numerical multiscale methods for coupled oscillators. *Multiscale Modeling & Simulation*, 7(3):1387–1404, 2009.

[AGK+11] Zvi Artstein, Charles William Gear, Ioannis G. Kevrekidis, Marshall Slemrod, and Edriss S. Titi. Analysis and computation of a discrete KdV-burgers type equation with fast dispersion and slow diffusion. *SIAM Journal on Numerical Analysis*, 49(5):2124–2143, 2011.

[AKST07] Zvi Artstein, Ioannis G. Kevrekidis, Marshall Slemrod, and Edriss S. Titi. Slow observables of singularly perturbed differential equations. *Nonlinearity*, 20(11):2463, 2007.

[ALT07] Zvi Artstein, Jasmine Linshiz, and Edriss S. Titi. Young measure approach to computing slowly advancing fast oscillations. *Multiscale Modeling & Simulation*, 6(4):1085–1097, 2007.

[AR06] Amit Acharya and Anish Roy. Size effects and idealized dislocation microstructure at small scales: Predictions of a phenomenological model of mesoscopic field dislocation mechanics: Part i. *Journal of the Mechanics and Physics of Solids*, 54:1687–1710, 2006.

[Art02] Zvi Artstein. On singularly perturbed ordinary differential equations with measure valued limits. *Mathematica Bohemica*, 127:139–152, 2002.

[AS01] Zvi Artstein and Marshall Slemrod. The singular perturbation limit of an elastic structure in a rapidly flowing nearly inviscid fluid. *Quarterly of Applied Mathematics*, 61(3):543–555, 2001.

[AS06] Amit Acharya and Aarti Sawant. On a computational approach for the approximate dynamics of averaged variables in nonlinear ODE systems: toward the derivation of constitutive laws of the rate type. *Journal of the Mechanics and Physics of Solids*, 54(10):2183–2213, 2006.

[AV96] Zvi Artstein and Alexander Vigodner. Singularly perturbed ordinary differential equations with dynamic limits. *Proceedings of the Royal Society of Edinburgh*, 126A:541–569, 1996.

[Bab97] Marijan Babic. Average balance equations for granular materials. *International Journal of Engineering Science*, 35(5):523 – 548, 1997.

[CAA18] Sabyasachi Chatterjee, Amit Acharya, and Zvi Artstein. Computing singularly perturbed differential equations. *Journal of Computational Physics*, 354:417–446, 2018.

[CPZ+] Sabyasachi Chatterjee, Giacomo Po, Xiaohan Zhang, Amit Acharya, and Nasr Ghoniem. An approach to plasticity without phenomenology. *In preparation.*

[DAS16] Amit Das, Amit Acharya, and Pierre Suquet. Microstructure in plasticity without nonconvexity. *Computational Mechanics*, 57(3):387–403, Mar 2016.

[EA00] Anter El-Azab. Statistical mechanics treatment of the evolution of dislocation distributions in single crystals. *Physical Review B*, 61(18), 2000.

[EA06] Anter El-Azab. Statistical mechanics of dislocation systems. *Scripta Materialia*, 54(5):723–727, 2006.

[Esh57] John Douglas Eshelby. The determination of the elastic field of an ellipsoidal inclusion, and related problems. *Proc. R. Soc. Lond. A*, 241, 1957.

[FVE04] Ibrahim Fatkullin and Eric Vanden-Eijnden. A computational strategy for multiscale systems with applications to lorenz 96 model. *Journal of Computational Physics*, 200:605–638, 2004.

[GAM15] Akanksha Garg, Amit Acharya, and Craig E. Maloney. A study of conditions for dislocation nucleation in coarser-than-atomistic scale models. *Journal of the Mechanics and Physics of Solids*, 75:76 – 92, 2015.

[GCZ03] I. Groma, F.F. Csikor, and M. Zaiser. Spatial correlations and higher-order gradient terms in a continuum description of dislocation dynamics. *Acta Materialia*, 51(5):1271–1281, 2003.

[GON05] Julia R. Greer, Warren C. Oliver, and William D. Nix. Size dependence of mechanical properties of gold at the micron scale in the absence of strain gradients. *Acta Materialia*, 53(6):1821 – 1830, 2005.

[Gro97] I. Groma. Link between the microscopic and mesoscopic length-scale description of the collective behavior of dislocations. *Physical Review B*, 56(10), 1997.

[GZ09] H. Groh and H.M. Zbib. Advances in discrete dislocations dynamics and multiscale modeling. *J. Eng. Mater. Technol*, 131(4), 2009.

[Hoc16] Thomas Hochrainer. Thermodynamically consistent continuum dislocation dynamics. *Journal of the Mechanics and Physics of Solids*, 88:12 – 22, 2016.

[HS04] M. A. Haque and M. T. A. Saif. Deformation mechanisms in free-standing nanoscale thin films: A quantitative in situ transmission electron microscope study. *Proceedings of the National Academy of Sciences*, 101(17):6335–6340, 2004.

[HSZG14] Thomas Hochrainer, Stefan Sandfeld, Michael Zaiser, and Peter Gumbsch. Con-

tinuum dislocation dynamics: Towards a physical theory of crystal plasticity. *Journal of the Mechanics and Physics of Solids*, 63:167–178, 2014.

[HZG07] T. Hochrainer, M. Zaiser, and P. Gumbsch. A three-dimensional continuum theory of dislocation systems: kinematics and mean-field formulation. *Philosophical Magazine*, 87(8-9):1261–1282, 2007.

[JBG10] Andrew T. Jennings, Michael J. Burek, and Julia R. Greer. Microstructure versus size: Mechanical properties of electroplated single crystalline cu nanopillars. *Phys. Rev. Lett.*, 104:135503, Apr 2010.

[KAA75] U.F. Kocks, A.S. Argon, and M.F. Ashby. *Thermodynamics and Kinetics of Slip*. Progress in materials science. Pergamon Press, 1975.

[KGDP08] D. Kiener, W. Grosinger, G. Dehm, and R. Pippan. A further step towards an understanding of size-dependent crystal plasticity: In situ tension experiments of miniaturized single-crystal copper samples. *Acta Materialia*, 56(3):580 – 592, 2008.

[KGH+03] Ioannis G. Kevrekidis, C. William Gear, James M. Hyman, Panagiotis G. Kevrekidis, Olof Runborg, and Constantinos Theodoropoulos. Equation-free, coarse-grained multiscale computation: Enabling mocroscopic simulators to perform system-level analysis. *Communications in Mathematical Sciences*, 1(4):715–762, 2003.

[KGMW10] Oliver Kraft, Patric A. Gruber, Reiner Mönig, and Daniel Weygand. Plasticity in confined dimensions. *Annual Review of Materials Research*, 40(1):293–317, 2010.

[KM03] U.F. Kocks and H. Mecking. Physics and phenomenology of strain hardening: the FCC case. *Progress in Materials Science*, 48, 2003.

[LDK01] C. Lemarchand, B. Devincre, and L.P. Kubin. Homogenization method for a discrete-continuum simulation of dislocation dynamics. *Journal of the Mechanics and Physics of Solids*, 49(9):1969–1982, 2001.

[MZ18] Mehran Monavari and Michael Zaiser. Annihilation and sources in continuum dislocation dynamics. *Materials Theory*, 2:3, 2018.

[NN08] K.S. Ng and A.H.W. Ngan. Breakdown of schmid's law in micropillars. *Scripta Materialia*, 59(7):796 – 799, 2008.

[OJ14] Robert E. O'Malley Jr. *Historical Developments in Singular Perturbations*. Springer, 2014.

[PDA11] Saurabh Puri, Amit Das, and Amit Acharya. Mechanical response of multicrystalline thin films in mesoscale field dislocation mechanics. *Journal of the Mechanics and Physics of Solids*, 59(11):2400 – 2417, 2011.

[Pie83] D. Pierce. Shear band bifurcations in ductile single crystals. *Journal of the Mechanics and Physics of Solids*, 31(2):133–153, 1983.

[PK50] M. Peach and J. S. Koehler. The forces exerted on dislocations and the stress fields produced by them. *Phys. Rev.*, 80:436–439, Nov 1950.

[PMC+14] Giacomo Po, Mamdouh S. Mohamed, Tamer Crosby, Can Erel, Anter El-Azab, and Nasr Ghoniew. Recent progress in discrete dislocation dynamics and its applications to micro plasticity. *The Journal of The Minerals, Metals and Materials Society*, 66(10), 2014.

[RA05] Anish Roy and Amit Acharya. Finite element approximation of field dislocation mechanics. *Journal of the Mechanics and Physics of Solids*, 53(1):143 – 170, 2005.

[SA12] Marshall Slemrod and Amit Acharya. Time-averaged coarse variables for multiscale dynamics. *Quart. Appl. Math*, 70:793–803, 2012.

[San16] Anders W. Sandvik. Numerical Solutions of Classical Equations of Motion. `http://physics.bu.edu/~py502/lectures3/cmotion.pdf`, 2016. [Online; accessed 19-February-2017].

[SHZG11] Stefan Sandfeld, Thomas Hochrainer, Michael Zaiser, and Peter Gumbsch. Continuum modeling of dislocation plasticity: Theory, numerical implementation, and validation by discrete dislocation simulations. *Journal of Materials Research*, 26(5):623–632, 2011.

[SZ15] Stefan Sandfeld and Michael Zaiser. Pattern formation in a minimal model of continuum dislocation plasticity. *Modelling and Simulation in Materials Science and Engineering*, 23(6):065005, 2015.

[TAD13] Likun Tan, Amit Acharya, and Kaushik Dayal. Coarse variables of autonomous ode systems and their evolution. *Computer Methods in Applied Mechanics and Engineering*, 253:199–218, 2013.

[TAD14] Likun Tan, Amit Acharya, and Kaushik Dayal. Modeling of slow time-scale behavior of fast molecular dynamic systems. *Journal of the Mechanics and Physics of Solids*, 64:24–43, 2014.

[TOM10] Molei Tao, Houman Owhadi, and Jerrold E. Marsden. Nonintrusive and structure preserving multiscale integration of stiff and hamiltonian systems with hidden slow dynamics via flow averaging. *Multiscale Model. Simul*, 8:1269–1324, 2010.

[TVS85] Andrey Nikolayevich Tikhonov, Adelaida Borisovna Vasileva, and Alekse Georgievich Sveshnikov. *Differential Equations*. Springer-Verlag, Berlin, 1985.

[UDFN04] Michael D. Uchic, Dennis M. Dimiduk, Jeffrey N. Florando, and William D. Nix. Sample dimensions influence strength and crystal plasticity. *Science*, 305(5686):986–989, 2004.

[USD09] Michael D. Uchic, Paul A. Shade, and Dennis M. Dimiduk. Plasticity of micrometer-scale single crystals in compression. *Annual Review of Materials Research*, 39(1):361–386, 2009.

[VE03] Eric Vanden-Eijnden. Numerical techniques for multi-scale dynamical systems with stochastic effects. *Communications Mathematical Sciences 1*, pages 385–391, 2003.

[Ver05] Ferdinand Verhulst. Methods and applications of singular perturbations. *Texts in Applied Mathematics*, 50, 2005.

[Was65] Wolfgang Wasow. *Asymptotic Expansions for Ordinary Differential Equations*. Wiley Interscience, New York, 1965.

[XEA15] Shengxu Xia and Anter El-Azab. Computational modelling of mesoscale dislocation patterning and plastic deformation of single crystals. *Modelling Simul. Mater. Sci. Eng*, 23, 2015.

[YZK01] Hasan Yasin, Hussein M. Zbib, and Moe A. Khaleel. Size and boundary effects in discrete dislocation dynamics: coupling with continuum finite element. *Materials Science and Engineering: A*, 309-310:294–299, 2001.

[ZCA13] Y. Zhu, S.J. Chapman, and A. Acharya. Dislocation motion and instability. *Journal of the Mechanics and Physics of Solids*, 61:1835–1853, 2013.

[ZRB02] Hussein M. Zbib, Tomas Diaz de la Rubia, and Vasily Bulatov. A multiscale model of plasticity based on discrete dislocation dynamics. *J. Eng. Mater. Technol*, 124(1):78–87, 2002.